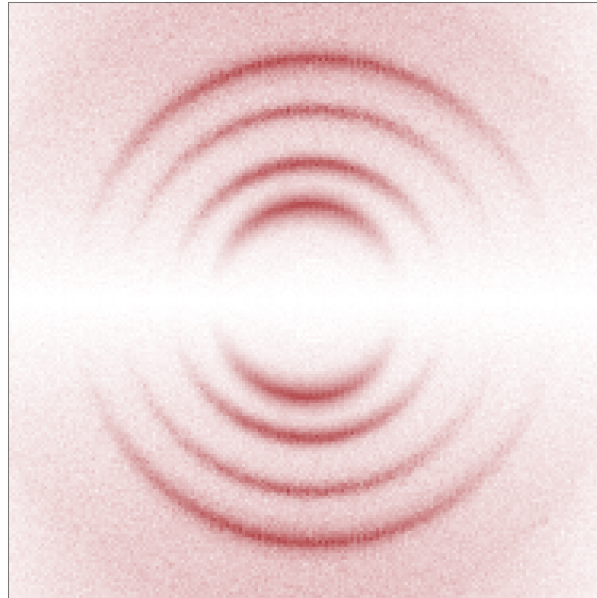


NONDIPOLAR PHOTOIONIZATION
OF ATOMS AND MOLECULES



Dissertation

zur Erlangung des Doktorgrades der Naturwissenschaften
vorgelegt beim Fachbereich Physik der
Johann Wolfgang Goethe-Universität in Frankfurt am Main von

Sven Eric Grundmann
aus Bad Homburg v. d. Höhe

Frankfurt 2022 (D30)

vom Fachbereich Physik der
Johann Wolfgang Goethe-Universität als Dissertation angenommen

Dekan:
Prof. Dr. Harald Appelshäuser

Gutachter:
Prof. Dr. Reinhard Dörner
Prof. Dr. Till Jahnke

Datum der Disputation: 1. April 2022

CONTENTS

1	INTRODUCTION	1
I BACKGROUND		
2	THE LIGHT PHASE AND THE PHOTON MOMENTUM	3
3	THE PHOTOIONIZATION CROSS SECTION	9
4	PHOTOELECTRON ANGULAR DISTRIBUTIONS	17
5	MULTIPLE IONIZATION	27
5.1	One-Photon Double Ionization of He and H ₂	27
5.2	K-Shell Ionization of N ₂ Followed by Auger Decay	30
6	THE MOLECULAR DOUBLE-SLIT EXPERIMENT	31
6.1	Interference in the Photoionization of Molecules	31
6.2	...Beyond the Dipole Approximation	41
7	INTERPLAY OF NONDIPOLE EFFECTS	49
II METHODS		
8	EXPERIMENT	53
8.1	Cold Target Recoil Ion Momentum Spectroscopy	53
8.2	Experimental Sessions	58
9	DATA ANALYSIS	63
9.1	Preparatory Steps	63
9.2	Electron Momentum and Energy Calculations	67
9.3	Ion Momentum and Energy Calculations	70
9.3.1	Zero Momentum in Light Propagation Direction	72
9.3.2	Correction of Lens Distortions	74
9.3.3	Sum Momentum Corrections	83
III RESULTS		
10	FORWARD/BACKWARD ASYMMETRIES IN PHOTOIONIZATION	89
10.1	The Origin of Photoion Backward Emission	90
10.2	Forward Momentum Sharing among Photoelectrons	97
11	THE QUASIFREE MECHANISM (QFM)	101
11.1	The QFM's Unique Fingerprint	102
11.2	A Pure Quadrupole Contribution to Photoionization	108
11.3	Probing the Two-Electron Cusp	110
12	THE SIMPLEST DOUBLE SLIT	115
12.1	Interference, Decoherence, and Entanglement	116
12.2	Zeptosecond Birth Time Delay	121
12.3	...of a Two-Electron Wave	125
13	MOLECULAR NITROGEN	129
13.1	Disentangling Gerade and Ungerade Quantum States	130
13.2	Parity-Resolved Nondipole Effects	137
13.3	Discussion	141
IV CONCLUSION		
14	SUMMARY	143
15	OUTLOOK	145

V	APPENDIX	
A	POLAR PLOTS AND THE POLE BIAS	147
B	MFPADS OF LINEAR MOLECULES	153
C	STANDARD MOMENTUM AND ENERGY DISTRIBUTIONS	157
	BIBLIOGRAPHY	174
	DEUTSCHE ZUSAMMENFASSUNG	186
	DANKSAGUNG	192
	OWN PUBLICATIONS	195
	PRESS REVIEW	199
	CONTRIBUTIONS TO CONFERENCES AND SEMINARS	202
	PRACTICAL EXPERIENCE RELATED TO RESEARCH	203
	AKADEMISCHER LEBENSLAUF	205

INTRODUCTION

Photoionization is one of the archetypal quantum-mechanical phenomena. Here, the photon transfers all its energy to a bound electron, which uses a fraction of it to overcome the binding energy and takes the rest as kinetic energy. The effect was arguably among the most important topics of 20th-century physics and it is still investigated in modern day research. Its explanation is attributed to A. Einstein [1], who developed it from M. Planck's quantum theory of radiation [2].

The present work deals with photoionization in the realm of the absorption of one single photon—as opposed to strong-field ionization (see p. 8). The formal treatment of one-photon ionization usually employs a semi-classical approach, where the electron's initial and final states are described as quantum-mechanical wave functions but the photon is treated as a classical electromagnetic wave (see p. 9). In the calculation of photoionization cross sections with this semi-classical method, there is an often used approximation which is called the *electric dipole approximation*. Mathematically, the application of the dipole approximation corresponds to truncating the series expansion of an exponential after the leading term (see Eq. 3.13). Physically, this means neglecting the linear photon momentum and the spatial dependence of the light field. The dipole approximation is valid if the wavelength of the light is much larger than the spatial extent of the target and if the photon momentum is small compared to the momenta of the reaction products, which is generally the case for photon energies short above the electron binding energy.

For the present work, we experimentally investigated *nondipolar photoionization*, i.e., one-photon ionization at high photon energies where the dipole approximation breaks down. In our experiments, we irradiated single atoms and molecules with such high-energetic photons and measured the three-dimensional momentum distributions of the reaction fragments to uncover the effects of the linear photon momentum and the spatially-dependent light field on photoionization. Our observations allow the first profound insight into photoionization that reveals all photon properties, i.e., photon energy, spin, linear momentum, and the speed of light. Hopefully, our efforts make a constructive contribution to the understanding and the further exploration of light-matter interaction.

Part I

BACKGROUND

 THE LIGHT PHASE AND THE PHOTON MOMENTUM

The present work deals with ionization of single atoms and molecules (the *targets*) upon absorption of single photons beyond the electric dipole approximation, i.e., with nondipolar photoionization. The dipole approximation is a simplification used regularly within the semi-classical formalism of light-matter interaction, which will be discussed in Ch. 3. The dipole approximation is valid at small photon energies where both of the following conditions are fulfilled:

1. The light wavelength λ is much larger than the spatial extent of the target and the light phase is therefore nearly constant over the whole relevant region of space.
2. The photon momentum is negligibly small compared to the momenta of the reaction fragments.

Accordingly, dipolar photoionization is driven by the photon energy and the photon spin alone, but the photon momentum and the spatial dependence of the light phase play no role.

The experiments conducted for this work do not meet the requirements of the dipole approximation. The present chapter introduces the two additional light properties that come into play here.

The light phase

Light is an electromagnetic wave. The electric field and the orthogonal magnetic field of the light wave oscillate in phase. To inspect the light phase, one can therefore simply consider the electric field independently. The electric field vector E of a light wave is given by

$$E(\mathbf{r}, t) \propto \hat{\mathbf{e}} \sin(\mathbf{k}_\gamma \cdot \mathbf{r} - \omega t) = \hat{\mathbf{e}} \sin \varphi, \quad (2.1)$$

where \mathbf{r} is the position vector, t is the time, $\hat{\mathbf{e}}$ is the polarization direction vector, ω is the angular frequency, and \mathbf{k}_γ is the wave vector that specifies the light propagation direction with the magnitude $k_\gamma = 2\pi/\lambda$.¹ For a certain time and position, the light phase φ , which is given in radians, indicates the state of the electric field vector within the wave's oscillatory cycle.

The Bohr radius a_0 —the most probable distance between the electron and the proton in a hydrogen atom—is a reasonable estimate for the magnitude of the target's spatial extent in photoionization. Figure 2.1 A shows a common illustration of the electric dipole approximation. Here, the light phase is constant over the whole relevant region of space, because the wavelength is much larger than the Bohr radius. For short wavelengths, this approximation breaks down, as indicated in Fig. 2.1 B. Here, the spatially extended target experiences different light phases at any point in time.

The wavelength and the photon energy E_γ are related through $E_\gamma = hc/\lambda$, where c is the speed of light and h is the Planck constant. The photon energies used in

¹Throughout this work, vectors are set in bold italics (\mathbf{a}). Vectors of unit length are denoted likewise with an additional circumflex ("hat", $\hat{\mathbf{a}}$). The magnitude of a vector is set in non-bold italics, as are scalar components (a , a_x). Also, the center dot is reserved for the vector dot product. If the intended meaning is multiplication, either the multiplication symbol (\times) is used or there is no space between the two parts of the expression. A multiplication symbol between two vectors denotes the vector cross product ($\mathbf{a} \times \mathbf{b}$).

the present work range from 300 eV to 2160 eV, which corresponds to wavelengths from 41.33 Å ($\approx 78 \times a_0$) to 5.74 Å ($\approx 11 \times a_0$). Even though these wavelengths are still larger than the Bohr radius, the results presented in this work cannot be explained by means of the dipole approximation alone.

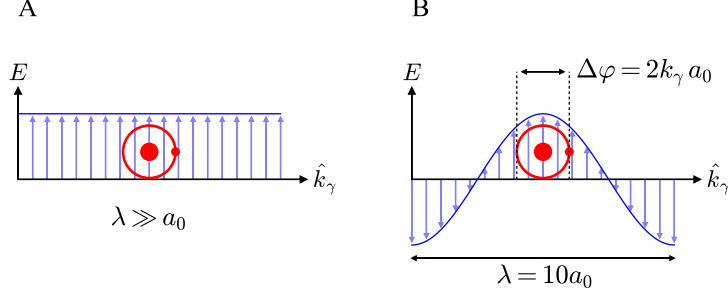


Figure 2.1: Snapshot of a hydrogen atom (red) exposed to a linearly polarized electromagnetic wave. (A) Electric dipole approximation: The light wavelength λ is much larger than the Bohr radius a_0 , the electric field (blue) has no spatial dependence, and the light phase is constant over the whole relevant region of space. (B) Wavelength and Bohr radius have the same order of magnitude and the light phase is spatially dependent.

In the corresponding literature, the spatially-dependent light phase provides the prevailing interpretative approach for the effects associated with nondipolar photoionization, but the role of the photon momentum is hardly given any attention (see, e.g., Refs. [3, 4] for reviews). This is probably because nondipole studies usually focus on the momentum distributions of photoelectrons, while the photon momentum is mostly imparted onto the center of mass of the ionized target—which is essentially given by the photoion (see p. 6). In the present work, we go beyond such an incomplete view of photoionization and specifically search for the photon momentum contribution in the ion momentum distribution.

The photon momentum

In his magnum opus titled *A Treatise on Electricity and Magnetism* that was published in 1873, J. C. Maxwell states that an electromagnetic wave exerts a radiation pressure parallel to its propagation direction [5]. The cause for this radiation pressure is the linear momentum carried by the wave. An expression for this momentum can be derived from the total Lorentz force acting on a charged particle and Newton's second law:

$$\frac{d\mathbf{p}_{mech}}{dt} = q(\mathbf{E} + \mathbf{v} \times \mathbf{B}), \quad (2.2)$$

where \mathbf{p}_{mech} is the mechanical momentum of the particle, q is its charge, and \mathbf{v} is its velocity. \mathbf{E} and \mathbf{B} are the electric and magnetic field vectors of the wave. Using the Maxwell equations and vector calculus (see, e.g., Ref. [6] for a detailed derivation), Eq. 2.2 can be transformed into

$$\frac{d\mathbf{p}_{mech}}{dt} + \epsilon_0\mu_0 \frac{d}{dt} \int_V \mathbf{S} dV = \oint_A \mathcal{T} dA, \quad (2.3)$$

where ϵ_0 is the vacuum permittivity, μ_0 is the vacuum permeability, \mathcal{T} is the Maxwell stress tensor, and \mathbf{S} is the Poynting vector. While the Poynting vector

represents magnitude and direction of the energy-flux density of the electromagnetic wave, the Maxwell stress tensor accounts for the interaction between the Lorentz force and the mechanical momentum. Hence, the right-hand side of Eq. 2.3 describes the momentum flow per unit area across the surface A into the volume V that acts on the combined system of particles and fields inside V . Without such external interaction, the rate of change of mechanical momentum of a particle interacting with the electromagnetic wave is given by

$$\frac{d\mathbf{p}_{mech}}{dt} = -\epsilon_0\mu_0 \frac{d}{dt} \int_V \mathbf{S} dV . \quad (2.4)$$

Hence, the following expression describes the momentum carried by the electromagnetic wave inside volume V :

$$\mathbf{p}_{em} = \epsilon_0\mu_0 \int_V \mathbf{S} dV . \quad (2.5)$$

In case of a monochromatic plane wave propagating parallel to the unit vector $\hat{\mathbf{x}}$, the Poynting vector is simply given by

$$\mathbf{S} = cu\hat{\mathbf{x}} , \quad (2.6)$$

where c is the speed of light and u is the volumetric energy density of the electromagnetic wave. With Eq. 2.6 substituted into Eq. 2.5, the momentum of the electromagnetic wave becomes

$$\mathbf{p}_{em} = \epsilon_0\mu_0 c \int_V u dV = \frac{E_{em}}{c} \hat{\mathbf{x}} , \quad (2.7)$$

where E_{em} is the energy of the electromagnetic wave inside volume V and where we have used the fundamental relation $\epsilon_0\mu_0 c^2 = 1$. Accordingly, the momentum of an electromagnetic wave equals its energy divided by the speed of light. Depending on the circumstances of the observation, light possesses wave- or particle-like properties. The particle nature of electromagnetic radiation was first acknowledged by A. Einstein in 1905: Studying the photoelectric effect led to him to the conclusion that light consists of energy quanta [1]. The term *photon* for these packets of light was later coined by G. Lewis in 1926 [7]. The photon momentum is given by²

$$\mathbf{p}_\gamma = \frac{E_\gamma}{c} \hat{\mathbf{x}} , \quad (2.8)$$

where E_γ is the photon energy. This relation follows from Eq. 2.7 if one thinks of the photon as a point-like particle that condenses its energy density u into an infinitesimally small volume element.

However, Eq. 2.8 can also be derived from the relativistic energy-momentum relation of a particle,

$$E^2 = (pc)^2 + (m_0c^2)^2 , \quad (2.9)$$

where E is the total energy of the particle, p is its momentum, and m_0 is its rest mass [8]. As the photon is a massless particle, Eq. 2.8 follows directly from Eq. 2.9 with $m_0 = 0$.

For easier use in our conventional units, we can rewrite Eq. 2.8 as

$$p_\gamma[\text{au}] = \frac{E_\gamma[\text{eV}] \cdot e}{c} \cdot \frac{a_0}{\hbar} \approx \frac{E_\gamma[\text{eV}]}{3729} , \quad (2.10)$$

²Throughout this work, \mathbf{p} indicates a momentum vector, while $|k| = k = 2\pi/\lambda$ describes a wave vector, where λ is the wavelength of the wave. The relation $p = \hbar k$ applies for light and matter waves. Only in atomic units, where $\hbar = 1$, \mathbf{p} and \mathbf{k} can be used interchangeably.

where e is the elementary charge, a_0 is the Bohr radius, and \hbar is the reduced Planck constant (all in SI units). Note that \hbar/a_0 equals 1 au of linear momentum.

The radiation pressure of light d_{rad} is closely related to the linear momentum. Radiation pressure is a many-particle phenomenon and an expression can be derived considering the rate of momentum change of a continuous stream of photons:

$$d_{rad} = \frac{d}{dt} \frac{Nk_\gamma}{A} = \frac{d}{dt} \frac{NE_\gamma}{Ac} = \frac{I}{c}, \quad (2.11)$$

where N is the number of absorbed photons impinging perpendicular on the area A during the time dt , and I is the intensity of the photon beam. Note that the notion of a radiation pressure is obsolete for one-photon ionization of atoms and molecules because no intensity can be assigned to a single photon.

Kinematics of photoionization

The prediction of detailed three-dimensional momentum distributions of the final-state reaction fragments of photoionization requires quantum mechanical calculations. However, considering the photon momentum, the photon energy, and the respective conservation laws, one can derive boundary conditions for these momentum distributions (see, e.g., Ref. [9]). With the least amount of free parameters, this becomes particularly useful in the case of one-photon single ionization, i.e., the emission of only one electron upon photoabsorption. Here, the momentum conservation law dictates that

$$\mathbf{p}_e + \mathbf{p}_i = \mathbf{p}_\gamma, \quad (2.12)$$

where \mathbf{p}_e and \mathbf{p}_i are the momentum vectors of the emitted electron (photoelectron) and the recoiling ion (photoion). Furthermore, the conservation of energy determines that

$$\frac{p_e^2}{2m_e} + \frac{p_i^2}{2m_i} = E_\gamma - E_{bin}, \quad (2.13)$$

where m_e and m_i are the electron and ion masses, and E_{bin} is the binding energy of the electron. Here, we assume that the target system is in the energetic ground state prior to and after the photoabsorption. For absorption of a photon propagating in \hat{x} direction and with Eq. 2.12 substituted into Eq. 2.13, we get the following relation

$$\frac{m_e p_{i,x}^2 + m_i (p_\gamma - p_{i,x})^2}{2m_e m_i} + \frac{(m_e + m_i)(p_{i,y}^2 + p_{i,z}^2)}{2m_e m_i} = E_\gamma - E_{bin}. \quad (2.14)$$

Through an intermediate step,

$$p_{i,x}^2 - \frac{2m_i p_\gamma p_{i,x}}{m_e + m_i} + \frac{m_i p_\gamma^2}{m_e + m_i} \times \frac{m_e + m_i}{m_e + m_i} + p_{i,y}^2 + p_{i,z}^2 = \frac{2m_e m_i}{m_e + m_i} (E_\gamma - E_{bin}), \quad (2.15)$$

Eq. 2.14 can be transformed into its final form

$$\left(p_{i,x} - \frac{m_i}{m_e + m_i} p_\gamma \right)^2 + p_{i,y}^2 + p_{i,z}^2 = \frac{2m_e m_i}{m_e + m_i} (E_\gamma - E_{bin}) - \frac{m_e m_i}{(m_e + m_i)^2} p_\gamma^2, \quad (2.16)$$

which is the equation of a sphere in momentum space for the ion. The right-hand side of the equation is the square of the radius and the correction to the \hat{x} component of the ion momentum on the left-hand side indicates that the sphere is not centered at the origin but shifted in positive \hat{x} direction. This shift indicates that the photon momentum is shared among the reaction fragments proportional to the ratios of the individual masses to the combined mass. Because $m_i \gg m_e$, the photon momentum appears almost alone in the measured ion momentum distributions (see Ch. 10).

However, the above derivation only holds true for single ionization. In case of double (or multiple) ionization, there are additional free parameters and the relations are less straightforward. For example, as outlined in Ch. 11, the photon momentum can be imparted onto the electrons alone in one-photon double ionization.

If the photon momentum is small compared to the momenta of the reaction fragments, the terms in Eq. 2.16 that depend on p_γ can be neglected. At small photon energies, where the electric dipole approximation is valid, this simplification is usually justified. On the other hand, this indicates how the high photon energies used in this work are favorable in order to uncover the effect of the photon momentum on photoionization.

Short review of photon momentum studies

Due to their close relationship, the photon momentum and the radiation pressure share a similar research history. After Maxwell's prediction of the radiation pressure in 1873, it took nearly 30 years for experiments to follow up. But then in 1901, even two independent experimental reports confirmed the existence of the radiation pressure. On the one hand, E. Nichols and F. Hull reported on the use of a torsion balance to measure the radiation pressure of the focused light of an electric light bulb [10]. In the same year, P. Lebedew published results of a similar experimental setup that measured the radiation pressure of light emitted by an arc lamp [11].

A process in which the momentum of single photons plays an important role is the Compton effect. A. H. Compton received the Nobel Prize in Physics in 1927 for its discovery [12]. The Compton effect describes the scattering of a photon by an electron that receives energy due to the momentum transferred onto it. In his experiment, Compton examined the wavelength of X-rays reflected from a graphite block and compared it to the direct X-rays. The photon's loss of energy to the electron became observable by the change of the light's wavelength. The Compton effect and its quantum-mechanical description are still investigated today (see, e.g., Ref. [13]).

The first demonstration of the photon momentum's influence on single atoms was performed by O. R. Frisch in 1933 [14]. In his experiment, Frisch showed that a beam of sodium atoms is deflected upon absorption of light emitted from a sodium spectral lamp.

At the end of the twentieth century, the photon momentum became the basis of some interesting applications. For instance, in 1997 the Nobel Prize in Physics was awarded to S. Chu, C. Cohen-Tannoudji and W. D. Phillips for their development of laser cooling, a technique that makes use of the linear momentum of light to trap and cool atoms with lasers [15]. Another intriguing example for an application of the radiation pressure are space propulsion techniques using solar-sails. This space technology is believed to support human and robotic exploration of the solar system in the future [16].

In recent years, the role of the photon momentum in photoionization received renewed interest from the side of fundamental research. The photoionization process can be considered in the one-photon (photoelectric effect) and strong-field

ionization regimes. In one-photon ionization, the energy of the absorbed photon must be larger than the binding energy of one or more electrons. For strong-field ionization, the photon-density in the focus of a laser beam must either be large enough for multiphoton absorption to take place, or the electric field has to be strong enough to distort the potential barrier in such a way that the electron tunnels through it (see, e.g., Ref. [17] for a comprehensive work on strong-field ionization). In 2014, S. Chelkowski et al. addressed the question of how the photon momentum is shared between the electron and the ion in these different photoionization regimes [18]. For strong-field ionization and for the photoelectric effect, they derived similar scaling rules for the average momentum shift of the reaction fragments in light propagation direction as function of the photon momentum. For strong-field ionization, these predictions were experimentally confirmed by A. Hartung et al. in 2019 [19] and a comprehensive study of the general role of the photon momentum in strong-field ionization can be found in Ref. [20]. The experimental confirmation of Chelkowski's photon momentum scaling rules for one-photon ionization (Eqs. 10.1 & 10.2) is covered in Ch. 10 of this work. Recently, K. Lin et al. further investigated nondipole effects in strong-field ionization. They found experimental evidence, that the energies of electrons depend on the emission direction because of the interaction between the moving electrons with the incident laser pulse [21].

The photoionization cross section σ quantifies the probability for the emission of an electron from an atom or molecule upon absorption of a photon. The cross section is traditionally given as an area in terms of *barn* [b], where $1 \text{ b} = 10^{-28} \text{ m}^2$. In order to estimate the reaction rate for an experiment, the cross section is multiplied by the photon current and the areal density of target particles. Vice versa, the cross section of a particular reaction can be determined in a dedicated experiment through measuring the reaction rate, if the current of projectiles and the areal density of target particles are known.

Usually, the cross section is not examined in absolute terms but as function of one or more parameters of the initial and final states of the reaction. For instance, the cross section for one-photon single ionization of a certain atom is commonly given as function of the photon energy and the energy level of the bound electron in the initial state [22]. Another example is the emission probability of an electron in photoionization as function of angles in a certain frame of reference (see Ch. 4). Such a cross section is called *differential* and one has to integrate over (all) the free parameters to get the (*total*) *integrated* cross section.

Integrated and differential cross sections are used throughout this work to compare theoretical predictions and experimental results. How the experimental results were obtained is the subject of Part II and the theoretical methods are referenced appropriately. Nevertheless, the following paragraphs provide a general overview and a minimal example on how the cross section can be calculated from quantum theory, which is partly adapted from Ref. [23].

Semi-classical description of light-matter interaction

In quantum mechanics, a stationary physical system can be described by the time-independent Schrödinger equation,

$$\hat{H}\Psi = E\Psi, \quad (3.1)$$

where \hat{H} is the Hamilton operator,¹ E is the system's energy, and Ψ is the wave function that characterizes the stationary state of the system (i.e., all observables are independent of time). Equation 3.1 is an eigenvalue equation and the wave function Ψ is an eigenfunction of the Hamilton operator with the corresponding eigenvalue E .

For single-photon ionization of atoms and molecules, the quantum mechanical treatment can be limited to the description of the free (a.k.a., *continuous*) and the bound electrons, while the light is treated as a classical electromagnetic wave (see, e.g., Ref. [24]).

In this semi-classical approximation, one mathematical method used regularly to calculate cross sections is the time-dependent perturbation theory, which is valid in situations where the perturbation is so weak that it does not distort the initial and final states (see, e.g., Ref. [25]). Perturbation theory splits the system's Hamilton operator \hat{H} into an unperturbed part \hat{H}_0 , whose eigenvalue problem has been solved, and a part of a small perturbation \hat{H}_p . In photoionization, the light accounts for the perturbation and the interaction of the photon with the system is described by the interaction Hamiltonian \hat{H}_{int} .

¹Throughout this work, operators of quantum theory are set in non-bold italics with an additional circumflex ("hat", \hat{H}).

The probability for a transition from the initial state Ψ_i to the final state Ψ_f upon photoabsorption is proportional to the squared modulus of the complex-valued transition amplitude (a.k.a., the transition matrix element),

$$\mathcal{P}_{i \rightarrow f} \propto |\mathcal{M}_{i \rightarrow f}|^2 \times \delta(E_f - E_i - E_\gamma), \quad (3.2)$$

where the Dirac delta function δ expresses energy conservation and the transition amplitude is given by

$$\mathcal{M}_{i \rightarrow f} = \int d^3r \Psi_f^* \hat{H}_{int} \Psi_i, \quad (3.3)$$

where Ψ_f^* is the complex conjugate of Ψ_f and $d^3r = dx dy dz$. The photoionization cross section is given by

$$\sigma = 4\pi^2 \alpha E_\gamma |\mathcal{M}_{i \rightarrow f}|^2, \quad (3.4)$$

where α is the fine-structure constant (see, e.g., Ref. [23] for an extensive derivation). Hence, in order to estimate the photoionization cross section we need to find expressions for the initial and final states of the reaction, and for the interaction Hamiltonian.

Initial-state wave function

To derive an expression for the initial-state wave function, we consider electrons trapped in a single-center Coulomb potential of an atomic nucleus of charge Z . For a N -electron atom, the nonrelativistic Hamilton operator is then given by

$$\hat{H} = \sum_{i=1}^N \left(\frac{-\hbar^2 \nabla_i^2}{2m_e} - \frac{Ze^2}{4\pi\epsilon_0 r_i} \right) + \sum_{i>j=1}^N \frac{e^2}{4\pi\epsilon_0 r_{ij}}, \quad (3.5)$$

where ∇_i is the partial derivative operator $(\frac{\partial}{\partial x_i}, \frac{\partial}{\partial y_i}, \frac{\partial}{\partial z_i})$,² r_i is the distance between nucleus and electron i , m_e is the electron mass, e is the electron charge, ϵ_0 is the vacuum permittivity, and r_{ij} is the distance between electrons i and j [24]. Accordingly, for a hydrogen-like atom ($N = 1$) the Hamilton operator simply becomes

$$\hat{H} = \frac{-\hbar^2 \nabla^2}{2m_e} - \frac{Ze^2}{4\pi\epsilon_0 r}. \quad (3.6)$$

With Eq. 3.6 inserted into Eq. 3.1, the following wave functions are exact analytic solutions (eigenfunctions) of the single-electron Schrödinger equation

$$\Psi_{n\ell m}(r, \vartheta, \varphi) = R_{n\ell}(r) Y_{\ell m}(\vartheta, \varphi), \quad (3.7)$$

where the tuple (r, ϑ, φ) characterizes the radial distance from the origin, the polar angle, and the azimuthal angle in a spherical coordinate system centered at the nucleus [26]. $R_{n\ell}(r)$ expresses the radial dependence and $Y_{\ell m}(\vartheta, \varphi)$ —the spherical harmonics (see Eq. 4.8)—describe the angular dependence of the wave function. The radial part is given by

$$R_{n\ell}(r) = \sqrt{\left(\frac{2Z}{na_0}\right)^3 \frac{(n-\ell-1)!}{2n((n+\ell)!)}} e^{-\rho/2} \rho^\ell L_{n-\ell-1}^{2\ell+1}(\rho), \quad (3.8)$$

where a_0 is the Bohr radius, ρ is shorthand for $\rho = 2Zr/(na_0)$, and $L_{n-\ell-1}^{2\ell+1}(\rho)$ are the associated Laguerre polynomials.

²Note that $-i\hbar\nabla$ is the position space representation of the momentum operator \hat{p} .

The principal quantum number n indicates the energy levels (eigenvalues) of the state,

$$E_n = -\frac{Z^2}{n^2} \times 13.6 \text{ eV} , \quad (3.9)$$

the second quantum number ℓ determines its orbital angular momentum ($\ell = 0, \dots, n-1$), and the magnetic quantum number m indicates the projection of ℓ onto the quantization axis ($m = -\ell, \dots, 0, \dots, \ell$).

The square of a wave function like Eq. 3.7 describes the spatial probability density of the electron as function of the angular coordinates and the distance from the nucleus. This probability density is shifted further away from the nucleus with increasing n . Hence, the principal quantum number ($n = 1, 2, 3, \dots$) is often termed *electron shell* (K, L, M, \dots) and the K -shell is closest to the nucleus. Similarly, the second quantum number ($\ell = 0, 1, 2, 3, \dots$) is called the *subshell* (s, p, d, f, \dots). For a certain set of quantum numbers, a position space wave function like Eq. 3.7 is called an *atomic orbital*.

In all experiments conducted for this work, the photoelectron originates from the K -shell of the atom or molecule. For K -shell photoionization, the photoelectron's initial state is characterized by $n = 1$ and $\ell = m = 0$. With these quantum numbers, we get the following expressions

$$Y_{00}(\vartheta, \varphi) = \sqrt{\frac{1}{4\pi}} , \quad L_0^0(\rho) = 1 , \quad \text{and} \quad R_{10}(r) = \sqrt{\frac{4Z^3}{a_0^3}} e^{-Zr/a_0} .$$

Hence, in the hydrogen approximation—i.e., neglecting all electrons other than the photoelectron—the ground-state wave function of an electron in a hydrogen-like atom of nuclear charge Z becomes

$$\Psi_{100}(r) = \sqrt{\frac{Z^3}{\pi a_0^3}} e^{-Zr/a_0} . \quad (3.10)$$

Later, we will use such a hydrogen-like one-electron wave function as the initial state for Eq. 3.3.

Beyond the hydrogen approximation, the electron-electron interaction (right sum term in Eq. 3.5) prevents solving the eigenvalue problem exactly. Even the two-electron Schrödinger equation for the helium atom has no exact analytic solution. There are two conceptionally different ways to approach this problem. Either the electron-electron interaction is ignored and the many-electron wave function is written as the product of many hydrogen-like one-electron wave functions with an appropriate Z (see, e.g., Ref. [27]), or numerical solutions of the Schrödinger equation are used (see, e.g., Ref. [28] for an overview of numerical approaches to describe the photo-double-ionization process of helium).

Interaction operator and electric dipole approximation

The interaction Hamiltonian for Eq. 3.3 can be obtained upon substituting the momentum operator $-i\hbar\nabla$ in Eq. 3.6 by $-i\hbar\nabla + \frac{|e|\hbar}{c}A(\mathbf{r}, t)$, where $A(\mathbf{r}, t)$ is the light's vector potential that describes the interaction of the electron with the time-dependent external electromagnetic radiation.

As shown in Ref. [24], the vector potential has the form

$$A(\mathbf{r}, t) \propto \hat{\mathbf{e}} e^{i(\mathbf{k}_\gamma \cdot \mathbf{r} - \omega t)} , \quad (3.11)$$

and the interaction Hamiltonian can be isolated from the unperturbed Hamiltonian and written as

$$\hat{H}_{int} \propto -i\hbar\nabla \cdot \hat{\mathbf{e}} e^{i\mathbf{k}_\gamma \cdot \mathbf{r}} e^{-i\omega t} , \quad (3.12)$$

where $\hat{\epsilon}$ is the direction of the light polarization, ω is the angular frequency of the radiation, and \mathbf{k}_γ is the light's wave vector with magnitude $k_\gamma = p_\gamma/\hbar$. This simplified form of the interaction Hamiltonian uses the Coulomb gauge for A , where $\nabla \cdot A = 0$, and it neglects the A^2 term that accounts for two-photon processes like the incoming and the outgoing photon in Compton scattering (see, e.g., Ref. [13]).

The $e^{ik_\gamma \cdot r}$ term from the interaction Hamiltonian can be expanded as

$$e^{ik_\gamma \cdot r} = 1 + ik_\gamma \cdot r + O(k_\gamma^2), \quad (3.13)$$

and replacing $e^{ik_\gamma \cdot r}$ by 1 in Eq. 3.12 indicates the application of the *electric dipole approximation* of light-matter interaction. Application of the dipole approximation is synonymous to neglecting the photon momentum and the spatially-dependent light phase: If $p_\gamma = 0$, then $k_\gamma = 0$ and $e^{ik_\gamma \cdot r} = 1$.

The present work demonstrates that the dipole approximation is not valid in general for photoionization at photon energies between 300 eV and 2160 eV. However, the influence of nondipole terms on the absolute cross section is very small (see Ch. 4, p. 19) and for the remainder of the present chapter we set $p_\gamma = 0$ accordingly.

To gain an explicit expression for the dipole interaction Hamiltonian, we assume linear polarization parallel to the \hat{z} direction, where $\nabla \cdot \hat{\epsilon}$ becomes $\frac{\partial}{\partial z}$. We also drop the term $e^{-i\omega t}$, because it becomes $|e^{-i\omega t}|^2 = 1$ when the modulus of transition amplitude is squared to get the transition probability. Hence, we can use

$$\hat{H}_{int} = \frac{-i\hbar}{m_e \omega} \frac{\partial}{\partial z}, \quad (3.14)$$

in Eq. 3.3 [23].

Final-state wave function and Born approximation

Eventually, we need an expression for the final-state wave function. As shown by H. Bethe and E. Salpeter [29], the continuum state of the photoelectron can be approximated as a free wave at high but non-relativistic energies, i.e., if $I_p \ll E_\gamma \ll m_e c^2$, where I_p is the binding energy and $m_e c^2 \approx 511$ keV is the rest mass of the electron. Bethe and Salpeter applied the so-called *Born approximation* [30] to photoionization and neglected the interaction between the photoelectron and the residual charged particles, i.e., the nucleus and other electrons in case of a multi-electron system.

The Hamilton operator of the interaction-free particle is given by

$$\hat{H} = \frac{-\hbar^2 \nabla^2}{2m_e}, \quad (3.15)$$

and a solution of the corresponding Schrödinger equation that can be used in Eq. 3.3 is the normalized plane wave

$$\Psi_k(r) = \sqrt{\frac{m_e k}{(2\pi)^3 \hbar^2}} e^{ik \cdot r}, \quad (3.16)$$

where k is the electron wave vector with magnitude $k = p/\hbar$ [23].

For more accurate calculations of photoionization cross sections beyond the Born approximation, final-state wave functions can take the form of Coulomb waves (see, e.g., Ref. [31]), or Hartree-Fock waves (see, e.g., Ref. [32]). While Coulomb

waves account for the behavior of the electron in a Coulomb potential, the Hartree-Fock method provides an approximation for the correlated wave function of a many-electron system.

Transition amplitude and cross section

With Eqs. 3.14 & 3.16 substituted into Eq. 3.3, the transition amplitude becomes

$$\mathcal{M}_{i \rightarrow f} = \frac{\sqrt{k}}{\hbar\omega\sqrt{m_e}} (2\pi)^{-(3/2)} \int \left(-i\hbar \frac{\partial}{\partial z} e^{-ik \cdot r} \right) \Psi_i(\mathbf{r}) d^3r. \quad (3.17)$$

Here, the differential operator acts on the final state instead of the initial state, which is allowed because of the identity

$$\int \Psi_f^* (\hat{O}\Psi_i) d^3r = \int (\hat{O}\Psi_f)^* \Psi_i d^3r \quad (3.18)$$

for each Hermitian operator \hat{O} including \hat{H}_{int} . The plane-wave final state $e^{-ik \cdot r}$ is an eigenstate of $-i\hbar \frac{\partial}{\partial z}$, which is the momentum operator parallel to the polarization direction. The corresponding eigenvalue is $\hbar k \cos \vartheta$, where ϑ is the angle enclosed by the electron momentum vector and the photon polarization direction. Hence, we can substitute $-i\hbar \frac{\partial}{\partial z} e^{-ik \cdot r}$ by $\hbar k \cos \vartheta e^{-ik \cdot r}$ and Eq. 3.17 becomes

$$\mathcal{M}_{i \rightarrow f} = \frac{k^{(3/2)}}{\omega\sqrt{m_e}} \cos \vartheta (2\pi)^{-(3/2)} \int e^{-ik \cdot r} \Psi_i(\mathbf{r}) d^3r. \quad (3.19)$$

Furthermore, the integral can be substituted by the Fourier transform of the initial-state wave function in position space,

$$\Psi_i(\mathbf{k}) = (2\pi)^{-(3/2)} \int e^{-ik \cdot r} \Psi_i(\mathbf{r}) d^3r, \quad (3.20)$$

where $\Psi_i(\mathbf{k})$ is the initial state in momentum space.³

Exact analytic expressions for the momentum-space wave functions of hydrogen-like atomic orbitals can be obtained directly from solving the respective Schrödinger equation in momentum representation (see, e.g., Ref. [34]). Here, we use an approximation for large electron momenta from Bethe and Salpeter (Ref. [29], Eq. 70.4) for initial ns states,

$$\Psi_n(\mathbf{k}) = \frac{2\sqrt{2}}{\pi a_0^{(5/2)}} \times \frac{Z^{(5/2)}}{n^{(3/2)} |\mathbf{k}|^4}. \quad (3.21)$$

Accordingly, we can rewrite Eq. 3.19 as

$$\mathcal{M}_{i \rightarrow f} = \frac{2\sqrt{2}}{\pi\omega\sqrt{m_e}a_0^{(5/2)}} \times \frac{Z^{(5/2)}}{n^{(3/2)}k^{(5/2)}} \cos \vartheta, \quad (3.22)$$

and the squared modulus of the transition amplitude as

$$|\mathcal{M}_{i \rightarrow f}|^2 = \frac{8}{\pi^2\omega^2 m_e a_0^5} \times \frac{Z^5}{n^3 k^5} \cos^2 \vartheta. \quad (3.23)$$

Before we insert the latter expression into Eq. 3.4 to calculate the cross section, we make use of the following approximation: If the photon energy is much larger

³As suggested by Eqs. 3.19 & 3.20, photoionization is sometimes referred to as "simply" the Fourier transform of the initial position-space wave function of the electron. Also, these relations support the idea that *the final-state momentum of the photoelectron must be present in its initial state already*, which is taught to Physics students at the Goethe University Frankfurt and which was used in Ref. [33] for the imaging of a molecular wave function.

than the binding energy of the photon, the photon and electron have roughly the same energy, i.e., $\hbar\omega = E_\gamma \approx (\hbar^2 k^2)/(2m_e)$. Hence, we can insert $k = \sqrt{2m_e E_\gamma}/\hbar$ into Eq. 3.23 and arrive at the expression

$$\begin{aligned} \frac{d\sigma}{d\Omega} &= \frac{32\alpha E_\gamma \hbar^2}{m_e a_0^5 \omega^2 \hbar^2} \times \frac{Z^5 \hbar^5}{n^3 (2m_e E_\gamma)^{(5/2)}} \cos^2 \vartheta \\ &= \frac{32\alpha \hbar^7}{2^{(5/2)} m_e^{(7/2)} a_0^5} \times \frac{Z^5}{n^3 E_\gamma^{(7/2)}} \cos^2 \vartheta, \end{aligned} \quad (3.24)$$

which is the angle-differential cross section and integration over all angles yields the integrated cross section

$$\sigma = \frac{128\pi\alpha\hbar^7}{3 \times 2^{(5/2)} m_e^{(7/2)} a_0^5} \times \frac{Z^5}{n^3 E_\gamma^{(7/2)}}. \quad (3.25)$$

For easier use in the conventional units, we can rewrite Eq. 3.25 as

$$\sigma[b] = 5.09 \times 10^{11} \frac{Z^5}{n^3 (E_\gamma[eV])^{(7/2)}}. \quad (3.26)$$

Equation 3.26 correctly reflects the key attributes of the cross section at high energies: On the one hand, the quick drop for higher electronic shells ($\sigma \propto n^{-3}$) and for increasing photon energies ($\sigma \propto E_\gamma^{-7/2}$). On the other hand, the rapid growth with higher proton numbers ($\sigma \propto Z^5$). However, at photon energies close to the ionization threshold I_p —where the Born approximation breaks down—Eq. 3.26 dramatically overestimates the cross section.

By means of two adjustments, the accuracy of the approximation can be considerably improved for the photon energies and reaction targets used in the present work. First, we can use an exact momentum-space wave function instead of Eq. 3.21 for the calculation of the transition amplitude (see Eqs. 8.10 & 70.6a in Ref. [29] and Eq. 5.79 in Ref. [23]). Second, we can abandon the hydrogen approximation and use the effective nuclear charge Z_{eff} [35] (instead of Z) that accounts for the shielding of the nuclear charge in a many-electron atom. Accordingly, Eq. 3.26 becomes

$$\sigma[b] = 5.09 \times 10^{11} \frac{Z_{eff}^5 (E_\gamma - I_p)^{(3/2)}}{n^3 (E_\gamma)^5}, \quad (3.27)$$

where the unit of all energies is eV. Accurate values for Z_{eff} can be found in Ref. [36].

The predictions of Eq. 3.27 for the 1s-shells of hydrogen, helium and nitrogen atoms are shown in Fig. 3.1 and tabulated in Tab. 3.1 for some relevant energies. As the neutral helium and nitrogen atoms have two 1s electrons in their ground states, the corresponding results of Eq. 3.27 have been doubled for the display in Fig. 3.1 and in Tab. 3.1. The approximations are compared to accurate calculations from Ref. [37] where the relativistic Dirac equation has been used instead of the Schrödinger equation and the final states were described as Hartree-Fock waves. The agreement between the approximation and the exact calculations is decent, which is somehow surprising: Although the exact Fourier transform of the initial state was used, the continuum state of the photoelectron is still described as a free wave. Accordingly, Eq. 3.27 is a result of the Born approximation which is only valid at photon energies high above threshold.

To sum up, Eq. 3.27 may prove useful in getting a quick estimate for K -shell photoionization cross sections. Its derivation is supposed to serve as an instructive example of how to calculate a photoionization cross section in general.

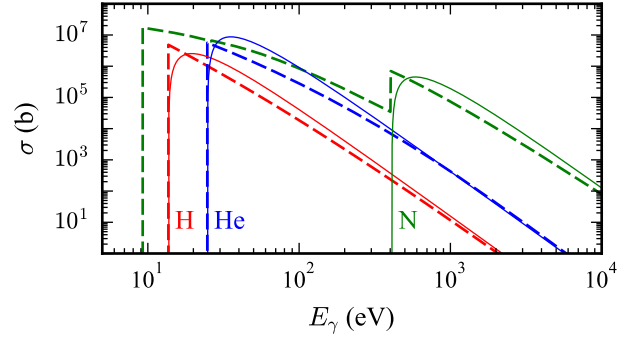


Figure 3.1: Photoionization cross section of H, He, and N as function of the photon energy. The solid lines show the results of Eq. 3.27 and the dashed lines present accurate calculations from Ref. [37].

	H	He	He	N	N
Z_{eff}	1	1.6875	1.6875	6.6651	6.6651
E_γ [eV]	800	300	1775	880	2160
Eq. 3.27	34.3 b	26.2 kb	57.9 b	258.6 kb	20.9 kb
Ref. [37]	24.4 b	16.1 kb	62.0 b	105.8 kb	8.5 kb

Table 3.1: Photoionization cross section of H, He, and N at some photon energies relevant for the present work.

A *photoelectron angular distribution* specifies the emission probability of the photoelectron under a certain angle in a set frame of reference. Neglecting the normalization factor, the term *angle-differential cross section* is often used synonymously. Photoelectron angular distributions are a sensitive probe of nondipole effects and consequently an important concept for this work. The present chapter deals with the photoelectron angular distribution in the laboratory frame of reference. If the target is a molecule, the photoelectron angular distribution can also be considered in the molecular frame of reference (MFPAD), which will be discussed in Ch. 6. The research field investigating angle-differential cross sections operates under the name *angle-resolved photoelectron spectroscopy* (ARPES). A comprehensive review of the early developments and milestone discoveries of ARPES was published by J. Jenkin in 1981 [38]. A more recent review that focuses on nondipole effects in photoelectron angular distributions is that of O. Hemmers et al. from 2004 [3].

Angular distribution of a photoelectron from a *s*-subshell

All photoelectrons measured for this work originate from the *K*-shell of the respective target where $\ell = 0$. In the following paragraphs, we will derive an expression for the shape of the angle-differential cross section of such photoelectrons that includes the effect of the nonzero photon momentum. Here, we are not concerned with the integrated value of the cross section. Therefore, some constants (a_0, m_e, \dots) and parameters (n, Z) are omitted occasionally and the wave functions are not necessarily normalized.

Any *s*-state has no angular dependency and we can simply use

$$\Psi_s(\mathbf{r}) = e^{-r} \quad (4.1)$$

for the position space wave function of the initial state.

To account for the effect of the photon momentum on the photoelectron angular distribution, the interaction Hamiltonian must include the leading order nondipole term. Accordingly, we truncate the series expansion of $e^{i\mathbf{k}_\gamma \cdot \mathbf{r}}$ only after the $i\mathbf{k}_\gamma \cdot \mathbf{r}$ term and the interaction Hamiltonian (Eq. 3.14) becomes

$$\hat{H}_{int} \propto \frac{\partial}{\partial z} + \frac{\partial}{\partial z} i\mathbf{k}_\gamma \cdot \mathbf{r}, \quad (4.2)$$

in which $i\mathbf{k}_\gamma \cdot \mathbf{r}$ and $\frac{\partial}{\partial z}$ commute because the light propagation is parallel to the \hat{x} direction. We let this differential operator act on $\Psi_s(\mathbf{r})$ and get

$$\hat{H}_{int} e^{-r} \propto \left(\frac{\partial}{\partial z} + i\mathbf{k}_\gamma \cdot \mathbf{r} \frac{\partial}{\partial z} \right) e^{-r} = \left(\frac{z}{r} + ik_\gamma \frac{xz}{r} \right) e^{-r}. \quad (4.3)$$

Following the substitution of Eq. 4.3 into Eq. 3.3, we can separate the transition amplitude into two parts,

$$\mathcal{D} \propto \int d^3r \Psi_f^*(\mathbf{r}) \frac{z}{r} e^{-r} \quad \text{and} \quad (4.4)$$

$$\mathcal{Q} \propto ik_\gamma \int d^3r \Psi_f^*(\mathbf{r}) \frac{xz}{r} e^{-r}, \quad (4.5)$$

where \mathcal{D} is the electric dipole (E1) term and \mathcal{Q} is the electric quadrupole (E2) term of the transition amplitude. In general, an additional magnetic dipole (M1)

contribution originates from the $ik_\gamma \cdot r$ term of the nondipole expansion but it vanishes for the initial s-state because of the missing angular dependency (see, e.g., Refs. [29, 39]).

In the previous chapter, we used a plane wave (Eq. 3.16) as the final state of the photoionization process. Plane waves are the eigenstates of the Hamilton operator of an interaction free particle (Eq. 3.15) in cartesian coordinates. In spherical coordinates, these eigenstates are given by

$$\Psi_{klm}(\mathbf{r}) = \frac{i^\ell}{\hbar} \sqrt{\frac{2m_e k}{\pi}} j_\ell(kr) Y_{\ell m}(\hat{\mathbf{r}}), \quad (4.6)$$

where $j_\ell(kr)$ are the spherical Bessel functions of the first kind and $Y_{\ell m}(\hat{\mathbf{r}})$ are the spherical harmonics. Equation 4.6 resembles a free spherical wave state and is commonly called a partial wave.

Through the plane wave expansion and the spherical harmonic addition theorem, any free plane wave can be expressed as the superposition of free spherical waves of all possible ℓ values [27]. Accordingly, the use of a plane wave guarantees that all partial waves are considered when calculating the integrated cross section. Here, we want to identify those partial waves that are accessible in the reaction, because their combination shapes the photoelectron angular distribution. The procedure is to search for such combinations of ℓ and m where either \mathcal{D} or \mathcal{Q} are non-zero by inserting Eq. 4.6 into Eqs. 4.4 & 4.5.

We solve this problem in spherical coordinates and choose $\hat{\mathbf{e}}$ as the quantization axis: $x = r \sin(\vartheta) \cos(\varphi)$, $y = r \sin(\vartheta) \sin(\varphi)$, and $z = r \cos(\vartheta)$.¹ Hence, Eq. 4.3 becomes

$$\hat{H}_{int} e^{-r} \propto \left(\cos \vartheta + ik_\gamma r \cos \vartheta \sin \vartheta \cos \varphi \right) e^{-r}, \quad (4.7)$$

and the real part of the spherical harmonics is given by

$$Y_{\ell m}(\vartheta, \varphi) = \sqrt{\frac{2\ell+1}{4\pi} \frac{(\ell-m)!}{(\ell+m)!}} P_{\ell m}(\cos \vartheta) \cos(m\varphi), \quad (4.8)$$

where $P_{\ell m}$ are the associated Legendre polynomials with $\cos \vartheta$ as the argument. In spherical coordinates, Eqs. 4.4 & 4.5 can be rewritten as

$$\mathcal{D} \propto \int d\Omega Y_{\ell m}^*(\vartheta, \varphi) \cos \vartheta \times \int dr j_\ell^*(kr) r^2 e^{-r} \quad \text{and} \quad (4.9)$$

$$\begin{aligned} \mathcal{Q} &\propto ik_\gamma \int d\Omega Y_{\ell m}^*(\vartheta, \varphi) \left(\cos \vartheta \sin \vartheta \cos \varphi \right) \\ &\quad \times \int dr j_\ell^*(kr) r^3 e^{-r}, \end{aligned} \quad (4.10)$$

where $d^3r = r^2 \sin \vartheta dr d\vartheta d\varphi = r^2 dr d\Omega$ is the volume element in spherical coordinates.

With the explicit forms of two associated Legendre polynomials,

$$P_{10}(\cos \vartheta) = \cos \vartheta \quad \text{and} \quad P_{21}(\cos \vartheta) = -3 \cos \vartheta \sin \vartheta,$$

we can write out the spherical harmonics,

$$Y_{10}(\vartheta, \varphi) = \sqrt{\frac{3}{4\pi}} \cos \vartheta \quad \text{and} \quad Y_{21}(\vartheta, \varphi) = -\sqrt{\frac{45}{24\pi}} \cos \vartheta \sin \vartheta \cos \varphi,$$

¹Here, k_γ is the azimuthal reference and parallel to $\hat{\mathbf{x}}$, while the direction of light polarization $\hat{\mathbf{e}}$ defines the polar axis and is parallel to $\hat{\mathbf{z}}$ (see Appx. A for the definition of polar and azimuthal angles).

and substitute them into Eqs. 4.9 & 4.10 to obtain

$$\mathcal{D} \propto \sqrt{\frac{4\pi}{3}} \int d\Omega Y_{\ell m}^*(\vartheta, \varphi) Y_{10}(\vartheta, \varphi) \times \int dr j_{\ell}^*(kr) r^2 e^{-r} \quad \text{and} \quad (4.11)$$

$$\begin{aligned} \mathcal{Q} &\propto -i \sqrt{\frac{24\pi}{45}} \int d\Omega Y_{\ell m}^*(\vartheta, \varphi) Y_{21}(\vartheta, \varphi) \\ &\times \int dr j_{\ell}^*(kr) k_{\gamma} r^3 e^{-r}. \end{aligned} \quad (4.12)$$

Conveniently, the spherical harmonics form an orthogonal system, i.e.,

$$\int d\Omega Y_{\ell m}^*(\vartheta, \varphi) Y_{\ell' m'}(\vartheta, \varphi) = \delta_{\ell \ell'} \delta_{m m'}, \quad (4.13)$$

where δ is the Kronecker delta function ($\delta_{ij} = 1$ for $i = j$, $\delta_{ij} = 0$ for $i \neq j$).

Hence, \mathcal{D} is only non-zero if $\ell = 1$ & $m = 0$, \mathcal{Q} is non-zero if $\ell = 2$ & $m = 1$, and the angular part of the final-state wave function of a photoelectron originating from a s -subshell can be written as

$$\psi_f(\vartheta, \varphi) = a_d + a_q := \mathcal{D} \cos \vartheta + \mathcal{Q} \cos \vartheta \sin \vartheta \cos \varphi, \quad (4.14)$$

where the angular dependencies resemble those of the spherical harmonics shown in Fig. 4.1.

The photoelectron angular distribution corresponds to the squared modulus of Eq. 4.14 and becomes

$$\frac{d}{d\Omega} \mathcal{P} \propto |a_d|^2 + 2 \times \text{Re}(a_d a_q) + |a_q|^2. \quad (4.15)$$

The explicit values for $|\mathcal{Q}|$ & $|\mathcal{D}|$ are mainly determined by the radial integrals of Eqs. 4.11 & 4.12 (see, e.g., Ref. [27]). The radial integral of \mathcal{Q} contains the acquainted factor $k_{\gamma} r$ that underlines how the quadrupole amplitude is insignificant in case of small photon momenta.

The ratio $|\mathcal{Q}|/|\mathcal{D}|$ is commonly expressed in terms of the so-called *nondipole (interference) parameter* γ , which is defined as

$$\gamma = 6 \frac{|\mathcal{Q}|}{|\mathcal{D}|} \quad (4.16)$$

for s -subshells [40].² Accordingly, the shape of the angular distribution of a photoelectron from a s -subshell can be written as

$$\frac{d}{d\Omega} \mathcal{P} \propto \cos^2 \vartheta + \frac{\gamma}{3} \cos^2 \vartheta \sin \vartheta \cos \varphi + \frac{\gamma^2}{36} \cos^2 \vartheta \sin^2 \vartheta \cos^2 \varphi. \quad (4.17)$$

For instance, the nondipole parameter γ has a value of approximately 1 in case of one-photon single ionization of helium at 1500 eV photon energy (see results shown in Fig. 10.4). However, to emphasize the nondipole effects, we choose $\gamma = 3$ and show the three individual terms of Eq. 4.17 in Figure 4.2 A (and their superposition in B) in the plane defined by the photon momentum and the linear polarization vector.

Apparently, the interference term $2 \times \text{Re}(a_d a_q)$ (dotted line in Fig. 4.2) does not change the absolute value of the cross section at all, but it does significantly change the shape of the photoelectron angular distribution. This nondipole effect

²In Ref. [40], the quadrupole amplitude is written independently of the photon momentum, which is why the definition of γ is a function of k_{γ} in the original reference. We have also omitted the factor $\cos \Delta\phi$, where $\Delta\phi$ is the phase difference of the two partial waves, because this phase difference vanishes in the Born approximation.

is an important concept throughout the present work and we will focus on its implications in Ch. 10.

The pure quadrupole part of the transition $|Q|^2$ is much weaker than the interference term. In the photon energy range considered in the present work, its implications are mostly insignificant and the contribution to the absolute cross section can be neglected. However, in case of one-photon double ionization of He and H₂, a neat trick will allow us to directly observe the quadrupole transition amplitude in a subset of experimental data where $\mathcal{D} = 0$ & $\mathcal{Q} > 0$ (see Ch. 11).

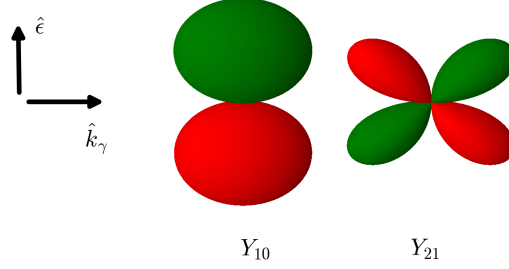


Figure 4.1: Modulus of the real spherical harmonics $\text{Re}(Y_{\ell m})$ where green resembles $\text{sgn}(\text{Re}(Y_{\ell m})) = +1$ and red corresponds to $\text{sgn}(\text{Re}(Y_{\ell m})) = -1$. Note that Y_{10} has odd parity (-1) because space inversion would swap the colors, but Y_{21} has even parity ($+1$) because it equals its space inverted counterpart. In general, the parity of the spherical harmonics is given by $(-1)^\ell$.

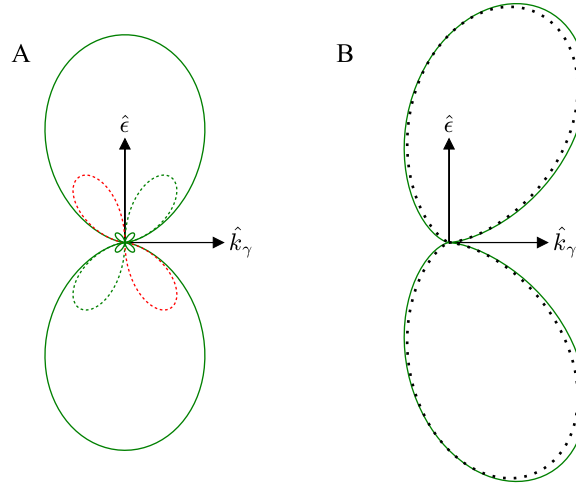


Figure 4.2: (A) Contributions to the angular distribution of a photoelectron from a s-shell (Eq. 4.17, $\gamma = 3$, $\varphi = 0$). The green two-lobed part is the pure dipole contribution, the green four-lobed part is the pure quadrupole contribution, and the dotted part is the dipole-quadrupole interference where red indicates $\text{sgn}(\text{Re}(2 \times \text{Re}(a_d a_q))) = -1$ and green resembles $\text{sgn}(\text{Re}(2 \times \text{Re}(a_d a_q))) = +1$. (B) Green solid line: Sum of all three individual contributions shown in B. Black dotted line: Eq. 4.26 for $\beta = 2$, $\gamma = 3$, $\delta = 0$, and $\varphi = 0$.

Partial waves and angular momentum

So far, we have shown that the wave function of the photoelectron can be described in terms of partial waves, but what exactly is the physical meaning of that?

The Hamilton operator of an interaction-free particle (Eq. 3.15) contains the *Laplace operator* $\nabla^2 = \nabla \cdot \nabla$. In spherical coordinates, the Laplace operator can be separated into a radial and an angular part:

$$\nabla^2 = \nabla_r^2 + \nabla_{\vartheta, \varphi}^2 .$$

The spherical harmonics are the eigenfunctions of the angular part of the Laplace operator which in turn is proportional to the square of the angular momentum operator \hat{L}^2 :

$$\hat{L}^2 = -\hbar^2 \nabla_{\vartheta, \varphi}^2 .$$

The two essential eigenvalue equations are

$$\hat{L}^2 Y_{\ell m}(\vartheta, \varphi) = \hbar^2 \ell(\ell + 1) Y_{\ell m}(\vartheta, \varphi) , \quad (4.18)$$

for the square of the angular momentum, and

$$\hat{L}_z Y_{\ell m}(\vartheta, \varphi) = \hbar m Y_{\ell m}(\vartheta, \varphi) , \quad (4.19)$$

for the projection of the angular momentum onto the quantization axis [27].

For a more convenient use with circularly polarized light and to be consistent with Sec. 11.2, we now choose the photon propagation direction as the quantization axis and as the polar axis of the spherical coordinate system. Consequently, after including the leading order nondipole term in the interaction Hamiltonian, we find the spherical harmonics $Y_{11}(\vartheta, \varphi)$ and $Y_{21}(\vartheta, \varphi)$ in the final state of a photoelectron originating from a *s*-subshell. The angular dependence of a *s*-subshell is proportional to $Y_{00}(\vartheta, \varphi) = \sqrt{1/(4\pi)}$ and the initial-state angular momentum of the electron is zero accordingly.

In an electric dipole transition, one unit of angular momentum is transferred to the photoelectron due to the photon spin. The photon spin vector is parallel (or antiparallel) to the photon propagation axis. Consequently, we get $\Delta\ell = 1$ and $\Delta m = 1$. In an electric quadrupole transition, on the other hand, one additional unit of angular momentum is transferred through the coupling of the photon momentum to the electron. In a classical picture, this corresponds to the angular momentum vector $\mathbf{p}_\gamma \times \mathbf{r}$ which is directed perpendicularly to the photon propagation axis. As a result, we get $\Delta\ell = 2$ and $\Delta m = 1$ in total.

Quantum theory determines that angular momentum is transferred only in integer units of \hbar . Note that $\mathbf{p}_\gamma \times a_0 \hat{\mathbf{r}} = \hbar$ requires $p_\gamma = 1$ au which corresponds to a photon energy of approximately 3729 eV (see Eq. 2.10). Hence, the probability to observe higher angular momenta in the final state is enhanced for large p_γ and for initial-state radial wave functions with a strong contributions at high r .

Intrinsic and orbital angular momentum

It is worth mentioning that the photon spin and the cross product of photon momentum and electron position vector $\mathbf{p}_\gamma \times \mathbf{r}$ did not appear when we let the interaction Hamiltonian act on the initial-state wave function in Eq. 4.3. Rather, we have used a classical electromagnetic wave to represent the light, where the notions of photon spin and momentum do not appear. However, the photon spin and the cross product have their classical analogs. As shown in many textbooks (see, e.g., Ch. 4B in Ref. [25]), the total angular momentum of a classical electromagnetic wave consists of the *intrinsic angular momentum* and the *orbital angular momentum*.

The intrinsic angular momentum does not depend on the choice of origin for the frame of reference and consequently it has no spatial dependence. It can be understood as the classical counterpart of the photon spin (it is also called *spin angular momentum*).

The orbital angular momentum, on the other hand, does depend on the choice of origin and it can be related to the term $\mathbf{p}_\gamma \times \mathbf{r}$.

General form of the photoelectron angular distribution

In 1948, C. N. Yang derived a general form for the angular distribution of reaction products in scattering processes where an unpolarized beam of projectiles impinges on a target nucleus [41]. Yang based his derivation on parity and angular-momentum conservation laws and stayed within the electric dipole approximation. The key points of the derivation were neatly summarized and applied to the photoionization process by J. Cooper and S. T. Manson [42]:

- (a) As only the photon propagation direction is specified before the reaction, the angle-differential cross section is of the form

$$\frac{d\sigma}{d\Omega} = \sum_{\ell} a_{\ell} P_{\ell}(\cos \vartheta_{\gamma}), \quad (4.20)$$

where $P_{\ell}(\cos \vartheta_{\gamma})$ are the Legendre polynomials and ϑ_{γ} is the angle enclosed by \mathbf{p}_{γ} and \mathbf{p}_e . There is no dependence on an additional azimuthal angle.

- (b) Odd values of ℓ in Eq. 4.20 imply a forward/backward asymmetry for the photoelectron angular distribution with respect to the light propagation direction. Such odd values of ℓ arise only from interference between final states of opposite parity (see Fig. 4.2, where the $\ell = 2$ and $\ell = 1$ final states interfere). However, all final states of an electric dipole transition, where $\Delta\ell = \pm 1$, have the same parity. Hence, only even values of ℓ are possible in Eq. 4.20.
- (c) If the incoming radiation carries angular momenta of up to ℓ' , the value of ℓ in Eq. (4.20) cannot be higher than $2\ell'$. This holds true for any angular momentum of the target's initial state. The proof of this statement can be found in Ref. [41]. In an electric dipole transition, the angular momentum of the incoming wave is $\ell' = 1$ due to the photon spin.

Accordingly, Eq. (4.20) becomes

$$\frac{d\sigma}{d\Omega} = a_0 P_0(\cos \vartheta_{\gamma}) + a_2 P_2(\cos \vartheta_{\gamma}), \quad (4.21)$$

where $P_0(\cos \vartheta_{\gamma}) = 1$ and $P_2(\cos \vartheta_{\gamma}) = (3 \cos^2 \vartheta_{\gamma} - 1)/2$, but it is more commonly used in the form introduced by J. Cooper and N. Zare in 1968 [43], which is given by

$$\frac{d\sigma}{d\Omega} = \frac{\sigma_{tot}}{4\pi} \left[1 - \frac{\beta}{2} P_2(\cos \vartheta_{\gamma}) \right] = \frac{\sigma_{tot}}{4\pi} \left[1 - \beta \frac{3 \cos^2 \vartheta_{\gamma} - 1}{4} \right], \quad (4.22)$$

where σ_{tot} is the total integrated cross section, and β is the so-called *dipole (asymmetry) parameter*.³

³Although often missed in the literature, Eq. 4.22 and a formula to calculate β are already implicitly contained in a work of H. Bethe from 1933 [44].

Equation 4.22 works for randomly and circularly polarized light, but for linearly polarized light it becomes

$$\frac{d\sigma}{d\Omega} = \frac{\sigma_{tot}}{4\pi} [1 + \beta P_2(\cos \vartheta_\epsilon)] = \frac{\sigma_{tot}}{4\pi} \left[1 + \beta \frac{3 \cos^2 \vartheta_\epsilon - 1}{2} \right], \quad (4.23)$$

where ϑ_ϵ is the angle enclosed by the polarization vector $\hat{\epsilon}$ and \mathbf{p}_e .

Expressions like Eqs. 4.22 & 4.23 are often called *parametrizations* because they write the angle-differential cross section in terms of parameters that define the multiplicative factors in a series of common angular functions.

The asymmetry parameter β can take values between -1 and 2 and it can be calculated through

$$\beta = \frac{\ell(\ell-1)R_{\ell-1}^2 + (\ell+1)(\ell+2)R_{\ell+1}^2 - 6\ell(\ell+1)R_{\ell-1}R_{\ell+1} \cos \Delta\phi}{(2\ell+1) [\ell R_{\ell-1}^2 + (\ell+1)R_{\ell+1}^2]}, \quad (4.24)$$

where ℓ is the second quantum number of the initial state, $R_{\ell\pm 1}$ are the dipole radial integrals that depend on the radial parts of the initial and final state wave functions (compare to Eq. 4.11), and $\cos \Delta\phi$ is the phase difference between the two partial waves that are characterized by $\ell-1$ and $\ell+1$ [42].⁴ Equations 4.22 & 4.23 are displayed in Fig. 4.3 for different values of β .

If the initial state is a *s*-subshell ($\ell = 0$), Eq. 4.24 always yields $\beta = 2$ and the prediction of Eq. 4.23 resembles the pure dipole term shown in Fig. 4.2 A. However, the electric dipole approximation was used to derive Eq. 4.23 and as a consequence it cannot reproduce the angular distribution displayed as the green solid line in Fig. 4.2 A.

A parametrization of the photoelectron angular distribution that considers first-order multipole corrections (E1-E2 and E1-M1 interferences, but not the pure contributions E2-E2 and M1-M1) was established by J. Cooper in 1990 [45]. Accordingly, Eqs. 4.22 & 4.23 become

$$\frac{d\sigma}{d\Omega} = \frac{\sigma_{tot}}{4\pi} \left[1 - \beta \frac{3 \cos^2 \vartheta_\gamma - 1}{4} + \left(\frac{\gamma}{2} \sin^2 \vartheta_\gamma + \delta \right) \cos \vartheta_\gamma \right] \quad (4.25)$$

for circular polarization, and

$$\frac{d\sigma}{d\Omega} = \frac{\sigma_{tot}}{4\pi} \left[1 + \beta \frac{3 \cos^2 \vartheta_\epsilon - 1}{2} + (\gamma \cos^2 \vartheta_\epsilon + \delta) \sin \vartheta_\epsilon \cos \varphi_\epsilon \right] \quad (4.26)$$

for linear polarization, where φ_ϵ is the azimuthal angle with respect to $\hat{\mathbf{k}}_\gamma$.

Note that Eq. 4.25 is simply an alternative form of

$$\frac{d\sigma}{d\Omega} = \sum_{\ell=0}^3 a_\ell P_\ell(\cos \vartheta_\gamma), \quad (4.27)$$

where $P_1(\cos \vartheta_\gamma) = \cos \vartheta_\gamma$ and $P_3(\cos \vartheta_\gamma) = [\cos \vartheta_\gamma(2 - 5 \sin^2 \vartheta_\gamma)]/2$. Assuming that the maximum orbital angular momentum of the incoming radiation is $\ell' = 2$, Eq. 4.27 follows directly from Yang's reasoning: The maximum value of ℓ in Eq. 4.21 is 4 and odd values of ℓ are allowed because the available final states do not all have the same parity ($\Delta\ell = 0, \pm 1, \pm 2$). Here, the $\ell = 4$ term is omitted because Cooper considered only those nondipole corrections to the cross section that scale

⁴The original publication of Cooper and Zare [43] contains a small error in the formula for calculating β : an additional factor of 3 in the denominator. In the later work, the factor was removed [42].

with $k_\gamma r$ while he left out the $(k_\gamma r)^2$ term, i.e., the pure electric quadrupole (E2-E2) contribution.

The nondipole parameters γ and δ characterize the E1-E2 and E1-M1 interferences and their values depend on the relative strengths of the E2 and M1 terms compared to the E1 term. The explicit general expressions (like Eq. 4.24) to calculate γ and δ can be found, e.g., in App. A of Ref. [39]. As shown in Fig. 4.4, both nondipole parameters break the forward/backward symmetry of the angular distribution if their values are nonzero.

In Fig. 4.2 B the black dotted line represents Eq. 4.26 for $\beta = 2$, $\delta = 0$, and $\gamma = 3$. Here, the reason for the small differences between the black dotted line and the green solid line is that Eq. 4.26 does not reflect the pure E2-E2 contribution.

A parametrization that extends Cooper's work by including the $(k_\gamma r)^2$ terms of the nondipole expansion was published by A. Derevianko et al. in 1999 [46]. For the scope of the present work, however, Cooper's nondipole parametrization (Eqs. 4.25 & 4.26) proved to be sufficient to adequately describe the measured photoelectron angular distributions in the laboratory frame of reference. Nevertheless, it should be noted that Cooper's formula is not the only nondipole parametrization of the angle-differential cross section and some other approaches can be found, e.g., in Refs. [47–49].

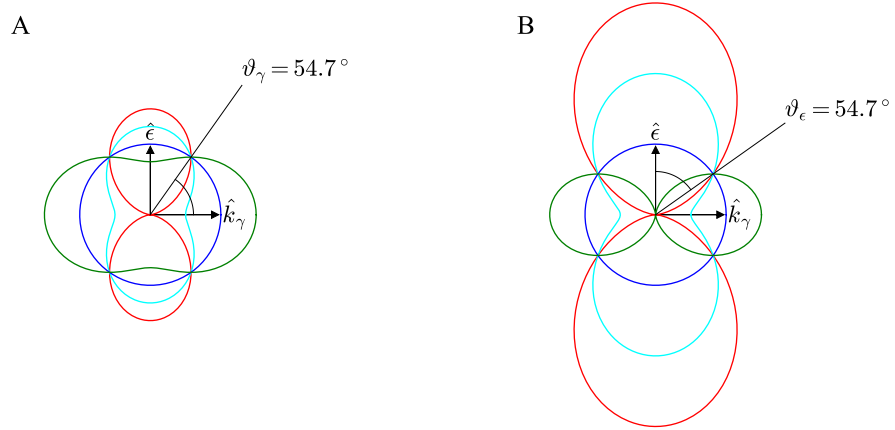


Figure 4.3: Photoelectron angular distributions for circular polarization (A, Eq. 4.22) and linear polarization (B, Eq. 4.23) displayed for different values of the dipole asymmetry parameter: $\beta = 2$ in red, $\beta = 1$ in cyan, $\beta = 0$ in blue, and $\beta = -1$ in green. The corresponding three-dimensional photoelectron angular distributions can be obtained by rotating the curves around the light axis \hat{k}_γ in case of circular polarization or around the polarization axis $\hat{\epsilon}$ for linear polarization. At $\vartheta \approx 54.7^\circ$ the second Legendre polynomial $P_2(\cos \vartheta)$ is zero. Here, the angle differential cross section is independent of β .

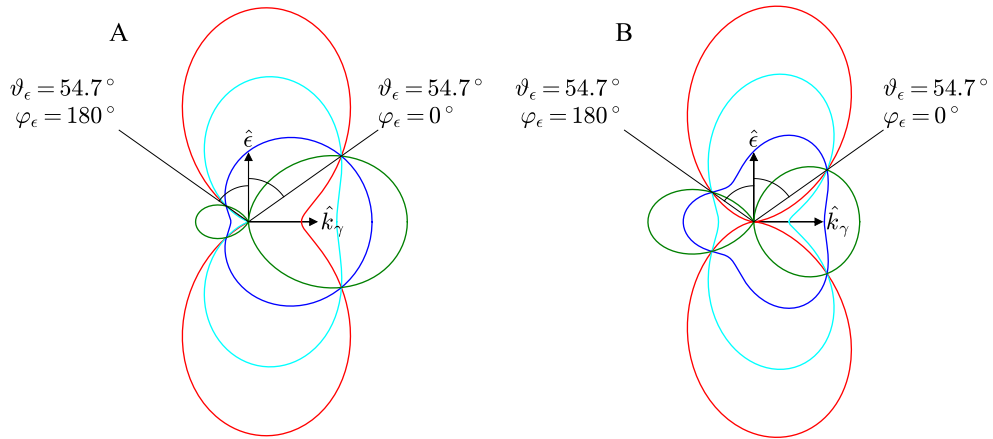


Figure 4.4: Photoelectron angular distributions with nondipole corrections for linear polarization (Eq. 4.26). (A) $\delta = 0.75$ & $\gamma = 0$. (B) $\delta = 0$ & $\gamma = 2$. Red: $\beta = 2$, cyan: $\beta = 1$, blue: $\beta = 0$, green: $\beta = -1$. At $\vartheta_\epsilon \approx 54.7^\circ$, the angle differential cross section does not depend on any parameter but on the azimuthal angle φ_ϵ .

MULTIPLE IONIZATION

So far, our discussion of photoionization has implicitly focused on single ionization. The present chapter briefly describes the processes that facilitate the emission of a secondary electron upon absorption of a single photon.

5.1 ONE-PHOTON DOUBLE IONIZATION OF HE AND H₂

For one-photon double ionization to happen, the photon energy must surpass the double ionization threshold of the respective target. The single ionization threshold of helium is $I_p^+ = 24.6$ eV, and the double ionization threshold is $I_p^{++} = 79$ eV. Here, the excess energy ($E_{exc} = E_\gamma - I_p$) is entirely transferred to and shared among the two electrons.

Single ionization of the hydrogen molecule requires at least 15.43 eV in a vertical transition at the equilibrium distance between the two protons. The complete breakup into two free protons and two free electron requires not less than 51 eV of energy. In photon double ionization of H₂, the fraction of the photon energy that exceeds the sum of the adiabatic double ionization energy (31.03 eV) and the variable sum of the kinetic energies of the protons (kinetic energy release, KER) is shared among the two electrons.

The one-photon double ionization of helium has been studied extensively in the past within the scope of the electric dipole approximation and comprehensive reviews can be found, e.g., in Refs. [28, 50]. In a dipole transition, the double ionization of helium is usually described and calculated by the means of a mixed quantum-classical model that splits the process into two "mechanisms":

1. The *two-step-one* (TS1) is pictured as a two-part process. First, the mechanism proceeds like one-photon single ionization where one electron is released from its bound state after absorption of the photon. Second, on its way to the continuum, the photoelectron collides with the second electron which is subsequently kicked out.¹ The second step is closely related to electron-impact ionization. Here, the total cross section decreases rapidly with increasing electron energy, because a certain interaction time is needed for the momentum exchange. Consequently, the TS1 is the dominant process of double ionization at relatively low excess energies [51].

The interaction between the electrons in TS1 transfers an arbitrary fraction of kinetic energy from the first electron to the second electron. As a consequence, the double-ionization cross section of TS1 as function of the so-called *electron energy sharing* $\epsilon = E_1/(E_1 + E_2)$, where $E_{1,2}$ are the energies of electrons 1 and 2, is a relatively flat curve. In TS1, the two electron momentum vectors $\mathbf{p}_{1,2}$ preferably enclose a mutual angle $\vartheta_{12} = \cos^{-1}[(\mathbf{p}_1 \cdot \mathbf{p}_2)/(p_1 p_2)]$ of 90° (see, e.g., Ref. [52]).

2. Double ionization via *shake-off* (SO) proceeds through the quasi-instantaneous removal of the first electron, whereas the second electron cannot relax adiabatically to the singly charged ionic ground state. Instead, the second electron

¹Because of the way the second step is pictured, the mechanism is also known as the knock-out process.

is either shaken up to a discrete excited state or shaken off to the continuum. The sudden change of ground states requires high excess energies and the ratio of double to single ionization probability converges to the so-called *shake-off limit* at high photon energies, where TS₁ no longer plays a role [53].

The SO is characterized by a highly asymmetric energy sharing and the distribution of the electron mutual angle ϑ_{12} is nearly isotropic [54].

Investigations of nondipole effects in the one-photon double ionization of helium are rare. In 2004 and 2005, A. Istomin et al. published a number of theory papers on how the angle-differential cross sections of He double ionization are modified by nondipole effects [49, 55–57], but dedicated experimental investigations are still pending.

In 1975, M. Amusia et al. predicted a third mechanism that facilitates helium double ionization by means of a pure quadrupole transition [58]:

3. The *quasifree mechanism* (QFM) ejects two electrons from the part of the initial-state two-electron wave function where both electrons are spatially close together [59]. As shown by J. Ludlow et al. [60], the quadrupole part of the interaction Hamiltonian can act directly on the relative electron position vector $\mathbf{r}_- = \mathbf{r}_{e1} - \mathbf{r}_{e2}$ (see p. 101 in Ch. 11 for the derivation). The respective part of the quadrupole contribution to double ionization is responsible for QFM. The name of the mechanism stems from the idea that the light interacts with a quasi-free electron pair without involvement of the nucleus.

The QFM is characterized by electrons emitted back-to-back ($\vartheta_{12} \approx 180^\circ$) with equal energy ($\epsilon \approx 0.5$), leaving the nucleus with close to zero recoil momentum [61]. This final-state pattern is forbidden in a dipole transition due to angular momentum conservation [62]. The absolute QFM cross section is predicted to decrease with an increase of the nuclear charge Z [63]. The relative contribution of QFM to the total double-ionization cross section is supposed to increase with rising photon energy, but it is expected to become the dominant mechanism only at hundreds of keV [64].

Feynman diagrams are a tool for the calculation of transition amplitudes [65], but they are also useful for the pure visualization of the interaction process itself. Figure 5.1 shows the Feynman diagrams of the three double-ionization mechanisms [58]. For two-step-one (Fig. 5.1 A), the electron-electron interaction happens after the photon absorption by means of a virtual photon. This supports the picture that the first electron collides with the second one on its way out of the system. In case of shake-off (Fig. 5.1 B), the initial-state correlation between the electrons facilitates the double ionization as indicated by the virtual photon exchange prior to the photon absorption. The Feynman diagram for the QFM (Fig. 5.1 C) depicts how the incoming photon couples directly to the electron pair.

The existence of the QFM was confirmed by M. Schöffler et. al in 2013 through the observation of doubly charged helium nuclei with close to zero recoil momenta in one-photon double ionization at 800 eV photon energy [66]. The investigation of the QFM in double ionization of helium continues in the present work with a focus on the electronic fingerprint in the final state, which was previously inaccessible (see Ch. 11).

The electronic structure of the hydrogen molecule is similar to that of the helium atom and the double ionization of H₂ can also be split into a shake-off and a two-step-one part within the scope of the electric dipole approximation [67]. Consequently, one can also expect the QFM in the quadrupole contribution to the

cross section of H₂ double ionization. This expected existence is confirmed in the present work (see Sec. 11.1).

Furthermore, we confirm that the relative contribution of QFM to the total double-ionization cross section increases with E_γ (see Fig. 11.1) and visualize that QFM is a pure quadrupole contribution to double ionization (see Sec. 11.2). Unfortunately, we cannot investigate the dependence of QFM on the nuclear charge Z . For $Z = 2$, however, we study the dependence as function of the distance between the two point charges (see Sec. 11.3).

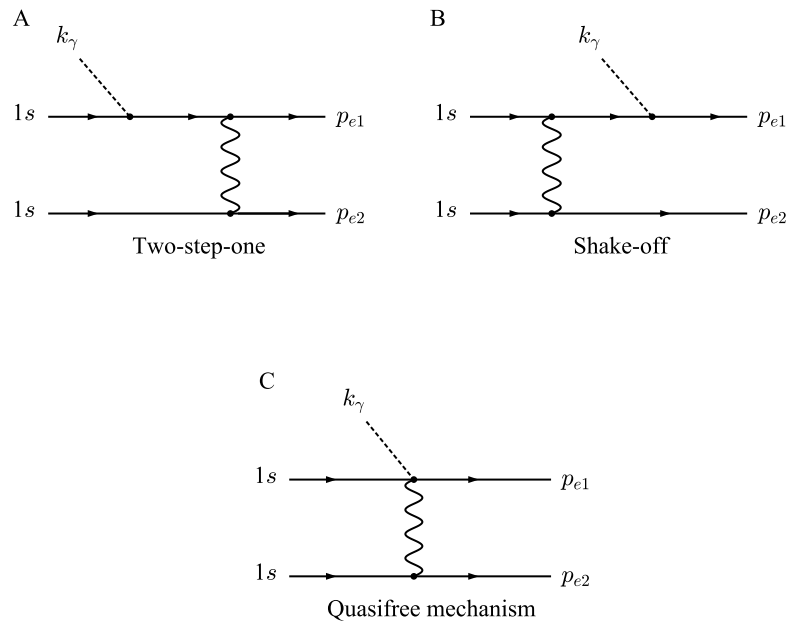


Figure 5.1: Feynman diagrams for the three double-ionization processes (adapted from Refs. [58, 68]).

5.2 K-SHELL IONIZATION OF N₂ FOLLOWED BY AUGER DECAY

The *K*-shell photoionization thresholds of N₂ are $I_p = 409.82$ eV, if the vacancy is left in the ungerade state, and $I_p = 409.93$ eV for the gerade vacancy respectively (see Ch. 6, p. 35 for the definition of gerade and ungerade parity). Here, the ion is left in its vibrational ground state. The energy splitting between these two states of different parity is far too small to be resolved with the experimental setup used in the present work and we consequently assume an average ionization threshold of $I_p = 409.88$ eV for *K*-shell ionization of N₂. The average internuclear distance of the N₂ molecule is $R = 2.07$ au in the neutral ground state and $R = 2.035$ au in the ground state with a *K*-shell vacancy [69].

The *K*-shell vacancy created upon photoionization is rapidly filled by a valence electron as the system returns to a lower energy state. The potential energy difference is either radiated through a photon or transferred to another weakly bound electron that is subsequently emitted. The radiationless decay—which is the dominant process—is better known as *Auger decay* and the secondary electron is called *Auger electron* (see Ref. [70] for a comprehensive work on the Auger decay).

In the present work, we inspect *K*-shell ionization of N₂ with photon energies of at least 880 eV that is followed by Auger electron emission at 370 eV kinetic energy and fragmentation into $N^+ + N^+$. Here, we investigate the influence of molecular effects on the forward/backward asymmetry of photoelectron emission in the laboratory frame (see Ch. 7 for further background).

As shown in Ref. [71], Auger decay and break-up of the intermediate N_2^{2+} ion happen fast compared to the typical rotation times of the molecule for any kinetic energy release and the two N^+ fragments are emitted along the direction of the molecular axis at the instant of photoabsorption (i.e, the axial recoil approximation is valid). Accordingly, we are also able to investigate the nondipole effects of photoelectron emission in the molecular frame of reference.

Nondipole effects in Auger electron emission, e.g., a forward/backward asymmetry in the emission probability, have never been investigated to the author's knowledge and are not subject of the present work.

If a photoelectron is emitted from a molecule, the photoelectron angular distribution can be transformed from the laboratory frame of reference into the body-fixed frame of the molecule to obtain a so-called *molecular frame photoelectron angular distribution* (MFPAD, see App. B on how to define the molecular frame). Diverse multi-center effects shape the MFPAD and set molecular photoionization apart from the atomic case. The present chapter features some of these peculiarities of one-photon ionization of molecules.

6.1 INTERFERENCE IN THE PHOTOIONIZATION OF MOLECULES

In the Born approximation, the electron's final-state wave function is described in terms of free waves. This approximation works well at high but non-relativistic electron energies, where the influence of the molecular potential on the photoelectron becomes insignificant. Within the scope of the Born approximation, simple wave-interference models can be used to predict features of photoelectron emission from molecules.

Cohen-Fano interference in the photoionization cross section

In 1965, J. Samson and R. Cairns reported on an experiment that obtained total photoabsorption cross sections for three homonuclear diatomic molecules (H_2 , N_2 , and O_2) for photon energies between 20 eV and 62 eV [72]. Their results showed that the downtrend of the photoabsorption cross section was superimposed by oscillations that were previously unknown from the atomic case. In the subsequent year, H. Cohen and U. Fano attempted to explain these observations [73]. The authors suggested that for photoionization the two centers of a diatomic homonuclear molecule may be considered as independent photon absorbers and indistinguishable sources of coherent photoelectron waves. The interference between these photoelectron waves modulates the photoionization cross section:

$$\sigma = \sigma_H(Z) \left[1 + \frac{\sin(2\pi R/\lambda_e)}{2\pi R/\lambda_e} \right], \quad (6.1)$$

where $\sigma_H(Z)$ is the cross section for a hydrogen-like atom of atomic number Z , R is the internuclear distance, and λ_e is the wavelength of the photoelectron matter wave. Stressing the relation $\lambda_e = 2\pi\hbar/p$ for matter waves (de Broglie wavelength), where p is the photoelectron momentum, and using atomic units, where $\hbar = 1$, Eq. 6.1 takes the more common form

$$\sigma = \sigma_H(Z) \left[1 + \frac{\sin(pR)}{pR} \right]. \quad (6.2)$$

The oscillatory factor in brackets in Eq. 6.2 quantifies the so-called *Cohen-Fano interference*. The factor is plotted in Fig. 6.1 for the average internuclear distances of H_2 and N_2 . The predictions according to the Cohen-Fano interference agreed with the observations reported by Samson and Cairns in 1965. Such modulations of total cross sections for molecular photoionization due to interference effects are still being investigated in modern day research (e.g., [74–78]).

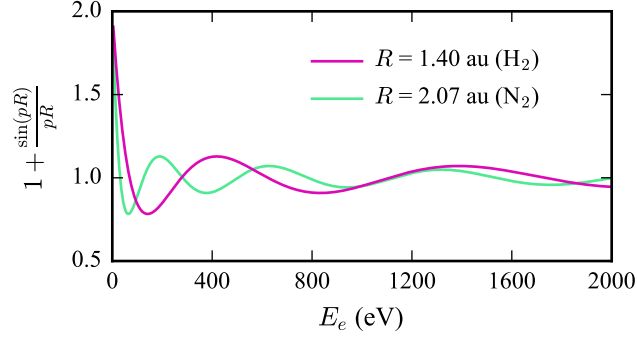


Figure 6.1: Modulations of the total photoabsorption cross section of homonuclear diatomic molecules due to two-center interference (Eq. 6.2) as function of the photoelectron energy E_e . Note that if the photoelectrons originate from states of different parity, twice as many maxima would emerge in any given interval of pR [73].

The molecular double-slit

Apart from the modulation of the total cross section as function of the photoelectron energy, the interference of photoelectron waves has another intriguing consequence that manifests in the molecular frame photoelectron angular distribution: Photoelectron emission from a homonuclear diatomic molecule mimics the double-slit experiment.

The concept of a classical double-slit experiment is illustrated in Fig. 6.2 B. Here, a plane wave impinges from below on a barrier that has two slits. Subsequently, these two slits behave like individual sources of coherent spherical waves whose amplitudes are superimposed behind the barrier, i.e., the two waves interfere with each other.

A double-slit experiment usually detects an *interference pattern*, which is the modulation of the intensity measured on a detector in the far field. This interference pattern is the result of different path lengths from each slit to the detection points. The path difference is given by

$$\Delta s = d \cos \alpha , \quad (6.3)$$

where d is the distance between the two slits and α is the angle enclosed by the slit axis and the emission direction. Equation 6.3 is only valid in the far field where the distance from the double-slit center to the detection point is much larger than d . Here, the two paths from each slit to any detection point run nearly parallel to one another. The path difference alters the relative phase between the two waves and the phase difference is given by

$$\Delta \phi = \frac{2\pi d \cos \alpha}{\lambda} , \quad (6.4)$$

where λ is the wavelength. Eventually, the intensity distribution on the detector in the far field becomes

$$I \propto \cos^2 \left[\frac{\Delta \phi}{2} \right] = \cos^2 \left[\frac{\pi d \cos \alpha}{\lambda} \right] . \quad (6.5)$$

An exemplary result of Eq. 6.5 is shown in Fig. 6.2 A.

In photoelectron emission from a homonuclear diatomic molecule, the internuclear distance R resembles the distance between the two slits and $\lambda = \lambda_e$ is the de Broglie wavelength of the electron matter wave. In analogy to Eq. 6.5, the probability

distribution for the detection of a single photoelectron on a detector in the far field can be predicted as

$$\mathcal{P} \propto \cos^2 \left[\frac{pR \cos \alpha}{2} \right]. \quad (6.6)$$

Figure 6.3 illustrates the concept of such a molecular double-slit experiment. Note that the angle α is defined in the molecular frame of reference. Hence, Eq. 6.6 makes a prediction about the molecular frame photoelectron angular distribution. It is important to stress that such a "pure" MFPAD could only be observed for an isotropic photoelectron emission probability in the laboratory reference frame, which is hardly ever the case. Rather, any observable MFPAD contains the anisotropy of the angle-differential cross section in the lab frame (see Ch. 7) and it depends on the orientation of the molecule with respect to the light polarization or propagation vectors. This aspect is not considered in Fig. 6.3.

A very instructive and comprehensive account of the interplay between molecular and laboratory frame photoelectron angular distributions can be found in Ref. [79]. Another instructive example that includes nondipole effects is shown in Fig. B.4 in the appendix of the present work.

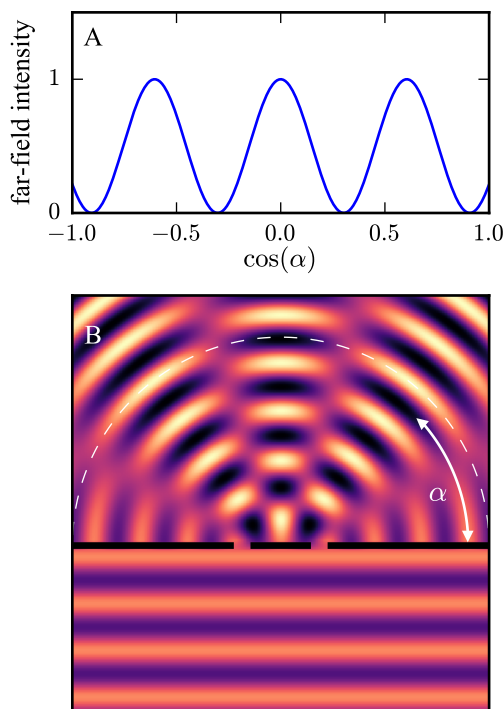


Figure 6.2: Classical double-slit experiment. (A) A plane wave (e.g., a water surface wave) impinges from below on a barrier that contains two slits, which become the sources of two coherent spherical waves that interfere behind the barrier. (B) Intensity behind the barrier measured in the far field as function of the angle α . The ratio between the slit distance and wavelength is $d/\lambda = 1.65$.

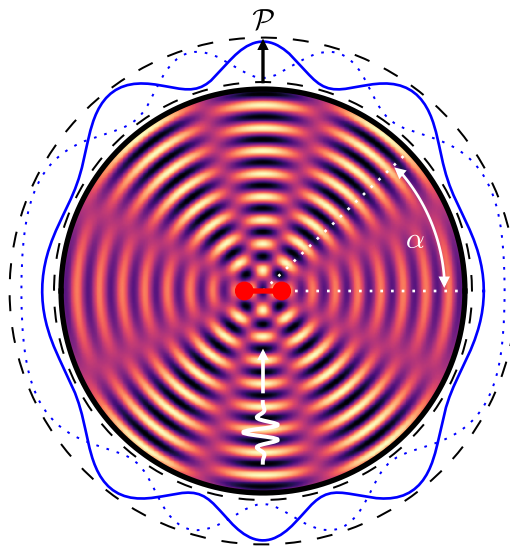


Figure 6.3: Photoelectron emission from a homonuclear diatomic molecule mimics the double-slit experiment. The photon (white) impinges on the molecule (red) and two coherent photoelectron waves are launched from the two atomic centers simultaneously. The superimposed waves create the distinct interference pattern that is familiar from the classical double-slit experiment. The probability for the detection of a single electron on a detector in the far field (Eq. 6.6) is indicated by the solid blue line. The dotted blue line represents the situation of opposite phases at the two atomic centers (Eq. 6.7). Here, $R/\lambda_e = 1.65$, which corresponds to 750 eV electron energy and 1.4 au internuclear distance. Note that in reality, the photoelectron waves propagate through all three spatial dimensions and cannot be described by the surface waves depicted here.

Gerade and ungerade initial states

Sometimes the interference pattern of a molecular double-slit experiment appears as if the two superimposing waves are born with opposite phases. In that case, Eq. 6.6 becomes

$$\mathcal{P} \propto \cos^2 \left[\frac{pR \cos \alpha \pm \pi}{2} \right], \quad (6.7)$$

and the positions of the interference maxima and minima on the detector are swapped, as demonstrated by the dotted blue line in Fig. 6.3. The reason for this phenomenon lies in the structure of the initial-state wave function from which the electron wave originates. In Ch. 3, we have discussed the properties of atomic orbitals. Here, we cover those concepts of *molecular orbitals*, i.e., position-space wave functions of electrons bound in a molecule, that are important for the molecular double-slit experiment.

The Hamilton operator of a single electron bound in a molecule must account for the multi-center Coulomb potential. For the simple H_2^+ ion, it is given by

$$\hat{H} = \frac{-\hbar^2 \nabla^2}{2m_e} - \frac{e^2}{4\pi\epsilon_0} \left[\frac{1}{r_a} + \frac{1}{r_b} \right], \quad (6.8)$$

where $r_{a,b} = |\mathbf{r} - \mathbf{R}_{a,b}|$ are the distances of the electron from the protons a and b . The internuclear distance is given by $R = |\mathbf{R}_a - \mathbf{R}_b|$. In H_2^+ , the electron is located at one of the two indistinguishable protons with equal probability.

If $R = 0$, Eq. 6.8 resembles the Hamiltonian of He^+ , whereas for $R \rightarrow \infty$ it represents two individual hydrogen atoms. In these two extreme cases, the atomic orbitals (Eq. 3.7) are solutions of the corresponding Schrödinger equation. Otherwise, one useful way to approximate the eigenfunctions of Eq. 6.8 is the *linear combination of atomic orbitals* (LCAO) [80].

By means of the LCAO method, two atomic orbitals—one from each atom and each centered around its respective nucleus—are superimposed and form the orbitals of the homonuclear diatomic molecule. The two atomic orbitals can overlap in two ways depending on their relative sign relationship. This difference is illustrated in Fig 6.4 for two hydrogen 1s orbitals. At each point in space where the two atomic orbitals share the same sign, the resulting spatial probability density is enhanced. Whereas for opposite signs, the probability density is reduced.

Determined by the subshells of the atomic orbitals and the parity of the combined wave function, a molecular orbital is either *binding* or *antibinding*. The parity of the molecular orbital is defined by how the sign of the wave function at each point in space behaves during space inversion. If the sign remains unchanged, the orbital has *gerade* (g) parity (Fig. 6.4 A). Whereas if the sign flips, the orbital has *ungerade* (u) parity (Fig. 6.4 C).¹ For the gerade combination of two s -type orbitals, the spatial probability density of the electron between the two protons is enhanced (Fig. 6.4 B). As a result, the molecular orbital is binding and the Coulomb repulsion between the protons is countered by their mutual attraction towards the electron. For the ungerade combination of two s -type orbitals, on the other hand, the probability density between the protons is reduced and the orbital is antibinding (Fig. 6.4 D). For two p -type atomic orbitals, on the other hand, gerade parity results in an antibinding and ungerade parity in a binding molecular orbital.

Apart from their parity, molecular orbitals are characterized by the projection of the orbital angular momentum onto the molecular axis and the shape of the

¹Conventionally, *gerade* and *ungerade* describe the parity of the orbital of a homonuclear diatomic molecule, whereas *even* and *odd* characterize the parity of an atomic orbital.

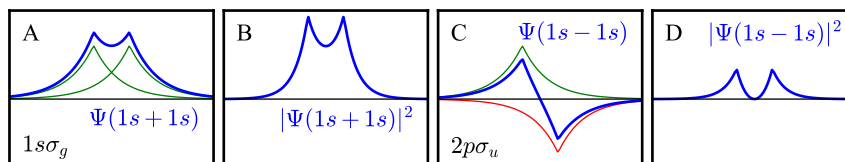


Figure 6.4: Symmetric (A) and antisymmetric (C) linear combination of two hydrogen 1s orbitals, separated by an internuclear distance of 1.4 au, and the corresponding spatial probability densities (B,D). The labels of the molecular orbitals, $1s\sigma_g$ (A) and $2p\sigma_u$ (C), describe the united-atom configuration.

orbital in the *united-atom configuration*. The angular momentum quantum number ($\lambda = |m| = 0, 1, 2, 3, \dots$) is usually indicated by Greek letters ($\sigma, \pi, \delta, \phi, \dots$). The united-atom configuration regards the molecular orbital at small but nonzero internuclear distances. Here, the symmetric combination of two 1s atomic orbitals still roughly resembles the shape of a 1s orbital. However, the antisymmetric combination is similar in shape to a 2p atomic orbital. These similarities determine the first two digits of the label of a molecular orbital.² Two exemplary labels are included in Fig. 6.4.

The sign of the wave function marks its phase. The absolute phase of a single orbital has no physical meaning but the relative phase between two mixing wave functions determines how they interfere with each other. Opposite signs resemble opposite phases and same signs resemble same phases. Accordingly, the parity of the molecular orbital from which the photoelectron originates determines the relative phase at birth time of the two superimposing waves in a molecular double slit experiment. For gerade parity in the initial state, both outgoing waves have the same phase (Eq. 6.6). Whereas for ungerade parity, the waves are born with opposite phases (Eq. 6.7).

Resolving states of gerade and ungerade parity

When atoms bond to form molecules, the number of molecular orbitals corresponds to the number of involved atomic orbitals. The electrons are distributed to the lowest-energy molecular orbitals first and each orbital can hold two electrons having opposite spins. For example, two atomic 1s orbitals make the $1s\sigma_g$ and $2p\sigma_u$ molecular orbitals. In the H_2^+ and H_2 ground states, only the $1s\sigma_g$ orbitals are populated, because they are energetically lower than the $2p\sigma_u$ states, and the overall parity of each system is gerade. Accordingly, the electron waves are born with the same phases in one-photon single ionization of H_2^+ and double ionization of H_2 .

For single ionization of H_2 , however, the residual H_2^+ molecule is not necessarily in the ground state, but the photon energy can be used in part to elevate the system to an excited state. If the electronic state of the residual H_2^+ ion is ungerade, parity conservation demands that the photoelectron waves are born with opposite phases at the two protons. To observe a double-slit interference pattern in one-photon single ionization of H_2 , either the parity of the remaining H_2^+ system needs to be resolved or one of the parity states must be predominantly populated. Otherwise the patterns described by Eqs. 6.6 & 6.7 overlap and yield an isotropic distribution because $\cos^2(\phi) + \cos^2(\phi \pm \pi/2) = 1$.

The molecular orbital of the H_2^+ ion and its parity may be identified from the kinetic energy release (KER) [33]. The kinetic energy release is the sum of the kinetic energies obtained by the reaction fragments (except for electrons) through conver-

²A more rigorous definition can be found, e.g., in Ref. [81].

sion of potential energy. The total potential energy of the H_2^+ ion is determined by the molecular orbital and the internuclear distance. The potential-energy curves for the three lowest-energy states of H_2^+ in the *Born-Oppenheimer approximation* are presented in Fig. 6.5 [81].³

In this so-called correlation diagram (Fig. 6.5), the single ionization of H_2 resembles a vertical transition from the potential energy curve of the H_2 ground state to a curve of a H_2^+ state. The distribution of internuclear distances in the H_2 ground state determines at which R' such a transition takes place. If the potential energy difference on the H_2^+ curve between R' and $R \rightarrow \infty$ is positive, the molecule dissociates and the potential energy difference results in the kinetic energy release. If the potential energy difference is negative, the H_2^+ molecule stays bound.

The distribution of R in the H_2 ground state is indicated by the grey line in Fig. 6.5. At the lower end of this distribution, the potential energy of the $1s\sigma_g$ state at R' can be larger than at $R \rightarrow \infty$. Here, the H_2^+ ion dissociates even though the $1s\sigma_g$ state has binding character, i.e., the minimum of the potential energy curve is not at $R \rightarrow \infty$. By measuring the small resulting kinetic energy release ($KER < 2$ eV), the population of the $1s\sigma_g$ state can be determined unambiguously in an experiment. On the other hand, the kinetic-energy-release distributions of the $2p\sigma_u$ and $2s\sigma_g$ states overlap, but regions where either one dominate have been identified: For a measured kinetic energy release below 15 eV, the H_2^+ ion was most likely in the $2s\sigma_g$ state. Above 15 eV, the $2p\sigma_u$ state prevails [33].

In the ground state of the N_2 molecule, the $1s\sigma_g$ and $2p\sigma_u$ states are populated by two electrons each. Accordingly, photoelectron emission from the K -shell leaves a gerade or ungerade vacancy that is filled by an outer-shell electron. The energy difference is transferred to another outer-shell electron that is subsequently emitted and called *Auger electron* (see Ch. 5). Similar to the dissociation of H_2^+ , the parity of the N_2^{2+} ion in the final state can be inferred from the kinetic energy release [83]. As Auger decay does not change the overall parity of the system, photoelectron and Auger electron states have the same parity in case of a gerade N_2^{2+} state and opposite parity for an ungerade final state of the ion [84].

Like photoelectron emission from a homonuclear diatomic molecule, the angular distribution of Auger electrons in the molecular frame also carries features of a double-slit-like interference pattern if the parity is resolved. By confining the kinetic energy release and the Auger electron emission angle in the molecular frame to regions of well defined parity, we will try to resolve the double-slit interference of photoelectrons emitted from the N_2 K -shell (see Refs. [84–87] for works from which we have adapted this technique).

³The key assumption of the Born-Oppenheimer approximation is that the nuclei are much heavier and move considerably slower than the electrons in a molecule. Accordingly, the electronic and nuclear wave functions can be separated and considered independently [82].

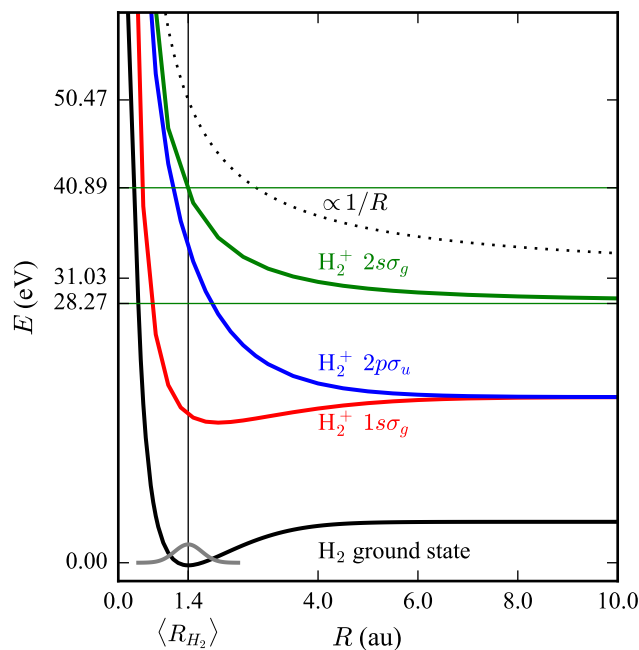


Figure 6.5: Potential-energy curves as function of the internuclear distance R for the H_2 ground state (solid black line) and the three lowest-energy states of H_2^+ (red: $1s\sigma_g$, blue: $2s\sigma_u$, green: $2s\sigma_g$) calculated in the Born-Oppenheimer approximation [81]. After single ionization of H_2 , the average kinetic energy release is the difference between potential energies of the H_2^+ state at the average internuclear distance of H_2 ($R = 1.4$ au) and at an infinite distance ($R \rightarrow \infty$). E.g., $\langle KER \rangle(2s\sigma_g) = 40.89 \text{ eV} - 28.27 \text{ eV} = 12.62 \text{ eV}$. With the double ionization of H_2 , the system is lifted onto the $1/R$ curve (dotted black line) and the resulting average kinetic energy release becomes $\langle KER \rangle = 50.47 \text{ eV} - 31.03 \text{ eV} = 19.44 \text{ eV}$, which equals the potential energy of two elementary charges that are 1.4 au apart. The grey line illustrates the distribution of R in the H_2 ground state.

History of molecular double-slit experiments performed by the Frankfurt Atomic Physics group

The molecular double-slit experiment was first proposed by I. Kaplan and A. Markin in 1969 for photoionization of H₂ [88]. The realization, however, proved to be challenging because it requires knowledge about the electron emission direction with respect to the molecular axis.

It was not until 2007 that D. Akoury et al. reported on the first successful molecular double-slit experiment [89]. The authors investigated one-photon double ionization of H₂ with circularly polarized light and photon energies of 160 eV and 240 eV. As suggested by the axial recoil approximation [90], the orientation of the molecular axis prior to the ionization was obtained from the measured three-dimensional relative momentum of the two protons. In double ionization of H₂, the excess energy is shared among the two electrons. For highly asymmetric energy sharing, the fast electron practically behaves like a photoelectron in single ionization [91]. The authors found that the measured MFPADs for such fast electrons at both photon energies were in good agreement with the predictions of Eq. 6.6.

Related studies on one-photon double ionization of H₂ later found that the momentum of the dielectron, i.e., the quasiparticle consisting of both electrons, exhibits the double-slit interference pattern in the molecular frame—even after integration over the energy sharing distribution [92–95]. This finding suggests that both electrons emerge from the same one of the two indistinguishable protons during the double ionization process and that the electrons should be considered as one two-particle wave instead of two one-particle waves.

This connection between the two electrons in one-photon double ionization of H₂ has been used to study decoherence, i.e., the transition from quantum to classical behavior. Experiments found that the double-slit interference pattern vanishes gradually for the fast electron, if the fraction of kinetic energy transferred to the secondary electron is increased [89, 95, 96].

In the experimental results of Akoury et. al [89] the double-slit interference pattern appeared to be rotated in the polarization plane. As outlined by J. Fernandez et al. in 2009 [97], this effect is a consequence of the circularly polarized light. The circularly polarized light encodes its sense of rotation in the phase of the electron wave. The scattering of the wave at the molecular potential translates the angular-dependent phase into a rotation of the MFPAD that can be observed. Thus, one can expect this rotation to vanish at high photoelectron energies where the Born approximation is valid.

The double-slit character of dielectron emission in photoionization of H₂ at 160 eV photon energy was further underlined by M. Schöffler et al. in 2008 when they found a similar dependence of the interference pattern on the internuclear distance as one would expect from altering the distance between the two slits [98]: With increasing R and constant p , the strength of the first-order interference maximum increased relative to the zeroth-order maximum. As indicated in Fig. 6.5, the internuclear distance prior to photon double ionization can be derived from the measured kinetic energy release through

$$KER = \frac{e^2}{4\pi\epsilon_0 R}, \quad (6.9)$$

where e is the elementary charge and ϵ_0 is the vacuum permittivity [90].

The double-slit character of Auger electron emission from dissociating N₂²⁺ ions was first demonstrated experimentally by M. Schöffler et al. in 2008 [84] and later theoretically underpinned by N. Cherepkov et al. [99]. At the photon energy of 419 eV used in the experiment, the kinetic energy of the photoelectrons was

roughly 9 eV and that of the Auger electrons around 370 eV. For the comparatively small photoelectron energy, the double-slit model does not appropriately describe the measured MFPAD, because the Born approximation is invalid and the photoelectron interacts with the residual charged particles [100]. The angular distribution of the Auger electrons, that have sufficiently high kinetic energy, exhibits double-slit interference features. Schöffler et al. utilized this molecular double-slit experiment to address the heavily discussed question of whether electrons—or the vacancies left upon photoionization—are localized at one center of a homonuclear diatomic molecule or delocalized over both [96, 101, 102]. They found that the answer to the question depends on how the entangled state—consisting of Auger electron and photoelectron—is measured in the experiment.

In 2016, H. Sann et al. reported on an experiment on *L*-shell photoionization of neon dimers at 36.56 eV photon energy that resulted in photoelectrons of around 15 eV kinetic energy [103]. Despite the small photoelectron energy, the angular distribution in the frame of reference of the dissociating Ne_2^+ dimer was in reasonable agreement with the double-slit model prediction for waves born with opposite phases (Eq. 6.7). Recently, double-slit electron interference has also been found in strong-field ionization of neon dimers [104].

In 2017, M. Waitz et al. reported on the first successful molecular double-slit experiment with one-photon single ionization of H_2 [33]. With the method already explained (see p. 37), the authors managed to resolve the final-state parity of the dissociating H_2^+ ion and could reveal the interference patterns of gerade and ungerade photoelectron states. At the photon energy of 400 eV, the measured molecular-frame angular distributions of the high-energetic photoelectrons were in good agreement with the predictions of Eqs. 6.6 & 6.7. Inspired by theory predictions [105, 106], Waitz et al. utilized this molecular double-slit experiment to visualize the ground state two-electron wave function (see Eq. 3.20 for comparison). A similar imaging technique was already successfully applied by M. Meckel et al. in 2008 for the highest occupied molecular orbital through strong-field ionization of O_2 and N_2 .

As it is not essential how the electron wave is released from the diatomic homonuclear molecule, the molecular double-slit experiment also works with different projectiles apart from one- and many-photon ionization. Some examples for electron and heavy ion impact ionization can be found in Refs. [107–109]. However, molecular double-slit experiments mainly employ photon impact to study interference in the ionization of molecules. Perhaps because of how the idea was originally presented by Cohen and Fano in 1966.

6.2 ...BEYOND THE DIPOLE APPROXIMATION

When two interfering waves that are born in a double slit have different phases at their source, the resulting interference pattern is tilted. An example is depicted in Fig. 6.6. The zeroth-order interference maximum occurs under the angle α_0 for which the far-field phase difference $\Delta\phi$ between both waves vanishes:

$$\Delta\phi = \frac{2\pi d \cos \alpha_0}{\lambda} - \Delta\varphi \stackrel{!}{=} 0, \quad (6.10)$$

where $\Delta\varphi$ is the phase difference between the two waves at birth. By means of measuring the angle α_0 , such an initial phase difference can be inferred. Accordingly, the molecular double-slit experiment is a sensitive probe for the initial phase difference between the two mixing photoelectron waves.

We have already discussed one possible origin of such a phase difference for the molecular double-slit experiment, namely an ungerade parity of the initial state from which the photoelectron originates. As outlined below, the initial phase difference $\Delta\varphi$ may also be the result of nondipole effects.

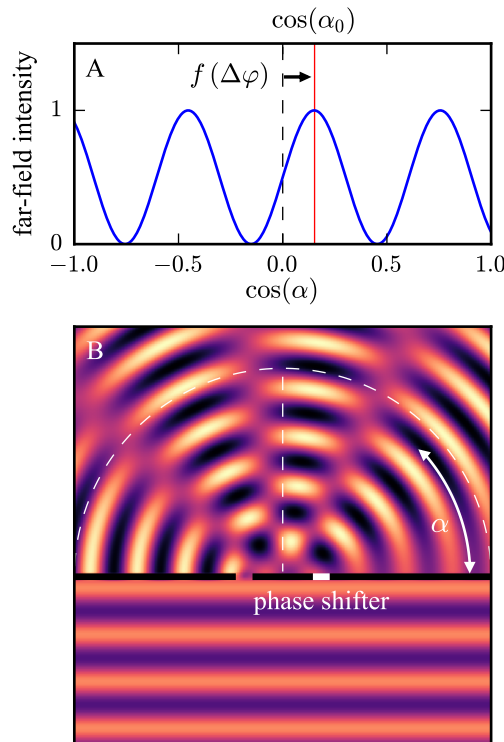


Figure 6.6: Classical double-slit experiment like Fig. 6.2, but the phase delay $\Delta\varphi$ in the right slit causes a tilt of the interference pattern ($\Delta\varphi = \pi/2$). Through Eq. 6.10, $\Delta\varphi$ can be inferred from α_0 , that is the angle to which the central interference maximum is shifted.

Spatially dependent light phase

One simplification of the electric dipole approximation—where k_γ is set to zero—is that the light wavelength λ presumably becomes infinite ($k_\gamma = 2\pi/\lambda$). Accordingly, the electric field and its phase are constant over the whole relevant region of space (see Fig. 6.7 A).

The electric dipole approximation breaks down in photoionization if the spatial extent of the molecular (or atomic) orbital and the light wavelength share the same order of magnitude. At the moment of photoabsorption in the nondipole regime, each location of the orbital might experience different electric field vectors and phases (see Fig. 6.7 B).

In the molecular double-slit experiment, the light phase is imprinted on the electron waves which results in an initial phase difference of

$$\Delta\varphi = \mathbf{k}_\gamma \cdot \mathbf{R} = k_\gamma R \cos \beta , \quad (6.11)$$

where β is the angle enclosed by the molecular axis and the light propagation direction (see Fig. B.2). With this expression inserted into Eq. 6.5, the probability distribution for the detection of a single photoelectron on a detector in the far field becomes

$$\mathcal{P} \propto \cos^2 \left[\frac{pR \cos \alpha - k_\gamma R \cos \beta}{2} \right] , \quad (6.12)$$

and the zeroth-order interference maximum is shifted to

$$\cos \alpha_0 = \frac{k_\gamma}{p} \cos \beta . \quad (6.13)$$

Figure 6.8 illustrates these nondipole corrections to the molecular double slit experiment.

Equation 6.12 was first presented by G. Yudin et al. in 2006 [110] as

$$\mathcal{P} \propto \cos^2 \left[\frac{pR \cos \alpha - k_\gamma R \cos \beta}{2} + \frac{1}{p} \ln \left(\frac{1 + \mathbf{p} \cdot \mathbf{R}/pR}{1 - \mathbf{p} \cdot \mathbf{R}/pR} \right) \right] , \quad (6.14)$$

where the additional term represents the influence of the molecular potential on the photoelectron wave (see, e.g., Fig. B.4). These nondipole corrections to electron emission in the body-fixed frame of a homonuclear diatomic molecule have never been observed in an experiment until the present work.

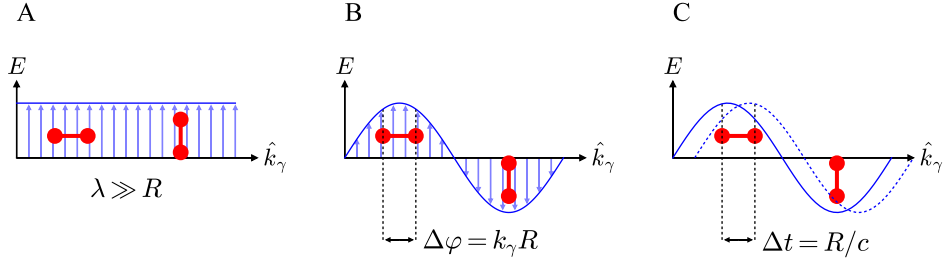


Figure 6.7: Homonuclear diatomic molecule exposed to a linearly polarized electromagnetic wave. (A) Electric dipole approximation: The photon wavelength λ is much larger than the internuclear distance R , the electric field (blue) has no spatial dependence, and the light phase is constant over the whole relevant region of space. (B, C) λ and R have the same order of magnitude: $R/\lambda = 0.15$. (B) Spatially dependent light phase: For parallel alignment of light and molecule, the light phase differs by $\Delta\phi = k_\gamma R$ at the two atomic centers. In case of photoionization, this phase difference is imprinted onto the two coherent waves that emerge from the two atomic centers. If light and molecule are perpendicular, the phase difference vanishes. (C) Birth time delay: A wavefront of constant phase sweeps across the molecule and the birth time of the two coherent photoelectron waves differs by $\Delta t = R/c$ for parallel alignment of molecule and light. The models presented in B and C resemble two different interpretations for nondipolar photoionization of molecules.

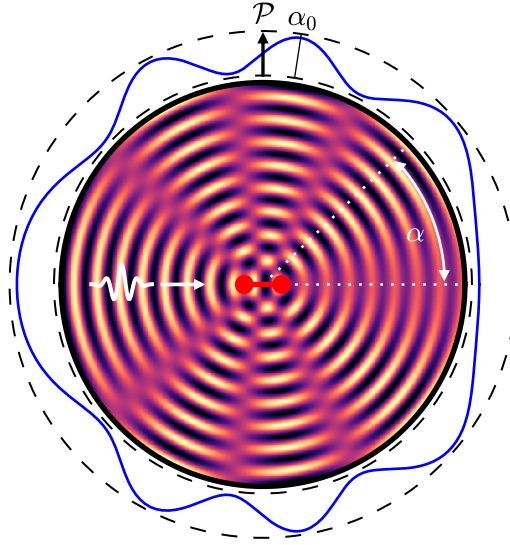


Figure 6.8: Photoelectron emission from a homonuclear diatomic molecule modified by nondipole effects. The photon propagation direction is parallel to the molecular axis and the two coherent photoelectron waves are launched from the two atomic centers with different phases. The probability for the detection of a single electron on a detector in the far field (Eq. 6.12) is indicated by the solid blue line. Like in Fig. 6.3, $R/\lambda_e = 1.65$, which corresponds to 750 eV electron energy and 1.4 au internuclear distance. For illustrative purposes, we chose $\Delta\phi = \pi/2$. For a photon of 800 eV energy, the wavelength λ_e is 15.5 Å. With the average bond length of H_2 ($R = 0.74$ Å), the initial phase difference becomes $\Delta\phi = \pi/20$.

Birth time delay

Two stones dropped into a lake at two positions simultaneously create an interference pattern on the surface that is symmetric around the center of the two drop points. A skipping flat pebble that jumps off the water surface once before it sinks at a position further away, results in an asymmetric interference pattern—like the one depicted in Fig. 6.6—that is shifted towards the position where the stone sunk. The reason for the asymmetry is the time delay between the birth of the two waves on the lake's surface.

This situation is an analogy⁴ to an alternative picture for nondipolar photoionization of a homonuclear diatomic molecule (Fig. 6.7 C). In this picture, a wavefront of constant phase sweeps across the molecular orbital and releases the two contributions to the total photoelectron wave upon arrival at each atomic center. Accordingly, the birth time of the two mixing waves differs by

$$\tau = \frac{R \cos \beta}{c}, \quad (6.15)$$

where c is the speed of light. We call this time difference *birth time delay*. Like surface waves on a lake generated by a skipping pebble, photoelectron waves are born at different times while the light traverses the molecule.

This physical picture is particularly appealing because it involves such ultrashort time spans that were previously beyond reach in atomic physics. To put things into perspective, we consider the speed of the particles involved in photon double ionization of H_2 at 800 eV photon energy. The average bond length of the hydrogen molecule (0.74 Å) is the reference distance. For a proton that receives 10 eV from the kinetic energy release of the molecular break-up, it takes roughly 1.7 fs (1 femtosecond = 1×10^{-15} s) to cover the reference distance. For an electron at 750 eV kinetic energy, it takes 4.56 as (1 attosecond = 1×10^{-18} s). The travel time of light to cover 0.74 Å is 247 zs (1 zeptosecond = 1×10^{-21} s).

The dynamics of atoms in chemical reactions on the femtosecond scale became accessible at the end of the 1980s through efforts led by A. Zewail [111]. Since the advent of attosecond technology by the mid-2000s, temporal aspects of electron dynamics have been investigated experimentally [112]. However, the travel time of light across a microscopic distance in the zeptosecond regime has never been resolved so far.

In a molecular double slit experiment, the birth time delay can be resolved because it leads to an initial phase difference between the two waves. One wave is emitted and propagates with the phase velocity $v_{ph} = E/p$ for the time τ before the second wave is born. The covered distance ($v_{ph} \tau$) constitutes an additional path length difference and the phase difference between the two waves at birth becomes

$$\Delta\phi = 2\pi \frac{v_{ph} \tau}{\lambda_e}. \quad (6.16)$$

Consequently, the far-field phase difference is

$$\Delta\phi = 2\pi \left[\frac{R \cos \alpha}{\lambda_e} - \frac{v_{ph} \tau}{\lambda_e} \right]. \quad (6.17)$$

Following Eq. 6.10, the birth time delay can be inferred from a measured angle α_0 through

$$\tau = \cos \alpha_0 \frac{R}{v_{ph}}. \quad (6.18)$$

⁴I did not come up with this analogy myself. Kudos go to Markus Bernards, the Science Communications Manager at Goethe-University.

To some extent, the internuclear distance R and the electron phase speed v_{ph} —i.e., the photoelectron energy—can be chosen by the experimentalist prior to conducting a molecular double-slit experiment. Intuitively, one might think that a larger R , that leads to a larger birth time delay τ , makes the measurement easier. However, the birth time delay is derived from the observable α_0 and that makes the situation less straightforward. After substituting Eq. 6.15 into Eq. 6.18, we can write

$$\cos \alpha_0 = \frac{v_{ph}}{c} \cos \beta. \quad (6.19)$$

As illustrated in Fig. 6.9, an increase of the phase speed v_{ph} has no effect on the birth time delay τ but magnifies the observable α_0 . On the other hand, increasing the internuclear distance R leads to a larger τ , but the magnitude of α_0 remains the same. Still, a larger R makes it easier to infer α_0 from the measurement because the width of the zeroth-order interference maximum decreases.

An obvious question is how are the two physical pictures for nondipolar photoionization of a homonuclear diatomic molecule related? Upon substituting Eq. 6.15, $v_{ph} = E/p$, and $\lambda_e = h/p$ into Eq. 6.16, it becomes

$$\Delta\varphi = 2\pi \frac{E}{hc} R \cos \beta. \quad (6.20)$$

If the binding energy of the electron is small compared to the photon energy, we can set $E \approx E_\gamma$ and use $\lambda = hc/E_\gamma$ in Eq. 6.20, that subsequently becomes

$$\Delta\varphi = \frac{2\pi}{\lambda} R \cos \beta = k_\gamma R \cos \beta, \quad (6.21)$$

which is exactly the same as Eq. 6.11. Hence, the ideas of the spatially dependent light field and the finite travel time of light across the relevant region of space are two closely related pictures to describe the same physical reality.

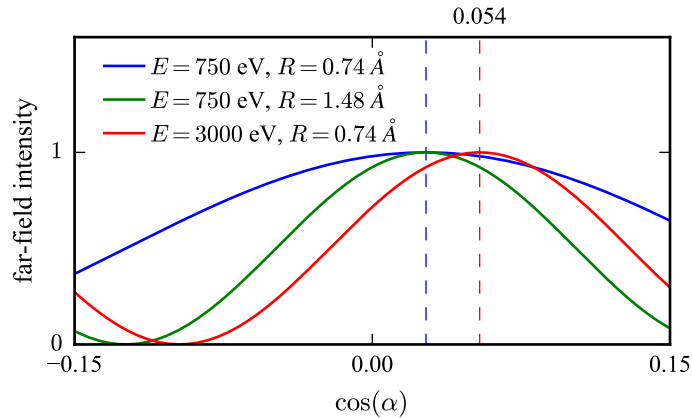


Figure 6.9: Shift of the zeroth-order interference maximum α_0 (dashed lines) due to birth time delay for different internuclear distances R and electron phase speeds $v_{ph} = E/p \propto \sqrt{E}$.

Shift of the initial-state momentum

Last but not least, the nondipole corrections to the molecular double-slit experiment can be considered in the momentum representation of the problem.

The diffraction of waves at periodic structures can lead to interference effects. The intensity distribution of a diffracted wave as function of magnitude and direction of the wave vector \mathbf{k} is given by

$$I(\mathbf{k}) \propto \left| \int e^{-i\mathbf{k}\cdot\mathbf{r}} \rho(\mathbf{r}) d^3r \right|^2, \quad (6.22)$$

where $\rho(\mathbf{r})$ is the function that describes the geometrical structure of the diffraction elements. Hence, the intensity of the wave as function of \mathbf{k} is proportional to the squared modulus of the Fourier transform of $\rho(\mathbf{r})$.

For the molecular double-slit experiment, the geometrical structure may be described as

$$\rho(\mathbf{r}) = \delta\left(\mathbf{r} \pm \frac{\mathbf{R}}{2}\right), \quad (6.23)$$

where δ is the Dirac delta function. By using Eq. 6.23 in Eq. 6.22 and substituting \mathbf{k} by \mathbf{p} —i.e., the electron wave vector that equals its momentum in atomic units—we get the following probability distribution for the observation of a photoelectron with momentum \mathbf{p}

$$\mathcal{P} \propto \left| e^{-i\mathbf{p}\cdot\frac{\mathbf{R}}{2}} + e^{i\mathbf{p}\cdot\frac{\mathbf{R}}{2}} \right|^2 \propto \cos^2 \left[\frac{\mathbf{p}\cdot\mathbf{R}}{2} \right], \quad (6.24)$$

which is the same as Eq. 6.6. Hardly surprising, both descriptions of the molecular double-slit experiment—i.e., in momentum and position representations—yield the same photoelectron probability distribution within the dipole approximation.

The electric dipole approximation breaks down if the photon momentum is not negligibly small compared to the momenta of the reaction fragments and corresponding nondipole corrections must manifest in the description of the molecular double-slit experiment in momentum representation. As discussed in *Kinematics of photoionization* (see p. 6), the photon momentum is imparted almost entirely onto the ion center of mass and the magnitude of the observable photoelectron momentum vector does not depend on its emission direction in the laboratory frame of reference. Accordingly, we cannot simply explain the nondipole corrections to the molecular double-slit experiment by the inclusion of the photon momentum in the final-state electron momentum.

An illustrative way to approach the molecular double slit in momentum space was presented by Waitz et al. in Ref. [33]. For one-photon single ionization of H_2 , the authors showed that the photoelectron angular distribution in the molecular frame of reference *images* the initial-state wave function. The authors presented the initial-state wave function in momentum space in a two dimensional coordinate system, where the two axes were parallel (p_{\parallel}) and perpendicular (p_{\perp}) to \mathbf{R} . In such a picture, the possible photoelectron momenta lie on a circle centered at the origin with radius p and probing the probability density of the initial-state wave function along the path of the circle yields the photoelectron angular distribution in the molecular frame of reference. In Fig. 6.10 A, we utilize the same method of representation but approximate the initial-state wave function in momentum space within the dipole approximation simply as the squared modulus of the Fourier transform of $\rho(\mathbf{r})$.

In the spirit of this approach, the nondipole corrections to the molecular double-slit experiment can be explained as follows. The observable magnitude of the

photoelectron momentum and the locations in position space, from where the two waves originate, remain unchanged. However, the photon momentum shifts the initial momentum-space distribution with respect to the reference frame of the observation. This situation is illustrated in Fig. 6.10 B. Here, the photoelectron angular distribution, which probes the structure of the initial-state wave function, becomes asymmetric. The shown detection probability is the same as in Fig. 6.8. To include these nondipole correction in Eq. 6.22, the Fourier transform of $\rho(\mathbf{r})$ has to be modified by writing

$$I(\mathbf{p}) \propto \left| \int e^{-i\mathbf{K}\cdot\mathbf{r}} \rho(\mathbf{r}) d^3r \right|^2, \quad (6.25)$$

where $\mathbf{K} = \mathbf{p} - \mathbf{k}_\gamma$, which accounts for the initial-state modification of the wave vector. Accordingly, Eq. 6.23 becomes

$$\mathcal{P} \propto \cos^2 \left[\frac{(\mathbf{p} - \mathbf{k}_\gamma) \cdot \mathbf{R}}{2} \right], \quad (6.26)$$

which is the same expression as Eq. 6.12. Accordingly, the momentum and the spatial representation of the problem yield the same nondipole corrections to the molecular double-slit experiment.

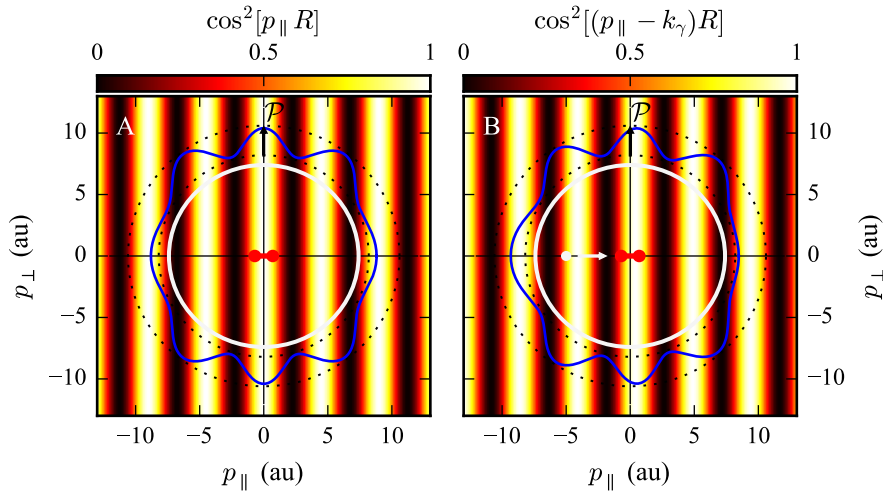


Figure 6.10: Imaging of the initial-state wave function in momentum space as suggested in Ref. [33]. The probability density of the wave function is encoded in the color bar and it is approximated as the squared modulus of the Fourier transform of Eq. 6.23, which describes the geometrical structure of the molecular double slit with $R = 1.4$ au. All observable photoelectron momenta lie on the white circle which is centered at the origin and has a radius of $p = 7.4$ au. Probing the probability density along the path of the circle yields the probability for the detection of an electron with a certain momentum, which is indicated by the solid blue line. (A) Dipole approximation. (B) The nondipole corrections manifest in a shift of the initial-state wave function in momentum space by k_γ . Here, $k_\gamma = 0.4$ and the photon momentum vector is parallel to the molecular axis, as indicated by the white arrow.

Review of nondipolar photoionization of molecules

Resolved in the laboratory-frame of reference, nondipole effects in photoionization of molecules have been extensively studied in the past. For example, experiments observed forward/backward asymmetries in photoelectron emission from H_2 [113, 114], from the N_2 K -shell [115–117], from the N_2 valence shell [118], and from the carbon K -shell of CO [119]. Further theory predictions and derivations can be found, e.g., in Refs. [120–122].

For the investigation of one-photon single and double ionization of H_2 , the experiment conducted for the present work used the highest photon energy up to this day (800 eV). The previous experiments on N_2 K -shell photoionization used photon energies up to a maximum of 700 eV [116]. Recently, M. Kircher et al. observed nondipole effects for photon energies between 12 and 40 keV [123]. The present work deals with the intermediate range between 880 eV and 2160 eV photon energy.

Experimental nondipole studies resolved in the molecular-frame of reference are much rarer. In 2002, R. Guillemin et al. reported on strong effects for K -shell ionization of N_2 at 660 eV photon energy [124]. However, the results were questioned (e.g., Ref. [117]) and never theoretically underpinned or verified in another experiment, as far as the author knows.

In 2019, M. Kircher et al. reported on K -shell ionization of N_2 at 40 keV photon energy and companion calculations [125]. The authors observed that the lab-frame nondipole effects depend on the orientation of the molecules with respect to the light, but they did not resolve the MFPAD.

The present work reveals nondipole effects on the molecular double-slit experiment conducted with K -shell ionization of H_2 and N_2 . The experiment on N_2 was conducted at several photon energies in order to uncover the interplay between laboratory- and molecular-frame nondipole effects, that are discussed in the next chapter.

INTERPLAY OF NONDIPOLE EFFECTS

How do the previously discussed nondipole effects in the laboratory- and the molecular-frame of reference influence each other?

The modifications of the laboratory-frame photoelectron angular distribution in K -shell photoionization of N_2 due to nondipole corrections to the MFPAD were computed by D. Toffoli and P. Decleva in 2006 [126].¹ As shown in Fig. 7.1 C & D, the authors found that the forward/backward asymmetry of photoelectron emission in the lab frame—measured in terms of the nondipole parameter γ (see Eqs. 4.25 & 4.26)—is modified by molecular nondipole effects, if the parity of the initial state is resolved.

At high photon energies (Fig. 7.1 D), we can derive a simple explanation for the calculated oscillations from the concepts introduced in the previous chapter. We assume circularly polarized light and parallel alignment between molecule and light propagation direction (i.e., $\cos \beta = 1$). Hence, the electron emission angles in the laboratory frame (ϑ_γ , see Eq. 4.25) and in the molecular frame (α , see Eq. 6.12) coincide. We assume no initial atomic nondipole effects ($\gamma = \delta = 0$) and a dipole parameter of $\beta = 2$. Accordingly, the probability distribution as function of the electron emission angle becomes

$$\mathcal{P}(\cos \vartheta_\gamma) \propto \cos^2 \left[\frac{pR \cos \vartheta_\gamma - k_\gamma R}{2} \right] \times [1 - P_2(\cos \vartheta_\gamma)] , \quad (7.1)$$

and the weighted average of $\cos \vartheta_\gamma$ is

$$\langle \cos \vartheta_\gamma \rangle = \int_{-1}^1 \cos \vartheta_\gamma \mathcal{P}(\cos \vartheta_\gamma) d \cos \vartheta_\gamma . \quad (7.2)$$

The blue line in Fig. 7.1 A & B shows $\langle \cos \vartheta_\gamma \rangle$ as function of the photon energy for $R = 2.07$ au and $I_p = 410$ eV, and the green line presents the counterpart of Eq. 7.2 for an ungerade initial state. If $\langle \cos \vartheta_\gamma \rangle > 0$, the nondipole parameter γ is increased and vice versa.

At high photon energies, the oscillations of $\langle \cos \vartheta_\gamma \rangle$ and the calculated values for γ are in phase. Accordingly, the nondipole corrections to the MFPAD—as presented in Eq. 6.12—explain the modulation of the forward/backward asymmetry of photoelectron emission in the laboratory frame. Note that for arbitrary orientation of the molecular axis relative to the photon propagation direction, the derivation becomes more complex and harder to imagine, but still yields the same result. At low photon energies, where the Born approximation breaks down, the calculated modulation of γ cannot be explained by the nondipole corrections to the molecular double-slit experiment.

The magenta line in Fig. 7.1 A & B shows the Cohen-Fano interferences for comparison (Eq. 6.2). Because of the mutual physical origin, the Cohen-Fano interferences are in phase with the gerade oscillations of $\langle \cos \vartheta_\gamma \rangle$ at high photon energies.

The dashed purple lines in Fig. 7.1 B & D indicate the photon energies used in our experiments to confirm the calculations presented by Toffoli and Decleva.

¹The authors were so kind to provide us with the numerical results of their study.

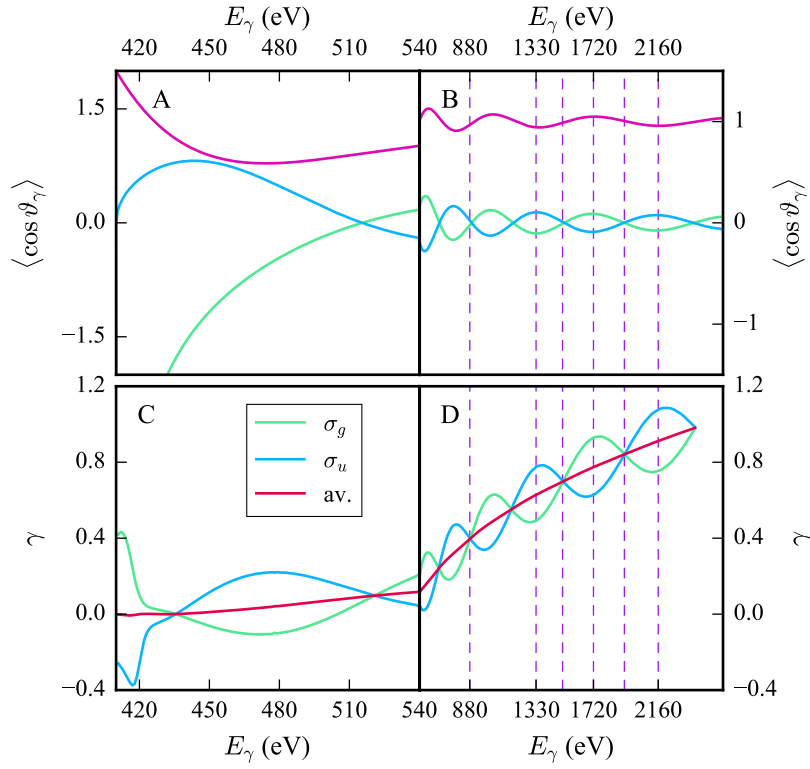


Figure 7.1: (A, B) Green: Average photoelectron emission angle in the laboratory frame of reference for parallel alignment of light and homonuclear diatomic molecule ($\cos \beta = 1$) under the assumption of no atomic nondipole effects ($\beta = 2$, $\gamma = \delta = 0$), as calculated from Eq. 7.2 for $R = 2.07$ au, $I_p = 410$ eV, and a molecular orbital of gerade parity. Blue: Like green, but for ungerade parity. Magenta: Cohen-Fano interferences (Eq. 6.2). (C, D) Calculated nondipole parameter γ as function of the photon energy resolved for photoelectron emission from the gerade (green) and ungerade (blue) K -shell state of N_2 [126].

Vice versa, atomic nondipole effects modify photoelectron emission measured in the molecular frame. Again, we assume circular polarization and parallel alignment between molecule and light ($\cos \beta = 1$), but we set $k_\gamma = 0$, $\beta = 2$, $\gamma = 3$, and $\delta = 0$. Now, the probability distribution as function of the electron emission angle becomes

$$\mathcal{P}(\cos \alpha) \propto \cos^2 \left[\frac{pR \cos \alpha}{2} \right] \times \left[1 - P_2(\cos \alpha) + \frac{3}{2} \sin^2 \alpha \cos \alpha \right]. \quad (7.3)$$

The red line in Fig. 7.2 displays Eq. 7.3 for $R = 1.4$ au and $p = 7.4$ au. Even though there is no initial phase difference between the two interfering waves, the center of the zeroth-order interference maximum ($\cos \alpha_0$) is shifted due to the atomic nondipole effect. Accordingly, if the initial phase shift is calculated from a measured $\cos \alpha_0$ (see Eq. 6.10), this has to be kept in mind.

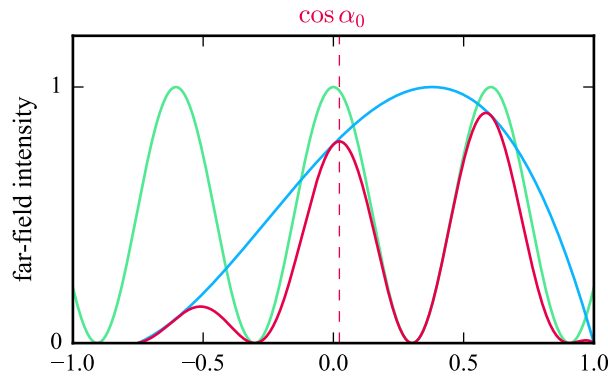


Figure 7.2: Shift of the zeroth-order interference maximum $\cos \alpha_0$ due to the atomic nondipole effect. Here, we have assumed $R/\lambda_e = 1.65$, $k_\gamma = 0$, parallel alignment of light and homonuclear diatomic molecule ($\cos \beta = 1$), $\beta = 2$, $\gamma = 3$, and $\delta = 0$.

Part II

METHODS

EXPERIMENT

The purpose of this chapter is two-fold. First, it provides any reader with a broad overview of how the experimental setup works while detailed literature is referenced throughout the text. Second, it contains all necessary information needed by an expert experimentalist to reproduce the raw data.

8.1 COLD TARGET RECOIL ION MOMENTUM SPECTROSCOPY

To obtain the experimental results of this thesis, we employed a method called *cold target recoil ion momentum spectroscopy* (COLTRIMS) [9].

The basic principles of this technique are the following (see Fig. 8.1): A supersonic jet of a target gas is intersected with a light beam at right angle inside an interaction chamber under vacuum. The charged reaction fragments—electrons and ions created via photoionization—are guided by electric and magnetic fields from the interaction zone towards two time- and position-sensitive detectors. From the time of flight and the position of impact, the three-dimensional momentum vector is determined for each detected particle.

The exceptional strength of the COLTRIMS technique is the coincident measurement scheme, which allows to group the detected particles into individual photoionization *events*. The subsequent analysis can be limited to sets of events that fulfill certain conditions. Given enough statistics, this concept allows to obtain conditional reaction probabilities depending on any observable degree of freedom of initial and final state, i.e., the fully-differential cross section of the process.

A machine implementing this technique is a COLTRIMS reaction microscope. An in-depth account of hardware employed in a reaction microscope can be found in Ref. [127]. In the following, we will briefly cover the essential components. A detailed review of the very reaction microscope used to obtain the results of the present work can be found in Ref. [87].

Photon source

All experiments for this thesis were carried out at beamline Po4 [128] of the synchrotron light source PETRA III at DESY in Hamburg, Germany. PETRA III is an electron storage ring of 2.3 km circumference. With a kinetic energy of up to 6.0 GeV, the orbiting electrons travel at close to speed of light. The COLTRIMS technique demands a certain minimum time between two photoionization events, mainly to prevent the time-of-flight distributions from two consecutive events to overlap. Thus, PETRA III was operated in the so-called *time-resolved mode* during the experiments. Here, the total number of electrons orbiting the ring are grouped into 40 bunches that are equally spaced over the circumference. Accordingly, the elapsed time between two bunches passing a stationary location inside the ring was 192.17 ns.

Electrons, deflected from their straight paths by magnetic fields, emit the synchrotron light [129]. At beamline Po4, the custom magnetic field is created by an APPLE-2 *type undulator* [130] that forces electrons onto a slalom- or cork-screw-like path. While the former path generates linearly polarized photons, the latter makes circularly polarized light. The combination of both settings facilitates the undulator at Po4 to generate any elliptical polarization. In all our experiments, however,

we used circularly polarized photons because beamline Po4 was not yet able to provide linearly polarized light due to technical difficulties.

In the reference frame of the electron, a spectral line produced by the APPLE-2 undulator is roughly Gaussian shaped with a relative energy resolution (FWHM) of about $1/72$ (the relative energy resolution is inversely proportional to the number of undulator periods [131]). However, due to higher harmonics and Doppler frequency shifts, the observed overall spectrum is broadened and biased in the laboratory frame of reference (see, e.g., Fig. 6.6 in Ref. [129]). Thus, a *monochromator*, consisting of diffraction gratings and apertures, is used to cut a narrow energy peak from the undulator spectrum before delivering the photons to the experimental endstation.

Beamline Po4, in particular, is suitable for application in the photon energy range from 250 eV – 3000 eV. Using the standard monochromator gratings, a photon flux of up to 5×10^{12} photons/s can be achieved. For the H₂ experiment at 800 eV photon energy, we have used an aluminum blank mirror instead of the usual monochromator gratings. By setting the monochromator to zeroth order (diffraction angle equal to incident angle) we generated a so-called *pink beam* and increased the photon flux to an estimated maximum of 1.6×10^{14} photons/s. To remove contaminating low-energy photons, a stacked filter (Al 255.9 nm + B 716.5 nm + Cu 76.8 nm + polyamide) was inserted into the beam path. Because of the low cross section of H₂ double ionization at 800 eV photon energy, this high-flux pink beam was crucial for this experiment's success.

Target preparation system

The supersonic jet is initiated in an adiabatic expansion of the target gas from a high driving pressure into a low pressure container through a circular aperture (nozzle). The adiabatic expansion converts the inner energy of the gas into a directed momentum distribution. Using a special cone-shaped aperture (skimmer), a narrow jet is then sliced from this plume and guided towards the interaction region. A comprehensive account on this target preparation technique can be found, e.g., in Ref. [132].

Here we used the same target preparation system for all experiments and just exchanged the gas cylinders containing the target gases. A graphical illustration of the system's geometry can be found in Ref. [133]. The nozzle had a diameter of 0.03 mm and all target gases were at room temperature before the expansion. The individual properties of the target gas jet can be found in Sec. 8.2 for each experiment.

Spectrometer and electric field

The spectrometer generates the electric field which is one part of the ion optics that guide the charged reaction fragments towards their respective detectors. The spectrometer's geometry can be customized for each use of a reaction microscope in order to optimize the ion optics with regard to the process under investigation. The spectrometer kit used here consisted of square copper plates (100 mm edge length and 0.5 mm thickness) with a central circular hole (80 mm diameter), that could be stacked on top of each other (5 mm separation).

In a most basic version, the spectrometer creates an electric field that is homogeneous over the whole open volume. However, a more sophisticated custom electric field can compensate for the adverse effects of the extended (rather than point-like) reaction volume, i.e., the overlap of light beam and gas jet, on the momentum resolution (see, e.g., Ref. [134] for a detailed account).

First, a combination of a homogeneous acceleration field followed by a field-free drift region can project reaction fragments with the same initial momentum but

different starting positions in \hat{z} direction onto the same time of flight. Due to longer acceleration, particles starting further away from the detector gain more speed before entering the drift and catch up to particles that start closer to the detector. To optimize the focusing effect, the ideal configuration of acceleration length to drift length is at a ratio of two to one [135].

Second, an electrostatic lens can have a similar momentum focusing effect in the \hat{x} - \hat{y} plane. While a homogeneous electric field requires constant steps of potential changes from one spectrometer plate to the next one, a larger step creates such an electrostatic lens. It can project particles with the same initial momentum but different starting positions onto the same position of impact because the deflection angle depends on the trajectory's distance from the central axis while propagating through the lens. The focusing power of the lens is characterized by the lens factor which is the ratio of maximum field strength generated by the lens compared to the homogeneous acceleration field strength.

The spectrometer geometry, the acceleration field strength, and whether these focusing techniques are necessary or not depend on the details of the experiment. All those experimental parameters can be found in Sec. 8.2.

Helmholtz pair of coils and magnetic field

The magnetic field, i.e., the second essential part of the ion optics, is created by a Helmholtz pair of coils whose axis is aligned with the spectrometer axis (\hat{z} axis). The magnetic field is used to confine the electrons on a cyclotron motion inside the cylinder-shaped open volume of the spectrometer. Due to the much higher mass, ions are barely influenced by the magnetic field. Therefore, ions roughly follow a simple curved path, but electrons gyrate towards the detector on a more complex trajectory (see Fig. 8.1).

Each coil used here had 15 turns, a diameter of 145 cm, and was water cooled. The distance between the coils was 72 cm. This large size facilitated a homogeneous magnetic field covering the whole inside volume of the spectrometer's electron arm. The two power supplies in parallel operation that fed the coils could produce an electric current of up to roughly 300 A. Thus, the maximum value of the magnetic field is about 56 G.

The higher the electron energy, the stronger the magnetic field has to be to confine the electrons inside the spectrometer. Theoretically, the used reaction microscope could detect electrons of up to 1060 eV kinetic energy with initial momenta perpendicular to the \hat{z} direction, considering the maximum magnetic field strength of 56 G and the 80 mm diameter of the cylinder-shaped open volume of the spectrometer.

However, a high magnetic field has adverse effects on the quality of the measured relation between the particle's time of flight and position of impact, which is later used to calculate the vector momentum. A consequence of the electron's cyclotron motion is that after a certain time—the gyration period t_g —all electron trajectories intersect again with the \hat{z} -axis. This leads to the characteristic nodes in the histogram depicting the relation between the particle's time of flight and position of impact (see Fig. 9.1 C). The information about the initial vector momentum is lost for electrons whose time of flight is an integer multiple of the gyration period because the whole \hat{x} - \hat{y} momentum distribution is compressed into a single spot on the detector. The higher the magnetic field, the more unfavorable nodes are packed into a given electron time-of-flight distribution, because the gyration period is inversely proportional to the magnetic field strength. Consequently, the magnetic field strength should be chosen as high as necessary but as low as possible.

Detectors

The time- and position-sensitive detectors consist of two key components. One is the microchannel plate that detects a single particle's time of impact [136]. Such a plate is a glass wafer penetrated by parallel channels that are slightly tilted with regard to the plate's surface normal (bias angle). The face sides of the plate are electrically well conducting but the channel walls are covered by a high-resistance coating. When in operation, a voltage is applied between the face sides of the plate. If a particle impinges on a channel wall, an electron bunch is released and accelerated towards the channel exit. On its path, the bunch strikes the channel walls several times and grows in electron number. The time-of-impact signal is tapped from the current compensating the depletion of negative charge upon exit of the electron bunch.

The electron bunch is then accelerated towards a position-sensitive delay-line anode [137], the other key detector component. Here, the electron bunch generates a signal on a wire that propagates in opposite directions with constant velocity. The position of impact in one direction of the detector plane is calculated from the different arrival times of the signal at the two wire ends. A combination of at least two linearly independent delay-line wires facilitates position read-out within the whole detector plane.

The detectors used here were largely similar for electron and ion detection. Both had an active circular detection area of 80 mm diameter. Both used a stack of two microchannel plates arranged in the so-called *Chevron configuration* [136]. Two *hexagon delay-line anodes* [138] were used for position read-out, which—instead of two—consist of three delay-line wires at angles of 60° to each other. However, a *funnel microchannel plate* replaced the standard one on top of the stack for the ion detector in Session 2 and Session 3 to increase detection efficiency [139].

Signal processing and raw data acquisition

Ideally, each particle impinging on the detector generates seven analog signals for further processing: One microchannel-plate signal and six delay-line signals, one for each end of the three layers. After amplification, these signals enter a constant fraction discriminator that transforms the analog pulse shape into a rectangular pattern suitable for digitization via a time-to-digital converter. The time-to-digital converter passes the arrival time of each signal relative to some reference time to the acquisition program *COBOLD* that stores the raw data on a hard drive.

These arrival times are not stored in a continuous stream of data, but the recording produces self-contained events that should ideally resemble the single photoionization events. Each event includes ion and electron signals, and has its own reference time frame. One of the signal pipelines is assigned as the *trigger* that defines time zero when the corresponding channel of the time-to-digital converter registers the first signal. Along with establishing time zero, the trigger-channel's first signal opens a time window reaching into the past and the future, to which all channels contribute the time information of incoming pulses. The size of the time window is chosen according to the expected time span needed to include all particles from the reaction under investigation. To calculate the times of flight, the so-called *bunchmarker signal* is stored along with the particle signals within each event's time window (see p. 64 for further details).

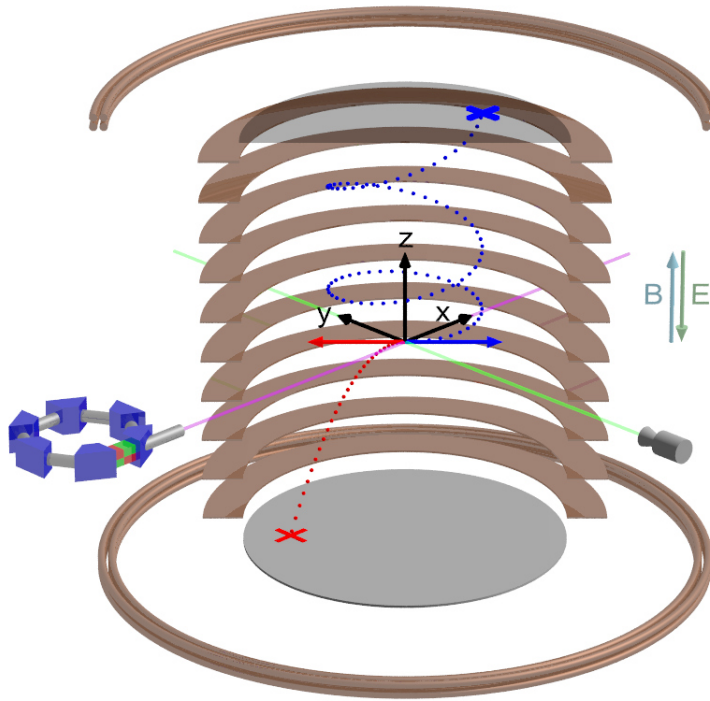


Figure 8.1: Concept of cold target recoil ion momentum spectroscopy (COLTRIMS) and the laboratory frame of reference. A supersonic jet (green) of a target gas is crossed with synchrotron light (violet) at right angle. A homogeneous electric field E , generated by a spectrometer (copper plates), and a homogeneous magnetic field B , created by a Helmholtz pair (copper rings), guide the charged reaction fragments (red trajectory: ion, blue trajectory: electron) towards time- and position-sensitive detectors. The initial three-dimensional vector momentum of each reaction fragment (blue and red arrows) is calculated from the time of flight and the position of impact on the detectors (marked with a red and a blue cross).

The right-handed coordinate system (black) shows the laboratory frame of reference. The positive \hat{x} direction is parallel to the light propagation and the positive \hat{y} direction is aligned to the jet. The positive \hat{z} direction points towards the electron detector. The origin of the coordinate system is centered at the intersection of light beam and gas jet (interaction point). The \hat{x} - \hat{y} plane is frequently called *detector plane*, because it is parallel to the detector surface. The \hat{y} - \hat{z} plane is frequently called *polarization plane*, because at the instant of photoionization the light polarization vector lies within that plane at an arbitrary angle in case of circular polarization.

8.2 EXPERIMENTAL SESSIONS

The raw data sets used for this thesis were recorded in three sessions at beamline Po4 at DESY. During each session, we sometimes changed the experimental parameters and took data in several *runs* to approach different research questions. This section provides an overview with the goals of each session, the different spectrometer designs, and those experimental parameters for each run that are relevant to reproduce the raw data.

Session 1: He QFM (June 16 - 24, 2016)

The main research goal of this experimental session was to obtain fully-differential cross sections of the quasi-free mechanism (QFM) in helium one-photon double ionization. Hence, the initial three-dimensional vector momentum of two electrons and the helium nucleus—independent of their orientation in the laboratory frame—had to be determined.

High photon energies are a prerequisite for QFM and capturing the resulting high energetic electrons without sacrificing full solid-angle acceptance while still achieving reasonable momentum resolution is a challenge in COLTRIMS experiments (see *magnetic field*, p. 55).

In each one of the three experimental sessions we faced a similar challenge and always approached it with the following well-established method: If a photoionization process produces N fragments but only the three-dimensional momentum vectors of $N - 1$ particles are detected, momentum conservation allows to reconstruct the vector momentum of the missing particle. In He double ionization the available excess energy E_{exc} is shared among the two electrons. If the magnetic field strength is chosen in order to detect electrons of up to $E_{exc}/2$ kinetic energy with full solid-angle acceptance, an undetected higher-energetic electron could always be inferred from momentum conservation.

Spectrometer geometry: The electron arm of the spectrometer consisted of an acceleration region of 91 mm length that terminated with a steel grating. The distance between the steel grating and the microchannel plate was roughly 7 mm. The ion arm had an acceleration length of 124 mm and a 800 mm drift which terminated with a steel grating, as well. The distance between the front of the ion detector and the grating was also roughly 7 mm. Situated between 88 mm and 94 mm away from the interaction zone, an electrostatic lens with a lens factor of 20.5 was part of the ion acceleration region. The relatively large size of the ion arm was a consequence of the low kinetic energies of helium ions after photoionization. The detector had to be placed at a far distance from the reaction point in order to use its whole active area for imaging the momentum distribution in the \hat{x} - \hat{y} plane.

Run 1A – Helium at 800 eV photon energy

- Cross section: 863 barn for one-photon single ionization [22], 19.6 barn for one-photon double ionization [140].
- Data acquisition time: 37 h.
- Data acquisition rates: 31 kHz electrons, 16 kHz ions.
- Jet: 0.03 mm nozzle diameter, 50 bar driving pressure, 300 K gas temperature before expansion. Estimated values: 0.63 mm jet diameter at interaction zone, 5.3×10^{11} atoms/cm² target area density, 3.1×10^{-4} mbar inner target pressure, 0.065 au (0.13 au) momentum uncertainty in jet direction (perpendicular to jet).
- Beamline: 0.3 mm exit slits, right circular polarization (positive undulator shift).
- Fields: 20.15 V/cm acceleration, 34.0 G magnetic field.
- Potential settings: +2628 V electron delay-line anode, –50 V electron microchannel-plate front, –202 V electron spectrometer grating, –914 V ion drift, –2050 V ion microchannel-plate front, +316 V ion delay-line anode.¹
- Vacuum interaction chamber: 8.5×10^{-10} mbar.
- Calibration measurements: Helium at 385.0 eV and argon at 248.9 eV, 250.9 eV, 253.9 eV, 258.9 eV, 278.9 eV, 308.9 eV, 348.9 eV, and 408.9 eV photon energy.

Run 1B – Helium at 1100 eV photon energy

- Cross section: 304 barn for one-photon single ionization [22], 7.6 barn for one-photon double ionization [141].
- Data acquisition time: 50 h.
- Data acquisition rates: 20 kHz electrons, 9 kHz ions.
- Jet: 0.03 mm nozzle diameter, 54 bar driving pressure, 300 K gas temperature before expansion. Estimated values: 0.63 mm jet diameter at interaction zone, 5.4×10^{11} atoms/cm² target area density, 3.2×10^{-4} mbar inner target pressure, 0.058 au (0.13 au) momentum uncertainty in jet direction (perpendicular to jet).
- Beamline: 0.4 mm exit slits, right circular polarization (positive undulator shift).
- Fields: 20.15 V/cm acceleration, 43.3 G magnetic field.
- Potential settings: +2696 V electron delay-line anode, –53 V electron microchannel-plate front, –202 V electron spectrometer grating, –913 V ion drift, –2207 V ion microchannel-plate front, +255 V ion delay-line anode.
- Vacuum interaction chamber: 3.3×10^{-9} mbar.
- Calibration measurements: Helium at 550.0 eV and 575.0 eV, and argon at 248.8 eV, 250.8 eV, 252.8 eV, 258.8 eV, 288.8 eV, 348.8 eV, and 708.8 eV photon energy.

¹Note that all further potentials were set via voltage dividing resistors.

Session 2: H₂ QFM and birth time delay (April 12 - 17, 2018)

The research goals of this experimental session were to confirm the quasi-free mechanism occurring in H₂ double ionization and to observe birth time delay in molecular photoionization for the first time ever. The three-dimensional vector momenta of two electrons and both protons had to be determined and again we made use of the momentum conservation trick: The magnetic field was set for full solid angle acceptance of electrons up to half of the excess energy. The momentum of an undetected high-energetic electron was determined from momentum conservation.

While determining the proper electric field strength for the experiment, we failed to consider the gain in kinetic energy due to the photoelectron recoil onto the protons. Thus, the electric field was set a little too low and the calculation of proton momenta required particular corrections (see p. 77).

Spectrometer geometry: The electron arm of the spectrometer consisted of a simple acceleration region of 73 mm length that terminated right at the front of the detector (no grating was used). The ion arm had an acceleration length of 119 mm and a 308 mm drift which terminated with a steel grating. The distance between the front of the ion detector and the grating was roughly 7 mm. This stretch of distance was used for post acceleration of ions to increase the kinetic energy for maximum detection efficiency. Situated between 113 mm and 119 mm away from the interaction zone, an electrostatic lens with a lens factor of 40 was placed at the end of the ion acceleration region. To shield the interaction zone from the influence of the strong electrostatic lens, spectrometer plates with a varying open diameter were used for some part of the ion acceleration. The spectrometer geometry is shown in Fig. 8.2.

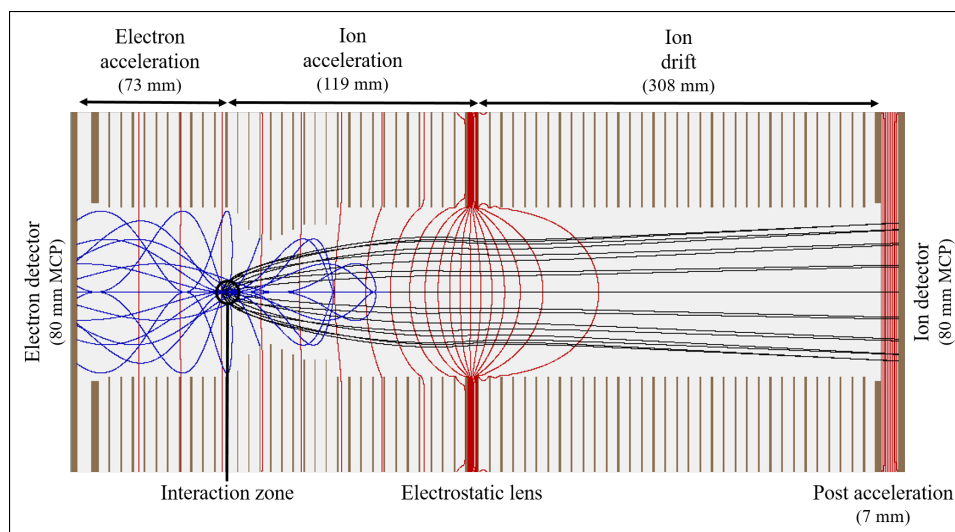


Figure 8.2: Geometry and electric field of the H₂ spectrometer. The red curves show the equipotential lines of the electric field. The black trajectories are from ions with a kinetic energy of 10 eV and different angular orientation of the initial momentum vector. The blue trajectories are from electrons at 400 eV kinetic energy. The magnetic field confines these electrons on a gyration inside the spectrometer.

Run 2A – H₂ at 800 eV photon energy

- Cross section: 62 barn for single ionization, 0.77 barn for double ionization [140].
- Data acquisition time: 132 h.
- Data acquisition rates: 16 kHz electrons, 3 kHz ions.
- Jet: 0.03 mm nozzle diameter, 12 bar driving pressure, 300 K gas temperature before expansion. Estimated values: 0.63 mm jet diameter at interaction zone, 1.1×10^{11} molecules/cm² target area density, 6.5×10^{-5} mbar inner target pressure, 0.255 au (0.085 au) momentum uncertainty in jet direction (perpendicular to jet).
- Vacuum interaction chamber: less than 5×10^{-10} mbar.
- Beamline: 0.5 mm exit slits, right circular polarization (positive undulator shift), pink beam (see p. 53).
- Fields: 39.0 V/cm acceleration, 36.15 G magnetic field.
- Potential settings: +2605 V electron delay-line anode, –229 V electron microchannel-plate front, –254 V electron spectrometer first electrode, –1758 V ion drift, –2627 V ion microchannel-plate front, +174 V ion delay-line anode.
- Calibration measurements: H₂ at 248.0 eV, and argon at 247.0 eV, 250.0 eV, 255.0 eV, 265.0 eV, 290.0 eV, 357.0 eV, 407.0 eV, and 607.0 eV photon energy.

Session 3: N₂ and He nondipole energy scans (March 28 - April 3, 2019)

The objective of this session was to observe the interplay of atomic and molecular nondipole effects in N₂ photoionization from gerade and ungerade initial orbitals. For Run 3A, the magnetic field was set to detect the Auger electron at about 370 eV kinetic energy. Again, the photoelectron was reconstructed from two detected N⁺ ions and the Auger electron by means of momentum conservation.

The energy scan on He photoionization, Run 3B, was measured to obtain a purely-atomic reference. Here, we only detected He⁺.

Spectrometer geometry: We have used a spectrometer of the exact same design as in Session 2 (see Fig. 8.2).

Run 3A – N₂ photon energy scan

- Total data acquisition time: 60 h.
- Photon energies used (and approximate² cross sections for single ionization [22]): 880 eV (0.22 Mbarn), 1330 eV (0.085 Mbarn), 1510 eV (0.063 Mbarn), 1720 eV (0.046 Mbarn), 1930 eV (0.035 Mbarn), and 2160 eV (0.027 Mbarn).
- Jet: 0.03 mm nozzle diameter, 14.5 bar driving pressure, 300 K gas temperature before expansion. Estimated values: 0.63 mm jet diameter at interaction zone, 4.1×10^{11} molecules/cm² target area density, 2.4×10^{-4} mbar inner target pressure, 0.783 au (0.318 au) momentum uncertainty in jet direction (perpendicular to jet).
- Vacuum interaction chamber: approx. 3.3×10^{-9} mbar.
- Beamline: 0.1 mm – 0.9 mm exit slits, right circular polarization (positive undulator shift).
- Fields: 43.3 V/cm acceleration, 36.0 G magnetic field.
- Potential settings: +2031 V electron delay-line anode, –228 V electron microchannel-plate front, –233 V electron spectrometer first electrode, –1913 V ion drift, –2120 V ion microchannel-plate front, +237 V ion delay-line anode.
- Calibration measurements: None.

Run 3B – He photon energy scan

- Total data acquisition time: 4 h.
- Photon energies used (and cross sections for single ionization [22]): 300 eV (17600 barn), 500 eV (3704 barn), 600 eV (2050 barn), 945 eV (498 barn), 1125 eV (367 barn), 1335 eV (170 barn), 1545 eV (101 barn), and 1775 eV (62 barn).
- Jet: 0.03 mm nozzle diameter, 28.5 bar driving pressure, 300 K gas temperature before expansion. Estimated values: 0.63 mm jet diameter at interaction zone, 1.7×10^{11} molecules/cm² target area density, 9.8×10^{-5} mbar inner target pressure, 0.138 au (0.130 au) momentum uncertainty in jet direction (perpendicular to jet).
- Vacuum interaction chamber: approx. 3.3×10^{-9} mbar.
- Beamline: 0.05 mm – 1.0 mm exit slits, right circular polarization (positive undulator shift).
- Fields: 42.1 V/cm acceleration, no magnetic field.
- Potential settings: +2031 V electron delay-line anode, –228 V electron microchannel-plate front, –233 V electron spectrometer first electrode, –1866 V ion drift, –2120 V ion microchannel-plate front, +267 V ion delay-line anode.
- Calibration measurements: None.

²Two times the atomic K-shell cross section.

This chapter covers the procedure for converting the signal arrival times stored in the raw data (see *Signal processing and raw data acquisition*, p. 56) into the three-dimensional momentum vector for each particle in a recorded photoionization event. We have used the *lmf2root*¹ analysis software to handle the raw data and to produce the histograms for data presentation.

The analysis of data generated in a COLTRIMS experiment usually follows the same steps that have been described extensively in the available literature. An in-depth and instructive account can be found, e.g., in Ref. [142].

The present chapter provides only a broad overview of the process in general, but thoroughly covers the parts where our analysis differed from the standard approach. This concerns in particular the calculation of ion momenta, where the effects of the electrostatic lens complicated the procedure.

A comprehensive collection of standard momentum and energy distributions generated from the data used for the present thesis—after application of all correction measures described below—can be found in Appendix C.

9.1 PREPARATORY STEPS

Along with the spectrometer’s geometry and the properties of the electromagnetic field, the calculation of a particle’s momentum requires the associated position of impact on the detector and the time of flight (*TOF*). As described below, these values were determined from the raw data.

A further preparatory step is to apply broad filters on the measured times of flight and positions of impact to limit the momentum calculation procedure to events that are physically reasonable. This step is called *presorting* and described on p. 66.

Position of impact

The procedure to determine the position of impact of a particle on the detector was the same for electrons and ions. For each of the three layers of the delay-line anode (labelled as *u*, *v*, and *w* layer), the position of impact along the layer’s delay-line direction was calculated as

$$u = \eta (t_{u1} - t_{u2}) , \quad (9.1)$$

where η is given in mm/ns and represents the propagation speed of the signal perpendicular to the wire, and t_{u1} and t_{u2} are the signal arriving times at the two ends of delay-line wire *u*. The *v* and *w* layers were treated in the same way.

A simple coordinate transformation yielded the position of impact in terms of *x* and *y* in the laboratory frame of reference (see Fig. 8.1). Note that the combination of at least two linearly independent delay-line directions would suffice, but the redundant information could be used for cross checks and the additional layer increased the multiple-hit readout capacity of the detector [138].

Figure 9.1 shows a histogram of the positions of impact in terms of *x* and *y*—i.e., a *detector image*—for electrons in subfigure A and for ions in B.

¹Version 3, developed by A. Czasch and T. Jahnke.

Time of flight

The time of flight (*TOF*) of a particle is the time that passes between the moment of the photoionization reaction and the moment of the particle's impact on the detector. Identifying the exact moment of photoionization from the measured data requires the following considerations.

The bunchmarker signal correlates to the moments at which an electron bunch passes a certain position inside the PETRA III electron storage ring. While taking experimental data, the bunchmarker signal was recorded repetitively every $T_{bm} = 192.17$ ns (bunchmarker period) during the time window opened upon registration of a signal in the trigger channel of the time-to-digital converter. However, due to the unknown length of the signal path, a constant offset Δt_{bm} materialized between the moment of the photoionization reaction and the corresponding time information that was stored in the raw data. Calculating the times of flight requires to accurately determine this offset.

As the longest possible electron time of flight was shorter than the bunchmarker period in all of our experiments, the value was always calculated as

$$TOF_e = \text{mod}(t_e - t_{BM}, T_{bm}) + \Delta t_{bm}, \quad (9.2)$$

where t_e is the electron's recorded time of impact, t_{BM} is an arbitrary bunchmarker signal, and mod is the modulo operation that returns the remainder of the division of $t_e - t_{BM}$ by T_{bm} .

To determine Δt_{bm} , we exploited that electrons return to their starting point in the \hat{x} - \hat{y} plane after integer multiples of the gyration period t_g due to their cyclotron motion inside the magnetic field. Hence, we varied Δt_{bm} until the first node in the histogram depicting the relation between the electron's time of flight and position of impact coincided with $TOF_e = t_g$, as shown in Fig. 9.1 C.

For all ions on the other hand, the times of flight were much longer than T_{bm} , but the ions shared the same Δt_{bm} against the recorded bunchmarker signal as the electrons. Accordingly, the ion time of flight could be calculated as

$$TOF_i = t_i - t_e + TOF_e, \quad (9.3)$$

where t_i is the ion's recorded time of impact. Figure 9.1 D exemplarily shows the relation between the time of flight and the position of impact for ions.

During the data acquisition of Run 3B (He photon energy scan), the electron detector was switched off and we only measured the photoions. Hence, the true time of flight could not be determined from the recorded data. To calculate the ion momentum in \hat{z} direction, we had to use the quantity

$$TOF_{i,bm} = \text{mod}(t_i - t_{BM}, T_{bm}) + \Delta t_{bm} \quad (9.4)$$

as a substitute for TOF_i in Eq. 9.12. This approach is justified because $TOF_i - TOF_{i,0} = TOF_{i,bm} - TOF_{i,bm,0}$, where $TOF_{i,0}$ and $TOF_{i,bm,0}$ correspond to an ion with zero initial momentum in \hat{z} direction. Note that for this approach to work, the true time-of-flight distribution of the particle must be narrower than the bunchmarker period.

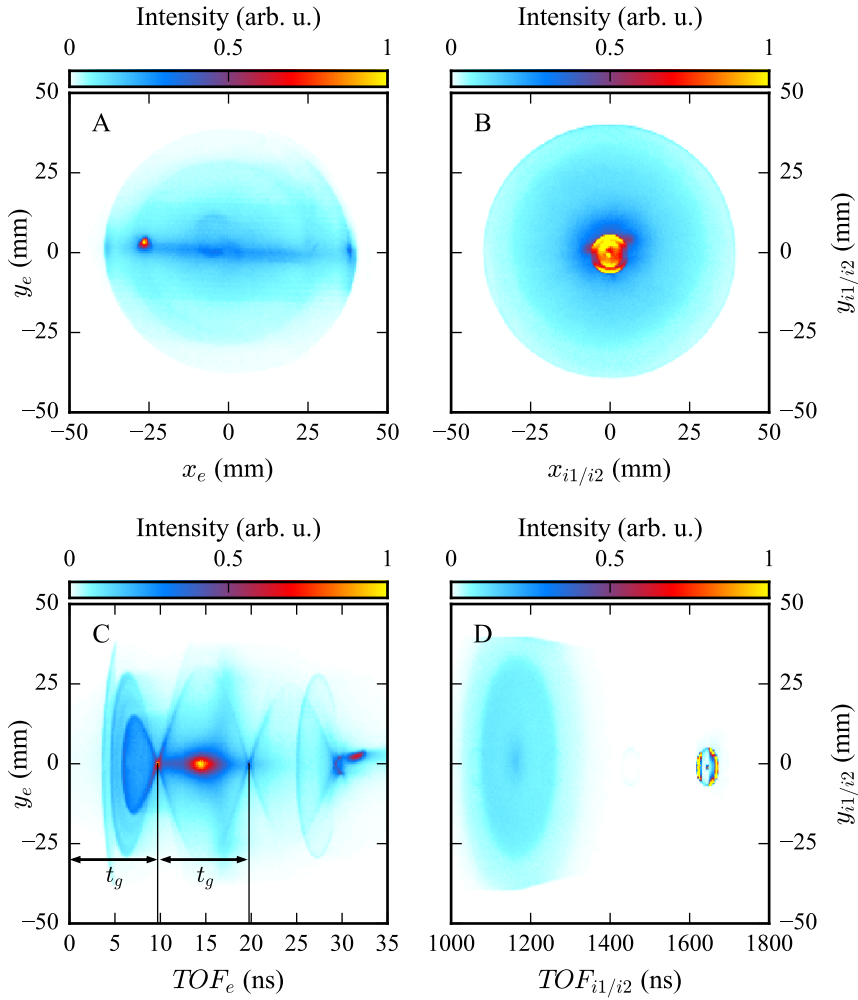


Figure 9.1: Detector images for electrons (A) and ions (B), and unfiltered time-of-flight versus position-of-impact distributions for electrons (C) and ions (D), all obtained from H_2 photoionization at 800 eV photon energy (Run 2A). Note that histograms B and D contain the first and second detected ion, whereas A and C show only one electron.

Presorting

To avoid unnecessary momentum calculations and thereby reduce computation time, the raw data of each experimental run was *presorted* prior to further processing. Here, the presorting reduced the raw data set to only those events where all expected particles were recorded within a reasonable time-of-flight range.

To identify valid events for the break-up of the diatomic molecules H_2 and N_2 , we have plotted the time of flight of the first detected ion against the time of flight of the second detected ion, as shown in Fig. 9.2. The conditions on the times of flight of the two ions, as used for presorting the raw data sets of Run 2A (H_2 at 800 eV photon energy) and Run 3A (N_2 photon energy scan), are indicated by the black rectangles. These conditions ensured that two ions with reasonable times of flight and one electron were present in each valid event, because the electron is a prerequisite for the calculation of the ion time of flight (see Eq. 9.3).

In case of Runs 1A and 1B (Helium at 800 eV and 1100 eV photon energy), the presorter demanded an ion time of flight in the range between 5310 ns and 5380 ns, which enclosed the entire distribution of He^{++} and which ensured one measured electron.

No presorter was used to preprocess the data of Run 3B (He photon energy scan).

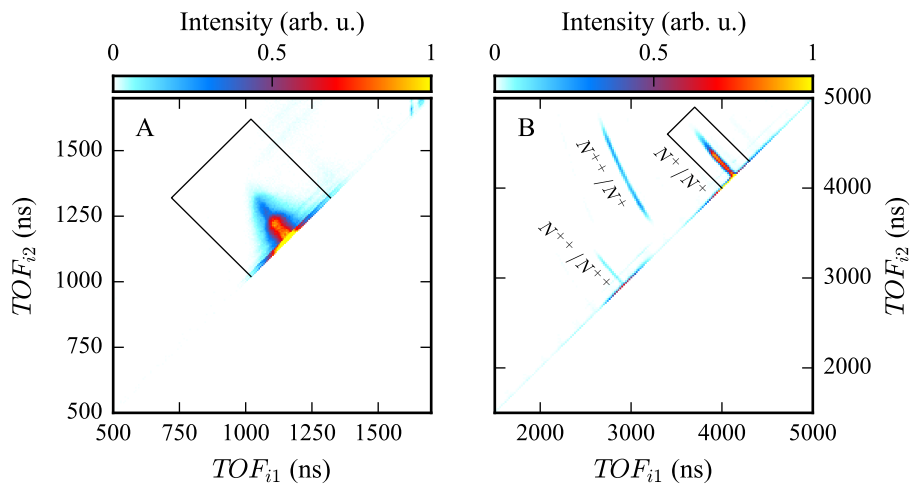


Figure 9.2: Measured photoion-photoion coincidences. (A) Time of flight (*TOF*) of the first detected particle as function of the time of flight of the second detected particle from Run 2A (H_2 at 800 eV photon energy). The black rectangle encloses the area within which two protons can be detected. The two protons originate from dissociation of H_2 (pale blue line), or from the photon-induced break-up of residual H_2O inside the vacuum chamber (broad red/yellow patch). (B) Time of flight of the first detected particle as function of the time of flight of the second detected particle from Run 3A (N_2 photon energy scan). The black rectangle encloses the area within which two singly charged nitrogen atoms can be detected.

9.2 ELECTRON MOMENTUM AND ENERGY CALCULATIONS

The electron arms of the spectrometers used for our experiments did not contain electrostatic lenses and the momentum calculation procedure could follow the typical steps. Under consideration of the magnetic (B) and electric (E) field strengths, and the length of the electron acceleration region (l), the initial momenta of the electrons were calculated from their positions of impact and times of flight.

The analytic solution of an electron's equation of motion in a homogeneous electromagnetic field yields the following relations [143]:

$$p_{e,x} = \frac{m_e(bx_e - ay_e)}{a^2 + b^2}, \quad (9.5)$$

$$p_{e,y} = \frac{m_e(-bx_e - ay_e)}{a^2 + b^2}, \text{ and} \quad (9.6)$$

$$p_{e,z} = m_e \left(\frac{l}{TOF_e} - \frac{1}{2} \frac{eE}{m_e} TOF_e \right), \quad (9.7)$$

with

$$a = \frac{1 - \cos(\omega \cdot TOF_e)}{\omega}, \quad b = \frac{\sin(\omega \cdot TOF_e)}{\omega}, \quad \text{and} \quad \omega = \frac{eB}{m_e},$$

where e and m_e are the electron charge and mass.

The electron's kinetic energy E_e is calculated from the squared magnitude of the momentum vector,²

$$E_e = \frac{p_e^2}{2m_e} = \frac{p_{e,x}^2 + p_{e,y}^2 + p_{e,z}^2}{2m_e}. \quad (9.8)$$

The value of B can be estimated from the properties of the Helmholtz pair (see p. 55) and the electric current that flows through the coils, but it is more accurate to calculate it from the gyration period,

$$t_g = (2\pi m_e)/(eB), \quad (9.9)$$

which can be determined from a time-of-flight versus position-of-impact spectrum as shown in Fig. 9.1 C.

The values of l and E were known approximately from the spectrometer design and power supply settings. However, finding more accurate values and accounting for possible field inhomogeneities to ensure that the momentum calculation yields correct values for all possible electron energies required the electron momentum calibration as described below.

Electron momentum calibration

The accuracy to which the parameters that enter the momentum calculation procedure can be identified from measuring the spectrometer's geometry and from using the set values of the power supplies is usually not sufficient. During most experimental runs, we have therefore conducted several calibration measurements to further straighten the calculation procedure.

For the calibration measurements, we produced electrons of well defined kinetic energies through photoionization that were subsequently recorded under the same

²For easier use in conventional units, we can rewrite Eq. 9.8 as $p_e[\text{au}] \approx \sqrt{E_e[\text{eV}]} \times 0.27$.

conditions as the main measurements. The resulting calibration data was then used as the input to the momentum calculation procedure and the parameters that enter the calculation could be fine-tuned until the procedure yielded the expected values for all calibration energies.

For most calibration measurements, we used argon as the target and addressed the Ar(2*p*) electrons, which resulted in photoelectrons with favorable angular distributions. The Ar(2*p*) electrons have binding energies of 250.6 eV (2*p*_{1/2}) and 248.4 eV (2*p*_{3/2}) and the photon energies were chosen so that the excess energies covered the whole range of electron energies that were expected in the corresponding main measurements.

For example, Fig. 9.3 shows the results of the calibration measurements conducted during Run 2A (H₂ at 800 eV photon energy) as calculated with the final parameters. Here, the electron energy is shown as function of the spherical coordinates $\varphi = \tan^{-1}(p_{e,x}/p_{e,y})$ and $\theta = \cos^{-1}(p_{e,z}/p_e)$.

The negative effects of the high magnetic field and the ion arm's electrostatic lens on the quality of the electron momentum measurement become apparent in Fig. 9.3 B & C. The distributions are intersected by curves where the intensity vanishes that correspond to the nodes in the time-of-flight versus position-of-impact distribution (see Fig. 9.1). In the vicinity of these curves, the momentum calculation becomes inaccurate because the whole momentum distribution in the \hat{x} - \hat{y} plane is compressed into a small area of impact on the detector.

Furthermore, the momentum vectors of electrons that follow trajectories influenced by the field of the ion lens cannot be calculated by means of the procedure introduced above. Figure 9.3 B shows that the calculation procedure is inaccurate at high electron energies if $\cos(\theta) > 0$, i.e., if the electrons are emitted towards the ion detector.

As an electrostatic lens was used on the ion side of the spectrometer in all experimental sessions, we generally removed those recorded events from the results presented in this work where the emission direction of the measured electron fulfilled $\cos(\theta) > 0$.

Reconstructing the momentum vector of the missing second electron

In most experimental runs, we have directly detected all reaction fragments except for one electron (Runs 1A, 1B, 2A, and 3A). This second electron's momentum vector was subsequently reconstructed using momentum conservation including the photon momentum through

$$\mathbf{p}_{e2} = \mathbf{p}_\gamma - (\mathbf{p}_{e1} + \mathbf{p}_i) , \quad (9.10)$$

where $\mathbf{p}_i = \mathbf{p}_{iSum} = \mathbf{p}_{i1} + \mathbf{p}_{i2}$ in case of the diatomic break-up of H₂ or N₂, or $\mathbf{p}_{rec} = \mathbf{p}_{He^{+/++}}$ in case of helium single or double ionization.

How the ion momenta used in Eq. 9.10 were calculated, is addressed in Sec. 9.3 below.

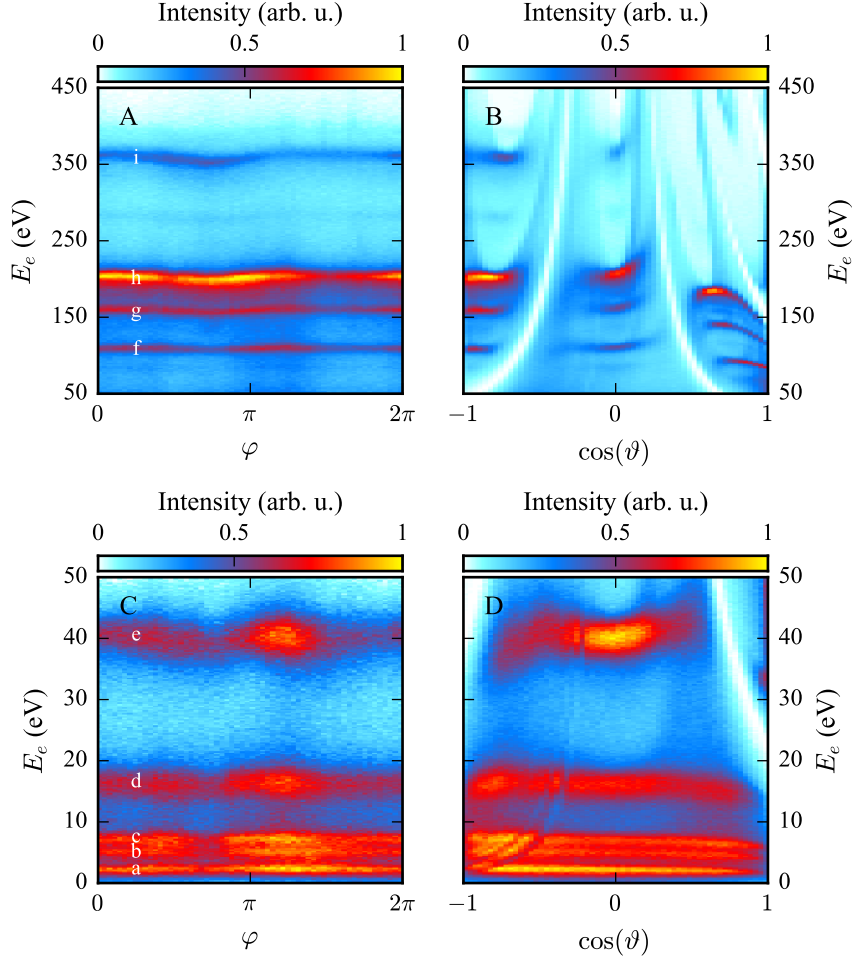


Figure 9.3: Results of the calibration measurements conducted during Run 2A: Photoionization of Ar($2p$) electrons at photon energies of 250.0 eV, 255.0 eV, 265.0 eV, 290.0 eV, 357.0 eV, 407.0 eV, and 607.0 eV. (A,C) Electron energies calculated through Eq. 9.8 as function of $\varphi = \tan^{-1}(p_{e,x}/p_{e,y})$. (B,D) Electron energies calculated through Eq. 9.8 as function of $\vartheta = \cos^{-1}(p_{e,z}/p_e)$. The expected electron energies were: (a) 0.6 eV, (b) 4.4 eV, (c) 6.6 eV, (d) ≈ 15.5 eV, (e) ≈ 40.5 eV, (f) ≈ 107.5 eV, (g) ≈ 157.5 eV, (h, Auger electron) ≈ 205.0 eV, and (i) ≈ 357.5 eV, according to $E_e = E_{bin} - E_\gamma$, where $E_{bin} = 250.6$ eV ($2p_{1/2}$) and $E_{bin} = 248.4$ eV ($2p_{3/2}$). Note that the energy splitting between Ar($2p_{1/2}$) and Ar($2p_{3/2}$) is only resolved for 250.0 eV and 255.0 eV photon energy.

9.3 ION MOMENTUM AND ENERGY CALCULATIONS

If an electrostatic lens is used in the ion arm of the spectrometer, an analytic retrieval of the momentum of the ions is practically impossible.

We have used the following approximations to calculate the momenta of singly and doubly charged helium ions (Runs 1A, 1B, and 3B). Assuming that the electrostatic lens does not affect the ion velocity in \hat{x} and \hat{y} direction, the respective momentum components can be approximated as

$$p_{i,x} = \frac{x_i}{TOF_i} m_i \quad \text{and} \quad p_{i,y} = \frac{y_i}{TOF_i} m_i, \quad (9.11)$$

where m_i is the mass of the ion.³ A similar linear relation can be used for the \hat{z} component,

$$p_{i,z} = \frac{q_i E}{f} (TOF_i - TOF_{i,0}), \quad (9.12)$$

where $f = 124.38 [C \cdot V \cdot s \cdot au^{-1} \cdot cm^{-1}]$ according to Ref. [134], q_i is the charge of the ion, and $TOF_{i,0}$ is the time of flight of an ion with zero initial momentum in \hat{z} direction.

As discussed in Ch. 2 on p. 6, the linear photon momentum shifts the center of the ion momentum distribution, which complicates the calculation of the ion momentum. The procedure to locate the position of impact in light propagation direction that corresponds to $p_{i,x} = 0$ is shown in Sec. 9.3.1.

To calculate the momenta of the ionic reaction fragments after the diatomic breakup of H_2 and N_2 , the calculation procedure introduced above proved to be not sufficiently precise. The alternative procedure used for the analysis of the data from Runs 2A (H_2 at 800 eV photon energy) and 3A (N_2 photon energy scan) is shown in Sec. 9.3.2.

If the correct ion momentum is obtained eventually, the ion's kinetic energy is given by⁴

$$E_i = \frac{p_i^2}{2m_i} = \frac{p_{i,x}^2 + p_{i,y}^2 + p_{i,z}^2}{2m_i}. \quad (9.13)$$

Sum and relative momentum

If the reaction produced two ionic fragments ($i1$ and $i2$), the sum momentum, the relative momentum, and the kinetic energy release (KER) were calculated as

$$\mathbf{p}_{iSum} = \mathbf{p}_{i1} + \mathbf{p}_{i2}, \quad (9.14)$$

$$\mathbf{p}_{rel} = \mathbf{p}_{i1} - \mathbf{p}_{i2}, \quad \text{and} \quad (9.15)$$

$$KER = E_{i1} + E_{i2} = \frac{|\mathbf{p}_{rel}|^2}{2m_{red}}, \quad (9.16)$$

where $m_{red} = (m_{i1}m_{i2})/(m_{i1} + m_{i2})$ is the reduced mass of the two ions with masses m_{i1} and m_{i2} .

³Note that in Runs 1A and 1B, the high magnetic field and the long ion arm of the spectrometer caused a slight rotation of the ion positions of impact in the \hat{x} - \hat{y} plane, which had to be corrected (see Ref. [133] for further details).

⁴For easier use in conventional units, we can rewrite Eq. 9.13 as $p_i[au] \approx \sqrt{E_i[eV] \times m_i[u]} \times 11.6$.

The sum momentum describes the motion of the center of mass of the two ions. This diatomic center of mass behaves like the photoion in ionization of an atomic target, i.e., the photon momentum and the electron recoil momenta are imprinted onto it.

Axial recoil approximation

The orientation of the molecular target in the laboratory frame prior to photoionization was determined a posteriori for every recorded event. For this, we assumed that the direction of the relative momentum vector \mathbf{p}_{rel} is parallel to the molecular axis, because the ionic fragments are emitted along the molecular axis at the moment of photoionization. This assumption is true, if the *axial recoil approximation* [144] is valid, i.e., if the fragmentation is fast in comparison to the rotation of the intermediate molecular ions ($\text{H}_2^{+/++}$ or N_2^{++}).

As shown, e.g., in Ref. [71] for *K*-shell ionization of N_2 followed by Auger decay and in Refs. [90, 98] for photo-double-ionization of H_2 , the axial recoil approximation is valid in the scope of the present work.

Hence, we define the direction of the molecular axis as

$$\hat{\mathbf{R}} = \mathbf{p}_{rel} / |\mathbf{p}_{rel}|. \quad (9.17)$$

In case of H_2 double ionization, the kinetic energy release is purely determined by the Coulomb repulsion of the two bare protons. Assuming the protons are at rest initially, the internuclear distance R —i.e., the molecular bond length—and the kinetic energy release are related through⁵

$$KER = \frac{e^2}{4\pi\epsilon_0 R}. \quad (9.18)$$

A more thorough discussion, that includes the role of initial momenta, and the relation to a quantum treatment can be found in Ref. [145].

⁵For easier use in the conventional units note that $KER[\text{eV}]/27.211 \approx KER[\text{au}]$ and $KER[\text{au}] = 1/R[\text{au}]$.

9.3.1 Zero Momentum in Light Propagation Direction

The photon momentum modifies the momenta of the reaction fragments in nondipolar photoionization. In the photon energy regime covered in the present work, however, the photon momentum is still small compared to the momenta of the reaction fragments⁶ and measuring its effects requires a high precision of the momentum calibration. It is particularly important to precisely locate the position of impact and the time of flight that corresponds to zero particle momentum for each detector in each experimental run.

In the standard approach for the data analysis of a COLTRIMS experiment, the laboratory frame of reference is first described in terms of spherical coordinates. The zero position of impact and the zero time of flight are then located by eliminating any variation in the calculated magnitudes of the particle momenta (or energies) as function of the angular coordinates (see, e.g., Ref. [142]). This approach requires that all particle momenta are located on a sphere in momentum space that is centered around the origin. But as discussed in *Kinematics of photoionization* for one-photon single ionization (see p. 6), the electron and ion momentum spheres are shifted in positive \hat{x} direction due to the linear photon momentum. This shift is proportional to the ratios of the individual particle masses to the combined mass and can therefore be neglected for electrons. Accordingly, the standard approach to locate zero position of impact in \hat{x} direction is not suitable in nondipolar photoionization for the ion momentum calculation.

Figure 9.4 outlines how the zero position of impact in \hat{x} direction has been located for the ion momentum calculation in the data analysis for the present work. The approach is shown for one-photon single ionization of helium at 300 eV, 600 eV, 1125 eV, and 1775 eV photon energy (part of Run 3B, He photon energy scan), but it has been applied to all other data sets as well.

For each measured ion momentum, we have calculated

$$\rho = \mathbf{p}_i - \mathbf{p}_\gamma \quad \text{and} \quad \varphi_\gamma = \cos^{-1} [\rho_x / \rho] , \quad (9.19)$$

and plotted $|\rho|$ as function of φ_γ as shown in Fig. 9.4 C & D.

Note that in the cases of diatomic targets that broke up during the reaction, the sum momentum of the ionic fragments \mathbf{p}_{iSum} was used instead of the helium ion momentum \mathbf{p}_i in Eq. 9.19.

If the zero position in \hat{x} direction and all other momentum calculation parameters are set correctly, the distributions of $|\rho|$ as function of φ_γ should follow a straight line for each photon energy (see Fig. 9.4 D). For an incorrect set of momentum calculation parameters, the distributions vary as function of φ_γ , as shown in Fig. 9.4 C.

⁶E.g., $p_\gamma = 0.215$ au, $p_e = 7.521$ au for single ionization of He at $E_\gamma = 800$ eV.

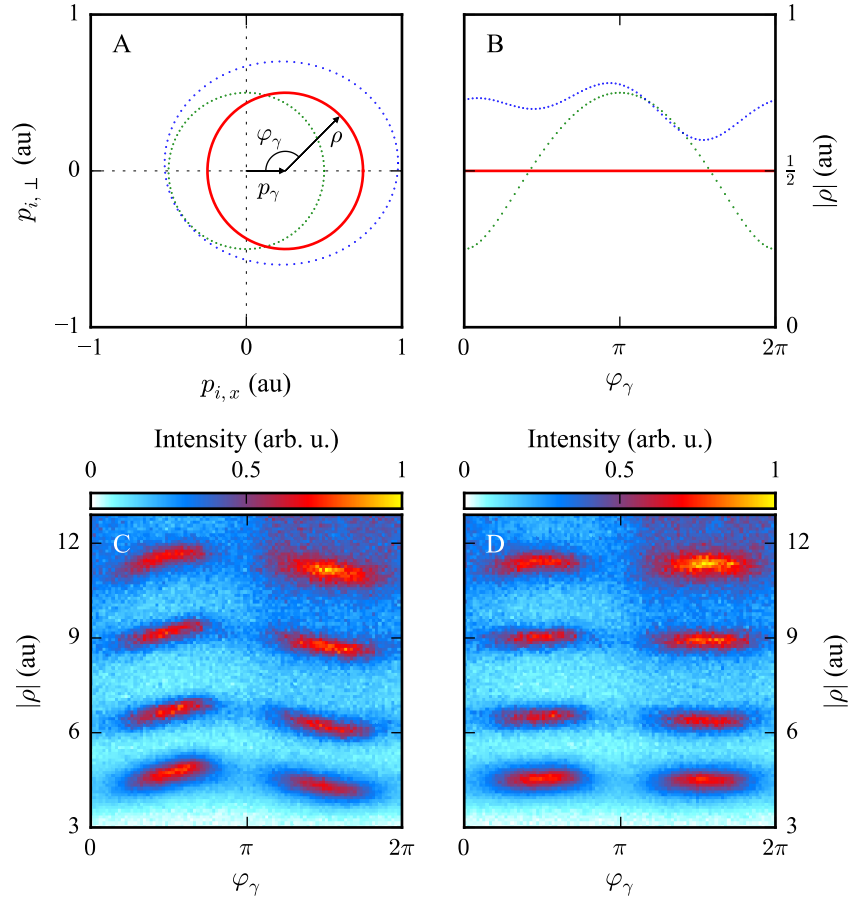


Figure 9.4: Approach to identify the zero position of impact in light propagation direction (\hat{x} direction). (A) In one-photon single ionization, all ion momenta are located on a sphere in momentum space that is shifted away from the origin by the linear photon momentum (solid red circle). The vector ρ (see Eq. 9.19) points from the origin of the shifted momentum sphere to its surface and encloses the angle φ_γ with the photon momentum vector p_γ . (B) Magnitude of ρ as function of φ_γ for correct choice of momentum calculation parameters (solid red line) and for two exemplary incorrect choices (dotted green and blue lines, compare to A). (C) Magnitude of ρ as function of α for helium single ionization at 300 eV, 600 eV, 1125 eV, and 1775 eV photon energy for an incorrect choice of parameters. (D) Same as C, but as calculated with the final set of parameters.

9.3.2 Correction of Lens Distortions

If an electrostatic lens is used in the ion arm of a spectrometer, it might distort the ion trajectories in such a way that a linear approximation alone (Eqs. 9.11 & 9.12) is not sufficient anymore to calculate initial momenta from the times of flight and positions of impact. Analysis of the data proved that the four-body break-ups ($\text{H}_2 + \gamma \rightarrow 2\text{H}^+ + 2\text{e}$ & $\text{N}_2 + \gamma \rightarrow 2\text{N}^+ + 2\text{e}$), where one electron momentum vector was reconstructed by means of momentum conservation instead of being measured directly, demanded a higher validity of the ion momentum calculation procedure than the linear approximation provided.

The alternative calculation procedure introduced below requires an accurate model of the spectrometer—including geometry and electric field—to simulate the trajectories of ions with particular initial momentum vectors. The approach is a two-step process:

- (1) The initial ion momenta p_i^{real} are set as an input to the simulation and they are subsequently recovered through a map that depends only on the simulated times of flight and positions of impact. This map consists of a simple linear relation that is subsequently modified by polynomial functions.
- (2) This map is applied on the measured times of flight and positions of impact to calculate the initial momentum vectors for the experimental data.

This approach is shown below for the analysis of the data obtained in Run 2A (H_2 at 800 eV photon energy), but it has also been applied for Run 3A (N_2 photon energy scan). We have used the SIMION[®] software package for the simulation. The model of the spectrometer model is depicted in Fig. 8.2.

In the simulation we took advantage of the spectrometer's cylindrical symmetry and let the \hat{x} direction represent any direction perpendicular to the \hat{z} axis (time-of-flight direction). We used protons of 5 eV, 10 eV, and 15 eV kinetic energy that were launched from a single point at the center of the reaction zone at angles of $\theta = \tan^{-1}(p_{i,x}^{real}/p_{i,z}^{real}) = 0^\circ, 5^\circ, 10^\circ, \dots, 350^\circ, \text{ and } 355^\circ$.

These particle properties were chosen to reflect the values expected during the actual experiment. We could expect that roughly 95% of the measured kinetic energy releases (KER) would fall into the range of 16 eV - 24 eV [98]. The KER is equally shared among the two protons. The fraction of the 800 eV photon energy that exceeds the sum of the adiabatic double ionization energy of H_2 (31.03 eV) and the KER is shared between the two electrons. Thus, for $KER = 24$ eV, the maximum possible recoil transferred to the H_2 center of mass is 10.4 au, if the two electrons are emitted into the same direction with half of the excess energy. Each proton carries half of the recoil momentum that may point in the same direction as the KER -related momentum of 40.2 au at 12 eV kinetic energy. Consequently, we have to expect proton momenta of up to 45.4 au and 15.3 eV kinetic energy to be present in the experimental data.

The distribution of the times of flight and positions of impact as obtained from the corresponding simulation is shown in Fig. 9.5.

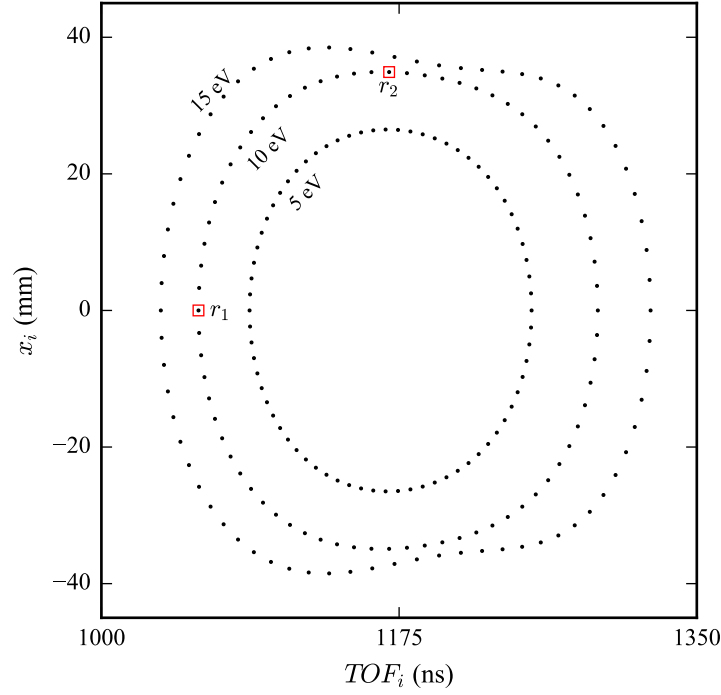


Figure 9.5: Times of flight and positions of impact as obtained from the simulation that models the spectrometer geometry and electric field of the H₂ experiment at 800 eV photon energy (Run 2A). The two reference points (r_1 and r_2) are required for Eqs. 9.20 & 9.21.

Linear relations

The alternative calculation procedure began with a linear relation between TOF_i and $p_{i,z}^{raw}$ (resp. x_i and $p_{i,x}^{raw}$), which was subsequently modified by correction functions to approach $p_{i,z}^{real}$ ($p_{i,x}^{real}$).

The two linear factors were gained from the two reference points (r_1 and r_2) which are displayed in Fig. 9.5. These reference points resemble the times of flight and positions of impact of protons with 10 eV kinetic energy—roughly the experimental expectation value—whose momentum vectors are either parallel or perpendicular to the \hat{z} direction.

Note that the kinetic energy related to these reference points should not be chosen randomly because here the final momentum calculation yields the most accurate results.

The resulting linear relations are

$$p_{i,x}^{raw} = x_i \cdot \frac{p_{r1}}{x_{r2}} \quad \text{and} \quad (9.20)$$

$$p_{i,z}^{raw} = (TOF_i - TOF_{r2}) \cdot \frac{p_{r1}}{TOF_{r1} - TOF_{r2}} \quad (9.21)$$

For this example we chose $p_{r1} = p_{r2} = 36.68$ au (momentum of a proton at 10 eV kinetic energy). We determined $x_{r2} = 34.9$ mm, $TOF_{r1} = 1057$ ns, and $TOF_{r2} = 1169$ ns from the simulated data.

The application of Eqs. 9.20 & 9.21 to all simulated data points yielded the raw momenta displayed in Fig. 9.6 (black dots). The real initial momenta are shown

for comparison (red squares). The black lines connect each raw momentum with its real initial counterpart. The average length of the black lines $\langle \Delta p \rangle$, determined for each kinetic energy separately, approximates the error of the momentum calculation.

Up to this point, the alternative calculation procedure is practically the same as the standard linear approximation (Eqs. 9.11 & 9.12). For the case that an electrostatic lens is employed, the heterogeneous nature of the errors—as indicated by the black lines in Fig. 9.6—highlights the inadequacy of the linear approximation, where the calculated momentum vectors are uniformly shifted and stretched until the errors are minimal. As apparent from Fig. 9.6, such a purely linear map would not suffice to obtain accurate momenta. To overcome this shortcoming, we used the momentum correction functions that are discussed below.

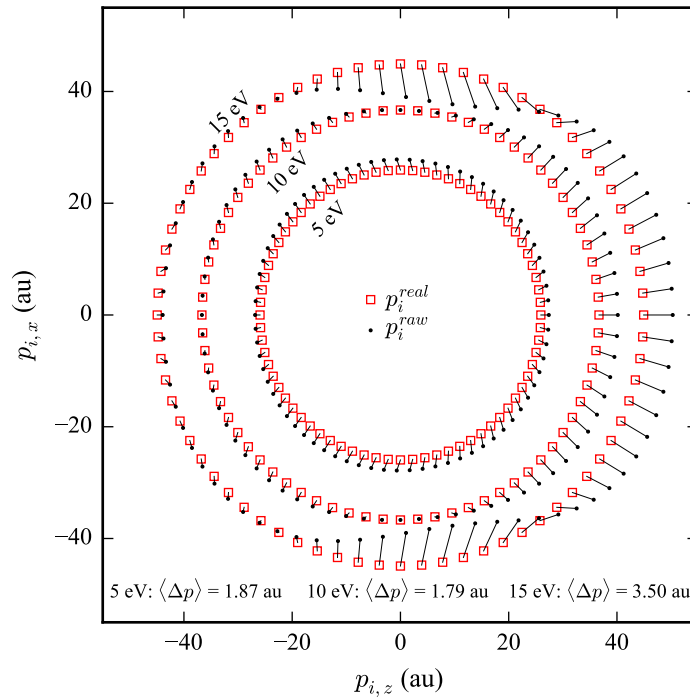


Figure 9.6: Comparison between the real initial momenta (red squares) and the calculated ones (black dots) using the linear relations from Eqs. 9.20 & 9.21. The black lines connect the calculated raw momenta to each real counterpart. The average lengths of these lines for each kinetic energy approximate the average errors $\langle \Delta p \rangle$.

(A) Momentum corrections in the \hat{x} - \hat{y} plane as function of the position of impact

If one considers that the electric field vector is perpendicular to the equipotential lines (see Fig. 8.2), it becomes apparent that an ion experiences acceleration perpendicular to the \hat{z} direction due to the electrostatic lens. While this allows for the momentum focusing of an extended target in \hat{x} and \hat{y} direction, it also implies that the position of impact does not depend linearly on the respective initial momentum component alone. The magnitude of $p_{i,x}^{real}$ determines at which distance to the central axis the trajectory passes through the lens. Similar to the spherical aberration of an optical lens, the further a trajectory is away from the central axis while passing through the lens, the shorter is the effective focus length. On our detector, located at a fixed distance from the lens and oriented perpendicular to the central axis, this spherical aberration causes the non-linear relation between x_i and $p_{i,x}^{real}$ that is depicted in Fig. 9.7 A. The protons used in this simulation were all launched parallel to the \hat{x} axis with kinetic energies ranging from 0 eV to 20 eV.

As Fig. 9.7 A further demonstrates, mapping the position of impact to a momentum can be ambiguous. The simulation showed that if $p_{i,x}^{real} > 43.4$ au (14 eV kinetic energy), then $dx_i/dp_{i,x}^{real} < 0$. This has the following consequence. If protons with $p_{i,x}^{real} > 43.4$ au occur experimentally, they will overlap with protons where $p_{i,x}^{real} < 43.4$ au on the detector. Here, retrieval of the correct initial momentum from the corresponding position of impact becomes impossible. We expect protons of up to 15.3 eV kinetic energy (45.4 au). If the momentum vector is parallel to the \hat{x} direction, the position of impact is $x_i = 37$ mm. Protons of 12.5 eV kinetic energy (41.0 au) get projected onto that same position of impact. Accordingly, if $x_i \geq 37$ mm, the proton and the associated event must be discarded.

Note that this unfortunate aspect is the consequence of an improper choice for the electric field strength during the experiment and it could have been avoided. As we failed to consider the gain in kinetic energy due to the electron recoil momentum, the electric field strength was set to low. In the later experiment (Run 3A, N₂ photon energy scan), the electric field allowed that all occurring $p_{i,x}^{real}$ were projected onto a unique position of impact.

For each simulated momentum vector that had a unique position of impact, we could derive the correction function to estimate $p_{i,x}^{real}$ from $p_{i,x}^{raw}$ and x_i . To this end, we plotted the ratio $p_{i,x}^{real}/p_{i,x}^{raw}$ as function of x_i for the valid data points and searched for a function $f_c(x_i)$ that accurately describes the behavior as shown in Fig. 9.7 B. Eventually, we could use

$$p_{i,x} = f_c(x_i) \times p_{i,x}^{raw} \quad (9.22)$$

to calculate the ion momentum in \hat{x} direction.

(B) Momentum corrections in \hat{z} direction as function of the time of flight

Next, we considered corrections to the linear relation between the time of flight and the ion momentum in \hat{z} direction. Figure 9.8 A shows the relationship between TOF_i and $p_{i,z}^{real}$ that resulted from our simulation, where we used $-36.7 \text{ au} \leq p_{i,z}^{real} \leq 36.7 \text{ au}$ and $p_{i,x}^{real} = 0$. The ratio $p_{i,z}^{real} / p_{i,z}^{raw}$ as function of TOF_i and the function $g_c(TOF_i)$ that describes the behavior are shown in Fig. 9.8 B. By means of this correction function, we could calculate the proton's momentum in \hat{z} direction through

$$p_{i,z} = g_c(TOF_i) \times p_{i,z}^{raw} . \quad (9.23)$$

The momenta calculated through Eqs. 9.22 & 9.23 from the simulated times of flight and positions of impact are shown in Fig. 9.9. Compared to the results shown in Fig. 9.6, the average error is decreased substantially.

(C) Momentum corrections in the \hat{x} - \hat{y} plane as function of the time of flight

An alternative way to correct for the spherical aberration of the electrostatic lens is shown in Fig. 9.8 C & D. Figure 9.8 C shows the relationship between TOF_i and $p_{i,x}^{real}$ resulting from our simulation, where $p_i^{real} = 36.7 \text{ au}$ and $\theta = \tan^{-1}(p_{i,x}^{real} / p_{i,z}^{real}) = 0^\circ, 5^\circ, 10^\circ, \dots, 175^\circ, \text{ and } 180^\circ$. Accordingly, the simulated data points reproduce a sphere in momentum space of protons at 10 eV kinetic energy. In Fig. 9.8 D we plot the ratio $p_{i,x}^{real} / p_{i,x}^{raw}$ as function of TOF_i for these data points and draw the fitted function $h_c(x_i)$ that accurately describes the behavior. As an alternative to Eq. 9.22, we can now calculate the proton's momentum in \hat{x} direction through

$$p_{i,x} = h_c(TOF_i) \times p_{i,x}^{raw} . \quad (9.24)$$

The momenta calculated through Eqs. 9.22 & 9.24 from the simulated times of flight and positions of impact are shown in Fig. 9.10.

From the comparison between the results shown in Figs. 9.9 & 9.10, we found that the application of the momentum correction function $f_c(x_i)$ (Eq. 9.22) yields good error reduction over a wide range of kinetic energies, but using $h_c(TOF_i)$ (Eq. 9.24) results in excellent error reduction for protons of one single kinetic energy.

For the analysis of the data obtained in Run 2A (H_2 at 800 eV photon energy), we have used the correction functions $f_c(x_i)$ and $g_c(TOF_i)$. The two reference points from the simulation (see Fig. 9.5) resembled protons with 10 eV kinetic energy. Figure 9.11 shows the comparison between the momentum calculation for the experimental data set using only the linear relations (Eqs. 9.20 & 9.21) and the calculation using the correction functions (Eqs. 9.22 & 9.24).

For the analysis of the data obtained in Run 3A (N_2 photon energy scan), on the other hand, we have used $g_c(TOF_i)$ and $h_c(TOF_i)$. Due to the rich structure of the KER -distribution, two separate sets of fit functions were constructed for N^+ ions at 3.9 eV and at 5.25 eV kinetic energy (see Fig. C.17 for a comparison).

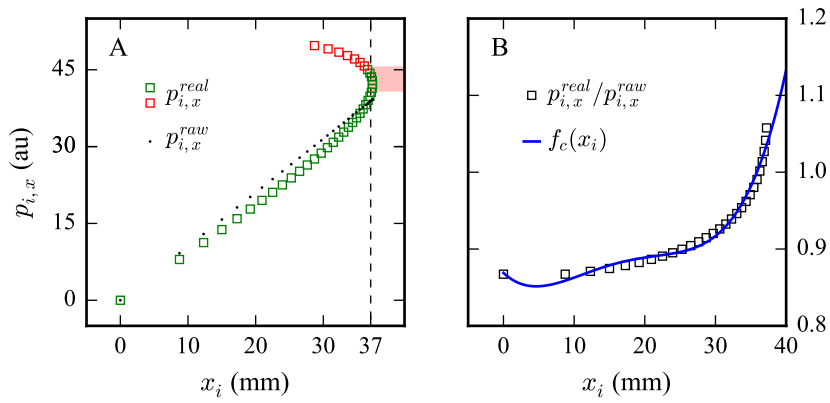


Figure 9.7: **(A)** Simulated positions of impact of protons launched parallel to the \hat{x} axis with kinetic energies ranging from 0 eV to 20 eV. The spherical aberration of the electrostatic lens results in the nonlinear relation between x_i and $p_{i,x}^{real}$. The green squares resemble momenta expected in the experiment (up to 45.4 au). The red squares show higher momenta to better illustrate the effect of the spherical aberration. The red region contains momenta and corresponding positions of impact that occur in the experiment but have to be discarded because of the ambiguous mapping ($41.0 \text{ au} < p_{i,x}^{real} < 45.4 \text{ au}$). **(B)** Ratio $p_{i,x}^{real} / p_{i,x}^{raw}$ as function of x_i (black squares) for all $x_i < 37$ mm and $p_{i,x}^{real} < 41.0$ au. The correction function $f_c(x_i)$ (blue line, polynomial of degree four) is obtained through curve fitting to the data points.

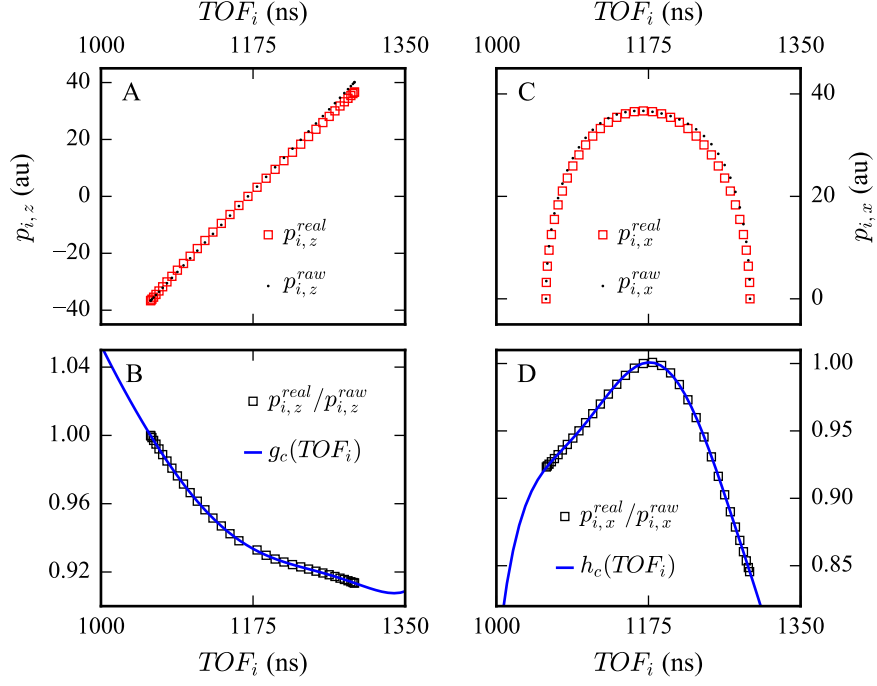


Figure 9.8: **(A)** Simulated times of flight of protons launched parallel to the \hat{z} axis with momenta ranging from -36.7 au to 36.7 au (red squares). **(B)** Ratio $p_{i,z}^{real}/p_{i,z}^{raw}$ as function of TOF_i (black squares). The correction function $g_c(x_i)$ (blue line, polynomial of degree three) is obtained through curve fitting to the data points. **(C)** Simulated positions of impact of protons launched at $\theta = \tan^{-1}(p_{i,x}^{real}/p_{i,z}^{real}) = 0^\circ, 5^\circ, 10^\circ, \dots, 175^\circ, \text{ and } 180^\circ$, where $p_i^{real} = 36.7$ au (red squares). **(D)** Ratio $p_{i,x}^{real}/p_{i,x}^{raw}$ as function of TOF_i (black squares). The correction function $h_c(x_i)$ (blue line, polynomial of degree five) is obtained through curve fitting to the data points.

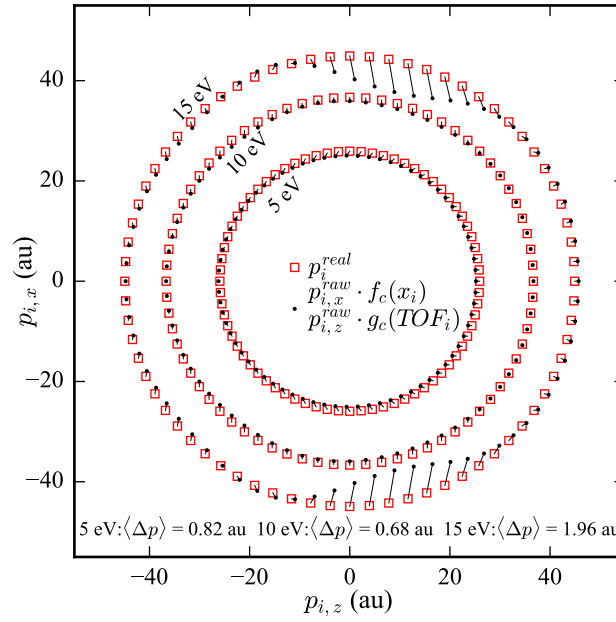


Figure 9.9: Comparison between the real initial momenta (red squares) and the calculated ones (black dots) using Eqs. 9.22 & 9.23.

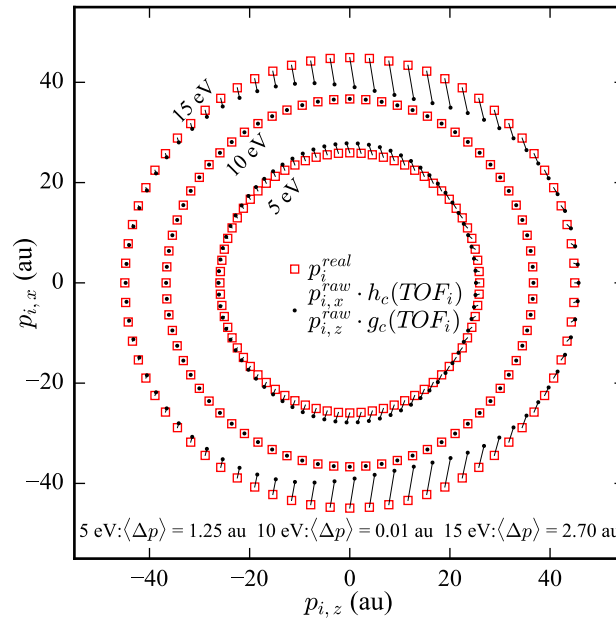


Figure 9.10: Comparison between the real initial momenta (red squares) and the calculated ones (black dots) using Eqs. 9.22 & 9.24.

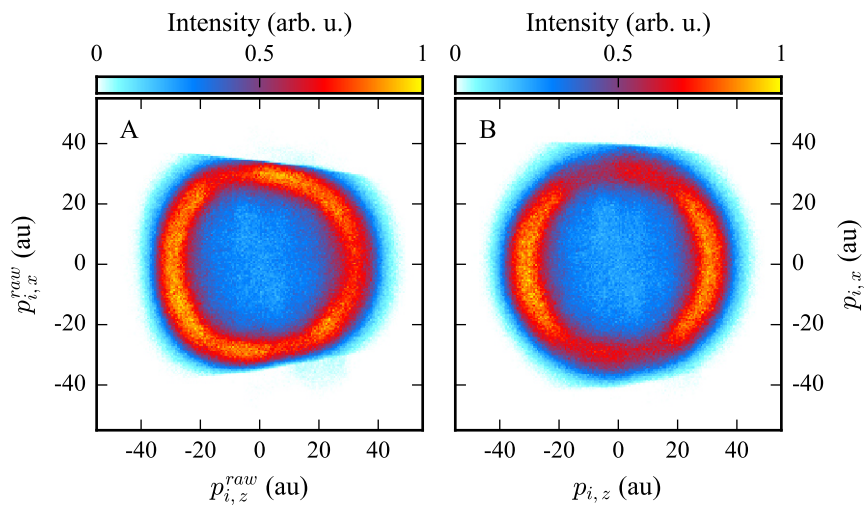


Figure 9.11: Ion momentum distribution of single protons from photo-double-ionization of H_2 at 800 eV photon energy. (A) Momentum calculated using only the linear relations (Eqs. 9.20 & 9.21). (B) Calculation using the correction functions (Eqs. 9.22 & 9.24). Here, the calculated momenta lie on a sphere in momentum space.

9.3.3 Sum Momentum Corrections

The reconstruction of the second electron's momentum vector using momentum conservation—as explained on p. 68—required to determine the ion sum momentum (Eq. 9.14) with the best possible accuracy. To further improve the quality of the ion momentum calculation, we followed the approach described in Ref. [87] and exploited that the recoil momentum transferred onto the ion center of mass is independent of the molecular orientation prior to the ionization and independent of the kinetic energy release. These corrections were necessary because the simulated spectrometer is only an imperfect model of the real one.

Corrections depending on the molecular orientation

The sum-momentum distributions along any of the laboratory-frame axes should not vary as function of the molecular orientation, which is related to the relative momentum (Eq. 9.17). To check this, we filled $p_{sum,m}^{raw}$ as a function of $p_{rel,n}/p_{rel}$ in a histogram, where $m = x, y, z$ and $n = x, y, z$. For each row of these nine histograms, we identified the center of the sum-momentum distribution through a Gaussian fit and determined the polynomial function $f_{m,n}$ that describes the position of these centers as function of $p_{rel,n}/p_{rel}$.⁷ The corrected sum momentum component is subsequently given by

$$p_{sum,m} = p_{sum,m}^{raw} - f_{m,n} . \quad (9.25)$$

The sum momentum, however, is calculated directly from the two single-ion momenta according to Eq. 9.14. Hence, we applied the correction functions to the single-ion momenta directly in equal parts:

$$p_{i1,m} = p_{i1,m}^{raw} - 0.5 \times f_{m,n} \quad \text{and} \quad (9.26)$$

$$p_{i2,m} = p_{i2,m}^{raw} - 0.5 \times f_{m,n} . \quad (9.27)$$

This correction procedure was applied to the ion momentum calculations of Run 2A (H₂ at 800 eV photon energy) and Run 3A (N₂ photon energy scan). As an example, Fig. 9.12 shows the procedure for Run 2A with $m = z$ and $n = y$.

Corrections depending on the kinetic energy release

During data analysis, we found that the sum-momentum distributions in \hat{z} direction from Run 2A and Run 3A varied as function of the kinetic energy release. The distributions in the \hat{x} and \hat{y} directions showed no such behavior. As shown in Fig. 9.13 exemplarily, we have again identified a correction function f_{KER} and the corrected sum momentum component in \hat{z} direction is subsequently given by

$$p_{sum,z} = p_{sum,z}^{raw} - f_{KER} . \quad (9.28)$$

Again, we applied the correction functions to the single-ion momenta directly in equal parts:

$$p_{i1,z} = p_{i1,z}^{raw} - 0.5 \times f_{KER} \quad \text{and} \quad (9.29)$$

$$p_{i2,z} = p_{i2,z}^{raw} - 0.5 \times f_{KER} . \quad (9.30)$$

This correction procedure was applied to the ion momentum calculations of Run 2A (H₂ at 800 eV photon energy) and Run 3A (N₂ photon energy scan).

⁷Note that we have also searched for similar correction functions that depend on $p_{rel,n}$ or even on the measured times of flight or positions of impact of the individual particles, but the method presented here proved to be most suitable.

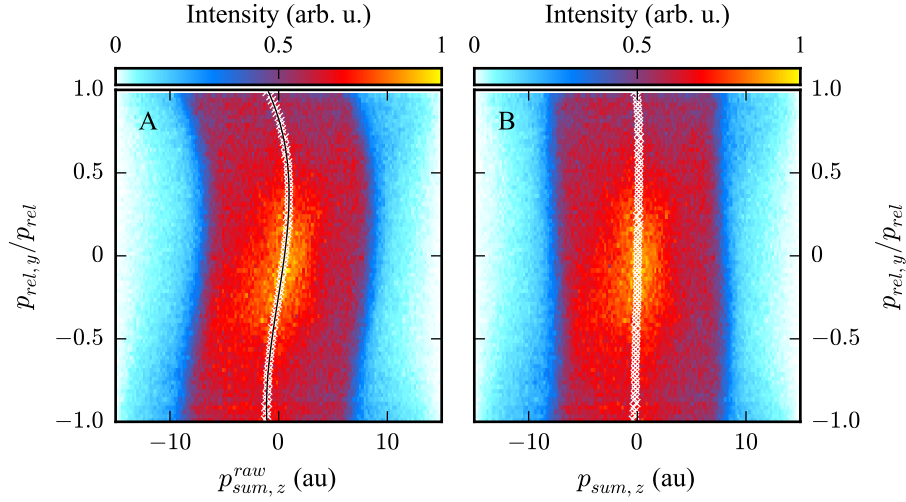


Figure 9.12: Sum momentum distribution in \hat{z} direction of the two protons from photo-double-ionization of H_2 at 800 eV photon energy as function of $p_{rel,y}/p_{rel}$. For each row of the histograms, the centers of the sum-momentum distribution (white crosses) were identified through a Gaussian fit. The positions of the centers as function of $p_{rel,y}/p_{rel}$ are described by $f_{z,y}$ (black line, polynomial of degree three) in A. (A) Sum momentum calculated without further corrections. (B) Sum momentum corrected according to Eq. 9.25.

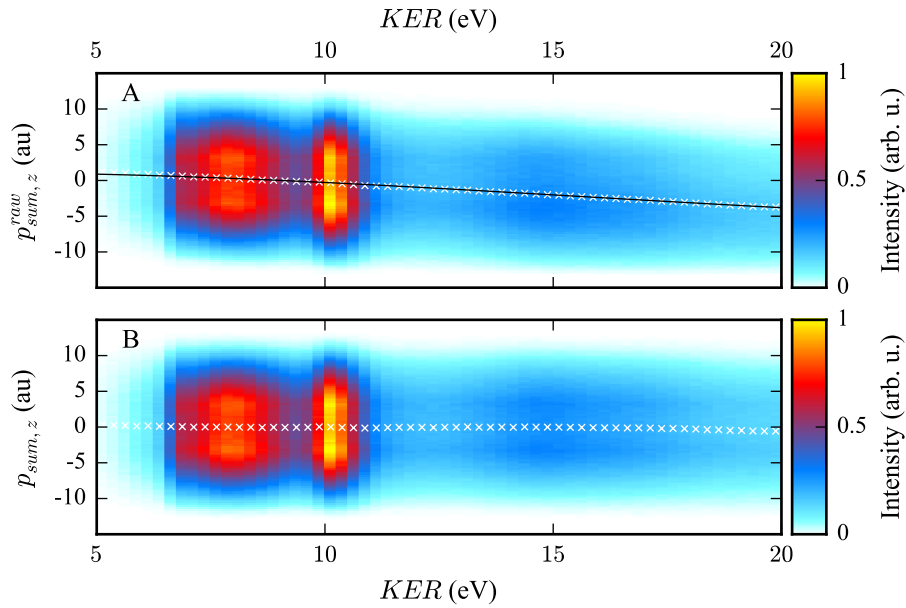


Figure 9.13: Sum momentum distribution in \hat{z} direction of the two nitrogen atoms from K -shell ionization of N_2 at 1330 eV photon energy followed by Auger decay as function of the kinetic energy release. For each column of the histograms, the centers of the sum-momentum distribution (white crosses) were identified through a Gaussian fit. The positions of the centers as function of the KER are described by f_{KER} (black line, polynomial of degree three) in A. (A) Sum momentum calculated without further corrections. (B) Sum momentum corrected according to Eq. 9.28.

Corrections depending on the data acquisition time

The power supplies that set the potentials of the spectrometer and the detectors showed unsteady performance over time during the experiments. One recurring problem was the triggering of a fuse and the subsequent deactivation of the corresponding power-supply channel. Depending on which one of the six used channels was affected, particles were either not detected anymore or they experienced a different electric field. Another problem was that the potentials supplied by the devices were not always constant, but could drift over time. Here, the detection of particles was not affected, but the particles were exposed to a time-dependent electric acceleration field. Such occurrences were not always recognized immediately and recorded in the laboratory journal by the experimentalist.

These changes of the electric field were observable in the ion momentum distribution in \hat{z} direction, but the distributions in the \hat{x} and \hat{y} directions were unaffected. Accordingly, it was mandatory to check the ion momentum distribution in \hat{z} direction in all recorded data sets as function of the time of acquisition, for which we used the *eventcounter* as a proxy variable. The eventcounter assigns an increasing number to each event in the presorted data file, where the data is still arranged in a chronological order.

In Fig. 9.14 we show the ion sum momentum distribution in \hat{z} direction as function of the eventcounter for N_2 *K*-shell ionization followed by Auger decay at 1330 eV photon energy. Figure 9.14 A reveals an electric field drift at the beginning of the data acquisition and a jump in the second half of the acquisition. As the drift was rather short in time, we discarded all events affected by it. After the electric field jump, the ion sum momentum distribution was shifted in \hat{z} direction by a constant offset. This offset was determined and considered in the calculation of the single-ion momenta in equal parts. Figure 9.14 B shows the ion sum momentum distribution in \hat{z} direction as function of the eventcounter after the correction measures were applied.

Similar measures had to be applied to the ion momentum calculations of Run 1A (see Ref. [52] for details) and for all remaining photon energies of Run 3A. We found that the electron momentum distributions remained unaffected by electric field jumps and drifts within the scope of our momentum resolution. During Runs 1B, 2A, and 3B, the electric field remained constant.

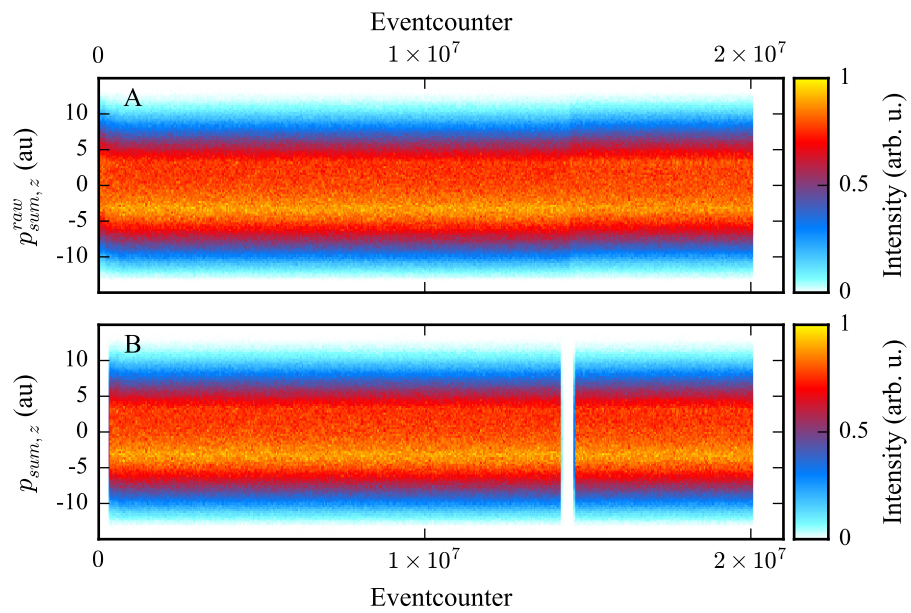


Figure 9.14: Ion sum momentum distribution in \hat{z} direction as function of the eventcounter for N_2 K-shell ionization followed by Auger decay at 1330 eV photon energy. (A) An electric field drift at the beginning of the data acquisition and a jump in the second half affect the sum momentum distribution. (B) The affected events are discarded and the momentum distribution after the jump was shifted by a constant factor.

Part III

RESULTS

The following results are based on six peer-reviewed publications [140, 141, 146–149] to which the author contributed substantially. In addition to the publications, further details and results are shown here.

FORWARD/BACKWARD ASYMMETRIES IN PHOTOIONIZATION

I have dealt with the theory of asymmetric photoelectron emission, and to my surprise I found a forward momentum greater by a factor of 9/5 than would have been expected on the simple momentum law.

— A. Sommerfeld in a letter to P. Auger (found in Ref. [38]).

In one of the earliest photoionization studies, performed in 1927, P. Auger and F. Perrin were puzzled by the observation that the average forward shift of photoelectron momenta was "more than 50% higher than the momentum of the photon" [150]. Soon afterwards, the application of wave mechanics on photoionization explained the effect as a result of the interference between electric dipole and electric quadrupole transitions (e.g., Ref. [151]). However, there are still misleading formulations on the photon momentum transfer in the literature. For instance, H. Bethe and E. Salpeter state that the "absorbed photon imparts its own momentum to the ejected electron", suggesting that this "kick" is responsible for the average forward shift of photoelectron momenta [29].

Momentum conservation demands that the photoion's final momentum equals the photon momentum minus the photoelectron momentum. Consequently, as first formulated by A. Sommerfeld and G. Schur in 1930 [151], photoionization might attract single atoms and molecules towards the light source because the photoelectron on average receives more forward-directed momentum than the photon provides. The photoion is essentially the system's center of mass and from intuition one would arguably expect that the radiation pressure pushes it away from the light source. Hence, the experimental confirmation of the *photoion backward emission* makes a significant and important contribution to the fundamental understanding of photoionization.

A closely related subject is that photoion backward emission must influence the dynamics of stellar outer layers and gaseous nebulae, as discussed theoretically since the 1970s (see, e.g., Refs. [152–157]). To our knowledge, astrophysical observations still lack confirmation and investigating the effect under laboratory conditions might be relevant for this research field.

In the present chapter, we show how the photon momentum itself and its additional orbital angular momentum transfer break the symmetry of photoionization along the light propagation direction. On the basis of one-photon single and double ionization of helium, we show forward/backward asymmetries for all reaction fragments and how they originate.

The experimental results shown in this chapter were obtained in Run 1A, Run 1B, and Run 3B. For helium double ionization, the experimental results are compared to calculations that solve the two-electron Time-Dependent Schrödinger Equation (TDSE) and that were performed by S.-G. Chen, W.-C. Jiang, H. Liang, M.-X. Wang, L.-Y. Peng, and Q. Gong [147].

10.1 THE ORIGIN OF PHOTOION BACKWARD EMISSION

In 2014, S. Chelkowski, A. Bandrauk, and P. Corkum derived explicit scaling rules for the "photon momentum sharing between an electron and an ion in photoionization" from a perturbative treatment [18].¹ Accordingly, for the average momentum in the light-propagation direction (\hat{x} direction) of photoions $\langle p_{i,x} \rangle$ and photoelectrons $\langle p_{e,x} \rangle$ the following applies:

$$\langle p_{e,x} \rangle = \frac{8}{5} \frac{E_\gamma - I_p}{c} = \frac{8}{5} p_\gamma \Big|_{I_p=0} \quad \text{and} \quad (10.1)$$

$$\langle p_{i,x} \rangle = -\frac{3}{5} \frac{E_\gamma - I_p}{c} + \frac{I_p}{c} = -\frac{3}{5} p_\gamma \Big|_{I_p=0}, \quad (10.2)$$

where $E_\gamma - I_p = E_e$ is the kinetic energy of the photoelectron, c is the speed of light, and I_p is the ionization potential which accounts for 24.6 eV in helium single ionization. We have extensively tested these scaling rules in our experiments.

In Fig. 10.1 we compare experimental results from helium photoionization to Eqs. 10.1 & 10.2. Shown in black are the measured mean momentum values in the direction of the light propagation for electrons (A) and ions (B) originating from helium single ionization as function of the photon energy. The solid red lines represent Eqs. 10.1 & 10.2 for helium single ionization and the solid blue line shows the photon momentum as function of the photon energy for comparison. The green data points in subfigure B show measured ion momenta from helium double ionization and the dotted red line represents Eq. 10.2 with $I_p^{++} = 79$ eV respectively.

The experimental observations are in excellent agreement with the scaling rules. They confirm the counterintuitive effect of photoion backward emission and emphasize that the photoelectron receives more forward-directed momentum than the photon carries.

As suggested by the results shown in Fig. 10.1 B, not only do the scaling rules apply for photoions generated in helium single ionization but also for helium double ionization. This is confirmed further in Fig. 10.2 where we compare the measured He^{++} momentum distribution in light propagation direction (black circles) to TDSE computations for photon energies of 385 eV (A), 800 eV (B), and 1100 eV (C). These computations have been performed either within the electric dipole approximation (solid green lines) or beyond (solid red lines) [147]. The dipole results are symmetric in forward/backward direction but the nondipole computations, that account for the nonzero photon momentum, show a forward/backward asymmetry and are in excellent agreement with the experimental results.

Furthermore, in Ref. [146] K-shell ionization of N_2 was investigated in the photon energy range of 12 keV–40 keV. This high-energy experiment was mainly conducted and analyzed by M. Kircher and it is consequently not shown in the present work. The scaling rules also agree nicely with these high-energy results.

Taken together, the experimental and TDSE results at hand attest a broad applicability of the scaling rules. The findings suggest that photoion backward emission is a prevalent phenomenon in photoionization.

Our fully differential experimental data, from which the results in Figs. 10.1 & 10.2 show only integrated values, allow to uncover how this photoion backward emission manifests.

¹S.G. finds that this is another instance of a misleading formulation on the photon momentum transfer.

In Fig. 10.3 we show the momentum distributions of He⁺ photoions and photoelectrons after ionization by photons with 300 eV, 600 eV, 1125 eV, and 1775 eV energy. The red concentric circles are centered at the origin in momentum space. Their radii correspond to

$$r[\text{au}] = \sqrt{(E_\gamma - I_p)[\text{eV}]} \times 0.27, \quad (10.3)$$

which is the absolute momentum expected for the photoelectron (see Eq. 9.8). The measured photoelectron momenta accumulate on those circles in Fig. 10.3 A. For the photoions in Fig. 10.3 B, however, the measured values are shifted against the red circles. This is best visible for the outermost events. Relative to the red circle, the blue one is moved to the right by the magnitude of the respective photon momentum ($p_\gamma = 0.476$ au). The blue circle properly indicates the position of the photoion momentum distribution. As discussed in *Kinematics of photoionization* on p. 6, the results underline that the photon momentum is mostly imparted onto the ion. This shift in momentum space is purely a consequence of energy and momentum conservation. Hence, it is irrespective of the details of the ionization process, i.e., of the orbital of the atomic or molecular species which is ionized. Furthermore, momentum conservation dictates that the angular distribution of the photoelectrons in the laboratory frame and the distribution of ions on a sphere shifted by the photon momentum are direct mirror images of each other, as shown in Fig. 10.3. To abide by the scaling rules, a backward-directed recoil momentum from the photoelectron emission must overcompensate the forward-directed photon momentum transfer.

As apparent in Fig. 10.3 A, the photoelectron angular distributions are not isotropic with respect to the angle ϑ_γ , which is enclosed by the photon propagation direction and the photoelectron momentum vector. As discussed in Ch. 4 on p. 23, the shape of these photoelectron angular distributions—which resemble angle-differential cross sections—can be parametrized as

$$\frac{d\sigma}{d\vartheta_\gamma} \propto 1 - \beta \frac{3 \cos^2 \vartheta_\gamma - 1}{4} + \gamma \frac{\sin^2 \vartheta_\gamma \cos \vartheta_\gamma}{2} \quad (10.4)$$

for circularly (and unpolarized) light [39, 45]. Here, β is the dipole anisotropy parameter and γ is the nondipole parameter characterizing the interference between electric dipole and quadrupole transitions. We neglect the magnetic dipole contribution and the corresponding parameter δ that appears in Eq. 4.25, because it vanishes for any initial s -state (see p. 17).

The measured photoelectron angular distributions from helium single ionization at 300 eV, 600 eV, 1125 eV, and 1775 eV photon energy are shown in Fig. 10.4 A-D. Such angle-differential cross sections are shaped by the coherent superposition of all possible angular momentum channels of the photoelectron in the final state. The initial state is He(1s) where $\ell = 0$ and the photon spin contributes one unit of angular momentum. Thus, the distributions have an approximate dipolar shape as the leading angular momentum in the final state is a dipole ($\ell = 1$). However, this dipolar shape is forward tilted, which becomes more and more apparent with rising photon energy. The reason for this is the transfer of additional orbital angular momentum that arises from the linear photon momentum and which allows for quadrupole transitions where $\ell = 2$ in the final state (see p. 21 for comparison). Classically, this corresponds to an angular momentum of $p_\gamma \times r_e$ which is directed perpendicularly to the light propagation.

While electric dipole and quadrupole transitions alone are both symmetric in light propagation direction, the interference between the two the complex-valued transition amplitudes breaks this symmetry. Hence, what we observe in Fig. 10.4 A-

D are dipole transitions modified by the interference term that becomes stronger with rising photon energy.

For a quantitative comparison, the red line represents a fit of Eq. 10.4 to the experimental data for each photon energy. The fit yields $\beta \approx 2$ for all measured photon energies, as expected for a final state dominated by $\ell = 1$. The nondipole parameters γ —as obtained from the fitted functions—are shown in Fig. 10.4 E and agree with published theory (green solid line) from Ref. [40].

As indicated by a positive and growing nondipole parameter, an increase of photon energy and photon momentum improves the chance to transfer an additional unit of angular momentum. Consequently, the interference term becomes stronger, increasing the forward tilt of the dipolar-shaped distribution.

A positive value for the nondipole parameter γ entails that the average photoelectron momentum is shifted forward in the direction of light propagation. It is curious that this interference-induced forward shift of the average photoelectron momentum equals $8/5$ times the photon momentum and is consequently larger than the photon momentum itself.

In conclusion, the presented results underline that the linear photon momentum is imparted onto the center of mass of the photoionization reaction, which is essentially the photoion. The interference between the $\ell = 1$ and $\ell = 2$ angular momentum channels shifts the average photoelectron momentum forward. As this shift is larger than the linear photon momentum itself, the recoil onto the photoion overcompensates the forward momentum of the photon. Eventually a single photoion is on average attracted towards the light source.

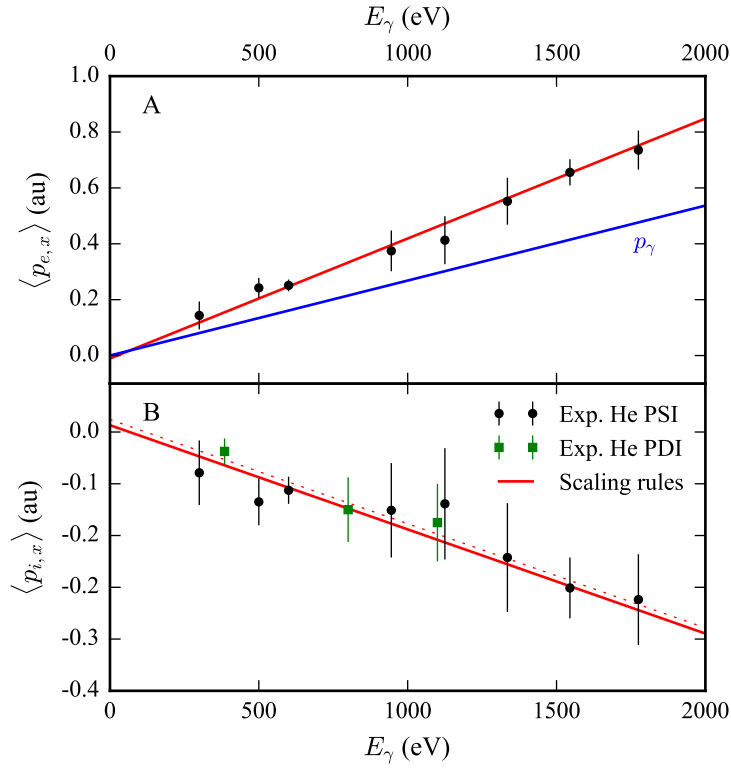


Figure 10.1: Average values of photoelectron (A) and photoion (B) momenta along the light propagation direction after one-photon single ionization (PSI) of helium with circularly polarized photons at 300 eV, 500 eV, 600 eV, 945 eV, 1125 eV, 1335 eV, 1545 eV, and 1775 eV photon energy (black circles). Solid red lines: photon momentum scaling rules (Eqs. 10.1 & 10.2 with $I_p = 24.6$ eV). Blue line: magnitude of the photon momentum as function of the photon energy for comparison. Green squares: average values for photoions after one-photon double ionization (PDI) of helium with circularly polarized photons at 385 eV, 800 eV, and 1100 eV. Dashed red line: respective scaling rule for helium double ionization where $I_p = 79$ eV. Figure adapted from Ref. [146].

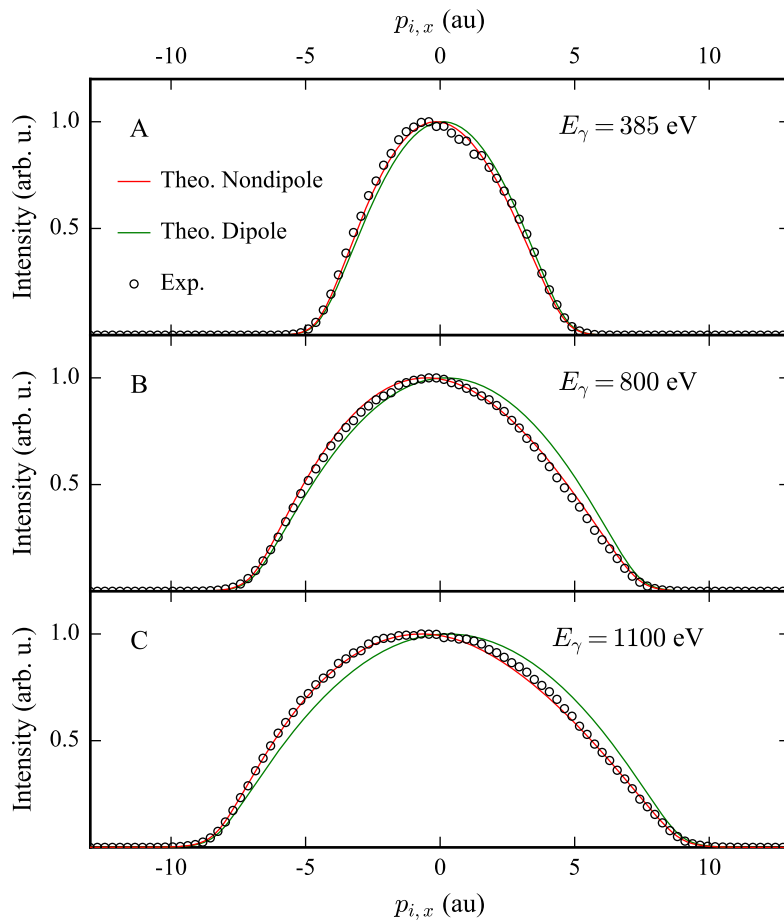


Figure 10.2: He^{++} ion momentum distributions along the light propagation direction after one-photon double ionization with circularly polarized photons at 385 eV (A), 800 eV (B), and 1100 eV (C) photon energy. Black circles: measured data. Red (green) line: two-electron nondipole (dipole) TDSE calculation. Figure adapted from Ref. [147].

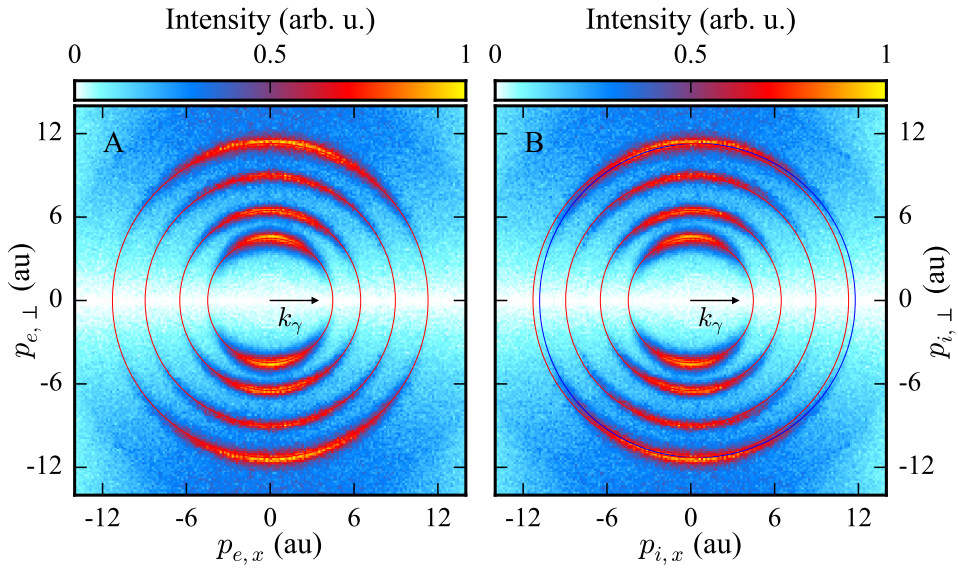


Figure 10.3: Momentum distributions of photoelectrons (A) and photoions (B) after one-photon single ionization of helium with circularly polarized photons at 300 eV, 600 eV, 1125 eV, and 1775 eV photon energy. Horizontal (vertical) axis: momentum component parallel (perpendicular) to the light propagation. In A and B, the lower halves are mirror images of the upper halves of the figures. The red circles are centered at the origin with a radii of $r[\text{au}] = \sqrt{(E_\gamma - I_p)[\text{eV}]} \times 0.27$. The blue circle is shifted to the right by the corresponding photon momentum of $p_\gamma = 0.476$ au. The data from the different photon energies are each normalized to the maximum bin value. Figure adapted from Ref. [146].

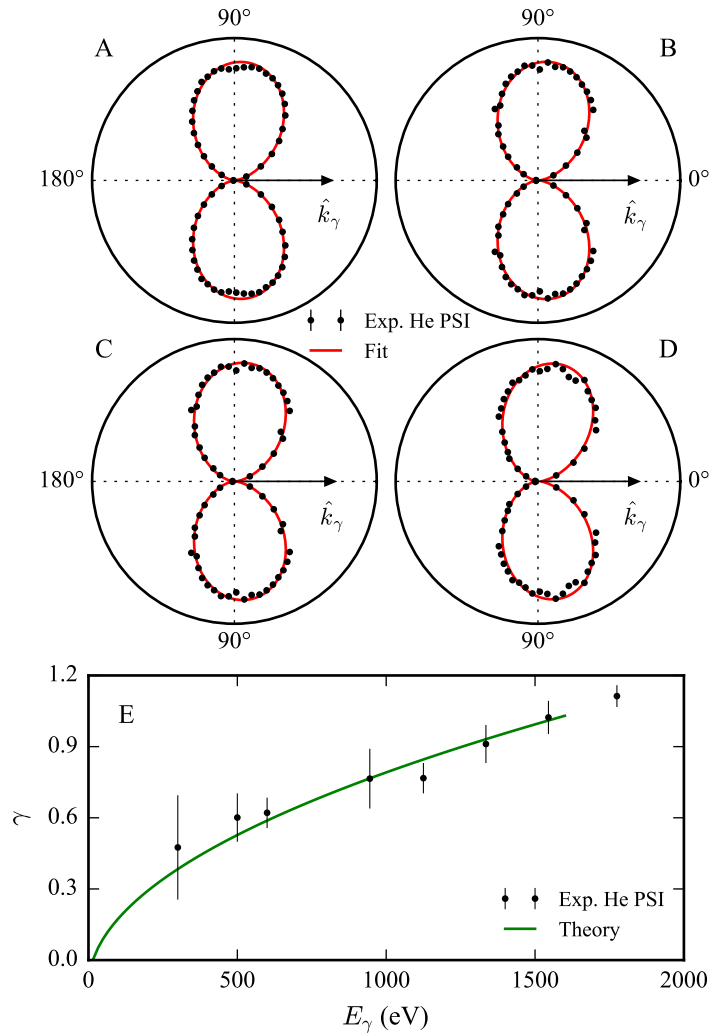


Figure 10.4: (A–D) Photoelectron angular distributions after one-photon single ionization (PSI) of He at 300 eV (A), 600 eV (B), 1125 eV (C), and 1775 eV (D) photon energy. Red lines: Fit using Eq. 10.4. (E) Nondipole parameter γ from fit of Eq. 10.4 to the data and theory prediction from Ref. [40] (green solid line). Figure adapted from Ref. [146].

10.2 FORWARD MOMENTUM SHARING AMONG PHOTOELECTRONS

The one-photon double ionization of helium is primarily facilitated by electron-electron correlation due to the shake-off and two-step-one processes (see Ch. 5). Within the electric dipole approximation, these mechanisms have been studied extensively in the past (e.g., Ref. [54]), but forward/backward asymmetries in the momentum distributions of the three reaction fragments in the final state have not been addressed yet. As presented in the last section (Fig. 10.1 B), the He^{++} average momentum in light propagation direction follows the scaling rule of Eq. 10.2. Hence, at least for the region of energy sharing which makes the biggest contribution to the double-ionization cross section, the sum momentum of the two electrons must comply with the scaling rule of Eq. 10.1. However, momentum conservation does not dictate how the forward shift of the sum momentum is partitioned among the two individual electrons. This is the subject that we investigate in the present section. In the nondipole photon energy regime, the shake-off dominates helium double ionization and the energy sharing between the two electrons is extremely unequal (see, e.g., Fig. 11.2 B). The energy sharing allows to distinguish between the primary (fast) electron and the secondary (slow) electron ($p_{eF} > p_{eS}$) for each photoionization event.

In Fig. 10.5 we show the average momentum in photon propagation direction of those fast and slow electrons as function of the photon energy. The solid black triangles represent the experimental results from helium double ionization at 385 eV, 800 eV, and 1100 eV. The blank red triangles show calculations solving the two-electron nondipole TDSE for photon energies from 99 eV to 1100 eV. The experimental results are in good agreement with the corresponding theoretical calculations. The solid black and the blank red squares resemble the measured and calculated momenta for the two-electron averages $\langle p_{eS,x} + p_{eF,x} \rangle / 2$ that agree nicely with the predictions of the scaling rule (solid green line). These results show that the total average forward momentum of $(8/5) \times p_\gamma$ is shared extremely unequally between the fast and the slow electron—as well known for the energy sharing. The fast electron acquires the forward shift almost entirely alone, while the slow electron receives only a little shift forward. The TDSE calculations allow to further examine this finding. Figure 10.6 displays the average forward shift of one electron as function of the energy sharing between the two electrons from TDSE calculations at 385 eV, 800 eV, and 1100 eV. For each photon energy, the results roughly follow a straight line similar to the scaling rule of Eq. 10.1 (green), indicating that the mean value of the forward momentum is roughly 8/5 times the electron energy divided by the speed of light. Hence, the fraction of the forward shift of an individual electron is roughly proportional to its fraction of the excess energy—i.e., $\epsilon \times 8/5 \times p_\gamma$. Small deviations from this rule appear in the region of equal energy sharing ($\epsilon \approx 0.5$) where the green line overestimates the actual mean value. At equal energy sharing, the quasifree mechanism (QFM) makes a small contribution to the double-ionization cross section of helium. As further outlined in Ch. 11, the helium nucleus is only a spectator in QFM and the photon momentum is not imprinted onto the photoion. The sum momentum of the two electrons carries the photon momentum but the photoelectron angular distribution of QFM electrons is characterized by a pure quadrupole transition and is not further forward-shifted due to interference. However, the interference-induced forward shift is larger than the photon momentum itself. Consequently, QFM electrons contribute less to the overall forward momentum shift of electrons in helium double ionization than electrons originating from SO or TS₁ and the slope of the red lines around $\epsilon \approx 0.5$ is smaller than that of the green line in Fig. 10.6.

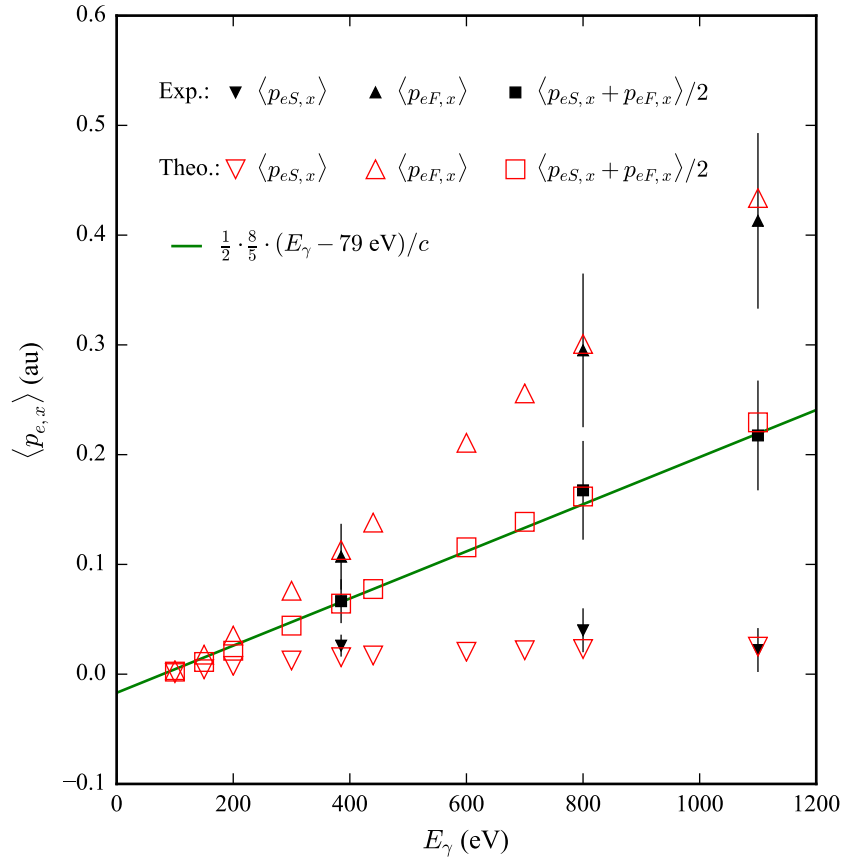


Figure 10.5: Measured (black) and calculated (red) average values of the fast, the slow, and the sum electron momenta in the direction of light propagation after one-photon double ionization of helium as function of the photon energy. The scaling rule of Eq. 10.1 (green line) has been modified in order to apply for the two-electron average momentum. Figure adapted from Ref. [147].

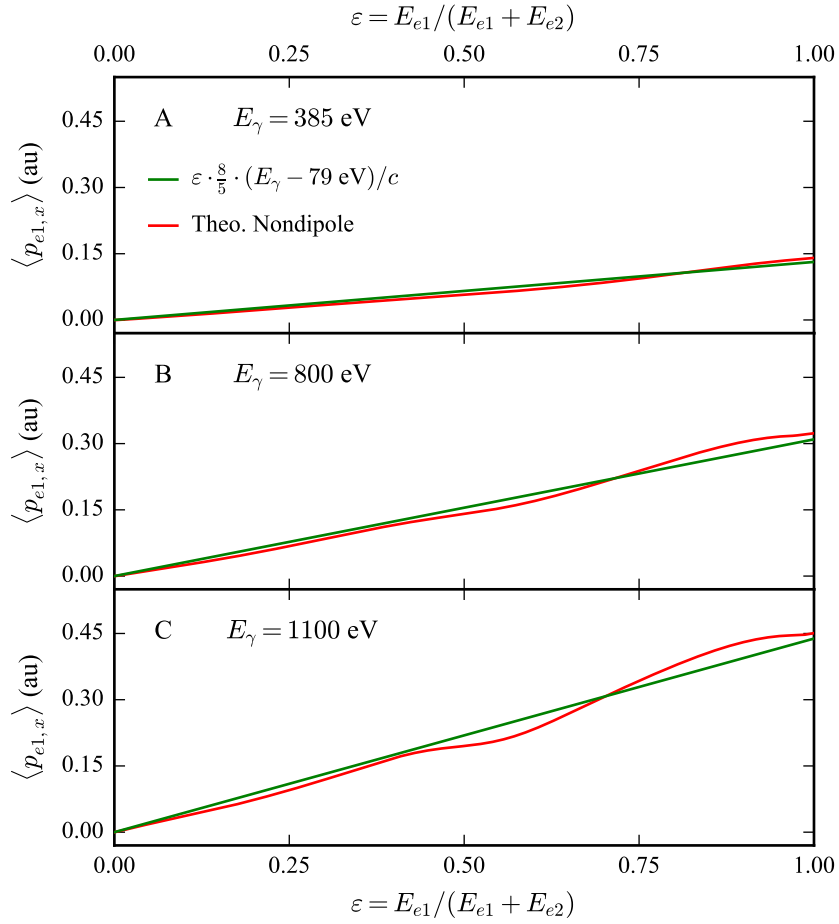


Figure 10.6: Calculated average electron momenta in light propagation direction as function of the electron energy sharing (solid red lines). The green lines show a modified version of the scaling rule of Eq. 10.1. Figure adapted from Ref. [147].

THE QUASIFREE MECHANISM (QFM)

The one-photon double ionizations of helium and the hydrogen molecule are among the most fundamental processes of atomic physics. Those are straightforward reactions because the final states consist of bare charged particles.

For decades, investigations of the processes have driven advances in theory and experiment (see, e.g., Refs. [28, 158] for reviews). Until recently, research has focused mainly on two sequential processes, namely the shake-off (SO) and two-step-one (TS1) [54, 67, 159, 160]. On the other hand, the quasifree mechanism (QFM) had been predicted in 1975 already [58], but received little attention until its experimental confirmation for helium double ionization in 2013 [66].

In double ionization through QFM, the photon is absorbed directly by two *quasi-free* electrons without involving the nucleus. As shown in Refs. [60, 140, 161], this concept becomes apparent in the formalism of light-matter interaction if one converts the two-electron Hamiltonian, truncated after the electric-quadrupole term,

$$\hat{H}_{int} = \hat{\epsilon} \cdot (\mathbf{r}_{e1} + \mathbf{r}_{e2}) + \frac{i}{2} [(\hat{\epsilon} \cdot \mathbf{r}_{e1})(\mathbf{k}_\gamma \cdot \mathbf{r}_{e1}) + (\hat{\epsilon} \cdot \mathbf{r}_{e2})(\mathbf{k}_\gamma \cdot \mathbf{r}_{e2})], \quad (11.1)$$

into the alternative form of

$$\hat{H}_{int} = 2\hat{\epsilon} \cdot \mathbf{r}_+ + i(\hat{\epsilon} \cdot \mathbf{r}_+)(\mathbf{k}_\gamma \cdot \mathbf{r}_+) + \frac{i}{4}(\hat{\epsilon} \cdot \mathbf{r}_-)(\mathbf{k}_\gamma \cdot \mathbf{r}_-), \quad (11.2)$$

by utilizing the Jacobian coordinates:

$$\mathbf{r}_- = \mathbf{r}_{e1} - \mathbf{r}_{e2} \text{ and } \mathbf{r}_+ = (\mathbf{r}_{e1} + \mathbf{r}_{e2})/2.$$

Here $\mathbf{r}_{e1/e2}$ are the position vectors of the two electrons relative to the nucleus, $\hat{\epsilon}$ is the polarization vector and \mathbf{k}_γ is the photon wave vector. The first term in Eq. 11.2 represents the electric-dipole contribution to the transition amplitude while the second and third term account for the electric quadrupole. The part of the electric quadrupole that acts directly on the electron-electron separation,

$$\hat{H}_- = \frac{i}{4}(\hat{\epsilon} \cdot \mathbf{r}_-)(\mathbf{k}_\gamma \cdot \mathbf{r}_-), \quad (11.3)$$

is responsible for QFM [60, 140]. Here, the appearance of \mathbf{k}_γ highlights that double ionization through QFM requires a nonzero photon momentum.

The fact that in QFM the photon couples directly to two electrons has extensive consequences for the momentum distributions in the final state. In the present chapter, we study in detail this distinctive fingerprint of QFM in double ionization of a two-electron target. We first show the experimental confirmation of the mechanism in H₂ and He double ionization and later utilize it to visualize the photoelectron angular distribution of a pure quadrupole transition. Finally, we show how the QFM cross section can be used to investigate the structure of the two-electron ground states of H₂ and He.

The experimental results shown in this chapter were obtained in Run 1A, Run 1B, and Run 2A. Complementing the experiment, we show total integrated and differential cross sections of H₂ and He double ionization at 800 eV photon energy that are the results of numerical computations using the external complex scaling

method in the prolate spheroidal coordinates (PSECS) [162]. These computations were performed by V. Serov, A. Bray, and A. Kheifets in the course of a theory-experiment collaboration that resulted in Ref. [140]. The TDSE theory results produced by Chen et al. [147] are also used again. Upon request by the author, Y. Fang generated the TDSE results shown in Fig. 11.3, utilizing the same code as Chen et al. [147].

11.1 THE QFM'S UNIQUE FINGERPRINT

Single ionization is a precursor to double ionization via shake-off or two-step-one and the photoion momentum spectra from either single or double ionization share two important similarities: A large recoil momentum and an almost dipolar shape of the angular distribution. However, for double ionization through the quasifree mechanism, the photon is absorbed by two free, strongly-correlated electrons without involvement of the nucleus. Hence, the nucleus is only a spectator that receives no recoil momentum.

This first aspect of the QFM fingerprint is addressed in Fig. 11.1 where we show the doubly-charged photoion yield as function of the magnitude of its momentum for H₂ double ionization at 800 eV and for He double ionization at 385 eV, 800 eV, and 1100 eV. Note that for H₂ double ionization, the photoion refers to a hypothetical particle represented by the two-proton center-of-mass momentum—i.e., $p_i = p_{sum}$ (see Eq. 9.14).

For He double ionization, the experimental results are compared to dipole and nondipole TDSE calculations. In each panel, we notice that the nondipole calculations perfectly agree with the results from the experimental measurements, but large discrepancies exist for the dipole calculations at low momenta. These discrepancies become more and more noticeable with rising photon energy. The enhancements at low momenta can be attributed to the QFM that leaves the photoion almost at rest. The need to consider nondipole terms in the TDSE calculations to account for these low photoion momenta emphasizes the nondipole character of QFM.

The results in Fig. 11.1 suggest that QFM grows relatively stronger with rising photon energy and by switching the two-electron target from He to H₂ at constant photon energy. The observed photon-energy dependence can be explained by the increasing relative strength of the electric quadrupole amplitude compared to the electric dipole that is also responsible for the growing forward shift of the dipolar-shaped photoelectron angular distributions in Helium single ionization (see Fig. 10.4). The increased relative QFM yield of H₂ double ionization compared to He double ionization is due to differences in the structure of the ground states which will be discussed further in Sec. 11.3.

By means of momentum and energy conservation, a vanishing recoil momentum requires the ejection of two electrons back-to-back with equal energy, which is the remaining aspect of the unique QFM fingerprint. For a dipole transition—that adds one unit of angular momentum—such back-to-back emission with equal energy sharing among the two electrons is forbidden for double ionization of He and H₂ whose ground-state wave functions both have the same ¹S symmetry [62, 90].

Hence, the QFM can be isolated particularly clearly in a differential cross section that shows the double-ionization yield as function of the electron energy sharing $\epsilon = E_{e1}/(E_{e1} + E_{e2})$ and the angle enclosed by the two electron momentum vectors $\vartheta_{12} = \cos^{-1}[\mathbf{p}_{e1} \cdot \mathbf{p}_{e2}/(|\mathbf{p}_{e1}| |\mathbf{p}_{e2}|)]$ (electron mutual angle).

This is done in Fig. 11.2 where we show such cross sections for double ionization of H₂ (A,C,E) and He (B,D,F) at 800 eV photon energy from the experimental measurements (A–D) and from PSECS calculations (E,F).

Note that subfigures A and B show the full range of the two variables, but panels C–F show only an excerpt as indicated by the dashed black lines in A and B. Note also the logarithmic scale display in panels D and F.

Comparison between panels A and B points out a strong resemblance in the electron emission patterns of H₂ and He double ionization, as expected from the similarities in the electronic ground states. A distinctive difference can be seen around equal energy sharing ($\epsilon = 0.5$) and back-to-back emission ($\cos \vartheta_{12} = -1$) where there appears to be a noticeable signal in subfigure A, corresponding to QFM, but a node in subfigure B. The excerpts shown in Fig. 11.2 C and D highlight this relevant region of the cross section. While the QFM is evident for H₂, a logarithmic scale display is required in subfigure D to unveil the weak relative contribution of QFM to the total double-ionization cross section of helium.

The PSECS calculations for double ionization of H₂ (E) and He (F) support the measured data. The displayed structures are in excellent agreement with their experimental counterparts.

As stated above, back-to-back emission of electrons at equal energy and zero recoil momentum entail each other. The relation between the magnitude of the recoil momentum p_i , the energy sharing ϵ , and the electron mutual angle ϑ_{12} can be written as

$$\frac{p_i^2}{2m_e} = 2E_{exc} \sqrt{\epsilon - \epsilon^2} \cos \vartheta_{12} - E_{exc} , \quad (11.4)$$

where m_e is the electron mass and E_{exc} is the available excess energy that is shared among the electrons.

For illustration, the solid black lines in Fig. 11.2 C and D indicate all the positions where $p_i = 2$ au. A signal at back-to-back emission and equal energy sharing corresponds to zero recoil momentum transferred to the photoion. Hence, the low photoion momenta in Fig. 11.1 and the contributions around back-to-back emission at equal energy sharing in Fig. 11.2 must stem from the same measured events.

A remaining open question concerns the transfer of the linear photon momentum in double ionization through QFM. For single ionization, momentum and energy conservation entail the transfer to the center of mass, i.e., essentially to the photoion (see *Kinematics of photoionization* on p. 6). However, the additional degrees of freedom make this relation less straightforward for the double-ionization process. As indicated by the results shown in Fig. 10.1, the scaling rule for the average momentum in light propagation direction (Eq. 10.2) also applies for photoions generated in helium double ionization at 385 eV, 800 eV, and 1100 eV photon energy. In the measured energy range, helium double ionization is dominated by the sequential processes, shake-off in particular, while the quasifree mechanism is negligible in absolute terms. Apparently, SO treats the photon momentum like single ionization does: The photon momentum is imparted onto the photoion but the photoelectron recoil momentum overcompensates this forward shift and pushes the photoion backwards. On the contrary, the quasifree mechanism proceeds without involvement of the nucleus as the photon couples directly with the two electrons. Hence, one can expect that the photon momentum is not imprinted onto the photoion.

In order to test this assumption, we inspect the momentum distributions of photoions after helium double ionization at 800 eV photon energy in Fig. 11.3 for SO (A) and QFM (B). Indicating the transfer of the photon momentum onto the

photoion, the measured SO photoion momenta accumulate on a circle that has a radius of the maximum electron momentum and that is moved to the right by the magnitude of the photon momentum. This is the same behavior that we have seen in Fig. 10.3 for He single ionization. However, the measured average momentum of QFM photoions in light propagation direction seems to be much closer to zero. This can best be seen in Fig. 11.3 C where we projected the distribution shown in panel B onto the \hat{x} axis (black line) and determined the center through a Gaussian fit (solid blue line). The experimental results speak in favor of the assumption that QFM photoions do not receive the photon momentum in the double-ionization process.

Further proof are the results of TDSE calculations for He double ionization at 800 eV photon energy and linearly polarized light that are shown in Fig. 11.3 D. The local maximum of the nondipole curve (red line) that corresponds to QFM is exactly at zero, while the outer local maxima are shifted to the right by the magnitude of the photon momentum.

In the present section, we have experimentally shown the unique fingerprint of the quasifree mechanism in one-photon double ionization of helium and the H_2 molecule: Two electrons emitted back-to-back at equal energy and a photoion that receives no recoil momentum. While the experimental confirmation of QFM for He double ionization is not new, the QFM in H_2 double ionization was actually first observed in the course of the present work. Furthermore, we have found evidence that the photon momentum is not imprinted onto QFM photoions which is in contrast to sequential double ionization through shake-off and single ionization in general. Our experimental observations are in excellent agreement with the results of two theory approaches.

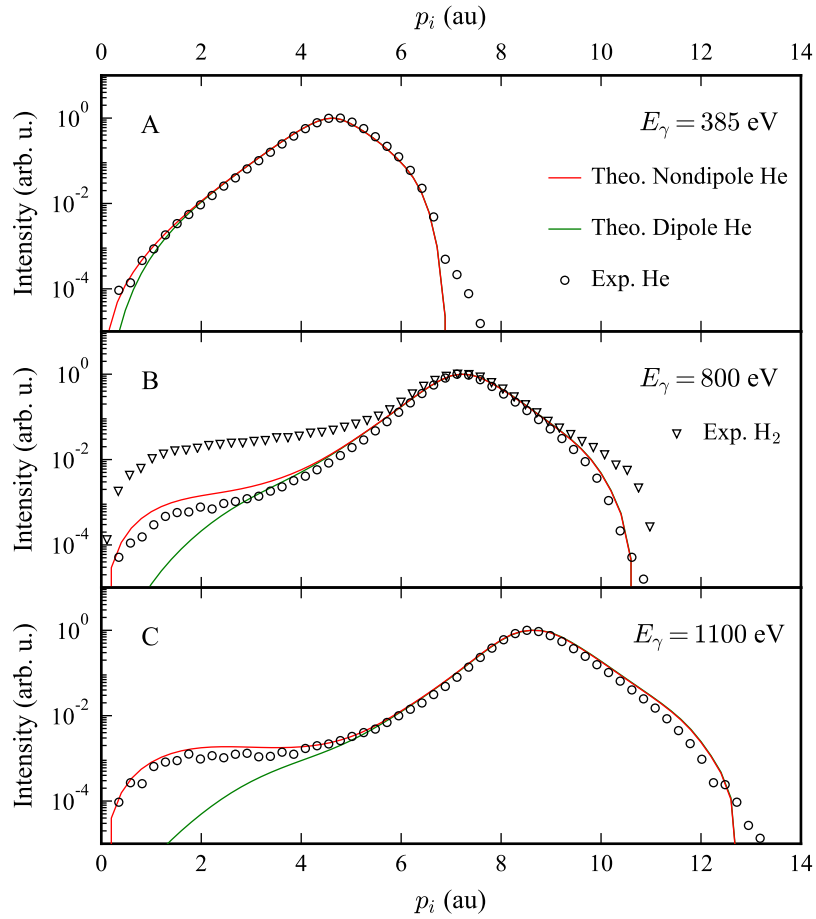


Figure 11.1: One-photon double ionization probability as function of the photoion momentum for He double ionization at 385 eV (A), 800 eV (B), 1100 eV (C), and for H₂ double ionization at 800 eV (B). Red (green) lines: two-electron nondipole (dipole) TDSE calculations for He double ionization. Note that $p_i = p_{sum}$ for H₂ double ionization. Figure adapted from Ref. [147].

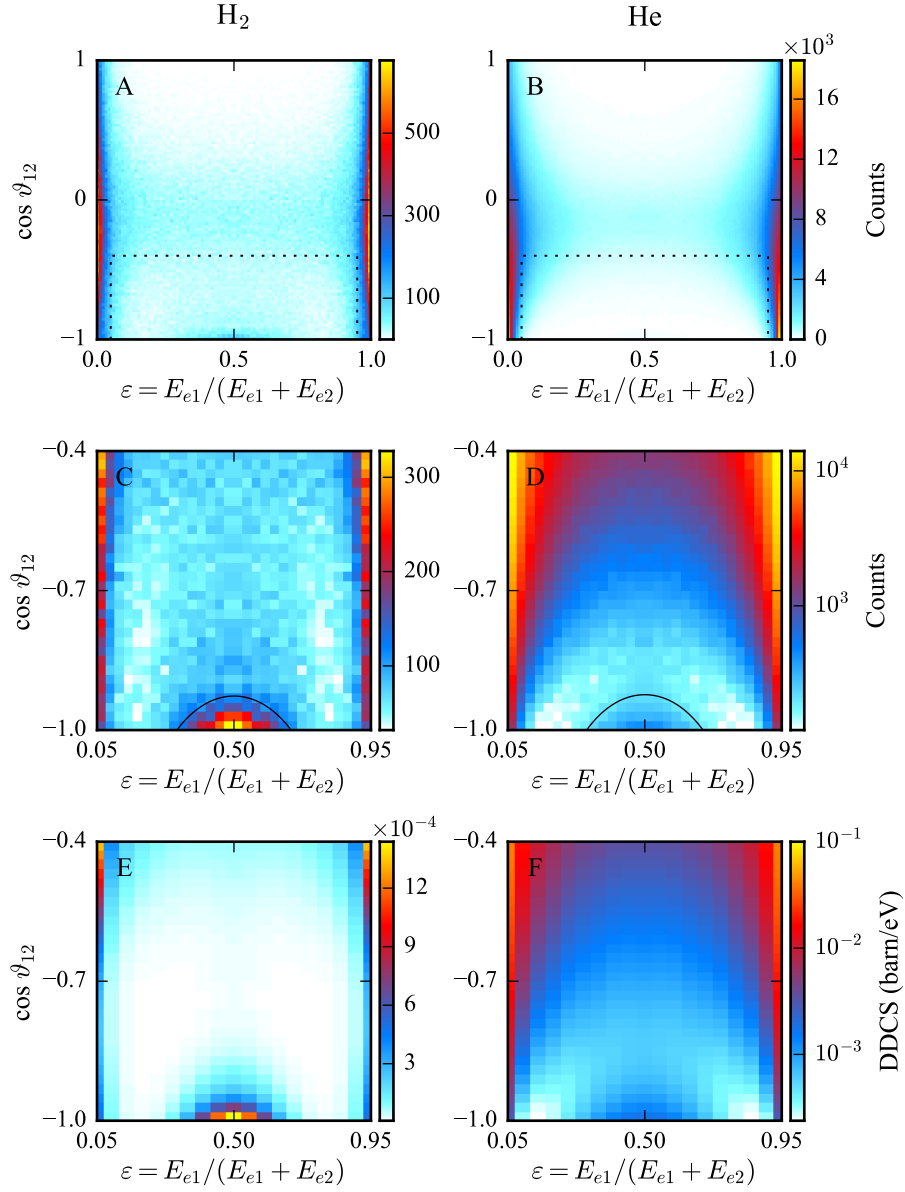


Figure 11.2: Doubly differential cross sections of H_2 double ionization (A,C,E) and He double ionization (B,D,F) by a single 800 eV circularly polarized photon. (A–E) Experimental results. (E,F) PSECS calculations. C and D are excerpts from A and B as indicated by the dashed black lines. The solid black lines in C and D indicate all the positions where $p_i = 2$ au. Contributions around $\cos \vartheta_{12} = -1$ and $\varepsilon = 0.5$ correspond to the QFM. Figure adapted from Ref. [140].

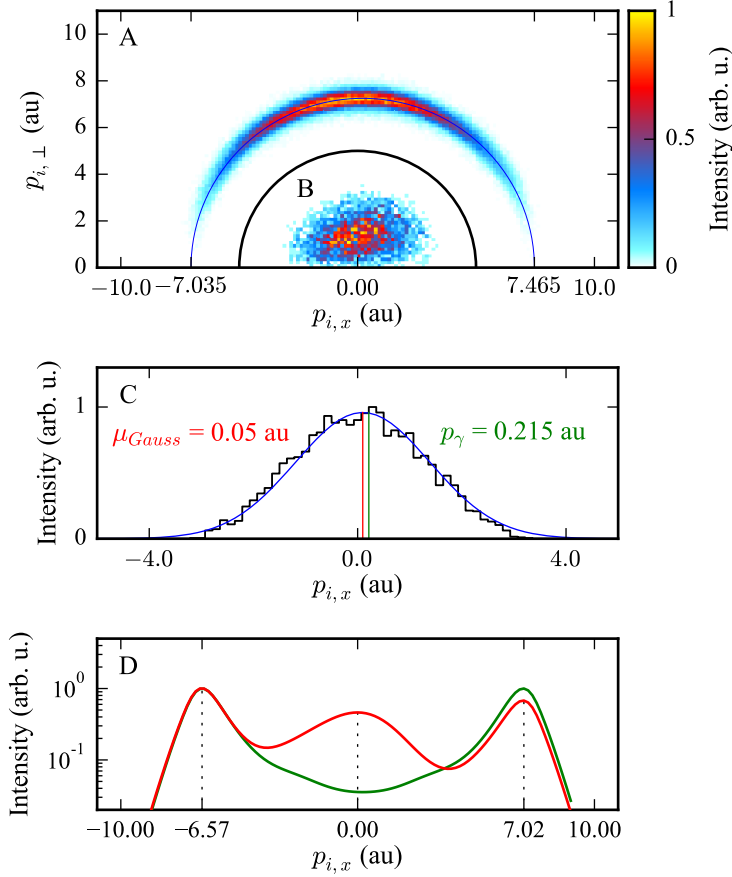


Figure 11.3: Momentum distributions of photoions after He double ionization at 800 eV photon energy. (A) The experimental data shown is limited to $\epsilon < 0.005$ or $\epsilon > 0.995$ and resembles double ionization via SO. The blue semicircle is shifted to the right by the photon momentum. The SO photoions accumulate on this semicircle. (B) The experimental data shown is limited to $0.25 < \epsilon < 0.75$ and $\theta_{12} > 160^\circ$. It resembles double ionization via QFM. (C) Projection of data from B onto the \hat{x} axis (black) and Gaussian fit (blue) to obtain the center of the momentum distribution of QFM photoions along the light propagation direction (red). The green line indicates the photon momentum for comparison. (D) Dipole (green) and nondipole (red) TDSE calculations for helium double ionization with 800 eV linearly polarized photons ($p_{i,y} = 0 \pm 2$ au & $p_{i,z} = 0 \pm 2$ au, the polarization vector is parallel to the \hat{z} axis). Experiment and theory suggest that the photon momentum is not imprinted onto QFM photoions.

11.2 A PURE QUADRUPOLE CONTRIBUTION TO PHOTOIONIZATION

The dominance of the electric-dipole contribution in photoionization makes it difficult to observe pure electric-quadrupole transitions in an experiment. Arguably, this is easier to achieve in theory predictions where one can switch off the dipole amplitude in calculations (see, e.g., Ref. [141]). So far, most nondipole phenomena observed experimentally are just dipole features slightly modified by the dipole-quadrupole interference term (see, e.g., Fig. 10.4 or Ref. [3] for a review). The following approach allows us to visualize a pure quadrupole transition in a subset of our experimental data.

Based on the conservation of angular momentum and parity, F. Maulbetsch and J. Briggs demonstrated how certain electron momentum configurations and quantum state combinations cannot be populated in the final state of a process that leads to the emission of two electrons [62]. One of these forbidden configurations is $\mathbf{p}_{e1} = -\mathbf{p}_{e2}$ if the parity of the two-electron wave function is ungerade. While an electric-dipole transition flips the parity of the wave function, it stays constant in an electric-quadrupole transition (compare to Fig. 4.1). The ground states of helium and the hydrogen molecule have gerade parity. Consequently, back-to-back emission at equal energy sharing ($\mathbf{p}_{e1} = -\mathbf{p}_{e2}$) after double ionization of He or H₂ is *dipole forbidden* but *quadrupole allowed*.

The corresponding region of the final-state momentum space stems from a quadrupole transition and is, by virtue of the selection rule, free of any otherwise dominating dipole contributions. Hence, by restricting the investigation of the measured data to electron pairs emitted back-to-back at equal energy, namely QFM electrons, we have experimental access to a pure quadrupole transition [56, 163].

The important physical difference between dipole and quadrupole transitions is in the angular momentum transfer (compare to *Partial waves and angular momentum* on p. 21). By definition, a dipole transition transfers one unit of angular momentum to the two-electron final state due to the photon spin, while two units of angular momentum are available in a quadrupole transition. The angular momentum of the outgoing electron wave becomes observable in the angular variation of the electron emission probability, i.e., the photoelectron angular distribution.

In Fig. 11.4 we show the measured angular distribution of electrons from double ionization of H₂ (A) and He (B) at 800 eV photon energy and circularly polarized light as function of ϑ_γ , i.e., the polar angle enclosed by the electron momentum vector and the light propagation direction. To filter out QFM electrons, the shown data is limited to $0.35 < \epsilon < 0.65$ & $\vartheta_{12} > 160^\circ$.

The red lines in Fig. 11.4 represent the square of the spherical harmonic for $\ell = 2$ and $m = 1$ normalized to the data points,

$$|Y_{21}(\vartheta_\gamma, \varphi = 0)|^2 \propto \cos^2 \vartheta_\gamma \times \sin^2 \vartheta_\gamma, \quad (11.5)$$

which describes the final-state angular distribution of electrons that result from a pure electric quadrupole transition from any initial *s*-subshell.

Here, we have chosen the photon propagation direction $\hat{\mathbf{k}}_\gamma$ as the quantization axis. The photon spin vector is (anti-)parallel to $\hat{\mathbf{k}}_\gamma$ and we get $\Delta\ell = 1$ and $\Delta m = 1$ through the transfer of the spin angular momentum. The additional unit of orbital angular momentum— $\mathbf{p}_\gamma \times \mathbf{r}_e = \hbar$ —is oriented perpendicular to the quantization axis. It increases the magnitude of the electron angular momentum but has no effect on its projection m onto $\hat{\mathbf{k}}_\gamma$.

The strong resemblances between the measured angular emission patterns and $|Y_{21}(\vartheta_\gamma, \varphi = 0)|^2$, as demonstrated in Fig. 11.4, underline that QFM electrons originate from a pure quadrupole contribution to photoionization.

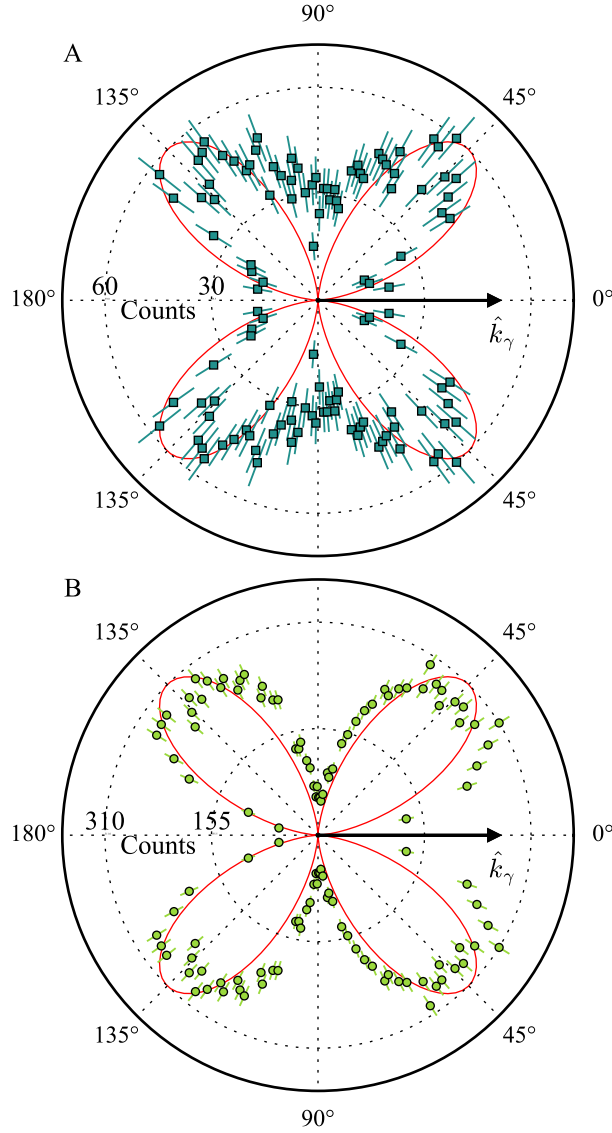


Figure 11.4: Photoelectron angular distribution of QFM electrons from one-photon double ionization of H₂ (A) and He (B) with 800 eV circularly polarized photons as function of the polar angle enclosed by the electron momentum vector and the light propagation direction (ϑ_γ). The shown data is limited to $0.35 < \epsilon < 0.65$ & $\vartheta_{12} > 160^\circ$. For this selection, the dipole contribution to photoionization vanishes. The red lines represent $|Y_{21}(\vartheta_\gamma, \varphi = 0)|^2$ normalized to the data points (see Eq. 11.5). Figure adapted from Ref. [141].

11.3 PROBING THE TWO-ELECTRON CUSP

By investigating the differential cross section of photoionization, one can draw conclusions about the properties of the respective initial state of the reaction. For example, one-photon single ionization of an atom has the potential to probe the angular and the radial part of a single-electron wave function in the initial state. On the one hand, from the photoelectron angular distribution one can determine the angular momentum (see *Partial waves and angular momentum* p. 21). On the other hand, the energy dependence of the cross section is related to the spatial probability density of electrons relative to the nucleus (compare to *Transition amplitude and cross section* on p. 13).

In the present section, we compare the differential cross sections from He and H₂ one-photon double ionization at 800 eV photon energy to reveal differences in the correlated structure of the two-electron wave functions in their respective ground states. Historically, this was the motivation for many theoretical and experimental studies of one-photon double ionization (see, e.g., Ref. [158] for a review).

Our approach is based on the idea that the absolute QFM cross section is a measure for the initial spatial probability density at the *two-electron cusp*, which is the point where both electrons coalesce [59, 164], i.e., $r_- = 0$. On first sight, this idea seems plausible because the part of the electric quadrupole responsible for QFM acts directly on $r_- = 0$ (see Eq. 11.3 and Ref. [60]). However, the rigorous formal relation between the absolute QFM cross section σ_{QFM} and the so-called *intracule* $h(r_-)$, which describes the initial spatial probability density of electrons relative to each other [165], is not so straightforward eventually. In the present section, we limit our thoughts to a mostly qualitative discussion, but an approach to approximate $h(0)$ from a measured or calculated σ_{QFM} can be found in Ref. [140]. A shortcoming of our experimental technique is that absolute cross sections cannot be retrieved from the experimental data. Accordingly, the results shown previously in Fig. 11.2 A–D are only differential double-ionization intensities and there is no possibility to internormalize the experimental results for H₂ and He. Hence, from the experimental data alone, we cannot judge and compare σ_{QFM} between the two targets. To that end, the theoretical results shown in Fig. 11.2 E and F present differential cross sections in absolute terms that we will use for normalization and quantitative comparisons.

So far, we have seen in Figs. 11.1 & 11.2 that the QFM contribution to the total cross section—in relative terms—was stronger for the hydrogen molecule than for helium.

For a better comparison of the results shown in Fig. 11.2, we integrate over $\theta_{12} = 165^\circ \pm 15^\circ$ (i.e., $\cos \theta_{12} < -0.866$) and display the cross sections as function of the energy sharing in Fig. 11.5. The experimental data sets are normalized to the PSECS calculations at equal energy sharing ($\epsilon = 0.5$). While agreement between theory and experiment is excellent for He, the minor discrepancies for H₂ are most likely due to systematic errors in the experiment.¹

In the present work, we define the absolute QFM cross sections σ_{QFM} for He and H₂ as the shaded areas in Fig. 11.5, i.e., the areas under the curves around equal energy sharing enclosed by the two minima of the W-shaped distributions. Those QFM cross sections are presented in Table 11.1 alongside PSECS calculations for the single and double ionization probabilities of He and H₂ at a photon energy of 800 eV. The PSECS calculations considered electric-dipole and electric-quadrupole

¹Remember that one electron momentum vector is reconstructed via momentum conservation. This is less accurate for H₂ because the center of mass has to be calculated from two protons instead of being measured via the doubly charged He²⁺ nucleus. Thus, the systematic errors propagating to the calculated electron are larger and the noise reduction (exploiting energy conservation) is less efficient in case of H₂.

contributions to the cross section, as shown individually for double ionization. Remember that the interference term between dipole and quadrupole does not alter the total integrated cross section (see p. 19).

As discussed in Sec. 5.1, the contributions to the double-ionization cross section at highly asymmetric energy sharing correspond to the shake-off process. The strength of the SO cross section σ_{SO} is determined by electron-electron correlation in the initial state, which can be pictured as the overlap of the two individual electronic wave functions.

In Fig. 11.6 we show the measured probability of creating two electrons emitted back-to-back in H_2 double ionization at 800 eV photon energy as function of the energy sharing and for different internuclear distances of the two protons. The internuclear distance is calculated by means of Eq. 9.18 from the kinetic energy release. We have also included He in the display, which corresponds to an internuclear distance of $R = 0$. The four subsets of experimental data shown in Fig. 11.6 are internormalized at the highly asymmetric energy sharing peaks to visualize the relative strength of σ_{QFM} compared to σ_{SO} as function of the internuclear distance.

What can be learned from the combined results shown in Table 11.1 and Figs. 11.1, 11.2, 11.5 & 11.6?

The findings underline that QFM is a pure quadrupole effect but it does not account for the whole quadrupole contribution to double ionization of a two-electron target. Furthermore, the relative contribution of QFM to the whole double-ionization cross section is stronger for H_2 than for He, but in absolute terms σ_{QFM} is still much weaker for H_2 than for He at 800 eV photon energy. The latter suggests that the intracule at $r_- = 0$ is much smaller for H_2 than for He, despite the similar electronic structure of the two systems. In fact, $h(0)$ is roughly six times larger for He than for H_2 [140, 166, 167], which is quite close to the ratio $\sigma_{\text{QFM}}^{\text{He}}/\sigma_{\text{QFM}}^{\text{H}_2} \approx 5$, as suggested by Table 11.1.

Apparently, through an increase of the internuclear distance R , SO and QFM cross sections decrease in absolute terms, but SO decreases at a faster rate and therefore the ratio $\sigma_{\text{QFM}}/\sigma_{\text{SO}}$ increases. This encourages the following physical picture about the behavior of the two-electron wave function upon increasing R . As the internuclear distance grows, the overlapping electronic wave functions are further separated, resulting in less electron-electron correlation and a strong suppression of double ionization through SO. For QFM, on the other hand, the decline of the cross section is less pronounced. A possible intuitive explanation is that the two-electron cusp is barely affected by a growing R because both electrons stay close to the center point between the two protons to partake in the bonding. Accordingly, the QFM cross section remains relatively strong.

(barn)	Single ionization	Double ionization		
		Dipole	Quadrupole	QFM
He	730	19.5	0.10	0.039
H ₂	62	0.75	0.015	0.008

Table 11.1: Cross sections obtained from PSECS calculations for one-photon single and double ionization of He and H₂ by a 800 eV circularly polarized photon. The total integrated cross sections of the QFM correspond to the shaded areas in Fig. 11.5. Table adapted from Ref. [140].

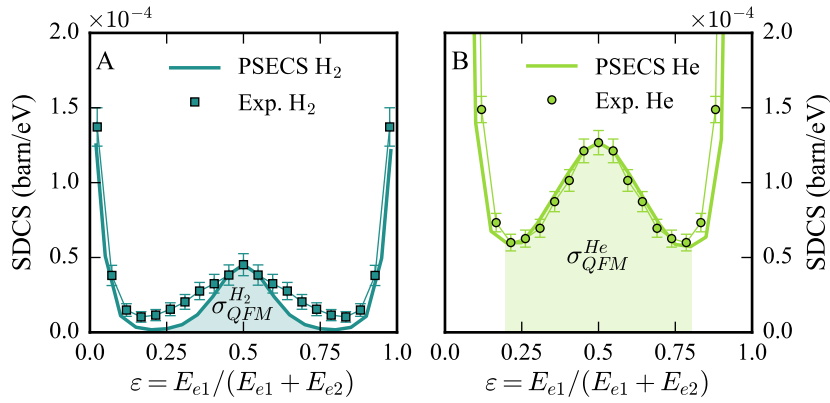


Figure 11.5: Singly differential cross sections for double ionization of H₂ (A) and He (B) by a single 800 eV circularly polarized photon for electrons emitted back to back ($\alpha = 180^\circ \pm 30^\circ$). The experimental datasets are normalized to theory at the equal energy sharing point. The colored areas under the theory curves represent the QFM cross sections tabulated in Table 11.1. Figure adapted from Ref. [140].

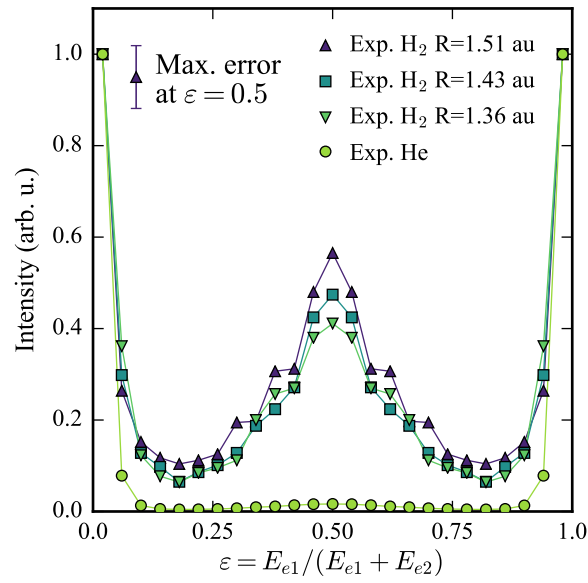


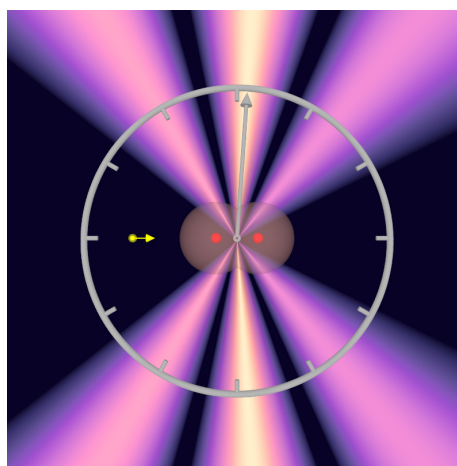
Figure 11.6: Measured probability of creating two electrons emitted back-to-back in one-photon double ionization at 800 eV photon energy as function of the energy sharing. The shown data is limited to $\vartheta_{12} > 150^\circ$ and broken down for different internuclear distances of the two protons, where the He data set corresponds to $R = 0$. The four subsets of data are internormalized at the highly asymmetric energy sharing peaks. Figure adapted from Ref. [140].

THE SIMPLEST DOUBLE SLIT

We choose to examine a phenomenon which is impossible, absolutely impossible, to explain in any classical way, and which has in it the heart of quantum mechanics. In reality, it contains the only mystery.

— R. Feynman about double-slit interference in his famous lectures [168].

Photoelectron emission from the H_2 molecule at high photon energies mimics the double-slit experiment because the two centers of the diatomic molecule behave like independent photon absorbers and subsequently as indistinguishable sources of coherent photoelectron waves [73]. Despite being well-established today, this insight cannot cease to fascinate as it bears some of the most intriguing concepts of quantum mechanics. That includes the wave-particle duality of electrons, decoherence of a quantum system, and entanglement among quantum particles. These concepts have already been addressed extensively in experimental works (see, e.g., Refs. [33, 89, 93, 95, 98]), but only at photon energies up to 400 eV. In the first section of this chapter, we will recapitulate some of these findings with our experimental results at 800 eV photon energy. In the remaining two sections of the chapter, we show that the double-slit behavior of H_2 photoionization unveils yet another fundamental fact of nature: the finite speed of light.¹



The experimental results shown here were obtained in Run 2A, where we irradiated H_2 by 800 eV circularly polarized photons. Our investigations are limited to the one-photon double ionization of H_2 . Here, we achieved full solid-angle coverage in the laboratory frame of reference for all reaction fragments by means of reconstructing one electron momentum vector through momentum conservation (see p. 68).² In Sec. 12.3, our experimental results are compared to calculations that solve the two-electron Time-Dependent Schrödinger Equation (TDSE) from H. Liang, Y.-K. Fang, L. Geng, Q. Gong, and L.-Y. Peng [149].

¹The figure in the top right corner illustrates the concept of the time measurement. The photon (yellow) launches electron waves out of the initial-state electron orbital (grey) of the hydrogen molecule (red: protons). The resulting interference pattern is slightly asymmetric, allowing the calculation of how long the photon required to travel through the molecule.

²Note that single ionization of H_2 creates just one bare proton and one high energetic electron (≈ 780 eV), for which we achieved only small solid-angle acceptance (see p. 58). The neutral hydrogen atom cannot be detected. Hence, most events in the corresponding data set lack information of two reaction fragments and we could not reconstruct their momentum vectors by means of momentum conservation. This "incomplete" data set is not investigated in the present work.

12.1 INTERFERENCE, DECOHERENCE, AND ENTANGLEMENT

The double-slit analogy was established for photoelectron waves born in one-photon single ionization of H_2 [73]. However, for highly asymmetric energy sharing, the fast electron from double ionization practically behaves like a photoelectron in single ionization [91]. This has been impressively demonstrated experimentally by Akoury et al. in Ref. [89]. However, as some of our interpretations heavily depend on this idea, we will first confirm the double-slit nature of H_2 double ionization again at 800 eV photon energy.

To that end, Fig. 12.1 A shows the angular distribution of the fast electron in the molecular frame of reference as function of the kinetic energy release. These results demonstrate how the number of interference fringes increases and how the angular separation of the maxima becomes smaller with a decreasing kinetic energy release, i.e., with a growing internuclear distance R (see. Eq. 9.18, and see Ref. [98] for similar experimental results). One would expect the same behavior from the interference pattern of a classical double-slit experiment when the slit distance d is increased. Figure 12.1 B shows the distribution of the electron energy sharing and the fast electrons used in Fig. 12.1 A are limited to $\epsilon_{eF} = E_{eF}/(E_{eF} + E_{eF}) > 0.96$, which corresponds to the red-shaded region in Fig. 12.1 B.

In Fig. 12.2 we show projections of the data from Fig. 12.1 A onto the horizontal axis for different regions of the KER. The green lines in the right column of Fig. 12.2 indicate the calculated intensity distributions of a classical double-slit experiment (Eq. 6.5). Here, we set $d = R$ according to Eq. 9.18 and $\lambda_e = 0.82$ au, which corresponds to the de Broglie wavelength of an electron of 800 eV kinetic energy. The agreement between the experimental data and the model prediction substantiate the double-slit analogy for the fast electrons from H_2 double ionization.

Note that these observations also underline the wave-particle duality of electrons. Our detector registers single electrons and we determine the particle's emission direction with respect to the molecular axis. Eventually, the wave behavior appears as the interference pattern after aggregation of many detected events.

Let us now briefly cover the concepts of *decoherence* and *entanglement*, and how they manifest in our experimental results.

Macroscopic objects are never isolated from their environment and therefore their wave function is not simply governed by the Schrödinger equation, which is applicable only to closed systems [169]. *Decoherence* describes the transition from quantum to classical behavior caused by the interaction of a system with its environment. These interactions shift the phases of the wave functions and potentially destroy the phase integrity—i.e., coherence—which is needed for interference effects (see, e.g., Refs. [170, 171] for experimental works on decoherence of molecular matter waves).

In their work on H_2 double ionization [89], Akoury et. al addressed the following significant question. How much interaction is needed to induce the transition from quantum to classical behaviour? They found that the interaction among the two emitted electrons can be enough, if the strength of the interaction is sufficiently high. This finding is underlined by our results shown in Fig. 12.1 C, where we depict the angular distribution of the fast electron in the molecular frame of reference as function of the electron energy sharing for the average internuclear distance of 1.4 au, i.e., for a kinetic energy release in the range of 19.4 ± 0.5 eV as indicated by the red-shaded region in Fig. 12.1 D. The more asymmetric the energy sharing, the smaller is the momentum transfer from the electron emitted

first to the secondary electron. Hence, the energy sharing serves as a measure of the strength of the interaction between the two electrons.

A projection of the top row of bins from Fig. 12.1 C onto the horizontal axis exactly corresponds to the results presented in Fig. 12.2 C & D. Here, the interference pattern is clearly visible. Starting at $\varepsilon = 1$ and moving to $\varepsilon = 0$, two things happen in Fig. 12.1 C. (1) The number of interference fringes diminishes because the de Broglie wavelength of the electron becomes larger as the kinetic energy decreases. This behavior is most apparent between $\varepsilon = 1$ and $\varepsilon = 0.75$. (2) The interference pattern gradually disappears until it is gone altogether. Arguably, this is an evidence of gradual decoherence.

Even for a violent interaction between the two electrons in H_2 double ionization—i.e., more symmetric energy sharing—the coherence is not destroyed, but it is conserved in the entangled two-electron system. This has been demonstrated by Akoury et al. in Ref. [89] and also by Waitz et al. in Ref. [95]. Accordingly, the sum momentum of the electron pair,

$$\mathbf{p}_{eSum} = \mathbf{p}_{e1} + \mathbf{p}_{e2} , \quad (12.1)$$

still continues to exhibit the interference pattern when projected onto the molecular axis. This holds true for any electron energy sharing, as demonstrated in Fig. 12.3 A, where we show the interference pattern of the two-electron wave in terms of

$$\cos \alpha_{eSum} = \hat{\mathbf{p}}_{eSum} \cdot \hat{\mathbf{R}} \quad (12.2)$$

as function of the electron energy sharing. Note that each row of bins in Fig. 12.3 A has been normalized individually to remove the effect of the highly-asymmetric energy sharing distribution from the display. The correlation between the two electron emission angles in the molecular reference frame is shown in Fig. 12.3 B–D for different electron energy sharings. The tilted fringes follow the relationship $p_{eF} R \cos \alpha_{eF} + p_{eS} R \cos \alpha_{eS} = \text{const.}$ and their appearance underlines that two electrons are an entangled pair for any electron energy sharing (see Refs. [95, 149] for comparison).

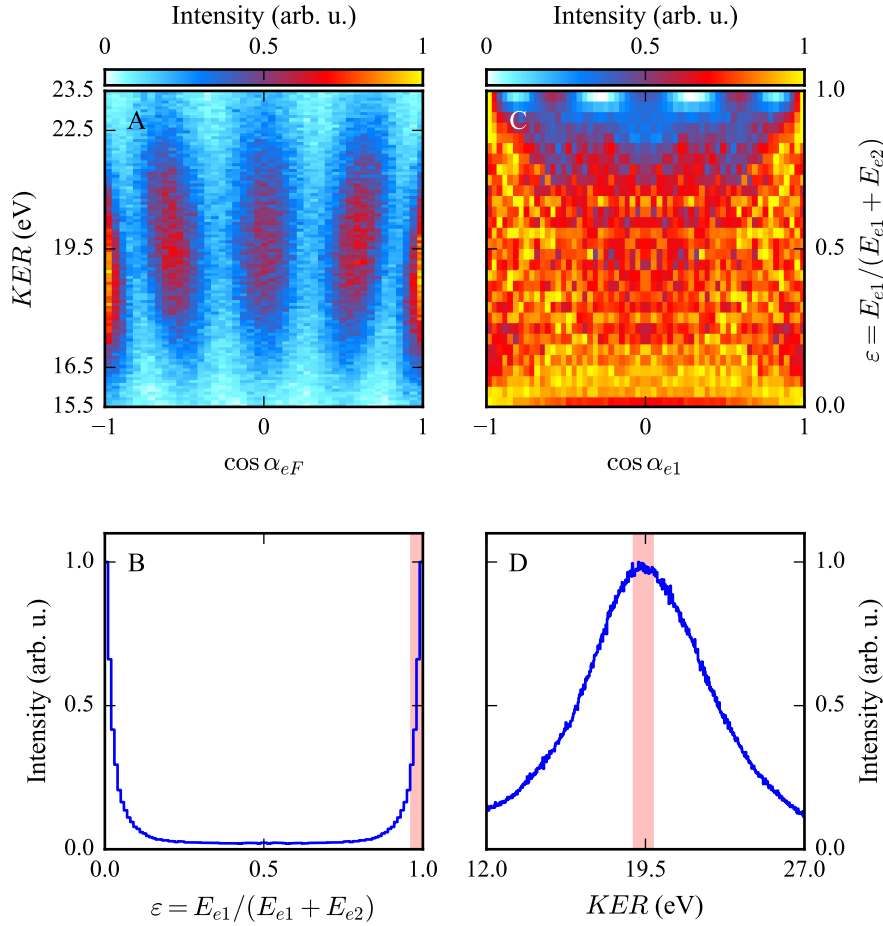


Figure 12.1: Double-slit nature of fast electron emission in one-photon double ionization of H₂ with 800 eV photon energy. (A) Fast electron emission angle in the molecular reference frame as function of the kinetic energy release. Subfigure adapted from Ref. [148]. (B) Electron energy sharing. The red-shaded region indicates $\varepsilon > 0.96$ and represents the gate used for the display of data in subfigure A. (C) Electron emission angle in the molecular reference frame as function of the electron energy sharing for the average internuclear distance of $R = 1.40 \pm 0.04$ au, which corresponds to the red-shaded region in subfigure D. Each row of bins in subfigure C has been normalized individually to remove the effect of the highly-asymmetric energy sharing distribution from the display. (D) Kinetic energy release. The red-shaded region indicates $KER = 19.4 \pm 0.5$ eV.

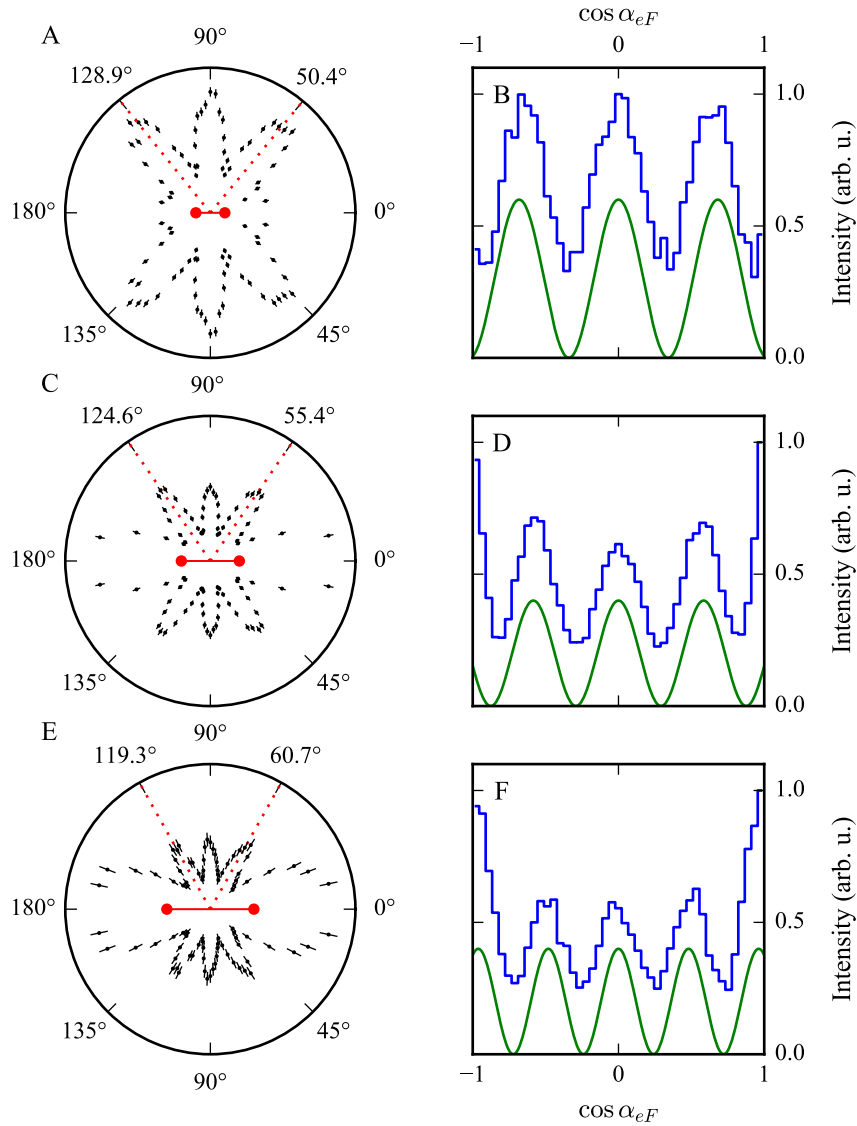


Figure 12.2: Molecular-frame fast-electron ($\epsilon_{eF} > 0.96$) angular distribution from one-photon double ionization of H_2 at 800 eV photon energy for different conditions on the KER . The two subfigures in each row are different representations of the same experimental data (see Appx. A for details). The green lines in the right subfigures represent double-slit interference (Eq. 6.6) where we set $p_{eF} = 7.64$ au and R as indicated in the following. **(A,B)** $KER = 23.0 \pm 0.5$ eV ($R \approx 1.2$ au). **(C,D)** $KER = 19.4 \pm 0.5$ eV ($R \approx 1.4$ au). **(E,F)** $KER = 16.0 \pm 0.5$ eV ($R \approx 1.7$ au).

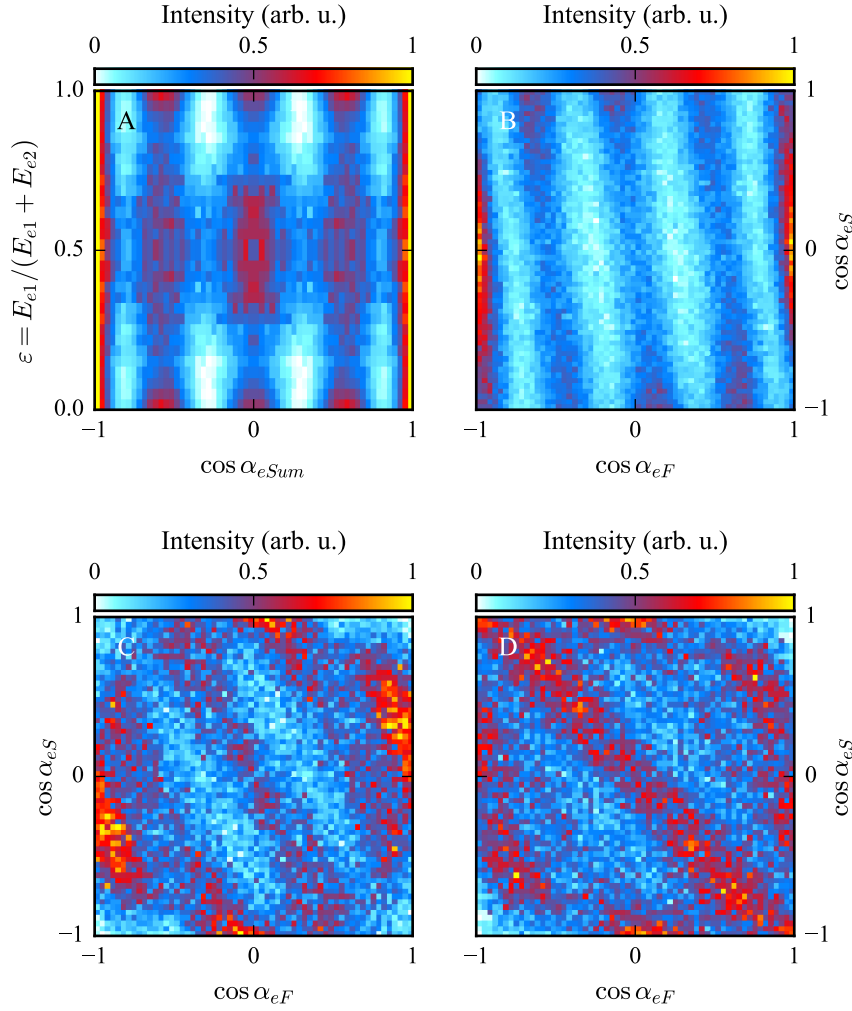


Figure 12.3: Correlation between the two electron emission angles in the molecular reference frame from one-photon double-ionization of H_2 at 800 eV photon energy for the average internuclear distance of 1.4 au ($KER = 19.4 \pm 0.5$ eV). (A) Orientation of the electron sum momentum vector with respect to the molecule as function of the electron energy sharing. Each row of bins in subfigure A has been normalized individually to remove the effect of the highly-asymmetric energy sharing distribution from the display. (B–D) Correlation between fast and slow electron emission angle for $\epsilon_{eF} > 0.96$ (B), $\epsilon_{eF} = 0.25 \pm 0.05$ (C), and $\epsilon_{eF} = 0.4 \pm 0.1$ (D). The idea for this figure is adapted from Ref. [95], where equivalent illustrations can be found for $E_\gamma = 400$ eV.

12.2 ZEPTOSECOND BIRTH TIME DELAY

The finite speed of light should affect the photoionization of spatially extended systems. This hypothesis is based on the idea that the photoelectron wave cannot be launched at the same time from anywhere of its initial position-space distribution while the photon arrives at different times. Accordingly, the contributions to the total photoelectron wave that originate from different positions along the photon travel path should be subject to *birth time delay*.

In the formal treatment of light-matter interaction, the assumptions of an infinitely long wavelength or an infinitely fast speed of light both result in the electric dipole approximation. Under both assumptions, the target experiences an electric field which is constant over the whole relevant region of space.

As previously discussed in Sec. 6.2 and illustrated in Fig. 6.7, there are two closely related physical pictures for nondipolar photoionization: (1) Time independent: The extended system is exposed to a spatially dependent light phase. The resulting phase differences are imprinted onto the individual contributions to the total electron wave. (2) Time dependent: During the process of photoionization, a wavefront of constant phase sweeps from one end of the system to another. This results in an inhomogeneous temporal structure of the total electron wave. Hence, any observable effect resulting from birth time delay qualifies as a nondipole effect.

In the present section, we test the hypothesis drawn up above and search for the effect of the finite speed of light on fast electron emission in one-photon double ionization of H_2 at 800 eV photon energy. By stressing the double-slit analogy of this process, we try to measure the birth time delay between the two waves that are launched coherently from the two atomic centers. This birth time delay should simply correspond to the travel time of the photon across the molecule, which is 247 zeptoseconds ($1 \text{ zs} = 10^{-21} \text{ s}$) for the average bond length of molecular hydrogen ($R = 1.4 \text{ au}$).

For the time measurement, we employ the approach introduced on p. 44 in Sec. 6.2: In the molecular double-slit experiment, birth time delay leads to an initial phase difference $\Delta\varphi$. If the two interfering waves in a double-slit experiment have different phases at birth, the symmetry of the interference pattern is broken. Accordingly, $\Delta\varphi$ can be determined from a measured angle α_0 to which the zeroth-order interference maximum is shifted. The initial phase shift depends on the angle β which is enclosed by the molecular axis and the light propagation direction. Hence, to measure birth time delay, we have investigated the angular distribution in the molecular frame of reference of fast electrons from one-photon double ionization of H_2 as function of β .

The results of our experimental study are shown in Fig. 12.4. Here, the fast electrons chosen for the display carry at least 96% of the excess energy ($\varepsilon_{eF} > 0.96$) and the internuclear distance was fixed around the average value, i.e., $KER = 19.4 \pm 0.5 \text{ eV}$. Figure 12.4 A shows the interference pattern of the fast electrons as function of $\cos\beta$. Apparently, the position of the central interference maximum is not constant, which indicates an initial phase difference that varies with the angle enclosed by molecule and light.

For a more quantitative analysis, we have determined $\cos\alpha_0$ by means of a Gaussian fit for each row of bins in the histogram. This procedure is shown exemplarily in Fig. 12.4 B for the top row of bins. Eventually, the mean values resulting from the Gaussian fits are displayed as the blue squares in Fig. 12.4 C as function of

$\cos \beta$. The errorbars include statistical and systematic errors.³ The dashed blue line is a linear function fitted to the experimental data points.

The birth time delay τ and the angle α_0 are related through Eq. 6.18, i.e.,

$$\tau = \cos \alpha_0 \frac{R}{v_{ph}} .$$

The left and the right vertical scales of Fig. 12.4 C are interlinked through this relation with $R = 1.4$ au and $v_{ph} = 0.027 \times c$, which corresponds to the phase speed of an electron of 750 eV kinetic energy. The solid black line in Fig. 12.4 C shows the simple model prediction of Eq. 6.15,

$$\tau = \frac{R}{c} \cos \beta ,$$

where $R = 1.4$ au and which is simply the photon travel time along the projection of the internuclear vector R onto the light propagation direction.

Apparently, the experimental results suggest a much larger birth time delay than the simple model predicts. There are two possible reasons for this deviation: Incorrect results or a wrong model. The relatively large systematic error is indicated by the blue-shaded region in Fig. 12.4 C (see footnote on p. 122 for details). Even within the systematic error range, however, the experimental results and the model prediction for the birth time delay do not agree.

Hence, we must assume that birth time delay is either not the true cause or not the only cause of an initial phase shift $\Delta\varphi$. An alternative cause is suggested by the prevailing interpretation of nondipolar photoionization. The dashed black line in Fig. 12.4 C shows Eq. 6.13, i.e.,

$$\cos \alpha_0 = \frac{k_\gamma}{p_{eF}} \cos \beta ,$$

which assumes that the initial phase shift between the two waves is induced by a spatially dependent light phase.

The small difference between the slopes of the solid and dashed black lines in Fig. 12.4 C points out that the two physical pictures are closely related but make slightly different predictions. We have shown on p. 45 that the two pictures are unanimous, only if the electron energy equals the photon energy. If the electron energy is smaller than the photon energy, the time-delay model predicts smaller initial phase differences $\Delta\varphi$ than the picture of a spatially dependent light phase. Eventually, this results in the smaller slope of the solid black line compared to the dashed one.

The physical reason for the small disagreement between the two models is a phase difference of $(I_p\tau)/\hbar$ that manifests in the bound state already. Accordingly, the two free electron waves have collected a phase difference prior to their departure into the continuum [149]. In order to keep it as simple and descriptive as possible, we have neglected this bound state phase in the time-delay model so far. If the bound state phase difference were considered in the model, the slopes of the solid and the dashed black lines in Fig. 12.4 C would be exactly the same. The easiest way to formally include it is to use the phase speed of a hypothetical electron in Eq. 6.18 for which the kinetic energy equals the photon energy. This will be done

³The accuracy to which we could specify the zero point of the electron momentum distribution was approximately ± 0.04 au in all three directions in space, i.e., roughly 20% of the magnitude of the photon momentum. Within this systematic uncertainty, we determined the maximum and minimum slope of the linear fit function in Fig. 12.4 C and indicated this range by the blue-shaded area. The statistical errors for each data point are the standard deviations of the mean values from the Gaussian fits estimated as the square root of the respective diagonal element of the covariance matrix [148].

in the next section where we test the time-delay model against the asymmetries observed in the interference pattern of the two-electron wave.

The two model predictions do not differ substantially and both still underestimate the experimental results. So far, we have not considered the two-electron nature of the double ionization process which could provide the missing explanation. The double-slit analogy is only approximately true for fast electron emission in one-photon double ionization of H_2 . Even for the highly asymmetric energy sharing used in the present section, the two electrons are still not independent and their phases are correlated (see Fig. 12.3 B for the experimental evidence). Hence, the additional initial phase shift observed in the experiment could be caused by the correlation among the fast and slow electrons. The correlated phases of the slow and fast electron waves and their implications on the initial phase difference $\Delta\varphi$ were taken into account in the TDSE calculations from Liang et al. [149]. The solid red line in Fig. 12.4 C shows the TDSE results for $\varepsilon_{eF} = 0.96$ and $R = 1.4$ au. The agreement with the experimental results is satisfactory.

On the one hand, this agreement between experiment and TDSE encourages the validity of the measured results. On the other hand, it suggests that neither model accurately accounts for the initial phase shift that breaks the symmetry of the fast-electron interference pattern. In other words, we have found experimental evidence of the birth time delay in molecular photoionization but the results remain ambiguous insofar that a birth time delay is not the only cause of the initial phase shift $\Delta\varphi$ in the subset of data inspected here.

The double-slit analogy works best in H_2 double ionization for the angular distribution of the combined electron pair in the molecular frame of reference (see Fig. 12.3 A for the experimental evidence). Hence, in the next section, we will test the time-delay model against the results obtained for the interference of a two-electron wave.

Note that in Ref. [148] we have included a model prediction that combined the atomic and molecular nondipole effects as discussed in Ch. 7 and as shown in Fig. 7.2. However, in Ref. [149] (see, e.g., Fig. 1 B therein) we found later that the TDSE results, that do not distinguish between the two effects, match with the predictions of Eq. 6.13, i.e., with the assumption of an initial phase shift due to a spatially dependent light phase alone. Apparently, the modifications of our observables due to the atomic nondipole effect are too small to play a significant role and they cannot be the reason for the additional initial phase shift. We have therefore neglected them here.

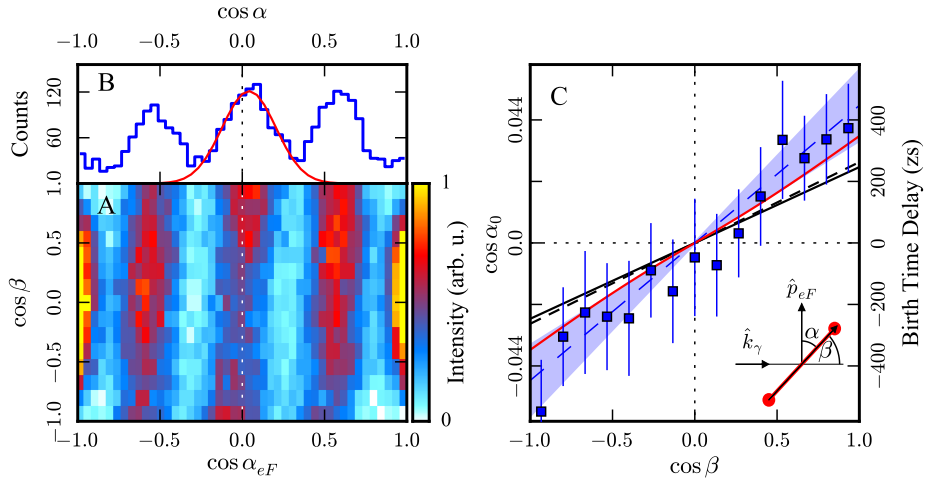


Figure 12.4: Birth time delay measurement for fast electrons from one-photon double ionization of H_2 at 800 eV photon energy. All data shown is limited to $\varepsilon_{eF} > 0.96$ & $KER = 19.4 \pm 0.5$ eV. **(A)** Angular distribution of the fast electron with respect to the molecular axis as function of $\cos \beta$, which measures the angle enclosed by light and molecule. **(B)** Angular distribution of the fast electron with respect to the molecular axis for parallel alignment of light and molecule, i.e., $\cos \beta > 0.87$ which corresponds to the top row of bins in subfigure A. The red curve is the Gaussian fit used to determine $\cos \alpha_0$. **(C)** Positions of the zeroth-order interference maxima $\cos \alpha_0$ as function of $\cos \beta$. All $\cos \alpha_0$ were obtained by means of Gaussian fits, as indicated exemplarily by the red curve in subfigure B. The error bars include statistical and systematic errors, and the blue-shaded region indicates the systematical error (see footnote on p. 122 for details). The vertical scales are related through Eq. 6.18 with $R = 1.4$ au and $v_{ph}/c = 0.027$. The solid black line shows the prediction of the time-delay model, i.e., the result of Eq. 6.15 for $R = 1.4$ au. The dashed black line resembles Eq. 6.13, i.e., an initial phase shift due to a spatially dependent light phase. The solid red line shows TDSE results from Ref. [149] for $\varepsilon_{eF} = 0.96$ and $R = 1.4$ au. Figure adapted from Ref. [148].

12.3 ...OF A TWO-ELECTRON WAVE

The quantum nature of H₂ double ionization should best be imagined as one two-electron wave originating at either atomic center instead of two single-electron waves that each launch from one center [93]. Accordingly, a robust double-slit-like interference pattern can be found in the sum-momentum distribution of the two electrons in the molecular frame of reference which even survives integration over the electron energy sharing distribution (see Fig. 12.3 A and Refs. [95, 149]). As the double-slit behavior is apparently more genuine for the two-electron quasiparticle than for a single fast electron from H₂ double ionization, we will now test the time-delay model for the electron sum momentum p_{eSum} .

Figure 12.5 shows the results of our birth-time-delay study for the collective electron momentum from one-photon double ionization of H₂ at 800 eV photon energy. The projection of the electron sum momentum onto the direction of the molecular axis, i.e.,

$$p_{eSum,\hat{R}} = p_{eSum} \cdot \hat{R}, \quad (12.3)$$

as function of the angle β enclosed by molecule and light is shown in Fig. 12.5 A for the experimental results and in Fig. 12.5 B for the TDSE calculations from Liang et al. [149]. For the TDSE calculations, the internuclear distance was fixed at $R = 1.4$ au. For the experimental results, we have integrated over $KER = 19.4 \pm 0.3$ eV. The TDSE predictions and the experimental results show the same distinct features. In particular, the position of the central interference maximum varies with $\cos \beta$, which suggests initial phase shifts due to nondipole effects.

In order to identify the positions of the zeroth-order interference maxima as function of $\cos \beta$, the subset of experimental data shown in Fig. 12.5 A underwent the same procedure as the data presented in Fig. 12.4 A. The result of the procedure is shown by the blue squares in Fig. 12.5 C (see footnote on p. 122 for details on the error bars and the blue-shaded systematic error region). The solid red line in Fig. 12.5 C presents TDSE results for $\cos \alpha_0$ as function of $\cos \beta$ [149]. The left and right vertical scales of Fig. 12.5 C are again linked through Eq. 6.18, but this time we have used $v_{ph} = 0.028 \times c$, which corresponds to the phase speed of an electron of 800 eV kinetic energy. By means of this small modification of the time-delay model, the right-hand sides of Eqs. 6.13 & 6.19 become equal, i.e., both models of nondipolar photoionization make the same predictions. The dashed black line in Fig. 12.5 C shows the birth time delay calculated through $\tau = (R/c) \cos \beta$ (Eq. 6.15). Experimental results, TDSE calculations, and the predictions of the time-delay model are all in decent agreement with each other. Our findings support the hypothesis that the finite speed of light affects the photoionization of spatially extended systems. The two contributions to the total two-electron wave that originate from the two atomic centers are subject to a birth time delay. Assuming that the phase speed of the two-electron wave equals that of a single-particle matter wave which contains the entire photon energy, the simple time-delay model (Eq. 6.15) complies with TDSE calculations and predicts the experimental data fairly well. Evidently, the birth time delay simply corresponds to the travel time of the photon along the projection of the internuclear distance onto the light propagation direction.

For fast electron emission in H₂ double ionization, the effect of birth time delay on the initial phase shift was likely observed but overshadowed by the impact of the correlated phases of the two electrons (see Sec. 12.2). For one-photon single ionization of H₂ [149] or H₂⁺ [172], however, TDSE results comply with the pre-

dictions of the modified time-delay model where $E_e = E_\gamma$. Although there are no further studies until now, we have no reason to believe that birth time delay is not a general phenomenon in the photoionization of extended systems.

I want to conclude this chapter with a personal answer on the following question. *Did we really conduct a time measurement with zeptosecond resolution?* We have measured the momentum distributions of the reaction fragments from photon double ionization of molecular hydrogen and found certain asymmetries that can be explained by means of a zeptosecond birth time delay. I leave it to the reader to decide whether this qualifies as a time measurement or not. The time-delay model is just one way to illustrate the physical reality of photoionization at high photon energies. I personally find this model much more attractive and intuitive than the prevailing idea of a spatially dependent light phase that drives nondipolar photoionization.

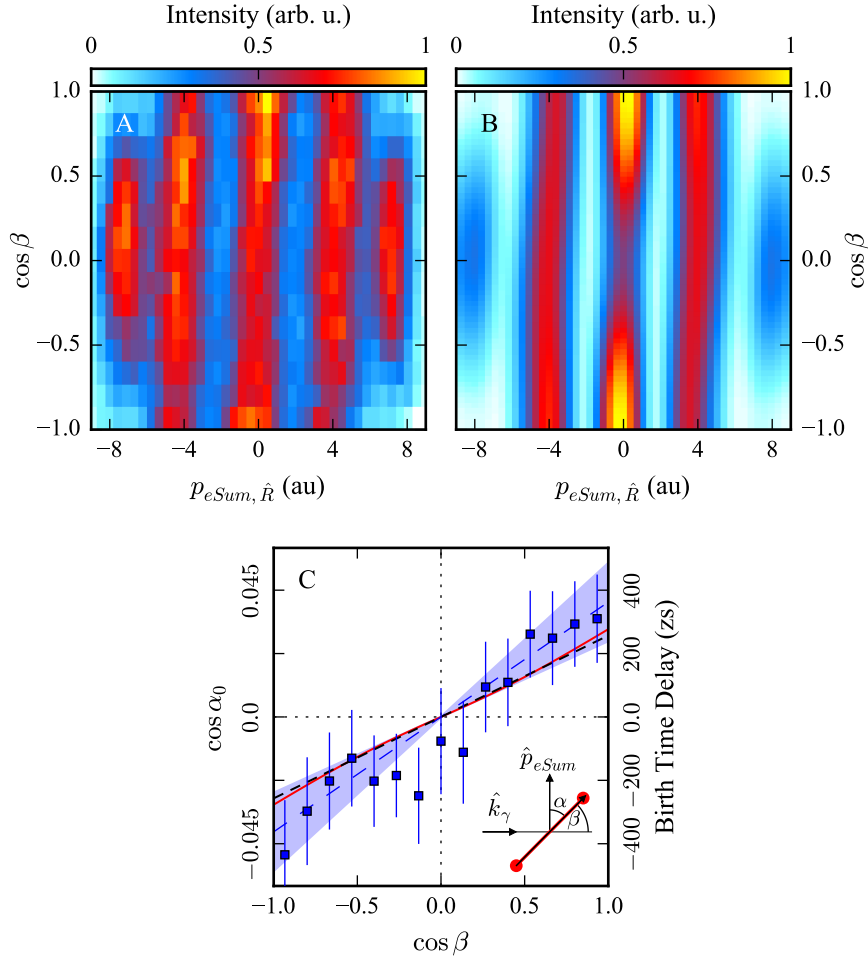


Figure 12.5: Birth time delay measurement for the two-electron wave from one-photon double ionization of H_2 at 800 eV photon energy. All experimental data shown is limited to $KER = 19.4 \pm 0.3$ eV. (A,B) Projection of the electron sum momentum onto the direction of the molecular axis, as determined from the experimental results (A) or predicted by means of solving the TDSE (B) [149]. (C) Positions of the zeroth-order interference maxima $\cos \alpha_0$ as function of $\cos \beta$. All $\cos \alpha_0$ were obtained by means of Gaussian fits like in Fig. 12.4. The error bars include statistical and systematic errors, and the blue-shaded region indicates the systematical error (see footnote on p. 122 for details). The vertical scales are related through Eq. 6.18 with $R = 1.4$ au and $v_{ph}/c = 0.028$. The dashed black line shows the prediction of the time-delay model for $R = 1.4$ au (Eq. 6.15). The solid red line shows corresponding TDSE results [149].

Predicted by Toffoli and Decleva in 2006, the forward/backward asymmetry of photoelectron emission in the laboratory frame of reference is modified by molecular nondipole effects if the parity of the photoelectron is resolved [126]. Due to a similar origin, such modifications should reveal the same oscillating behavior as function of the photon energy like the Cohen-Fano interferences in the photoionization cross section [73]. The experimental confirmation requires measuring the angular distribution of an electron from photoionization of a homonuclear diatomic molecule over a wide photon energy range and also a method to distinguish between gerade and ungerade parity of the photoelectron.

The experimental results presented here were obtained in Run 3A, where we used molecular nitrogen as the target and single circularly polarized photons at energies between 880 eV and 2160 eV as projectiles. Our subject of investigation was *K*-shell photoionization followed by Auger decay and the symmetric fragmentation of the molecule into $N^+ + N^+$. The kinetic energies of the *K*-shell photoelectrons are approximately given by $E_P = E_\gamma - 410$ eV and the *K*-shell vacancies are filled under emission of an Auger electron at approximately $E_A = 370$ eV. The average internuclear distance of N_2 is 2.07 au in the neutral ground state and 2.04 au for N_2^+ with a *K*-shell vacancy [70].

We achieved full solid-angle acceptance in the laboratory frame of reference for the detection of ionic fragments and the Auger electrons, but the experimental setup allowed only a small acceptance angle for the considerably faster photoelectrons. For each data point contributing to the results of the present chapter, we have measured one electron momentum vector and reconstructed the other one by means of momentum conservation (see p. 68).

We have collected the highest amount of data at the photon energy of 1330 eV. Hence, the respective data set is often used exemplarily for the display of results throughout the present chapter. Compared to the previous results chapters, the present one has a more explorative character.

13.1 DISENTANGLING GERADE AND UNGERADE QUANTUM STATES

The set goal for the experiment on N_2 photoionization was to investigate the forward/backward asymmetries of K -shell photoelectron emission in the laboratory frame of reference as function of the photoelectron parity. The prerequisite for achieving this goal is an effective procedure to identify subsets of our experimental data where the photoelectron has a well-defined parity. There are two conceptually different ways of doing this. **(1)** Assuming that the double-slit model (Eqs. 6.6 & 6.7) is valid for fast photoelectron emission from N_2 , the gerade and ungerade contributions to the total electron wave can be resolved by restrictions on the photoelectron emission angle in the molecular reference frame, i.e.,

$$\cos \alpha_P = \hat{p}_P \cdot \hat{R}, \quad (13.1)$$

where p_P is the photoelectron momentum vector and \hat{R} is the orientation of the molecular axis. In the present section, however, we follow the second way. **(2)** As outlined in Refs. [84–86], the parity of the photoelectron is determined if the parities of the Auger electron and the N_2^{2+} state are identified.

The mixing of the two Auger electron parity states shapes the angular distribution, which we investigate in terms of the Auger electron emission angle in the molecular frame of reference, i.e.,

$$\cos \alpha_A = \hat{p}_A \cdot \hat{R}, \quad (13.2)$$

where p_A is the Auger electron momentum vector. As shown in Refs. [99, 173] for K -shell ionization of N_2 , the molecular frame Auger electron angular distribution also carries features of a double-slit-like interference pattern. But even without validity of the double-slit model for Auger electron emission, the gerade and ungerade Auger electron waves have opposite phases and it should be possible to find regions of $\cos \alpha_A$ where either one dominates (see, e.g., Fig. 3 K in Ref. [84]). The nature of the N_2^{2+} state determines the kinetic energy release of the fragmentation. However, the mapping of the overall KER distribution onto the N_2^{2+} final states is ambiguous due to the multitude of possible repulsive potential energy surfaces [174, 175]. In other words, the KER distribution of a certain N_2^{2+} state will most likely overlap with the distributions of other states (see, e.g., Fig. 3 B in Ref. [33] for the easier case of H_2^+ dissociation). Fortunately, we only care about the parity of the dicationic final state and it seems to be possible to find regions in the overall KER distribution where either parity dominates [71, 85].

Surprisingly, we could not rely on the KER and $\cos \alpha_A$ regions that were identified in previous works to determine the parity of the photoelectron [84–86], but we had to try to identify suitable subsets from our own measured data. Figure 13.1 A1 shows the angular distribution of the Auger electron in the molecular frame of reference as function of the kinetic energy release. As indicated by the coloured rectangles, we have identified four KER regions where the distribution of $\cos \alpha_A$ is largely isotropic. The projections of the data within the KER regions onto the horizontal axis are shown in Figs. 13.1 A3–A6, and the projection integrated over $KER = 6 - 12$ eV is shown in Fig. 13.1 A2. Figures 13.1 A1–A6 present the same results for the photoelectron angular distribution.

Electron emission perpendicular to the molecular axis must be a robust indicator for a gerade parity of the outgoing electron wave. Independent of the wavelength and the internuclear distance, the superposition of two in-phase waves—that originate coherently at the two atomic centers—has an interference maximum at $\cos \alpha = 0$. Vice versa, the superposition of any two coherent waves with opposite phases has an interference minimum at $\cos \alpha = 0$.

In Fig. 13.2 we present our experimental data in the same scheme as in Fig. 13.1, but here we have applied a condition on the coincidentally measured other electron of $\cos \alpha = \pm 0.1$. The gates are indicated in Figs. 13.1 A2 & B2 by the blue shaded regions. The condition \mathcal{E}_P on the photoelectron was applied for the display of Auger electrons in Figs. 13.2 A1–A6, while \mathcal{E}_A was applied on the Auger electrons for the display of photoelectrons in Figs. 13.2 B1–B6.

Disappointingly, there are no substantial differences between the results shown in Fig. 13.1 and Fig. 13.2. With a condition on Auger electron emission perpendicular to the molecular axis, we would have expected to reveal the structure of gerade or ungerade molecular-frame photoelectron angular distributions. Obviously, this is not the case and we must assume that the parity of the N_2^+ state cannot be resolved from the *KER* distribution in the present experiment. Accordingly, the photoelectron angular distributions shown in Fig. 13.2 still contain the superposition of gerade and ungerade contributions. As previous works have shown that the strategy to disentangle the parity states works at lower photon energies [84–86], we conclude that either the high photon energies and the large electron recoil momentum alter the fragmentation process or the resolution of the present setup was not sufficient.

We have tested the procedure that underlies Fig. 13.2 for virtually all reasonable restrictions on $\cos \alpha$ but did not find many substantial deviations compared to Fig. 13.1 in the structure of photo- or Auger electron angular distributions. One exception is shown in Fig. 13.3. Here, the restrictions on $\cos \alpha$ demand that the coincidentally measured other electron was emitted parallel to the molecular axis. The changes in the displayed electron angular distributions compared to Fig. 13.1 are clearly noticeable and most significant for the *KER* gate \mathcal{D} (6.85 – 7.2 eV). As suggested by the appearance of the central fringe at $\cos \alpha_P = 0$ in Fig. 13.3 B1, a gate on Auger electron emission parallel to the molecular axis apparently retrieves to some extent the gerade contribution to the molecular frame photoelectron angular distribution without further restrictions on the *KER*.

In Fig. 13.4 we show the correlation between photo- and Auger electron angular distributions in the molecular reference frame for the *KER* gate \mathcal{D} (6.85 – 7.2 eV). By investigating the correlation map in Fig. 13.4 C, we have identified the region of $\cos \alpha_A$ where the coincidentally detected photoelectron reveals the most distinct ungerade features. The resulting gerade and ungerade photoelectron angular distributions are shown in Fig. 13.4 A and compared to the respective double-slit models (Eqs. 6.6 & 6.7).

For the ungerade case, the overall agreement between model and experimental results is rather poor, but at least the positions of some interference minima and maxima coincide.

For the gerade case, the agreement is much better. Apparently, a gate on Auger electron emission parallel to the molecular axis is an effective way to select a subset of our experimental data where the photoelectron wave has mainly gerade parity. Additional confirmation for the validity of this procedure is shown in Fig. 13.5.

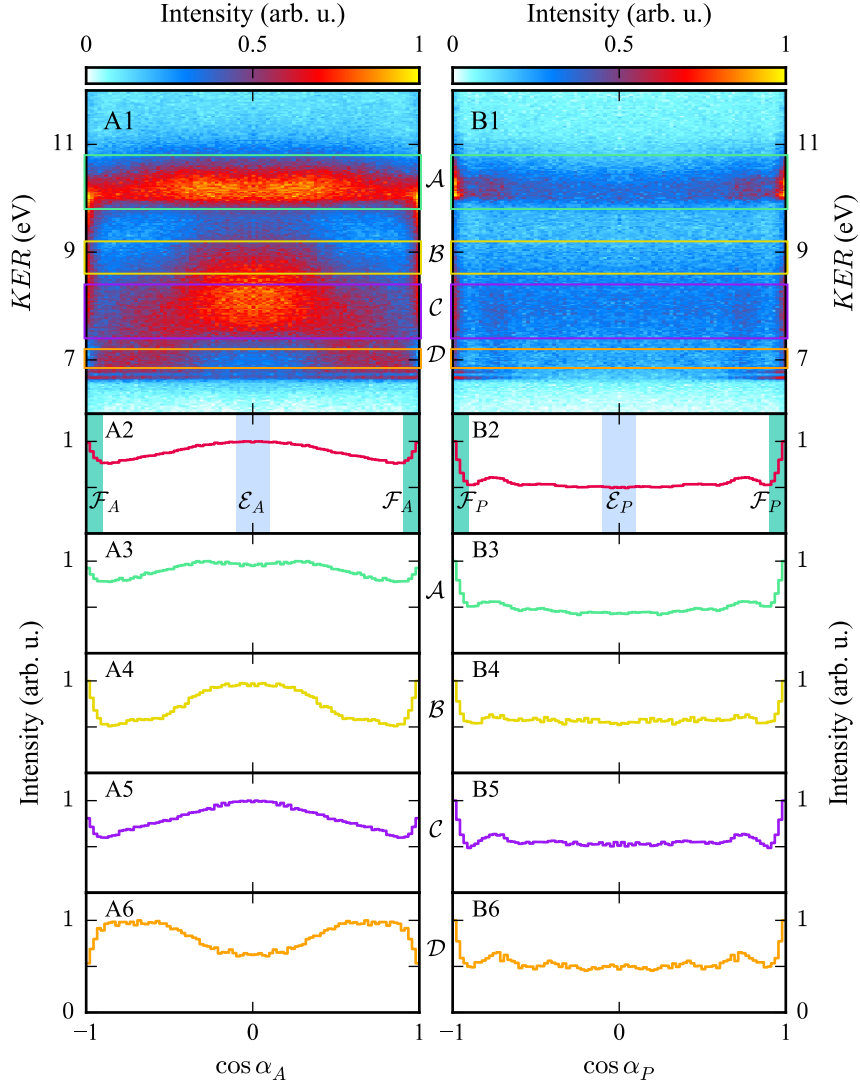


Figure 13.1: Molecular frame photo- and Auger electron angular distributions from K-shell ionization of N_2 at 1330 eV photon energy. (**A1–A6**) Auger electrons. (**B1–B6**) Photoelectrons. (**A1,B1**) Angular distributions as function of the kinetic energy release. KER gates: 9.8 – 10.8 eV (**A**, green), 8.6 – 9.2 eV (**B**, yellow), 7.4 – 8.4 eV (**C**, purple), 6.85 – 7.2 eV (**D**, orange). (**A2,B2**) Angular distributions for $KER = 6 - 12$ eV. Angle gates: $\cos \alpha = \pm 0.1$ (**E**, blue-shaded), $|\cos \alpha| > 0.9$ (**F**, green-shaded). (**A3–A6,B3–B6**) Angular distributions for the four KER gates.

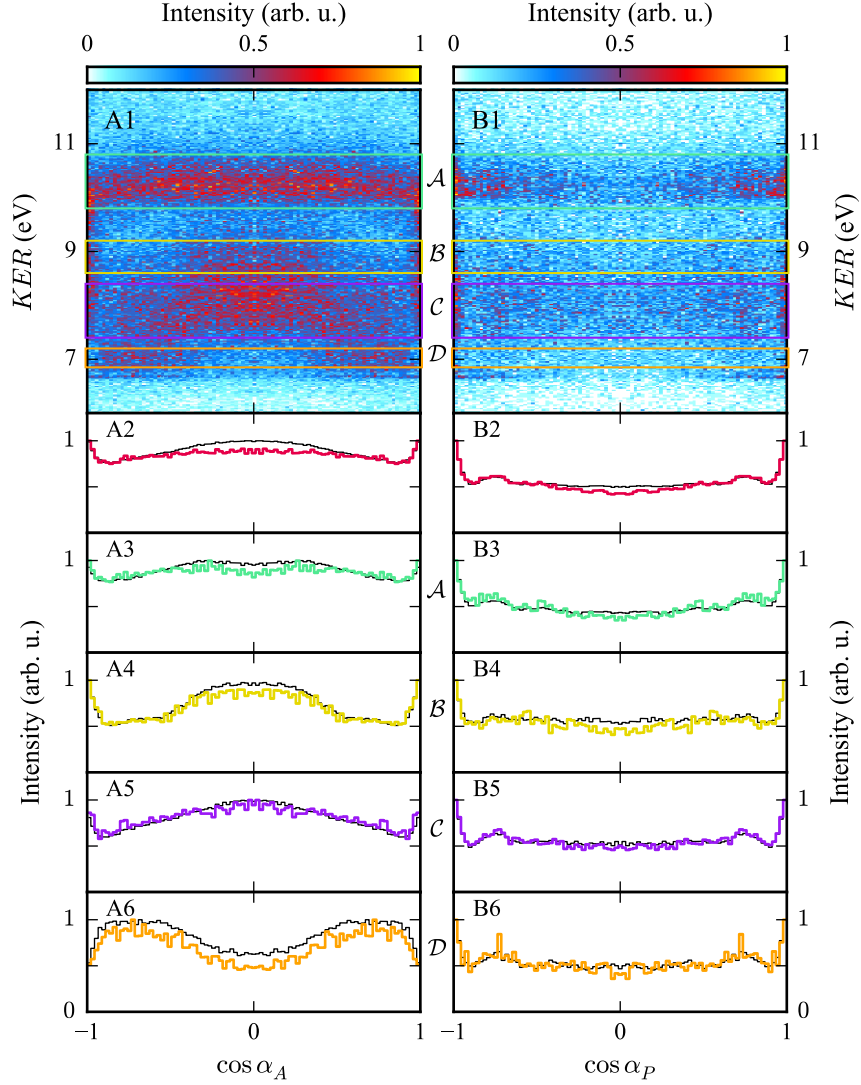


Figure 13.2: Molecular frame photo- and Auger electron angular distributions from K -shell ionization of N_2 at 1330 eV photon energy under the condition that the other electron is emitted **perpendicular** with respect to the molecular axis. **(A1–A6)** Distributions of Auger electrons for $\cos \alpha_P = \pm 0.1$ (\mathcal{E}_P). **(B1–B6)** Distributions of photoelectrons for $\cos \alpha_A = \pm 0.1$ (\mathcal{E}_A). The black lines in subfigures A2–A6 and B2–B6 show the respective data from Fig. 13.1 A2–A6 and B2–B6 for comparison. See Fig. 13.1 for all other details.

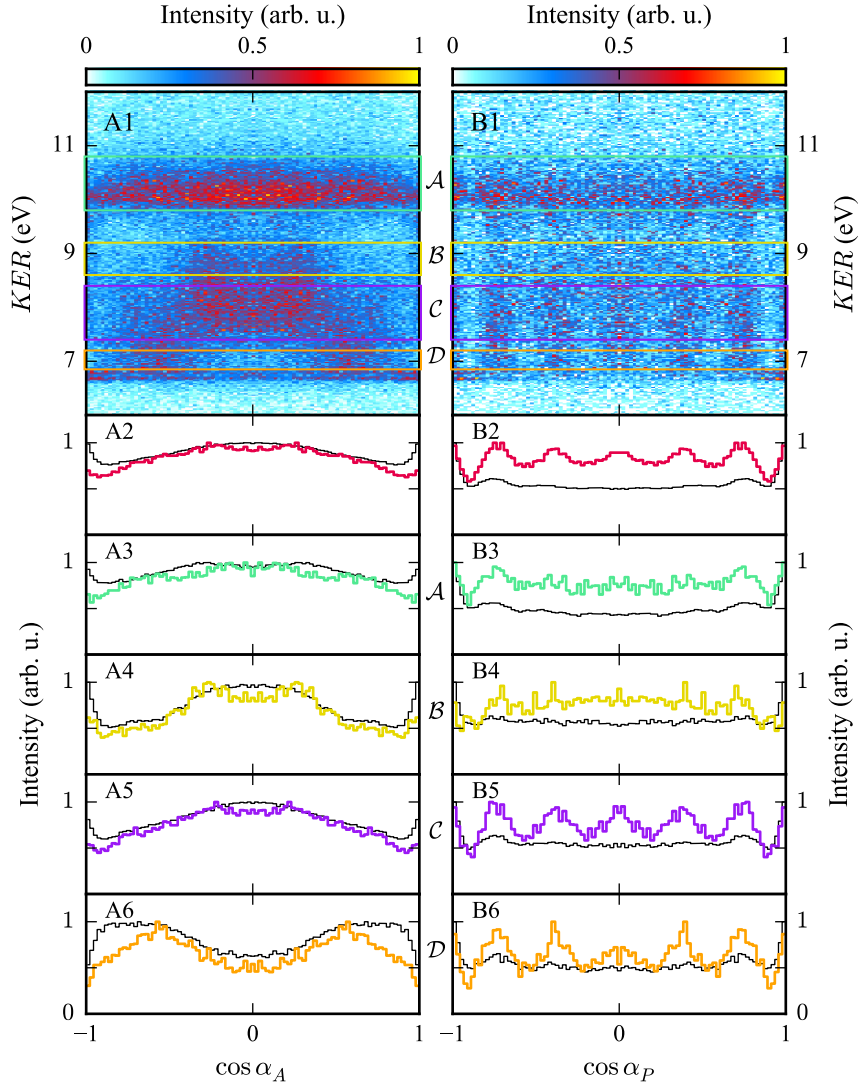


Figure 13.3: Molecular frame photo- and Auger electron angular distributions from K -shell ionization of N_2 at 1330 eV photon energy under the condition that the other electron is emitted **parallel** with respect to the molecular axis. **(A1–A6)** Distributions of Auger electrons for $|\cos \alpha_P| > 0.9$ (\mathcal{F}_P). **(B1–B6)** Distributions of photoelectrons for $|\cos \alpha_A| > 0.9$ (\mathcal{F}_A). The black lines in subfigures A2–A6 and B2–B6 show the respective data from Fig. 13.1 A2–A6 and B2–B6 for comparison. See Fig. 13.1 for all other details

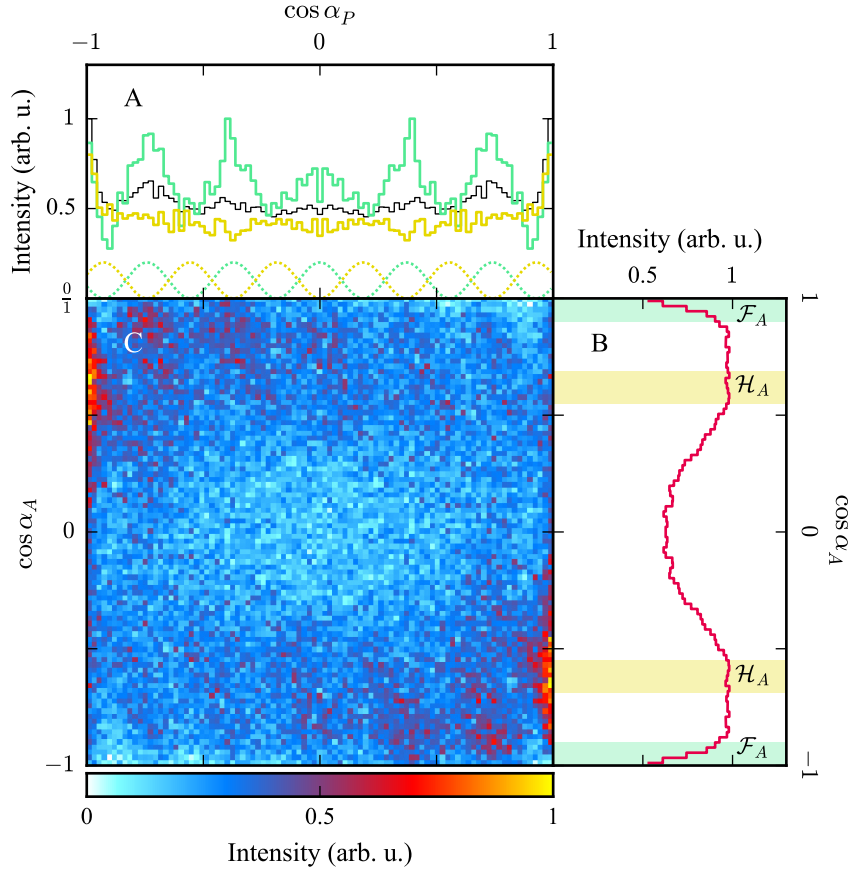


Figure 13.4: Interdependence of photo- and Auger electron angular distributions in the molecular reference frame from K -shell ionization of N_2 at 1330 eV photon energy under the condition of a low kinetic energy release ($KER = 6.85 - 7.2$ eV, \mathcal{D}). (A) Photoelectron angular distributions generated from different projections of the data in subfigure C onto the horizontal axis. Solid green line: $|\cos \alpha_A| > 0.9$ (\mathcal{F}_A , green-shaded region in subfigure B). Solid yellow line: $|\cos \alpha_A| = 0.55 \pm 0.07$ (\mathcal{H}_A , yellow-shaded region in subfigure B). Black line: integrated over the whole range of $\cos \alpha_A$ (same data as shown in Fig. 13.1 B6). Dotted green line: Double-slit interference for gerade photoelectrons (Eq. 6.6, $R = 2.07$ au, $p_p = 8.19$ au). Dotted yellow line: Double-slit interference for ungerade photoelectrons (Eq. 6.7). (B) Auger electron angular distribution generated from the projection of the data in subfigure C onto the vertical axis (integrated over the whole range of $\cos \alpha_p$, same data as shown in Fig. 13.1 A6). (C) $\cos \alpha_p$ as function of $\cos \alpha_A$.

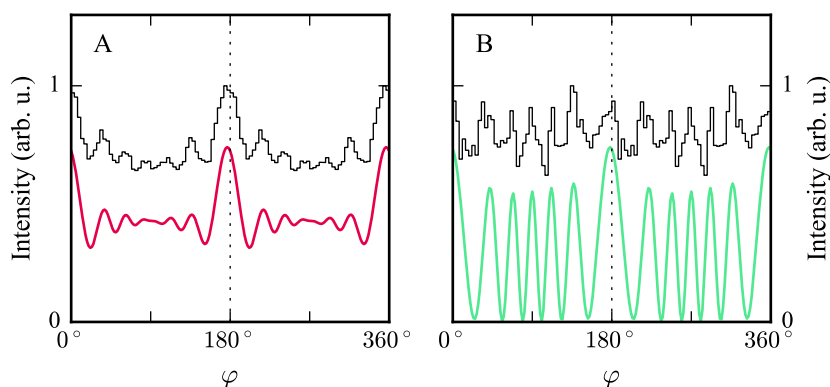


Figure 13.5: Molecular-frame photoelectron angular distribution in the polarization plane after K -shell photoionization of N_2 at 1330 eV photon energy (circular polarization) and subsequent Auger decay and dissociation into $N^+ + N^+$ (see Fig. B.1 for geometry and definition of φ). (A) All photoelectrons. The black line shows the experimental results (Conditions: $KER = 6.0 - 12.0$ eV, photoelectron measured directly and emitted inside polarization plane, i.e., $\cos \vartheta = 0 \pm 0.2$) and the red line presents corresponding theory predictions. (B) Gerade photoelectrons. The black line shows the experimental results with the additional condition that the coincidentally measured Auger electron was emitted parallel to the molecular axis ($|\cos \alpha_A| > 0.9$). The green line presents corresponding theory results for a gerade photoelectron parity. Both theory predictions were taken from Ref. [176] with the permission of P. Demekhin.

13.2 PARITY-RESOLVED NONDIPOLE EFFECTS

We assume that a molecular-frame photoelectron angular distribution that is asymmetric with respect to the light propagation direction (see, e.g., Fig. 12.4) influences the forward/backward asymmetry of photoelectron emission in the laboratory frame of reference (see Ch. 7 for further details). To observe this, the parity of the photoelectron has to be resolved because otherwise inverse effects cancel out each other. In the last section, we have identified a procedure that apparently results in a subset of experimental data which contains a surplus of gerade photoelectrons. In the present section, we use this procedure to test the above assumption.

Our experimental results are compared to calculations by D. Toffoli and P. Decleva [126].

The forward/backward asymmetry of photoelectron emission in the laboratory frame of reference can be specified in terms of the two nondipole parameters δ and γ that appear in Eq. 4.25. Here, we do not care about the total photoionization cross section, but only about the parameters that shape the photoelectron angular distribution. Accordingly, we rewrite Eq. 4.25 as

$$\frac{d\sigma}{d\vartheta_\gamma} \propto 1 - \beta \frac{3 \cos^2 \vartheta_\gamma - 1}{4} + \left(\frac{\gamma}{2} \sin^2 \vartheta_\gamma + \delta \right) \cos \vartheta_\gamma \quad (13.3)$$

for the purpose of the present section. The two nondipole parameters characterize the interferences between the electric quadrupole (γ) or the magnetic dipole (δ) with the electric dipole amplitude. Both parameters break the forward/backward symmetry of the angular distribution if their values are nonzero (see Fig. 4.4 for exemplary photoelectron angular distributions).

In Ref. [126], the authors calculated the angular distributions of *K*-shell photoelectrons from one-photon ionization of N_2 and subsequently determined the three parameters of Eq. 13.3 from their results. These calculations differentiated between gerade (*g*) and ungerade (*u*) photoelectrons and allowed to determine the parameters for each case individually. The corresponding results are shown in Tab. 13.1 for the set of photon energies which we have used in our experiment.

The combined results of our study are presented in Fig. 13.6. Subfigure A shows the nondipole parameter γ of *K*-shell photoelectrons from one-photon ionization of N_2 as function of the photon energy. The solid lines represent the results of the calculation from Ref. [126] for all photoelectrons (red) and the gerade (green) or ungerade (blue) contribution.

Subfigures B1–D3 exemplarily show how the experimental results for γ were obtained at the photon energies of 1330 eV, 1510 eV, and 1720 eV. As the procedure to identify gerade photoelectrons seemed most effective for the two *KER* gates *C* and *D* ($KER = 6.85 - 7.2$ eV & $KER = 7.4 - 8.4$ eV, see Fig. 13.1), we have limited all the experimental data that contributed to the results shown in Fig. 13.6 to these two *KER* regions.¹ Subfigures B1–D1 show the photoelectron angular distribution as function of the angle enclosed by the photoelectron momentum vector and the light propagation direction for all photo- and Auger electron emission angles in the molecular frame of reference. The red lines show the measured data and the black lines represent the fit of Eq. 13.3 to the data. The parameters β_{av} and γ_{av} that resulted from the fit are shown in Tab. 13.1 and γ_{av} is plotted in Fig. 13.6 A (red dots).

¹We have identified a small dependence of γ on the *KER* in the experimental data. This is most likely due to the correction routine described in Sec. 9.3.2 which is—in the way applied here—most accurate at low *KER*. By limiting the *KER* to the same regions for all results shown in Fig. 13.6, we prevent that a possible *KER*-dependence of γ contaminates the results.

Note that the magnetic dipole term of the transition amplitude vanishes for initial s -states. Accordingly, δ is expected to be zero for photoelectrons that originate from the K -shell. The calculations of Ref. [126] yielded that $\delta \approx 0$ for all relevant photon energies and when we fitted Eq. 13.3 to the experimental results, δ was always set to zero.

The solid purple lines in Figs. 13.6 B₃–D₃ show the molecular-frame photoelectron angular distributions under the condition that the coincidentally measured Auger electron was emitted parallel to the molecular axis ($|\cos \alpha_A| > 0.9$). The dotted lines indicate double-slit interference for gerade (green) and ungerade (yellow) photoelectrons. The comparison between measured data and model predictions underlines once more that the photoelectron has apparently gerade parity. To further remove contributions of ungerade photoelectrons from the subsets of data shown in subfigures B₃–D₃, we have applied restrictions on $\cos \alpha_P$ around the positions of the zeroth, first, and second order interference maxima—as indicated by the green-shaded regions. For the resulting subsets, the green lines in subfigures B₂–D₂ show the photoelectron angular distribution as function of $\cos \vartheta_\gamma$ and the black lines represent the fit of Eq. 13.3 to the data. The parameters β_g and γ_g that resulted from the fit are shown in Tab. 13.1 and γ_g is plotted in Fig. 13.6 A (green dots).

According to the qualitative explanation in Ch. 7 and the predictions of Ref. [126], the measured nondipole parameter γ_g should oscillate around the average parameter γ_{av} and follow the solid green line. Apparently, this is not the case. We have intensively tried to find the reason for this disagreement but have not succeeded so far.

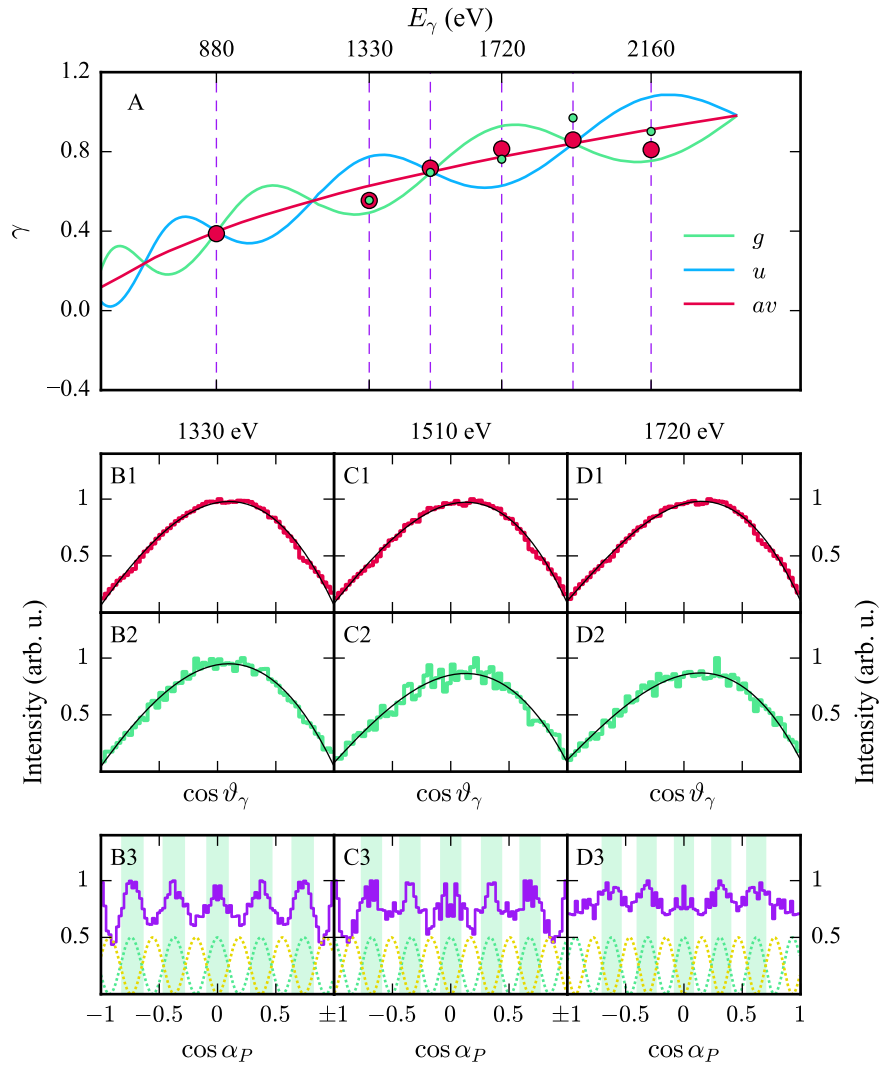


Figure 13.6: K -shell photoelectron angular distributions from one-photon ionization of N_2 . See text for details.

E_γ [eV]	880	1330	1510	1720	1930	2160
β_{av}	1.96	1.98	1.99	1.99	1.99	1.99
δ_{av}	0.0014	0.0011	0.0009	0.0008	0.0007	0.0006
[126] γ_{av}	0.397	0.628	0.698	0.774	0.842	0.912
γ_g	0.394	0.492	0.694	0.929	0.842	0.754
γ_u	0.4	0.775	0.702	0.629	0.841	1.076
δ	$\stackrel{!}{=} 0$	$\stackrel{!}{=} 0$	$\stackrel{!}{=} 0$	$\stackrel{!}{=} 0$	$\stackrel{!}{=} 0$	$\stackrel{!}{=} 0$
Exp. β_{av}	1.60 ± 0.01	1.81 ± 0.01	1.75 ± 0.01	1.70 ± 0.01	1.67 ± 0.01	1.68 ± 0.01
γ_{av}	0.39 ± 0.05	0.55 ± 0.05	0.72 ± 0.05	0.81 ± 0.04	0.86 ± 0.04	0.81 ± 0.04
β_g		1.86 ± 0.02	1.73 ± 0.03	1.65 ± 0.02	1.70 ± 0.02	1.65 ± 0.02
γ_g		0.56 ± 0.08	0.73 ± 0.13	0.76 ± 0.10	0.97 ± 0.13	0.90 ± 0.13

Table 13.1: Parameters that shape the photoelectron angular distribution in the laboratory frame of reference as used in Eq. 13.3. The experimental values have been determined by means of a fit of Eq. 13.3 to the data. The errors indicate only the square roots of the respective diagonal elements of the covariance matrix from the fitting routine.

13.3 DISCUSSION

Although we had partial success in identifying photoelectrons of mainly gerade parity, the results shown in the present chapter did not meet our expectations and raise numerous questions. The following list contains some issues that require further investigations.

- We cannot explain yet why the procedure used in Refs. [84–86] to disentangle gerade and ungerade photoelectrons did not work for our experimental data. A possible reason is that the previous works measured at photon energies relatively close above the *K*-shell ionization threshold where the energy splitting (see p. 30) between the parity states could have caused a different weighting of the contributions to the total photoelectron wave.
- Electron emission perpendicular to the molecular axis must be an indicator for a gerade parity of the outgoing electron wave and we do not understand why there is no substantial difference between the data shown in Figs. 13.1 & 13.2.
- Our measured *KER* distributions (see Fig. C.17 C) resemble those measured in the previous works (see, e.g., Fig. 8 in Ref. [86]). With a suitable gate on the emission angle of the photo- or Auger electron in the molecular frame, we should see regions in the *KER* distribution where either parity of the N_2^{2+} state dominates (see, e.g., Fig. 2 in Ref. [85]). But as shown in Fig. 13.3 B1, the parity of the N_2^{2+} state appears to be constant over the whole *KER* range.
- A condition on Auger electron emission parallel to the molecular axis seems to produce a subset of data where the contribution of gerade photoelectrons is enhanced. This works particularly well for low *KER* regions (see Fig. 13.3 B5 & B6), but also for a *KER* between 6.0 eV and 12.0 eV (see Fig. 13.5). According to the qualitative explanation in Ch. 7 and the predictions of Ref. [126], the nondipole parameter γ_g for this subset of data should oscillate around the average parameter γ_{av} . This could not yet be observed in our experimental results.

To resolve these outstanding issues, we propose a joint experimental and theoretical study of nondipolar photoionization of N_2 which has not been initiated in the course of the present work. A collaboration of this type has been very successful in the past and produced the results of Refs. [84–86].

Part IV

CONCLUSION

SUMMARY

We have investigated nondipolar photoionization of He, H₂, and N₂ with a COLTRIMS reaction microscope and compared the experimental results to various theoretical predictions. Here, nondipolar photoionization describes photoionization at high photon energies where the effects of the linear photon momentum (p_γ) and the spatially-dependent electromagnetic field are not negligible and become observable in the final-state momentum distributions of the reaction fragments.

In Ch. 10 we focused on the forward/backward asymmetries in light propagation direction of the momentum distributions from one-photon single and double ionization of He between 300 eV and 1775 eV photon energy. For double ionization of He, we showed that the photoelectron receives a large average forward shift of $8/5 \times p_\gamma$. The corresponding recoil momentum onto the He nucleus overcompensates the linear photon momentum transfer—which is imprinted onto the center of mass—and the nucleus is attracted towards the light source with an average momentum of $-3/5 \times p_\gamma$. Our results experimentally confirmed the 90-year-old counterintuitive prediction by A. Sommerfeld and G. Schur of backward-directed ions created by light that exerts a forward-directed radiation pressure [151]. Furthermore, we showed for He double ionization that the two electrons share the forward momentum shift of $8/5 \times p_\gamma$ proportional to their share of the excess energy. Our experimental results on He single and double ionization are in excellent agreement with TDSE calculations.

In Ch. 11 we investigated the quasifree mechanism (QFM) of He and H₂ double ionization. The QFM has a distinct fingerprint in the final-state momentum distribution of the reaction fragments. The two electrons are emitted back-to-back with equal kinetic energy and the recoil momentum vanishes accordingly. This pattern is forbidden in dipolar photoionization and the QFM is hence a pure quadrupole effect. We found the QFM fingerprint for He and H₂ double ionization and showed that in this special case the linear photon momentum is not imprinted onto the He⁺⁺ ion or the H₂⁺⁺ intermediate state. Furthermore, we introduced how the QFM cross section may be used to probe the correlated structure of a two-electron wave function.

Chapter 12 dealt with the molecular double-slit experiment, i.e., with photoelectron emission from H₂ viewed within the molecular frame of reference. First, we recapitulated some findings of previous studies concerning decoherence and entanglement between the two electrons in double ionization of H₂ with our results at 800 eV photon energy and we reestablished the double-slit analogy for the emission of a fast electron in double ionization of H₂. Then we focused on the nondipolar corrections to the molecular double-slit experiment that manifest in an asymmetry of the interference pattern that changes depending on the angle enclosed by the molecular axis and the light propagation direction. The cause of this asymmetry is that the two contributions to the total photoelectron wave, that originate from the two protons, start with different phases. As discussed in Sec. 6.2, there are several related physical pictures that can explain this phase difference and for the interpretation of our experimental results we chose the concept of the *birth time delay*. In this picture, a wavefront of constant phase sweeps across the molecule

and releases the two contributions to the total photoelectron wave upon arrival at each atomic center. We tested the corresponding model predictions against our experimental results for fast electron emission and found that the model underestimates the experiment. However, when we used the sum momentum of the two electrons instead of the momentum of one fast electron for the comparison, the model predictions and the experimental results agreed eventually.

The travel time of light to cover the average bond length of molecular hydrogen is 247 zs (1 zeptosecond = 1×10^{-21} s) and by measuring the birth time delay between the emission of two waves from the two centers of H₂ we have (arguably) conducted a very fast time measurement.

In Ch. 13 we tried to resolve the parity of the photoelectron in *K*-shell ionization of N₂ to observe modifications of the forward/backward asymmetry of photoelectron emission in the laboratory frame due to molecular nondipole effects. While we apparently succeeded in isolating photoelectrons of gerade parity, we could unfortunately not confirm the predictions of the oscillating behavior of the nondipole parameter as function of the photon energy. This disagreement between expectations and experimental results requires further investigations and provides an opportunity for future studies of this type.

OUTLOOK

The present thesis constitutes a comprehensive experimental work on nondipolar photoionization. With our studies on one-photon single and double ionization of He and H₂, we have shown extensively how the photon momentum and the spatially-dependent light field affect the photoionization process. However, many interesting parts remain undiscovered or unclear in this area of research. The following list contains some suggestions for future studies of this type.

- Our studies dealt with *K*-shell photoionization of atoms and molecules. Future works could extend the study of nondipole asymmetries to different atomic and molecular orbitals.
- Our molecular targets, H₂ and N₂, were rather simple homonuclear diatomic molecules. In a first step, future experimental nondipole studies with a reaction microscope could focus on a heteronuclear diatomic molecule like carbon monoxide [177]. Due to the localization of the electron in its initial state at the carbon or the oxygen atom, the photoelectron wave emerges from a well-defined site in the molecule and it is subsequently scattered at the opposite atomic center. Later, even more complex molecules like sulfur hexafluoride could be investigated likewise [178]. The interplay of nondipole effects and the scattering process should yield interesting modifications of the molecular-frame photoelectron angular distributions.
- The experimental results of our birth time delay measurement suggest a slightly larger initial phase shift than the simple model and TDSE calculations predict. While model and calculations are within the systematic error range of the experimental results, we cannot be ultimately certain that there is no further additional phase shift in nature that the experiment has uncovered. Hence, it may be desirable to repeat the experiment with higher accuracy—e.g., at the newly constructed reaction microscope at PIPE [179]. Furthermore, a new experiment could aim for a higher photoelectron energy or internuclear distance (see Fig. 6.9 for the motivation).
- Our effort to observe parity-resolved nondipole effects in the laboratory frame of reference for photoionization of N₂ did not succeed and raised some issues that require further investigations (see Sec. 13.3).
- Photoelectron circular dichroism (PECD) is another cause of a forward/backward asymmetry of electron emission with respect to the light propagation direction. The effect occurs in photoionization of randomly oriented chiral molecules with circularly polarized light (see, e.g., Ref. [180] for a comprehensive work on circular dichroism). Here, the chiral structure of the molecule acts as a gearbox, which translates the rotation of the electric field vector into a linear forward or backward motion of the emitted electron [79]. As a future research topic, we suggest to study the interplay of PECD and asymmetries induced by nondipole effects.

Part V

APPENDIX

POLAR PLOTS AND THE POLE BIAS

Let us assume that the world population is uniformly distributed across the surface of the earth, i.e., in each square kilometer on the globe live the same amount of people (and not just on land). This situation is illustrated in Fig. A.1 where each green dot represents 1 million people.

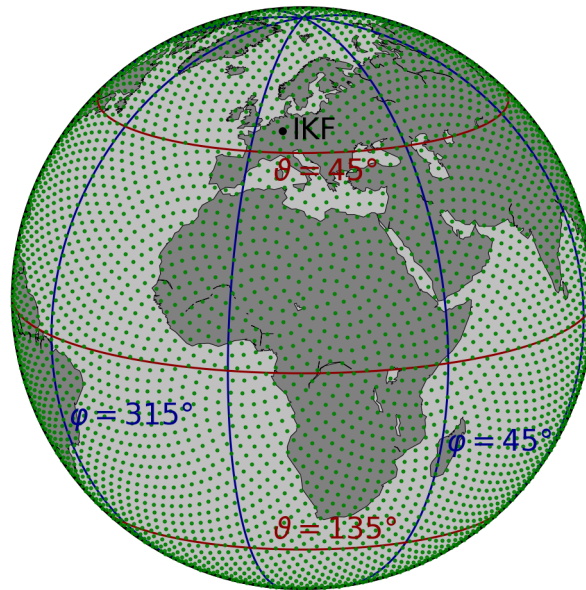


Figure A.1: Illustration of a uniform population distribution on earth. Each green dot represents 1 million people. The dots are placed on a spherical fibonacci lattice.

The position of a point on a sphere is commonly specified by two angles within a spherical coordinate system. Here, the radial coordinate is constant because all points lie on the surface and the center of the sphere is chosen as the origin of the coordinate system. To establish the angular references, one needs to specify a *polar axis* that passes through the origin. This axis can be chosen freely but it is helpful to use a meaningful axis (e.g., the axis of rotation). The *polar angle* ϑ of a point on the sphere is enclosed by the polar axis and the vector pointing from the center of the sphere to the point's position (*position vector*). The polar angle ranges from 0° to 180° and it equals 0° for parallel orientation of position vector and polar axis. Next, the *equatorial plane* is defined as the plane perpendicular to the polar axis that contains the center of the sphere. The equatorial plane contains the *azimuthal reference*, a vector that points from the origin to a (relevant) position on the surface. The *azimuthal angle* φ is the angle enclosed by the azimuthal reference and the projection of the position vector onto the equatorial plane. The azimuthal angle ranges from 0° to 360° and the sense of rotation is usually defined by the right-hand rule with the thumb pointing along the polar axis.

In the geographic coordinate system charted in Fig. A.1, the polar axis points from the geographic south pole to the geographic north pole and the projection of the position vector of the Royal Greenwich Observatory in London onto the equatorial plane serves as the azimuthal reference. Note that lines on a globe where the polar angle is constant are called *parallels* (red lines in Fig. A.1) while lines of

constant azimuthal angle are *meridians* (blue lines in Fig. A.1). The intersection of the equatorial plane and the sphere's surface is the longest parallel and called *equator*.

Let us now examine the uniform distribution of people on earth as function of the polar and azimuthal angles. For that purpose, we divide the range of each angle into a series of bins and count how many people fall into each bin. The result is shown in the two histograms in Fig. A.2 where the width of each bin is 10° (*uniform binning method*).

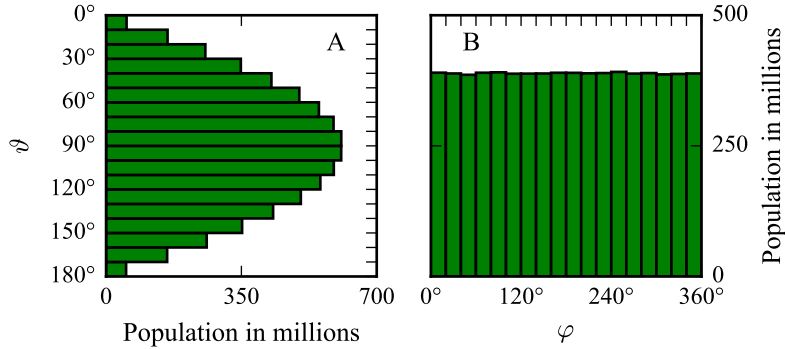


Figure A.2: Hypothetical world population as function of the polar angle θ (A) and the azimuthal angle φ (B).

As one would expect from the uniform distribution of population on the globe, Fig. A.2 B shows an uniform distribution as function of the azimuthal angle. On the other hand, Fig. A.2 A may come as a surprise, because it suggests that less people live at the poles than around the equator despite the uniform population distribution.

The representation of data as function of a polar angle in a histogram is subject to the *pole bias*. The reason for this bias, in technical terms, is that the volume element in a spherical coordinate system depends on the polar angle, but it is independent of the azimuthal angle:

$$d^3r = r^2 \sin \theta \, dr \, d\theta \, d\varphi. \quad (\text{A.1})$$

A closely related statement, that might be easier to grasp, is that parallels differ in length but all meridians have the same length. Hence, the area enclosed by parallels that are uniformly spaced over the polar angle is a function of the polar angle itself. For example, if one counts people living close to the north pole where $\theta = 5^\circ \pm 5^\circ$, the search area is small compared to the area around the equator enclosed by $\theta = 90^\circ \pm 5^\circ$.

It is very important to note that Fig. A.2 A is a correct representation of the data. However, it is sometimes desirable to adjust for the pole bias to obtain a more intuitive representation. There are two common ways to do this: (1) One can divide the count of each bin by the sine of each bin's center $\sin(\theta_c)$. (2) Instead of presenting the distribution as function of θ , display it as function of $\cos(\theta)$. Both options are presented in Fig. A.3 and both show a uniform distribution.

The division by $\sin(\theta_c)$ in Fig. A.3 A corrects for the fact that each bin in Fig. A.2 A corresponds to a different surface area on the globe. On the other hand, a uniform distribution of bins over the range of $\cos(\theta)$ instead of θ entails that each bin in Fig. A.3 B corresponds to the same surface area (*cosine binning method*). The different angular widths of the two binning methods are compared in Fig. A.4 and drawn on the globe in Fig. A.5.

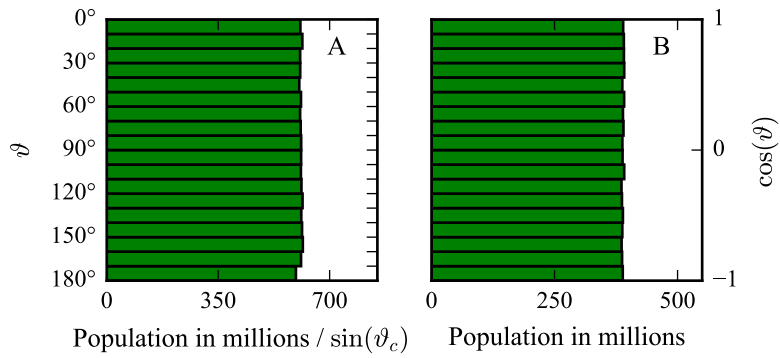


Figure A.3: Adjusting for the pole bias: (A) Each bin count is divided by the sine of the bin center $\sin(\theta_c)$. (B) Bins are equally spaced over the range of $\cos(\theta)$. Both representations suggest a uniform distribution of population over the polar angle.

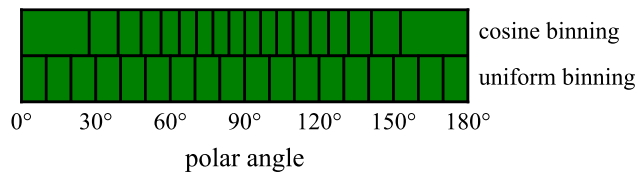


Figure A.4: Comparison of the angular widths of the two binning methods.

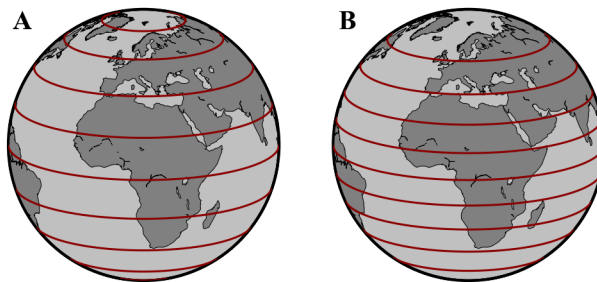


Figure A.5: Comparison of the uniform binning method (A) and the cosine binning method (B) for the range of the polar angle. In B, all areas separated by the parallels have the same surface area.

The distribution of data as function of an angle is commonly presented in a *polar plot*. Accordingly, Fig. A.6 presents the hypothetical world population as function of the polar angle in a polar plot using the uniform binning method (A) and the cosine binning method (B). Arguably, Fig. A.6 B is the more appropriate representation of the data.

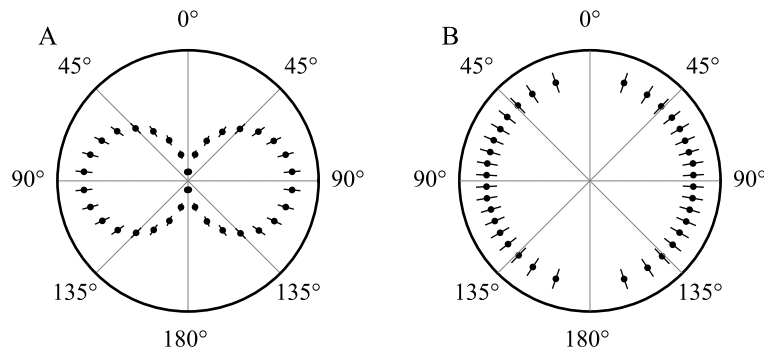


Figure A.6: Polar plots of the hypothetical world population as function of the polar angle ϑ using the uniform binning method (A) and the cosine binning method (B).

Some common practices are applied in Fig. A.6 concerning the use of polar plots in general and polar plots as function of a polar angle in particular: The displayed figures are histograms but the bar-chart design is replaced by data points indicating the center of each bin where the bin count is mapped onto the distance between data point and origin. As the polar angle ranges from 0° to 180° only, the corresponding distribution is mirrored at the axis between 0° and 180° for aesthetic purposes. Sometimes there is no radial grid indicating the bin count of a datapoint but the length of each errorbar equals the square root of the respective bin count. The angular width of each bin can be recognized from the angular distance between datapoints. A constant angular distance indicates the uniform binning method (Fig. A.6 A). Without explicit mention, the cosine binning method is usually used in polar plots that show data as function of a polar angle. However, this can be easily recognized by the varying angular distance between the datapoints (Fig. A.6 B).¹

The display of experimental data as function of spherical coordinates is subject to the same distortion as the above example. If you want to plot a histogram of data as function of an angle, determine first if this angle is a polar or an azimuthal angle and then choose the appropriate representation. **For the present work, I have always used the cosine binning method when experimental data is shown as function of a polar angle.**

¹Failure to comply with the common practices may result in the following response from your supervisor: "Für alle Polarplots: Kannst du bitte Datenpunkte mit Fehlerbalken verwenden. Die Fehlerbalken sind wichtig und die Farben finde ich völlig sinnlos. In einer Veröffentlichung geht das nicht, in einer Masterarbeit sieht es sehr eigenwillig aus, ich würde nachdrücklich davon abraten."

Although less important for the present work, let us briefly discuss the implications of the r^2 -dependence of the volume element in spherical coordinates (Eq. A.1). We assume a uniform distribution of particles inside the volume of a unit sphere and show this distribution of particles as function of the radius r as a histogram in Fig. A.7 A. As bins at smaller r correspond to a smaller volume than bins at higher r , the representation of the distribution in the histogram is biased accordingly. As shown in Fig. A.7 B, one can adjust for this bias by dividing the count of each bin by the value of each bin's center r_c .

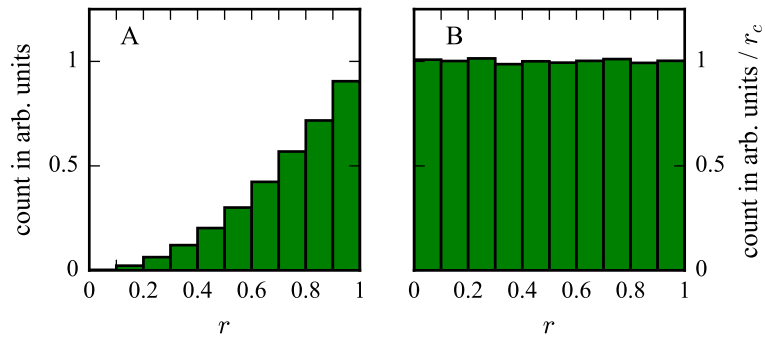


Figure A.7: Hypothetical world population as function of the polar angle ϑ (A) and the azimuthal angle φ (B).

A molecular-frame photoelectron angular distribution characterizes the probability of photoelectron emission as function of angles defined in the body-fixed coordinate system of the molecule. Unfortunately, there is no standardized method on how to establish the coordinate system and the comparison is not always straightforward. In each specific case, particular attention must be paid on how the angles are defined.

For diatomic molecules, the molecular axis provides a natural choice for one reference axis. However, the diatomic (or any linear) molecule specifies no further direction in space, which is necessary in order to establish a three-dimensional coordinate system. One of the axes of the laboratory frame can function as such, as long as it is linearly independent of the molecular axis.

The spherical coordinates ϑ and φ , that are shown in Fig. B.1, are commonly used to present a MFPAD. Here, the photon propagation direction (\hat{x}) is chosen as the polar axis and the projection of the molecular axis (\mathbf{R}) onto the equatorial plane serves as the azimuthal reference. Additionally, in order to establish an explicit reference of the polar angle ϑ to the molecular axis, the polar angle β , that is enclosed by \mathbf{R} and \hat{x} , has to be fixed. To that end, the molecular axis is often kept close to the polarization plane ($\beta \approx 90^\circ$). One example of a MFPAD as function of ϑ and φ is shown in Fig. B.3 A.

For circularly and randomly polarized light, the laboratory-frame photoelectron angular distribution depends on the angle ϑ alone (see Eq. 4.22, $\vartheta = \vartheta_\gamma$ therein). Accordingly, a MFPAD as function of φ —after integration over a relevant region of ϑ —does not resolve the anisotropy of the angle-differential cross section in the lab frame (see Ch. 4) and exhibits mainly molecular effects. An example is shown in Fig. B.1 B. Note that circularly polarized light encodes its sense of rotation in the phase of the emerging photoelectron wave, which affects the appearance of the MFPAD as function of φ [79].

Another option to examine the photoelectron angular distribution in the molecular frame is to analyse the MFPAD as function of the angle enclosed by molecular axis and photoelectron momentum vector. In the present work, we label this polar angle as α and it is shown in Fig. B.2.

An example of an MFPAD as function of α is shown in Fig. B.4. Here, the laboratory-frame photoelectron angular distribution envelopes the molecular contribution.

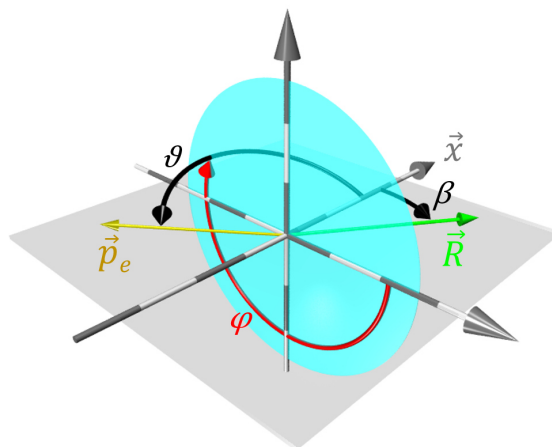


Figure B.1: Spherical coordinate system defined by the light direction (x , polar axis) and the projection of the molecular axis (R , green, azimuthal reference) onto the equatorial plane (blue). To unambiguously identify the orientation of the photoelectron vector (p_e , yellow) relative to the molecular axis through ϑ and φ , the angle β needs to be fixed.

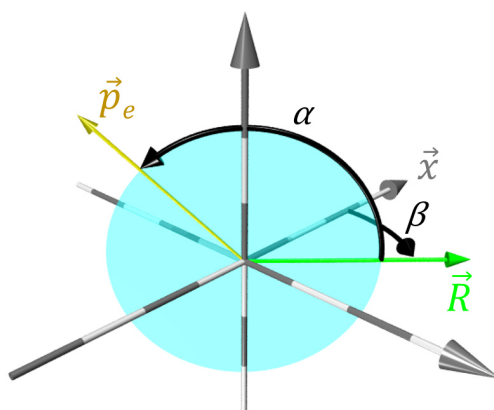


Figure B.2: The orientation of the photoelectron vector (p_e , yellow) relative to the molecular axis (R , green) is unambiguously defined by the polar angle α . R and p_e define a plane (blue). Here, α is defined as the smaller one of the two angles enclosed by R and p_e .

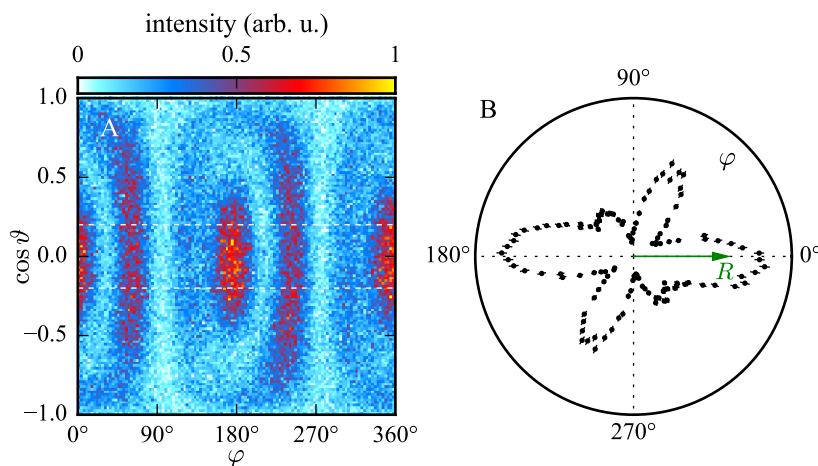


Figure B.3: Molecular-frame photoelectron angular distribution (MFPAD) after K -shell photoionization of N_2 at 420 eV photon energy (circular polarization) and subsequent dissociation into $N^+ + N^+$. The energy of the photoelectron is around 10 eV, the kinetic energy release is fixed between 6.5 and 20 eV, and the molecular axis encloses an angle with the light propagation direction of $90^\circ \pm 15^\circ$. The presented data was recorded during the commissioning of the new stationary reaction microscope at beamline Po4 (PETRA III, DESY, Hamburg) in March 2021. (A) The angles φ and ϑ are defined as shown in Fig. B.1. The cosine binning method was used to display the dependence of the MFPAD on the polar angle ϑ (see App. A). (B) MFPAD as function of the azimuthal angle φ after integration over $\cos \vartheta = 0 \pm 0.2$ (area enclosed by the dashed white lines in A). Accordingly, molecular axis and photoelectron vector lie in or close to the polarization plane. Here, the photoelectron emission probability in the laboratory frame is isotropic and molecular effects become particularly evident. The physical interpretation of the shown data can be found in Ref. [181].

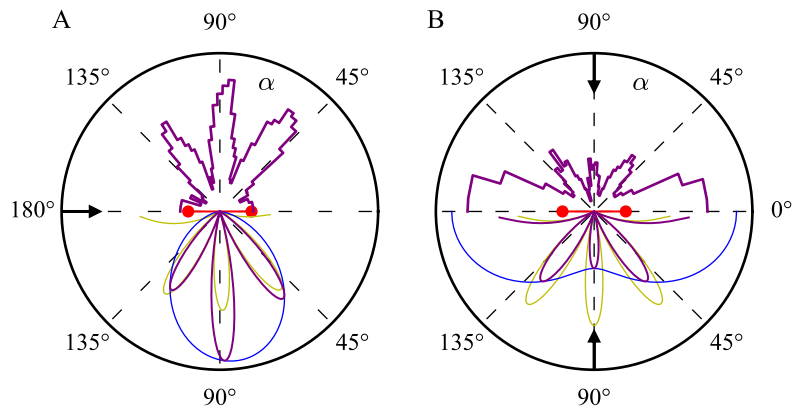


Figure B.4: Upper hemispheres: Measured molecular-frame photoelectron angular distributions of fast electrons ($E_e = 735 \pm 15$ eV) from one-photon double ionization of H_2 by 800 eV circularly polarized photons for the average internuclear distance of $R = 1.4 \pm 0.04$ au and different orientations between molecular axis and light propagation direction. (A) Parallel alignment ($\cos \beta > 0.87$) between light propagation (black arrow) and molecule (red barbell). (B) Perpendicular alignment between light propagation and molecular axis ($\cos \beta = 0 \pm 0.065$). Lower hemispheres, yellow lines: Double-slit interference patterns with nondipole corrections (Eq. 6.14) for $R = 1.4$ au and $\lambda = 0.85$ au (average de Broglie wavelength of the fast electron). Blue lines: Laboratory-frame photoelectron angular distributions transformed into the two-dimensional molecular frame of reference for the respective orientation of the molecule. Note that in panel B, the light impinges from any direction perpendicular to the molecule. Purple lines: Superposition of the double-slit interference pattern and the laboratory-frame envelope. The differences between the model and the measured data are most likely due to the integration over $\cos \beta$ that are necessary for the display of the experimental results. Figure taken from the supplementary material of Ref. [148].

Run 1A (Helium at 800 eV photon energy)
Measured ion momentum

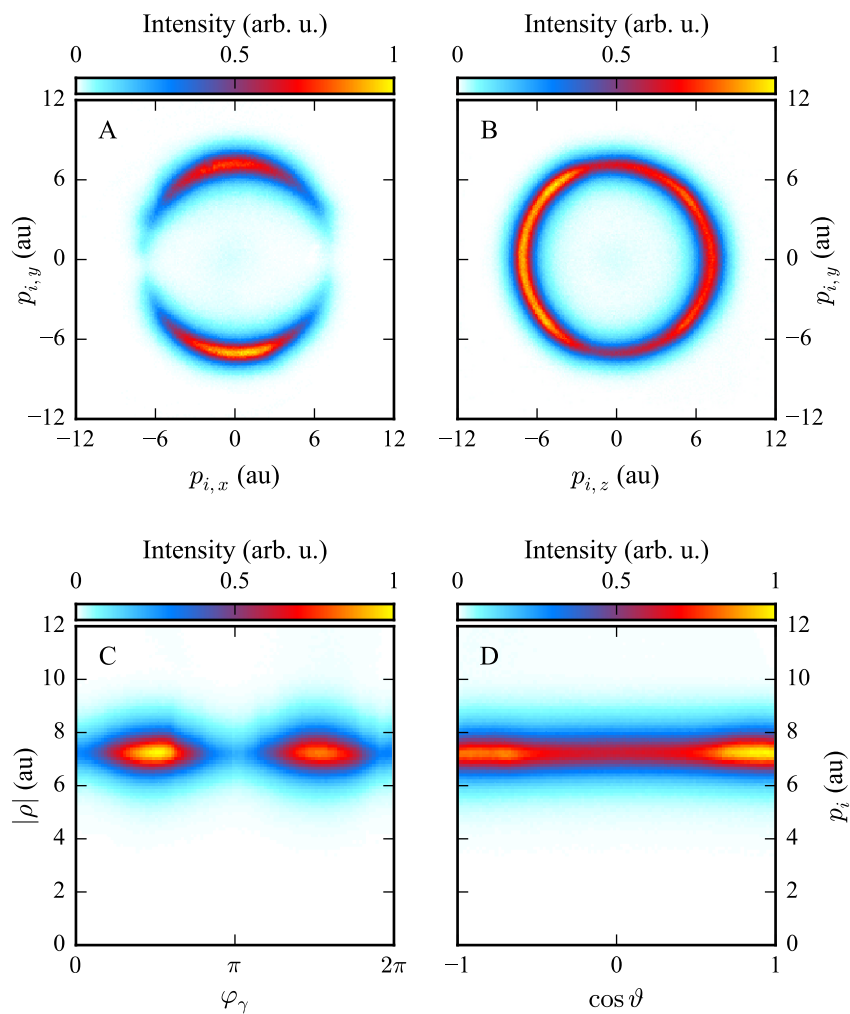


Figure C.1: Measured photoion (He^{++}) momentum distributions from one-photon double ionization of helium at 800 eV photon energy. (A) Detector-plane momentum distribution. The data shown is limited to $p_{i,z} = 0 \pm 2$ au. (B) Polarization-plane momentum distribution. The data shown is limited to $p_{i,x} = 0 \pm 2$ au. (C) Magnitude of ρ as function of φ_γ (compare to Fig. 9.4 and see Sec. 9.3.1 for details). (D) Photoion momentum as function of $\cos \vartheta = p_{i,z}/p_i$.

Run 1A (Helium at 800 eV photon energy)
Measured electron momentum and energy

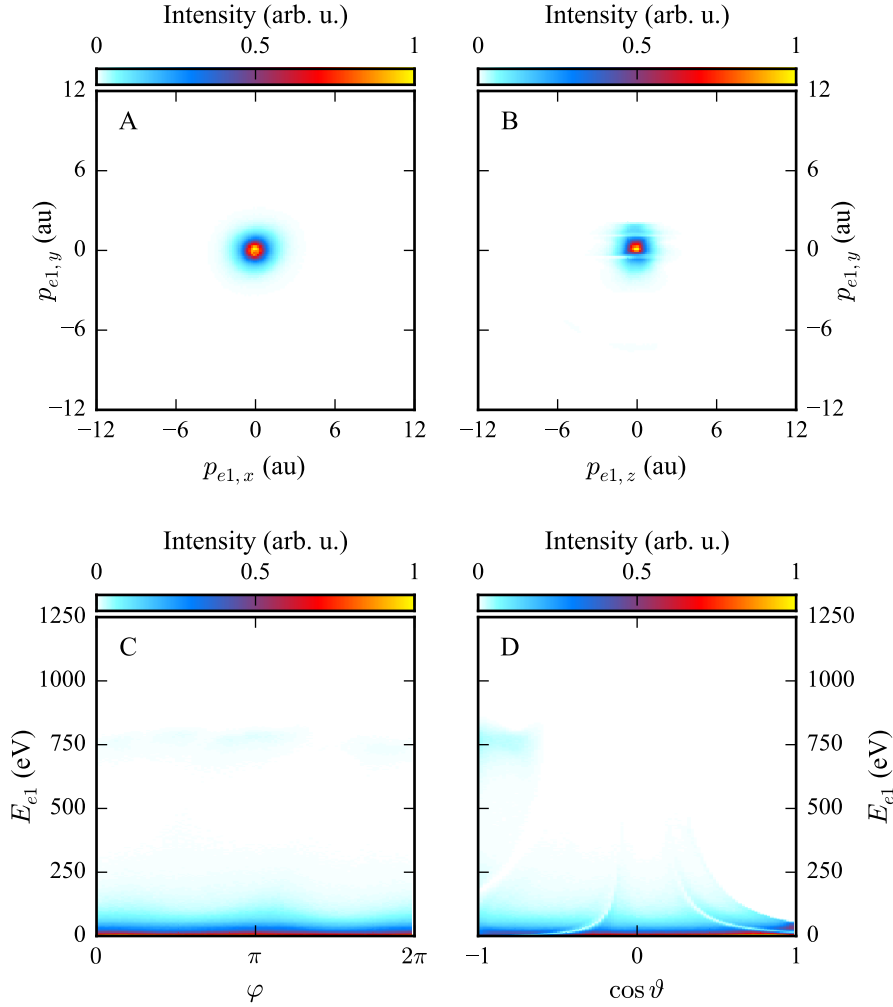


Figure C.2: Measured electron momentum and energy distributions from one-photon double ionization of helium at 800 eV photon energy. (A) Detector-plane momentum distribution. The data shown is limited to $p_{e1,z} = 0 \pm 2$ au. (B) Polarization-plane momentum distribution. The data shown is limited to $p_{e1,x} = 0 \pm 2$ au. (C,D) Electron energy as function of the spherical coordinates $\varphi = \tan^{-1}(p_{e1,x}/p_{e1,y})$ and $\cos \vartheta = p_{e1,z}/p_{e1}$ (see Sec. 9.2 for details).

Run 1A (Helium at 800 eV photon energy)
Reconstructed electron momentum and energy

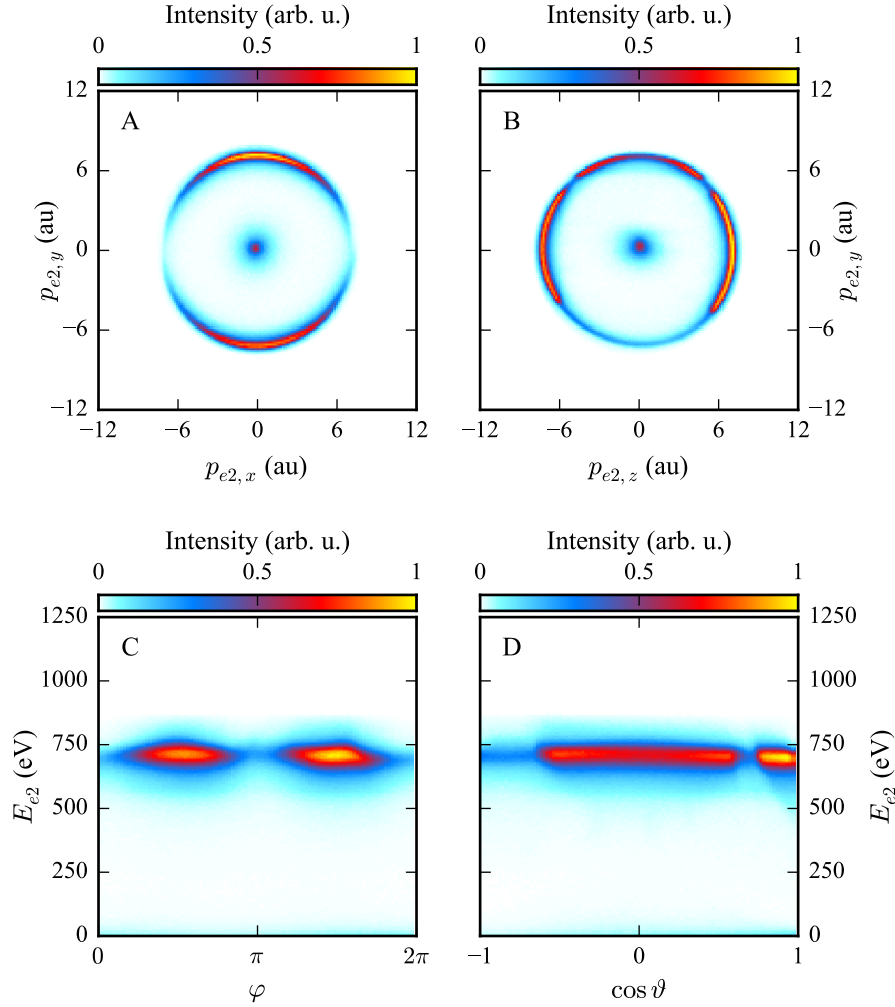


Figure C.3: Reconstructed electron momentum and energy distributions from one-photon double ionization of helium at 800 eV photon energy (see p. 68 and Eq. 9.10 for details). (A) Detector-plane momentum distribution. The data shown is limited to $p_{e2,z} = 0 \pm 2$ au. (B) Polarization-plane momentum distribution. The data shown is limited to $p_{e2,x} = 0 \pm 2$ au. (C,D) Electron energy as function of the spherical coordinates $\varphi = \tan^{-1}(p_{e2,x}/p_{e2,y})$ and $\cos \vartheta = p_{e2,z}/p_{e2}$ (see Sec. 9.2 for details).

Run 1B (Helium at 1100 eV photon energy)
Measured ion momentum

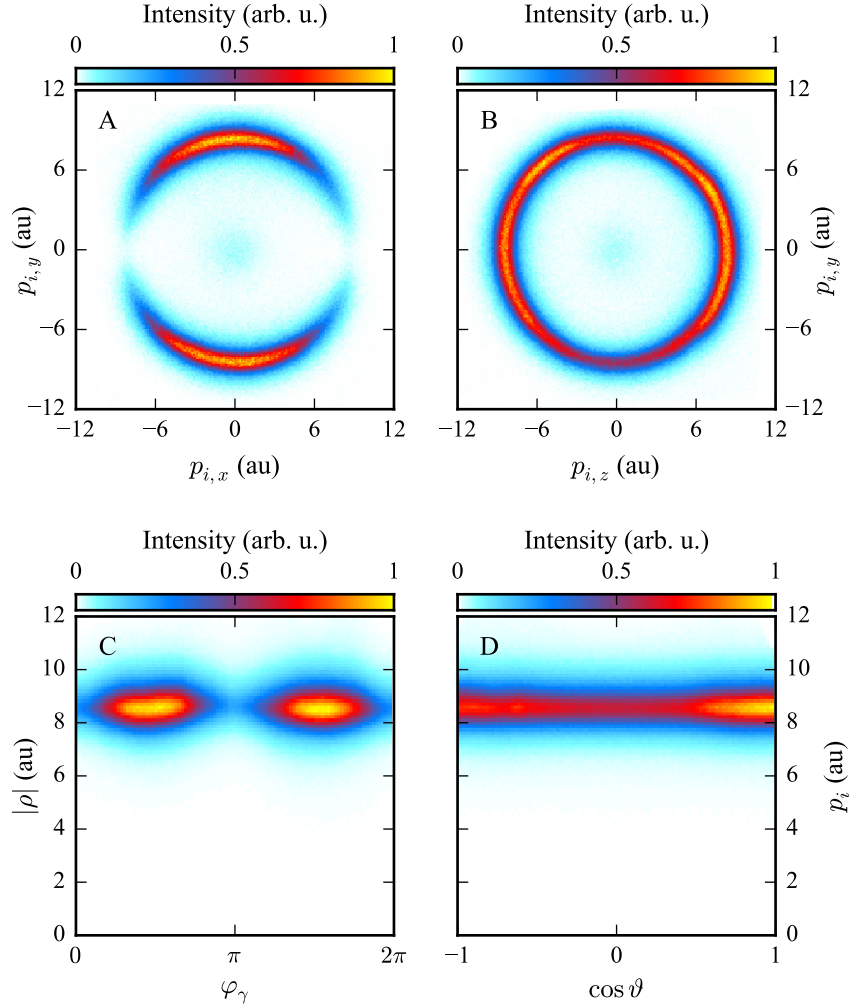


Figure C.4: Measured photoion (He^{++}) momentum distributions from one-photon double ionization of helium at 1100 eV photon energy. (A) Detector-plane momentum distribution. The data shown is limited to $p_{i,z} = 0 \pm 2$ au. (B) Polarization-plane momentum distribution. The data shown is limited to $p_{i,x} = 0 \pm 2$ au. (C) Magnitude of ρ as function of φ_γ (compare to Fig. 9.4 and see Sec. 9.3.1 for details). (D) Photoion momentum as function of $\cos \vartheta = p_{i,z}/p_i$.

Run 1B (Helium at 1100 eV photon energy)
Measured electron momentum and energy

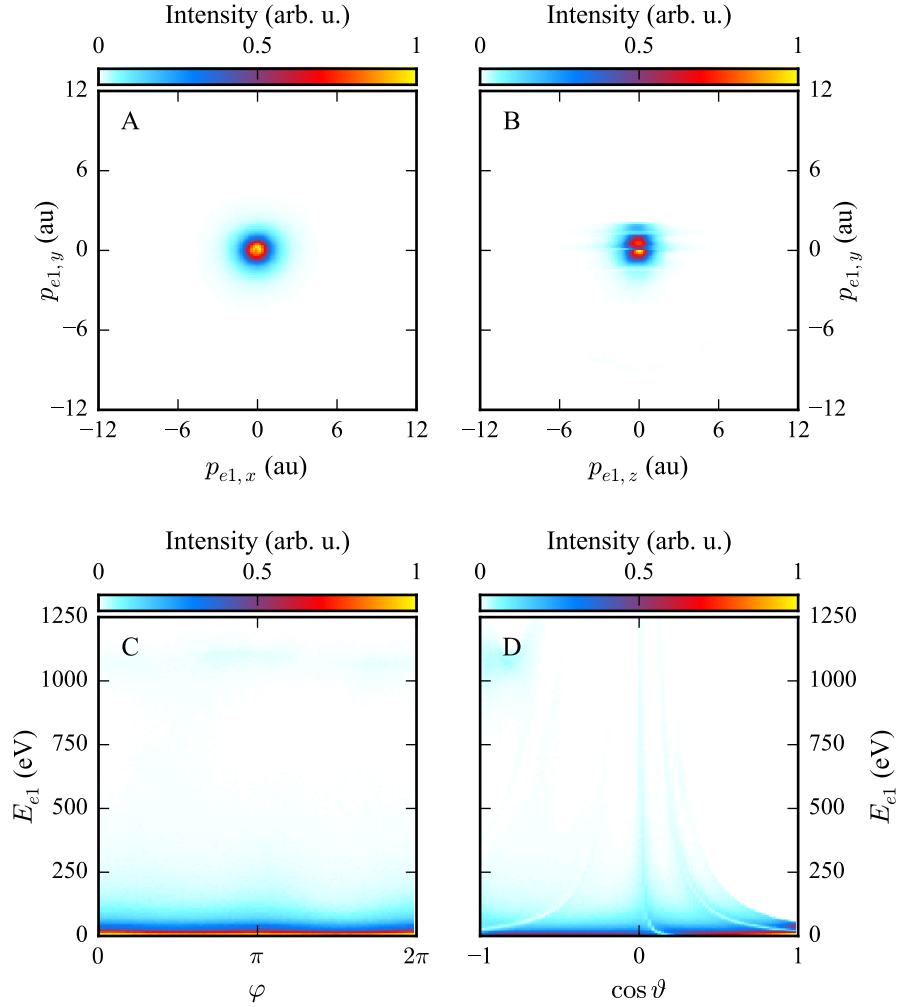


Figure C.5: Measured electron momentum and energy distributions from one-photon double ionization of helium at 1100 eV photon energy. **(A)** Detector-plane momentum distribution. The data shown is limited to $p_{e1,z} = 0 \pm 2$ au. **(B)** Polarization-plane momentum distribution. The data shown is limited to $p_{e1,x} = 0 \pm 2$ au. **(C,D)** Electron energy as function of the spherical coordinates $\varphi = \tan^{-1}(p_{e1,x}/p_{e1,y})$ and $\cos \vartheta = p_{e1,z}/p_{e1}$ (see Sec. 9.2 for details).

Run 1A (Helium at 1100 eV photon energy)
Reconstructed electron momentum and energy

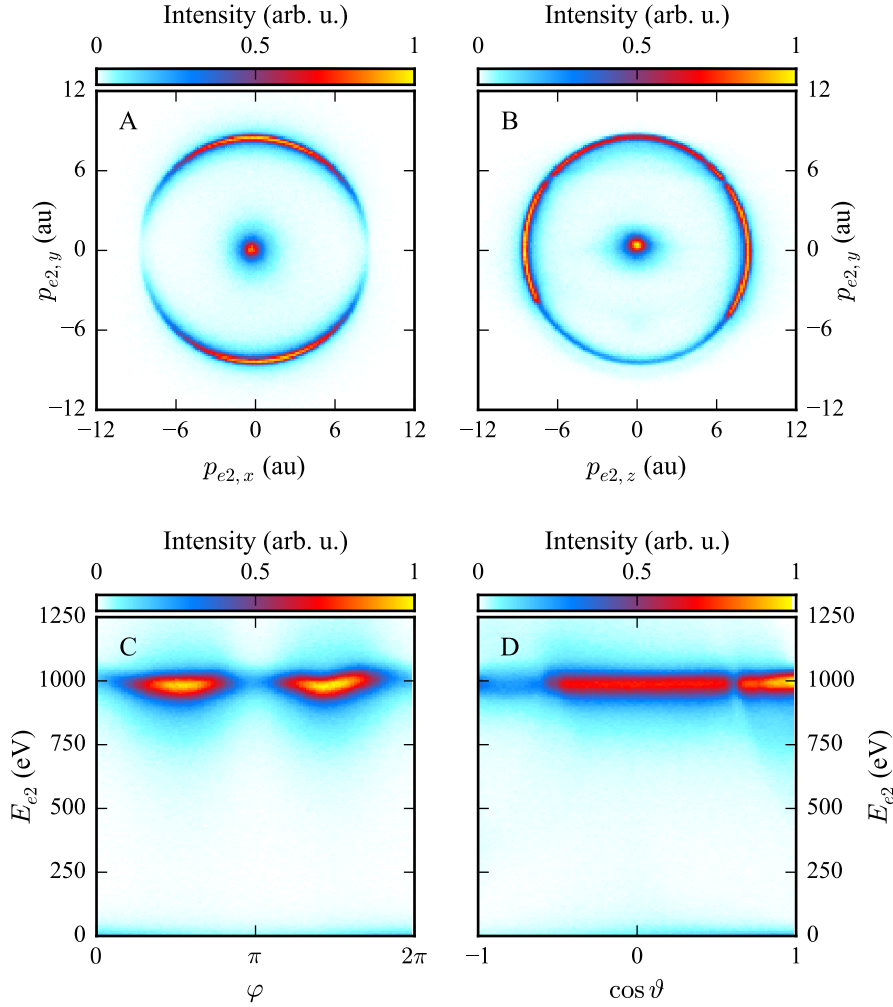


Figure C.6: Reconstructed electron momentum and energy distributions from one-photon double ionization of helium at 800 eV photon energy (see p. 68 and Eq. 9.10 for details). (A) Detector-plane momentum distribution. The data shown is limited to $p_{e2,z} = 0 \pm 2$ au. (B) Polarization-plane momentum distribution. The data shown is limited to $p_{e2,x} = 0 \pm 2$ au. (C,D) Electron energy as function of the spherical coordinates $\varphi = \tan^{-1}(p_{e2,x}/p_{e2,y})$ and $\cos \vartheta = p_{e2,z}/p_{e2}$ (see Sec. 9.2 for details).

Run 2A (H₂ at 800 eV photon energy)
Measured ion momentum

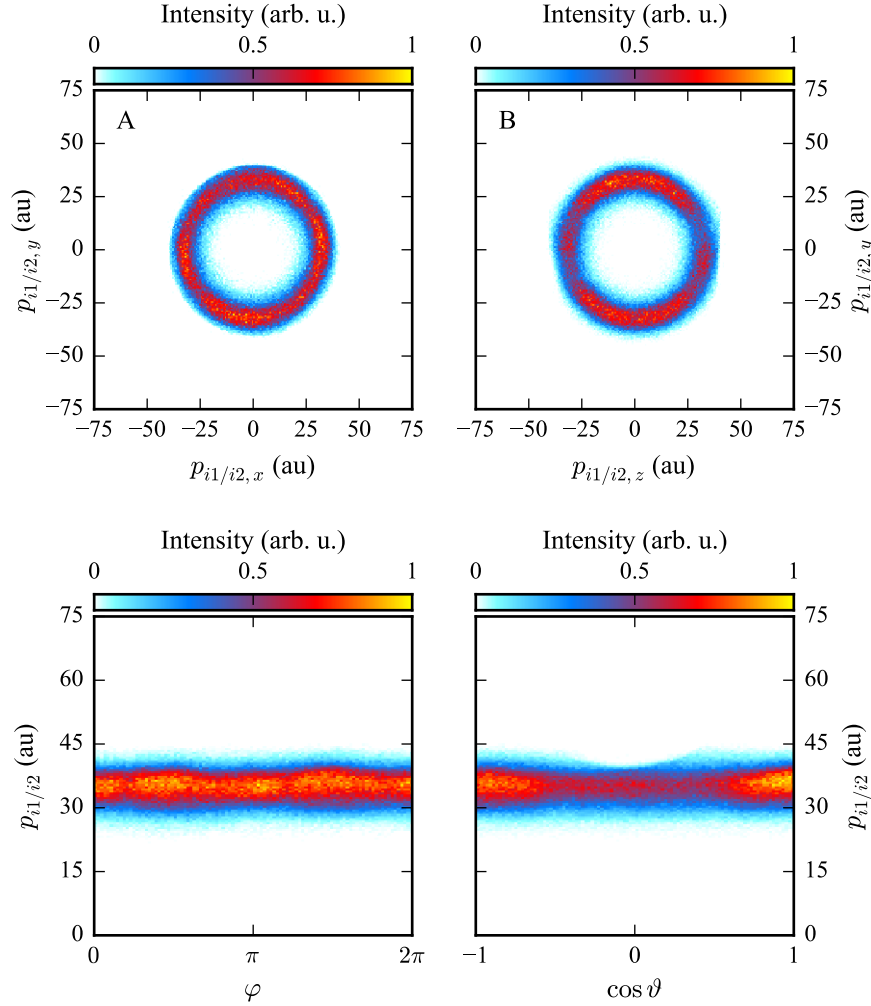


Figure C.7: Measured ion (H⁺) momentum distributions from one-photon double ionization of H₂ at 800 eV photon energy, followed by dissociation into H⁺ & H⁺. All histograms contain the first and second detected ion. **(A)** Detector-plane momentum distribution. The data shown is limited to $p_{i,z} = 0 \pm 20$ au. **(B)** Polarization-plane momentum distribution. The data shown is limited to $p_{i,x} = 0 \pm 20$ au. **(C)** Ion momentum as function of $\varphi = \tan^{-1}(p_{i,x}/p_{i,y})$. **(D)** Ion momentum as function of $\cos \vartheta = p_{i,z}/p_i$.

Run 2A (H₂ at 800 eV photon energy)
Measured electron momentum and energy

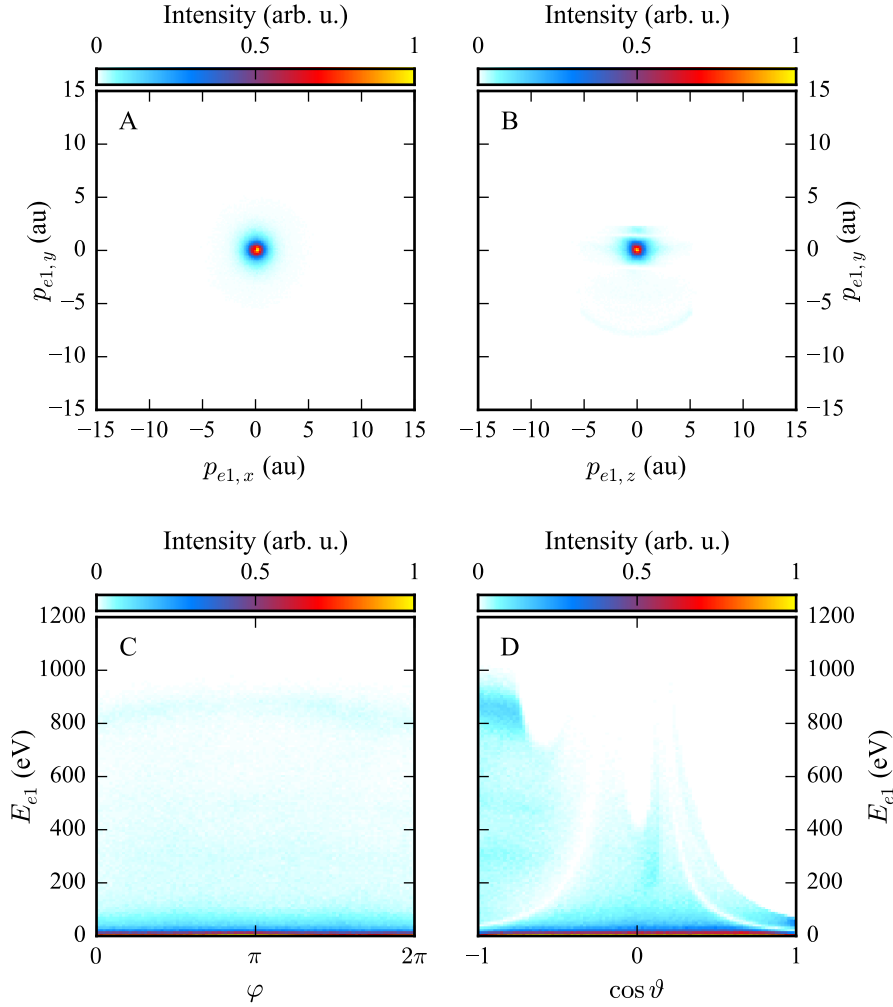


Figure C.8: Measured electron momentum and energy distributions from one-photon double ionization of H₂ at 800 eV photon energy, followed by dissociation into H⁺ & H⁺. (A) Detector-plane momentum distribution. The data shown is limited to $p_{e1,z} = 0 \pm 2$ au. (B) Polarization-plane momentum distribution. The data shown is limited to $p_{e1,x} = 0 \pm 2$ au. (C,D) Electron energy as function of the spherical coordinates $\varphi = \tan^{-1}(p_{e1,x}/p_{e1,y})$ and $\cos \vartheta = p_{e1,z}/p_{e1}$ (see Sec. 9.2 for details).

Run 2A (H₂ at 800 eV photon energy)
Measured ion sum momentum

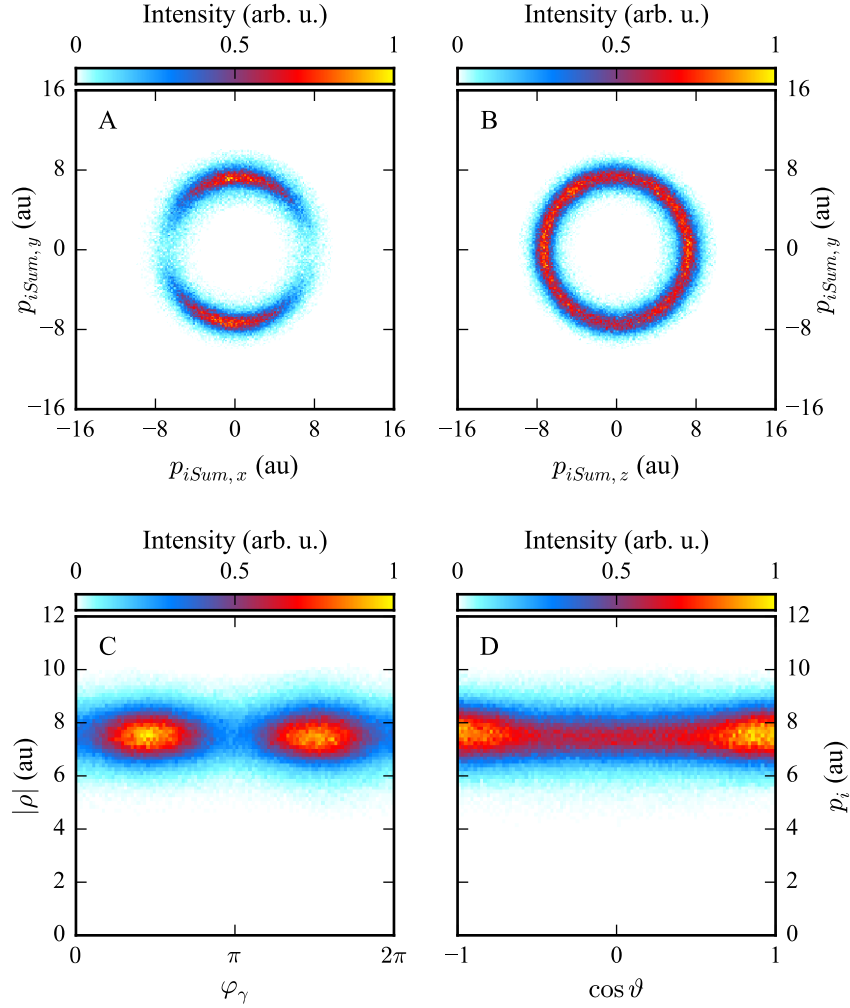


Figure C.9: Measured ion sum momentum distributions from one-photon double ionization of H₂ at 800 eV photon energy, followed by dissociation into H⁺ & H⁺ (see p. 70 and Eq. 9.14 for details). A condition of $\epsilon_{eF} > 0.9$ was applied to all data shown in the present figure. (A) Detector-plane momentum distribution. The data shown is limited to $p_{iSum,z} = 0 \pm 2$ au. (B) Polarization-plane momentum distribution. The data shown is limited to $p_{iSum,x} = 0 \pm 2$ au. (C) Magnitude of ρ as function of φ_γ (compare to Fig. 9.4 and see Sec. 9.3.1 for details). (D) ion sum momentum as function of $\cos \vartheta = p_{i,z}/p_i$.

Run 2A (H₂ at 800 eV photon energy)
Reconstructed electron momentum and energy

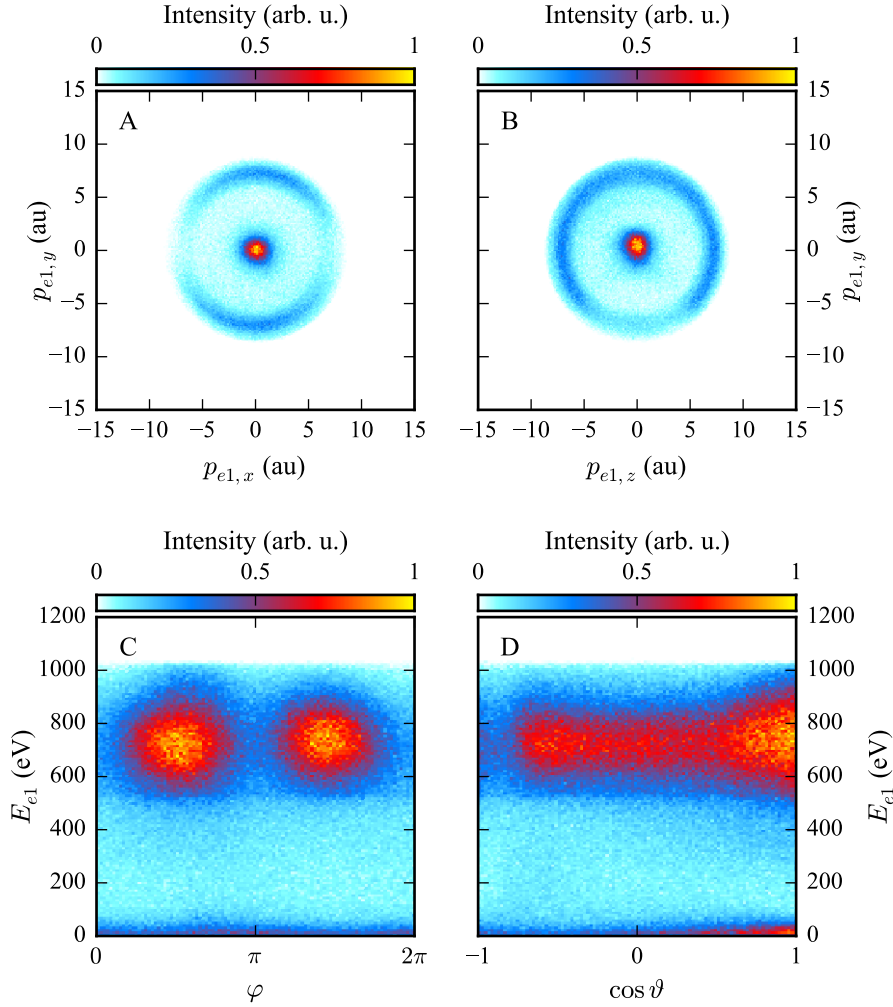


Figure C.10: Reconstructed electron momentum and energy distributions from one-photon double ionization of H₂ at 800 eV photon energy, followed by dissociation into H⁺ & H⁺ (see p. 68 and Eq. 9.10 for details). (A) Detector-plane momentum distribution. The data shown is limited to $p_{e2,z} = 0 \pm 2$ au. (B) Polarization-plane momentum distribution. The data shown is limited to $p_{e2,x} = 0 \pm 2$ au. (C,D) Electron energy as function of the spherical coordinates $\varphi = \tan^{-1}(p_{e2,x}/p_{e2,y})$ and $\cos \vartheta = p_{e2,z}/p_{e2}$ (see Sec. 9.2 for details).

**Run 2A (H₂ at 800 eV photon energy)
Sum energy and kinetic energy release**

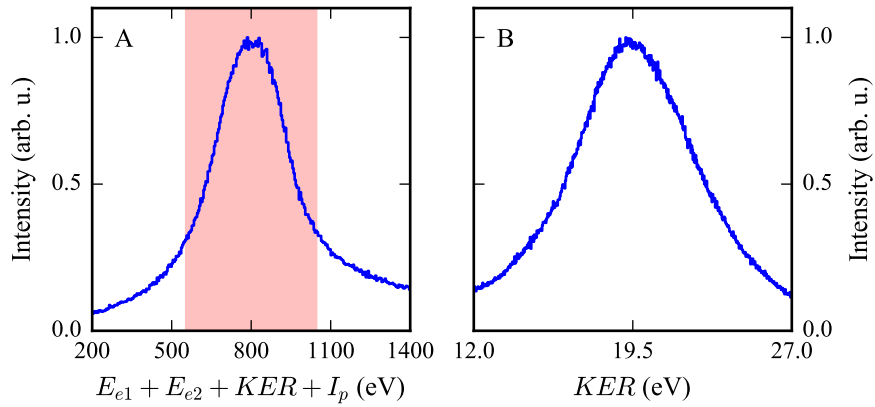


Figure C.11: Measured energies from one-photon double ionization of H₂ at 800 eV photon energy, followed by dissociation into H⁺ & H⁺. (A) Sum energy of all reaction fragments where $I_p = 31.03$ eV is the adiabatic double ionization energy of H₂. The red shaded region indicates a gate on the sum energy of 800 ± 250 eV that was applied on **all** the shown data from Run 2A in the present work. (B) Kinetic energy release (see p. 70 and Eq. 9.16 for details).

Run 3A (N₂ photon energy scan), e.g., 1330 eV photon energy
Measured ion momentum

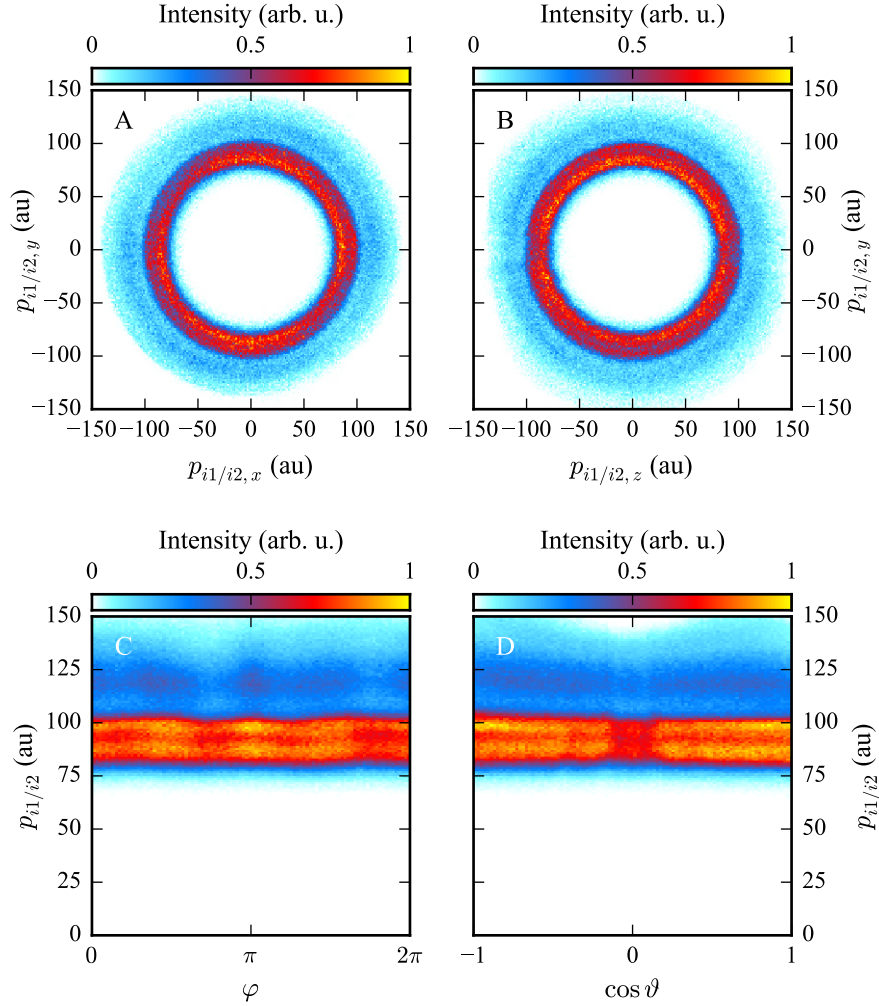


Figure C.12: Measured ion (N⁺) momentum distributions from one-photon *K*-shell ionization of N₂ at 1330 eV photon energy, followed by Auger decay and dissociation into N⁺ & N⁺. All histograms contain the first and second detected ion. (A) Detector-plane momentum distribution. The data shown is limited to $p_{i,z} = 0 \pm 20$ au. (B) Polarization-plane momentum distribution. The data shown is limited to $p_{i,x} = 0 \pm 20$ au. (C) Ion momentum as function of $\varphi = \tan^{-1}(p_{i,x}/p_{i,y})$. (D) Ion momentum as function of $\cos \vartheta = p_{i,z}/p_i$.

Run 3A (N₂ photon energy scan), e.g., 1330 eV photon energy
 Measured electron momentum and energy

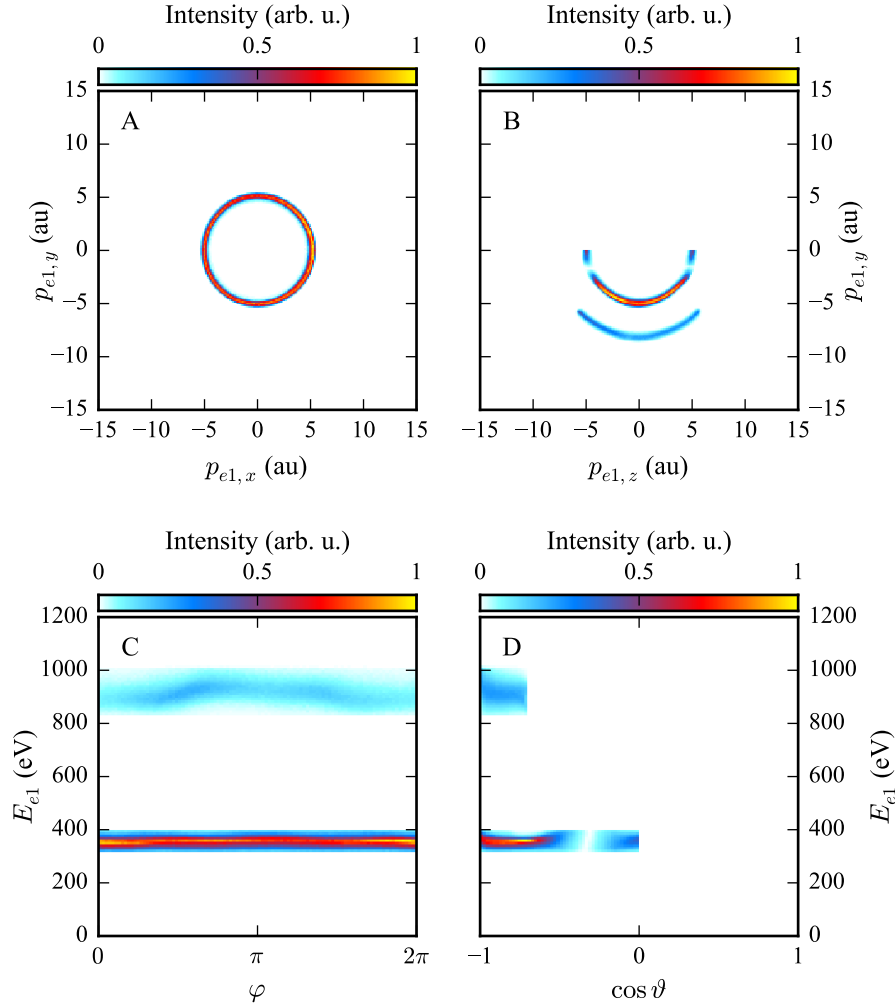


Figure C.13: Measured electron momentum and energy distributions from one-photon K-shell ionization of N₂ at 1330 eV photon energy, followed by Auger decay and dissociation into N⁺ & N⁺. **(A)** Detector-plane momentum distribution. The data shown is limited to $p_{e1,z} = 0 \pm 2$ au. **(B)** Polarization-plane momentum distribution. The data shown is limited to $p_{e1,x} = 0 \pm 2$ au. **(C,D)** Electron energy as function of the spherical coordinates $\varphi = \tan^{-1}(p_{e1,x}/p_{e1,y})$ and $\cos \vartheta = p_{e1,z}/p_{e1}$ (see Sec. 9.2 for details).

Run 3A (N₂ photon energy scan), e.g., 1330 eV photon energy
 Measured ion sum momentum

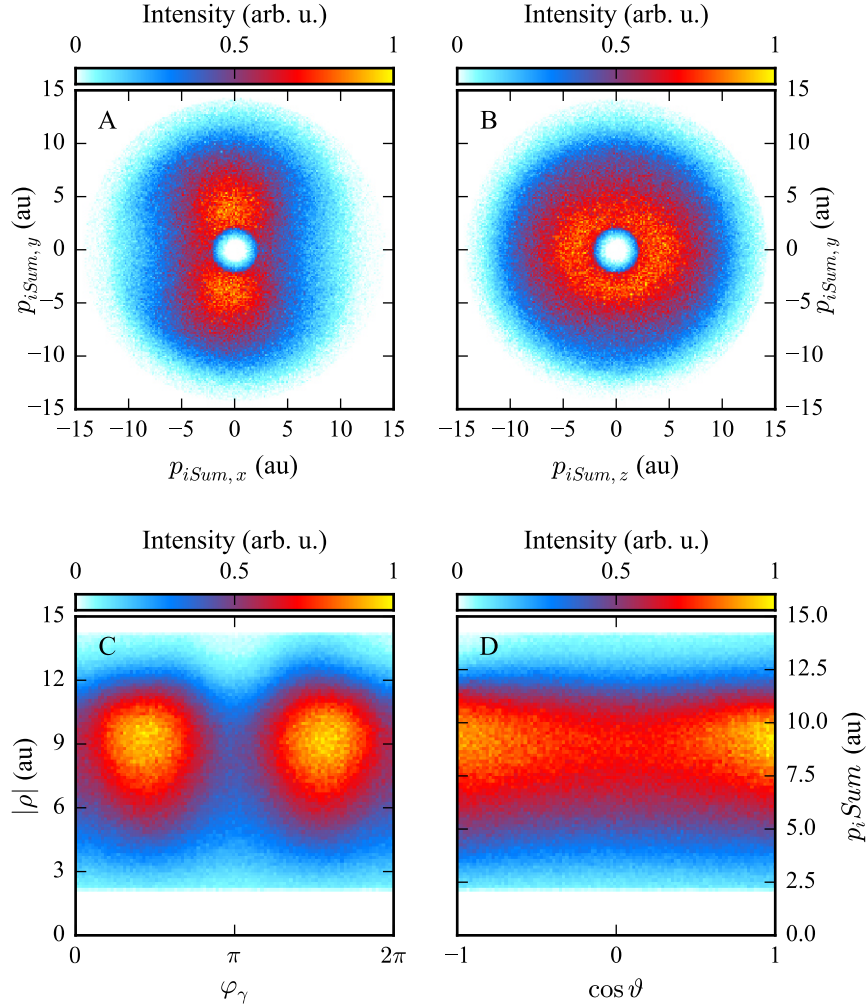


Figure C.14: Measured ion sum momentum distributions from one-photon *K*-shell ionization of N₂ at 1330 eV photon energy, followed by Auger decay and dissociation into N⁺ & N⁺ (see p. 70 and Eq. 9.14 for details). (A) Detector-plane momentum distribution. The data shown is limited to $p_{iSum,z} = 0 \pm 2$ au. (B) Polarization-plane momentum distribution. The data shown is limited to $p_{iSum,x} = 0 \pm 2$ au. (C) Magnitude of ρ as function of φ_γ (compare to Fig. 9.4 and see Sec. 9.3.1 for details). (D) ion sum momentum as function of $\cos \vartheta = p_{i,z}/p_i$.

Run 3A (N₂ photon energy scan), e.g., 1330 eV photon energy
 Reconstructed Auger electron momentum and energy

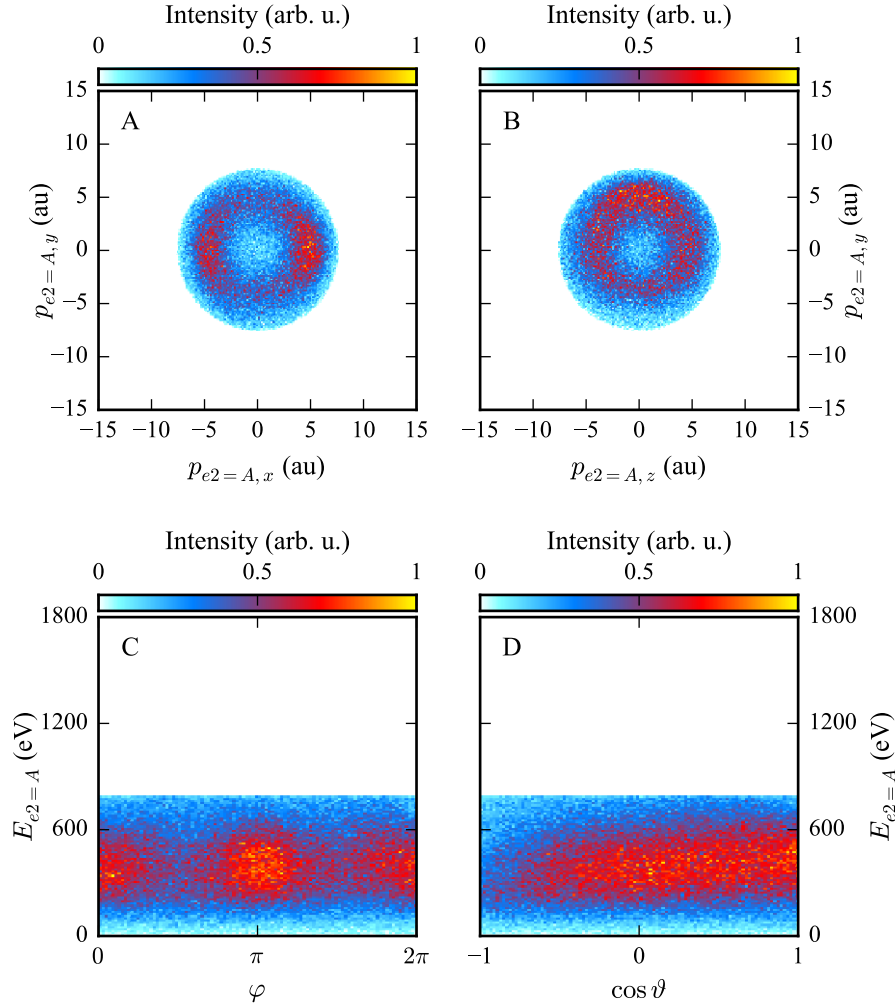


Figure C.15: Reconstructed Auger electron momentum and energy distributions from one-photon K-shell ionization of N₂ at 1330 eV photon energy, followed by Auger decay and dissociation into N⁺ & N⁺ (see p. 68 and Eq. 9.10 for details). (A) Detector-plane momentum distribution. The data shown is limited to $p_{e2,z} = 0 \pm 2$ au. (B) Polarization-plane momentum distribution. The data shown is limited to $p_{e2,x} = 0 \pm 2$ au. (C,D) Electron energy as function of the spherical coordinates $\varphi = \tan^{-1}(p_{e2,x}/p_{e2,y})$ and $\cos \vartheta = p_{e2,z}/p_{e2}$ (see Sec. 9.2 for details).

Run 3A (N₂ photon energy scan), e.g., 1330 eV photon energy
Reconstructed photoelectron momentum and energy

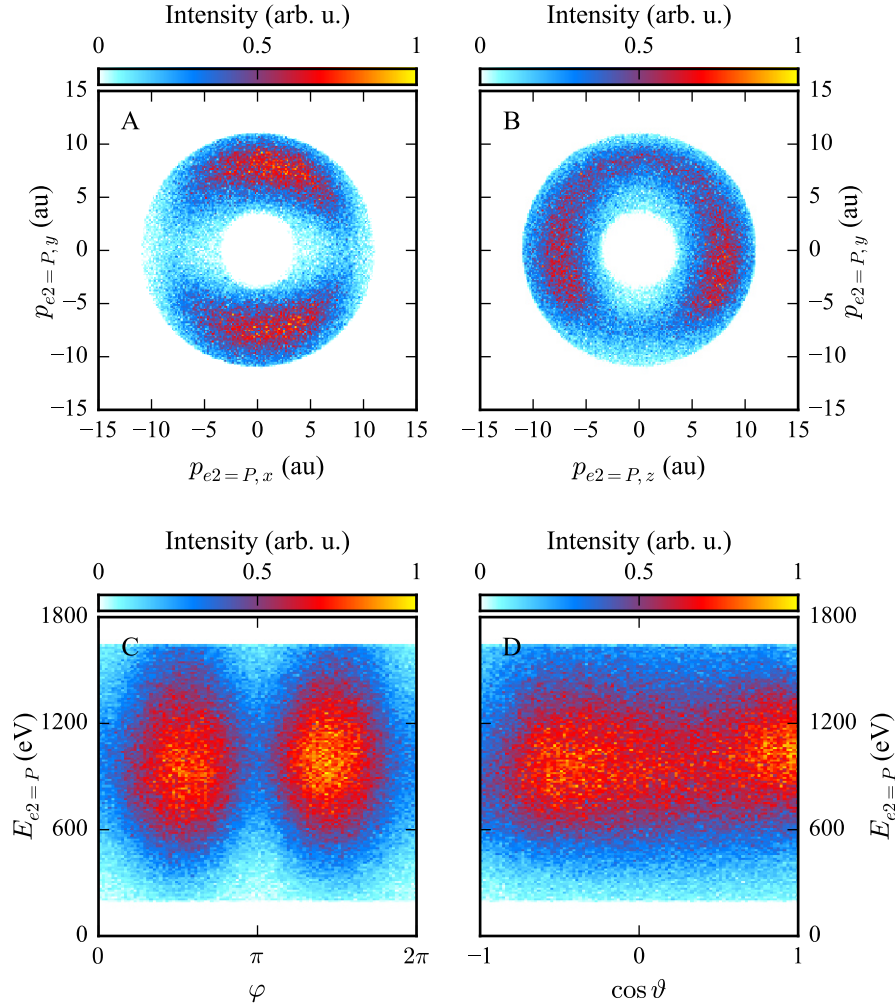


Figure C.16: Reconstructed photoelectron momentum and energy distributions from one-photon K-shell ionization of N₂ at 1330 eV photon energy, followed by Auger decay and dissociation into N⁺ & N⁺ (see p. 68 and Eq. 9.10 for details). (A) Detector-plane momentum distribution. The data shown is limited to $p_{e2,z} = 0 \pm 2$ au. (B) Polarization-plane momentum distribution. The data shown is limited to $p_{e2,x} = 0 \pm 2$ au. (C,D) Electron energy as function of the spherical coordinates $\varphi = \tan^{-1}(p_{e2,x}/p_{e2,y})$ and $\cos \vartheta = p_{e2,z}/p_{e2}$ (see Sec. 9.2 for details).

Run 3A (N₂ photon energy scan), e.g., 1330 eV photon energy
 Measured kinetic energy release

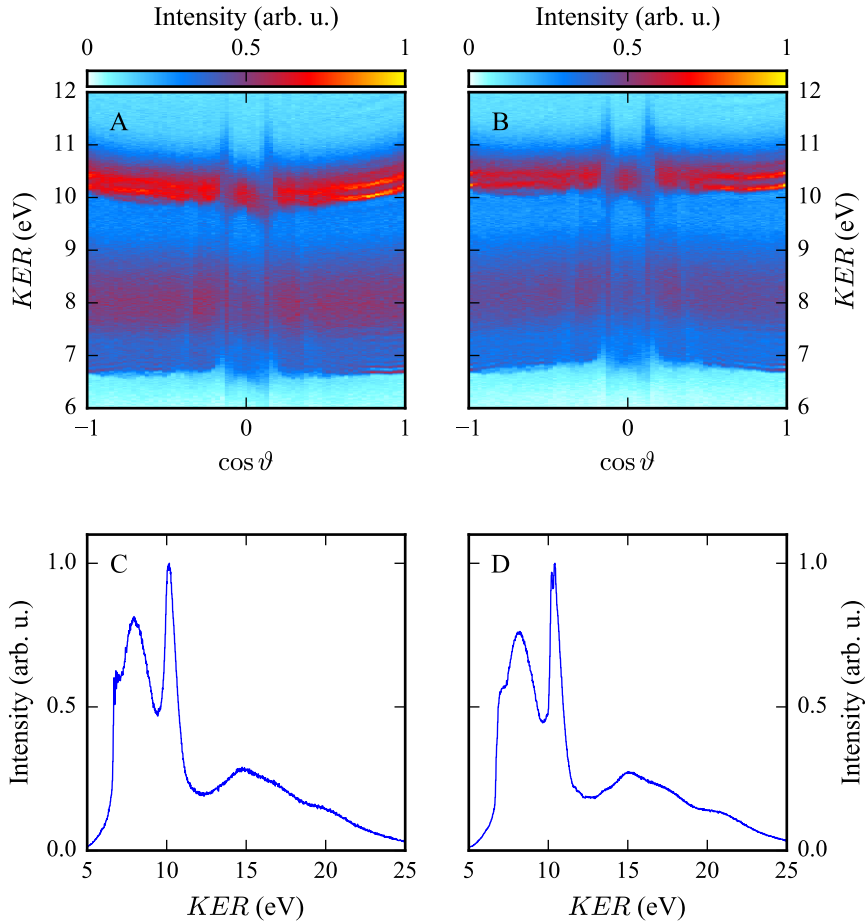


Figure C.17: Measured kinetic energy release distributions from one-photon K -shell ionization of N₂ at 1330 eV photon energy, followed by Auger decay and dissociation into N⁺ & N⁺. (A,C) Correction routine as described in Sec. 9.3.2 optimized for 3.9 eV kinetic energy of N⁺ ions. (B,D) Correction routine optimized for 5.25 eV kinetic energy of N⁺ ions. (A,B) Kinetic energy release as function of $\cos \vartheta = p_{rel,z}/p_{rel}$. (C,D) Kinetic energy release distribution (see p. 70 and Eq. 9.16 for details on the KER calculation).

BIBLIOGRAPHY

- [1] A. Einstein. "Über einen die Erzeugung und Verwandlung des Lichtes betreffenden heuristischen Gesichtspunkt." In: *Ann. Phys.* 17 (1905), pp. 132–148. DOI: [10.1002/andp.19053220607](https://doi.org/10.1002/andp.19053220607) (cit. on pp. 1, 5).
- [2] Max Planck. "Zur Theorie des Gesetzes der Energieverteilung im Normalspektrum." In: *Verhandl. Dtsch. Phys. Ges.* 2 (1900), p. 237 (cit. on p. 1).
- [3] O. Hemmers, R. Guillemin, and D. W. Lindle. "Nondipole effects in soft X-ray photoemission." In: *Radiat. Phys. Chem.* 70 (2004), p. 123. DOI: [10.1016/j.radphyschem.2003.12.009](https://doi.org/10.1016/j.radphyschem.2003.12.009) (cit. on pp. 4, 17, 108).
- [4] M.-X. Wang, S.-G. Chen, H. Liang, and L.-Y. Peng. "Review on non-dipole effects in ionization and harmonic generation of atoms and molecules." In: *Chinese Phys. B* 29 (2020), p. 013302. DOI: [10.1088/1674-1056/ab5c10](https://doi.org/10.1088/1674-1056/ab5c10) (cit. on p. 4).
- [5] J. C. Maxwell. *A Treatise on Electricity and Magnetism*. Oxford: Clarendon Press, 1873 (cit. on p. 4).
- [6] J. D. Jackson. *Classical Electrodynamics*. New York: Wiley, 1962 (cit. on p. 4).
- [7] G. N. Lewis. "The Conservation of Photons." In: *Nature* 118 (1926), pp. 874–875. DOI: <https://doi.org/10.1038/118874a0> (cit. on p. 5).
- [8] A. Einstein. "Ist die Trägheit eines Körpers von seinem Energieinhalt abhängig?" In: *Ann. Phys.* 17 (1905), pp. 639–641. DOI: [10.1002/andp.19053231314](https://doi.org/10.1002/andp.19053231314) (cit. on p. 5).
- [9] R. Dörner, V. Mergel, O. Jagutzki, L. Spielberger, J. Ullrich, R. Moshhammer, and H. Schmidt-Böcking. "Cold Target Recoil Ion Momentum Spectroscopy: a 'momentum microscope' to view atomic collision dynamics." In: *Phys. Rep.* 330 (2000), p. 95. DOI: [10.1016/S0370-1573\(99\)00109-X](https://doi.org/10.1016/S0370-1573(99)00109-X) (cit. on pp. 6, 53).
- [10] F. Hull and E. E. Nichols. "The Pressure due to Radiation." In: *Phys. Rev.* 17 (1903), pp. 26–50. DOI: [10.1103/PhysRevSeriesI.17.26](https://doi.org/10.1103/PhysRevSeriesI.17.26) (cit. on p. 7).
- [11] P. Lebedew. "Untersuchungen über die Druckkräfte des Lichtes." In: *Ann. Phys.* 4 (1901), pp. 433–458. DOI: [10.1002/andp.19013111102](https://doi.org/10.1002/andp.19013111102) (cit. on p. 7).
- [12] A. H. Compton. "A Quantum Theory of the Scattering of X-rays by Light Elements." In: *Phys. Rev.* 21 (1923), pp. 483–502. DOI: [10.1103/PhysRev.21.483](https://doi.org/10.1103/PhysRev.21.483) (cit. on p. 7).
- [13] M. Kircher et al. "Kinematically complete experimental study of Compton scattering at helium atoms near the threshold." In: *Nat. Phys.* 16 (2020), pp. 756–760. DOI: [10.1038/s41567-020-0880-2](https://doi.org/10.1038/s41567-020-0880-2) (cit. on pp. 7, 12).
- [14] O. R. Frisch. "Experimenteller Nachweis des Einsteinschen Strahlungsrückstoßes." In: *Z. Physik* 86 (1933), pp. 42–48. DOI: [10.1007/BF01340182](https://doi.org/10.1007/BF01340182) (cit. on p. 7).
- [15] W. D. Phillips. "Laser cooling and trapping of neutral atoms." In: *Rev. Mod. Phys.* 70 (1998), pp. 721–741. DOI: [10.1103/revmodphys.70.721](https://doi.org/10.1103/revmodphys.70.721) (cit. on p. 7).
- [16] L. Johnson, R. Young, E. Montgomery, and D. Alhorn. "Status of solar sail technology within NASA." In: *Adv. Space Res.* 48 (2011), pp. 1687–1694. DOI: [10.1016/j.asr.2010.12.011](https://doi.org/10.1016/j.asr.2010.12.011) (cit. on p. 7).

- [17] S. Eckart. *Strong Field Ionization in Two-Color Fields*. PhD thesis, 2019 (cit. on p. 8).
- [18] S. Chelkowski, A. D. Bandrauk, and P. B. Corkum. "Photon Momentum Sharing between an Electron and an Ion in Photoionization: From One-Photon (Photoelectric Effect) to Multiphoton Absorption." In: *Phys. Rev. Lett.* 113 (2014), p. 263005. DOI: [10.1103/PhysRevLett.113.263005](https://doi.org/10.1103/PhysRevLett.113.263005) (cit. on pp. 8, 90).
- [19] A. Hartung et al. "Magnetic fields alter strong-field ionization." In: *Nat. Phys.* 15 (2019), pp. 1222–1226. DOI: [10.1038/s41567-019-0653-y](https://doi.org/10.1038/s41567-019-0653-y) (cit. on p. 8).
- [20] A. Hartung. *Der Photonenimpuls in der Starkfeldionisation*. PhD thesis, 2019 (cit. on p. 8).
- [21] K. Lin et al. "Photoelectron energy peaks shift against the radiation pressure in strong field ionization." In: (2021). arXiv: [2110.04027](https://arxiv.org/abs/2110.04027). URL: <http://arxiv.org/abs/2110.04027> (cit. on p. 8).
- [22] *Atomic Calculation of Photoionization Cross-Sections and Asymmetry Parameters*. URL: <https://vuo.elettra.eu/services/elements/WebElements.html> (visited on 01/08/2021) (cit. on pp. 9, 59, 62).
- [23] I. V. Hertel and C.-P. Schulz. *Atome, Moleküle und optische Physik 1*. Berlin: Springer, 2017. DOI: [10.1007/978-3-662-53104-4](https://doi.org/10.1007/978-3-662-53104-4) (cit. on pp. 9, 10, 12, 14).
- [24] A. F. Starace. "Photoionization of Atoms." In: *Handbook of Atomic, Molecular, and Optical Physics*. New York: Springer, 2006, pp. 379–388. DOI: [10.1007/978-0-387-26308-3](https://doi.org/10.1007/978-0-387-26308-3) (cit. on pp. 9–11).
- [25] G. Grynberg, A. Aspect, and C. Fabre. *Introduction to Quantum Optics*. Cambridge: Cambridge University Press, 2010. DOI: [10.1142/9789812839671](https://doi.org/10.1142/9789812839671) (cit. on pp. 9, 21).
- [26] R. N. Hill. "Hydrogenic Wave Functions." In: *Handbook of Atomic, Molecular, and Optical Physics*. New York: Springer, 2006, pp. 153–170. DOI: [10.1007/978-0-387-26308-3](https://doi.org/10.1007/978-0-387-26308-3) (cit. on p. 10).
- [27] J. J. Sakurai and J. Napolitano. *Modern Quantum Mechanics*. San Francisco: Pearson, 1985 (cit. on pp. 11, 18, 19, 21).
- [28] J. S. Briggs and V. Schmidt. "Differential cross sections for photo-double-ionization of the helium atom." In: *J. Phys. B* 33 (2000), R1. DOI: [10.1088/0953-4075/33/1/201](https://doi.org/10.1088/0953-4075/33/1/201) (cit. on pp. 11, 27, 101).
- [29] H. A. Bethe and E. E. Salpeter. *Quantum Mechanis of One- and Two-Electron Atoms*. Berlin: Springer, 1957 (cit. on pp. 12–14, 18, 89).
- [30] M. Born. "Quantenmechanik der Stoßvorgänge." In: *Z. Physik* 38 (1926), pp. 803–840. DOI: [10.1007/BF01397184](https://doi.org/10.1007/BF01397184) (cit. on p. 12).
- [31] S. Gozem, A. O. Gunina, T. Ichino, D. L. Osborn, J. F. Stanton, and A. I. Krylov. "Photoelectron Wave Function in Photoionization: Plane Wave or Coulomb Wave?" In: *J. Phys. Chem. Lett.* 6 (2015), p. 4532. DOI: [10.1021/acs.jpcllett.5b01891](https://doi.org/10.1021/acs.jpcllett.5b01891) (cit. on p. 12).
- [32] J. R. Swanson and L. Armstrong. "Multiconfiguration Hartree-Fock calculation of photoionization cross sections of the rare gases. II. Final-state correlation." In: *Phys. Rev. A* 16 (1977), p. 1117. DOI: [10.1103/PhysRevA.16.1117](https://doi.org/10.1103/PhysRevA.16.1117) (cit. on p. 12).
- [33] M. Waitz et al. "Imaging the square of the correlated two-electron wave function of a hydrogen molecule." In: *Nat. Comm.* 8 (2017). DOI: [10.1038/s41467-017-02437-9](https://doi.org/10.1038/s41467-017-02437-9) (cit. on pp. 13, 36, 37, 40, 46, 47, 115, 130).

- [34] N. Yükcü and S. A. Yükcü. “Fourier transform of hydrogen-type atomic orbitals.” In: *Can. J. Phys.* 96 (2018), pp. 724–726. DOI: [10.1139/cjp-2017-0728](https://doi.org/10.1139/cjp-2017-0728) (cit. on p. 13).
- [35] J. C. Slater. “Atomic Shielding Constants.” In: *Phys. Rev.* 36 (1930), p. 57. DOI: [10.1103/PhysRev.36.57](https://doi.org/10.1103/PhysRev.36.57) (cit. on p. 14).
- [36] E. Clementi and D. L. Raimondi. “Atomic Screening Constants from SCF Functions.” In: *J. Chem. Phys.* 38 (1963), p. 2686. DOI: [10.1063/1.1733573](https://doi.org/10.1063/1.1733573) (cit. on p. 14).
- [37] C. T. Chantler, K. Olsen, R. A. Dragoset, J. Chang, A. R. Kishore, S. A. Kotochigova, and D. S. Zucker. *Detailed Tabulation of Atomic Form Factors, Photoelectric Absorption and Scattering Cross Section, and Mass Attenuation Coefficients for Z = 1-92 from E = 1-10 eV to E = 0.4-1.0 MeV*. URL: <https://www.nist.gov/pml/x-ray-form-factor-attenuation-and-scattering-tables> (visited on 01/15/2021) (cit. on pp. 14, 15).
- [38] J. G. Jenkin. “The development of angle-resolved photoelectron spectroscopy; 1900-1960.” In: *J. Electron Spectrosc. Relat. Phenom.* 23 (1981), pp. 187–273. DOI: [10.1016/0368-2048\(81\)80034-5](https://doi.org/10.1016/0368-2048(81)80034-5) (cit. on pp. 17, 89).
- [39] J. W. Cooper. “Photoelectron-angular-distribution parameters for rare-gas subshells.” In: *Phys. Rev. A* 47:3 (1993), pp. 1841–1851. DOI: [10.1103/PhysRevA.47.1841](https://doi.org/10.1103/PhysRevA.47.1841) (cit. on pp. 18, 24, 91).
- [40] M. Y. Amusia, A. S. Baltentkov, L. V. Chernysheva, Z. Felfli, and A. Z. Msezane. “Nondipole parameters in angular distributions of electrons in photoionization of noble-gas atoms.” In: *Phys. Rev. A* 63 (2001), p. 052506. DOI: [10.1103/PhysRevA.63.052506](https://doi.org/10.1103/PhysRevA.63.052506) (cit. on pp. 19, 92, 96).
- [41] C. N. Yang. “On the angular distribution in nuclear reactions and coincidence measurements.” In: *Physical Review* 74:7 (1948), pp. 764–772. DOI: [10.1103/PhysRev.74.764](https://doi.org/10.1103/PhysRev.74.764) (cit. on p. 22).
- [42] J. W. Cooper and S. T. Manson. “Photo-Ionization in the soft x-ray range: Angular distributions of photoelectrons and interpretation in terms of subshell structure.” In: *Phys. Rev.* 177 (1969), pp. 157–163. DOI: [10.1103/PhysRev.177.157](https://doi.org/10.1103/PhysRev.177.157) (cit. on pp. 22, 23).
- [43] J. Cooper and R. N. Zare. “Angular distribution of photoelectrons.” In: *J. Chem. Phys.* 48 (1968), p. 942. DOI: [10.1103/PhysRev.38.1078](https://doi.org/10.1103/PhysRev.38.1078) (cit. on pp. 22, 23).
- [44] H. A. Bethe. “Quantenmechanik der Ein- oder Zweielektronenprobleme.” In: *Quantentheorie*. 1933, pp. 273–551 (cit. on p. 22).
- [45] J. W. Cooper. “Multipole corrections to the angular distribution of photoelectrons at low energies.” In: *Phys. Rev. A* 42:11 (1990), 6942(R). DOI: [10.1103/PhysRevA.42.6942](https://doi.org/10.1103/PhysRevA.42.6942) (cit. on pp. 23, 91).
- [46] A. Derevianko, W. R. Johnson, and K. T. Cheng. “Non-Dipole Effects in Photoelectron Angular Distributions for Rare Gas Atoms.” In: *At. Data Nucl. Data Tables* 73 (1999), pp. 153–211. DOI: [10.1006/adnd.1999.0818](https://doi.org/10.1006/adnd.1999.0818) (cit. on p. 24).
- [47] J. H. Scofield. “Angular and polarization correlations in photoionization and radiative recombination.” In: *Phys. Rev. A* 40 (1989), p. 3054. DOI: [10.1103/PhysRevA.40.3054](https://doi.org/10.1103/PhysRevA.40.3054) (cit. on p. 24).
- [48] A. Bechler and R. H. Pratt. “Higher multipole and retardation corrections to the dipole angular distributions of L-shell photoelectrons ejected by polarized photons.” In: *Phys. Rev. A* 42 (1990). DOI: [10.1103/PhysRevA.42.6400](https://doi.org/10.1103/PhysRevA.42.6400) (cit. on p. 24).

- [49] A. Y. Istomin, A. F. Starace, N. L. Manakov, A. V. Meremianin, A. S. Kheifets, and I. Bray. "Parametrizations and dynamical analysis of angle-integrated cross sections for double photoionization including nondipole effects." In: *Phys. Rev. A* 72 (2005), p. 052708. DOI: [10.1103/PhysRevA.72.052708](https://doi.org/10.1103/PhysRevA.72.052708) (cit. on pp. 24, 28).
- [50] A. Knapp. *Photodoppelionisation von Helium*. PhD thesis, 2005 (cit. on p. 27).
- [51] A. Kheifets. "On different mechanisms of the two-electron atomic photoionization." In: *J. Phys. B* 34 (2001), p. L247 (cit. on p. 27).
- [52] S. Grundmann. *Photodoppelionisation von Helium: Der erste vollständige differentielle Blick auf den Quasifrei-Mechanismus*. Bachelor Thesis, 2017 (cit. on pp. 27, 85).
- [53] T. Aberg. "Asymptotic Double-Photoexcitation Cross Section of the Helium Atom." In: *Phys. Rev. A* 2.5 (1970), p. 1726. DOI: [10.1103/PhysRevA.2.1726](https://doi.org/10.1103/PhysRevA.2.1726) (cit. on p. 28).
- [54] A. Knapp et al. "Mechanisms of photo double ionization of helium by 530 eV photons." In: *Phys. Rev. Lett.* 89 (2002), p. 033004. DOI: [10.1103/PhysRevLett.89.033004](https://doi.org/10.1103/PhysRevLett.89.033004) (cit. on pp. 28, 97, 101).
- [55] A. Y. Istomin, N. L. Manakov, A. V. Meremianin, and A. F. Starace. "Circular dichroism at equal energy sharing in photo-double-ionization of He." In: *Phys. Rev. A* 70 (2004), p. 010702. DOI: [10.1103/PhysRevA.70.010702](https://doi.org/10.1103/PhysRevA.70.010702) (cit. on p. 28).
- [56] A. Istomin, N. L. Manakov, A. V. Meremianin, and A. F. Starace. "Nondipole Effects in Photo-Double-Ionization of He by a vuv Photon." In: *Phys. Rev. Lett.* 92 (2004), p. 063002. DOI: [10.1103/PhysRevLett.92.063002](https://doi.org/10.1103/PhysRevLett.92.063002) (cit. on pp. 28, 108).
- [57] A. Y. Istomin, N. L. Manakov, A. V. Meremianin, and A. F. Starace. "Nondipole effects in the triply differential cross section for double photoionization of He." In: *Phys. Rev. A* 71 (2005), p. 052702. DOI: [10.1103/PhysRevA.71.052702](https://doi.org/10.1103/PhysRevA.71.052702) (cit. on p. 28).
- [58] M. Y. Amusia, E. G. Drukarev, V. G. Gorshkov, and M. P. Kazachkov. "Two-electron photoionization of helium." In: *J. Phys. B* 8 (1975), p. 1248. DOI: [10.1088/0022-3700/8/8/016](https://doi.org/10.1088/0022-3700/8/8/016) (cit. on pp. 28, 29, 101).
- [59] T. Suric, E. G. Drukarev, and R. H. Pratt. "Characterization of high-energy photoionization in terms of the singularities of the atomic potential. I. Photoionization of the ground state of a two-electron atom." In: *Phys. Rev. A* 67 (2003), p. 022709. DOI: [10.1103/PhysRevA.67.022709](https://doi.org/10.1103/PhysRevA.67.022709) (cit. on pp. 28, 110).
- [60] J. A. Ludlow, J. Colgan, T.-G. Lee, M. S. Pindzola, and F. Robicheaux. "Double photoionization of helium including quadrupole radiation effects." In: *J. Phys. B* 42 (2009), p. 225204. DOI: [10.1088/0953-4075/42/22/225204](https://doi.org/10.1088/0953-4075/42/22/225204) (cit. on pp. 28, 101, 110).
- [61] M. Y. Amusia, E. G. Drukarev, and E. Z. Liverts. "Small recoil momenta double ionization of He and two-electron ions by high energy photons." In: *Eur. Phys. J. D* 74 (2020), pp. 1–8. DOI: [10.1140/epjd/e2020-10226-1](https://doi.org/10.1140/epjd/e2020-10226-1) (cit. on p. 28).
- [62] F. Maulbetsch and J. S. Briggs. "Selection rules for transitions to two-electron continuum states." In: *J. Phys. B* 28 (1995), p. 551. DOI: [10.1088/0953-4075/28/4/007](https://doi.org/10.1088/0953-4075/28/4/007) (cit. on pp. 28, 102, 108).

- [63] R. Krivec, M. Y. Amusia, and V. B. Mandelzweig. "Calculation of the contribution of the quasifree mechanism to the two-electron photoionization cross section." In: *Phys. Rev. A* 64 (2001), p. 012713. DOI: [10.1103/PhysRevA.64.012713](https://doi.org/10.1103/PhysRevA.64.012713) (cit. on p. 28).
- [64] E. G. Drukarev and F. F. Karpeshin. "The relativistic double photoeffect." In: *J. Phys. B* 9 (1976), p. 399. DOI: [10.1088/0022-3700/9/3/008](https://doi.org/10.1088/0022-3700/9/3/008) (cit. on p. 28).
- [65] R. P. Feynman. "Space-time approach to quantum electrodynamics." In: *Phys. Rev.* 76 (1949), p. 769. DOI: [10.1103/PhysRev.76.769](https://doi.org/10.1103/PhysRev.76.769) (cit. on p. 28).
- [66] M. S. Schöffler et al. "Ejection of quasi-free-electron pairs from the helium-atom ground state by single-photon absorption." In: *Phys. Rev. Lett.* 111 (2013), p. 013003. DOI: [10.1103/PhysRevLett.111.013003](https://doi.org/10.1103/PhysRevLett.111.013003) (cit. on pp. 28, 101).
- [67] C. Siedschlag and T. Pattard. "Single-photon double ionization of the hydrogen molecule." In: *J. Phys. B* 38 (2005), pp. 2297–2310. DOI: [10.1088/0953-4075/38/13/021](https://doi.org/10.1088/0953-4075/38/13/021) (cit. on pp. 28, 101).
- [68] M. Kircher et al. "Ion and Electron Momentum Distributions from Single and Double Ionization of Helium Induced by Compton Scattering." In: (2021). arXiv: [2110.09831](https://arxiv.org/abs/2110.09831). URL: <http://arxiv.org/abs/2110.09831> (cit. on p. 29).
- [69] M. Ehara et al. "Symmetry-dependent vibrational excitation in N 1s photoionization of N₂: Experiment and theory." In: *J. Chem. Phys.* 124 (2006), p. 124311. DOI: [10.1063/1.2181144](https://doi.org/10.1063/1.2181144) (cit. on p. 30).
- [70] M. Weller. *Der Auger-Effekt in kleinen Molekülen*. PhD thesis, 2020 (cit. on pp. 30, 129).
- [71] Th. Weber et al. "K-shell photoionization of CO and N₂: Is there a link between the photoelectron angular distribution and the molecular decay dynamics?" In: *J. Phys. B* 34 (2001), p. 3669. DOI: [10.1088/0953-4075/34/18/305](https://doi.org/10.1088/0953-4075/34/18/305) (cit. on pp. 30, 71, 130).
- [72] J. A. R. Samson and R. B. Cairns. "Total Absorption Cross Sections of H₂, N₂, and O₂ in the Region 550–200 Å." In: *J. Opt. Soc. Am.* 55 (1965), p. 1035. DOI: [10.1364/JOSA.55.001035](https://doi.org/10.1364/JOSA.55.001035) (cit. on p. 31).
- [73] H. D. Cohen and U. Fano. "Interference in the Photo-Ionization of Molecules." In: *Phys. Rev.* 150 (1966), p. 30. DOI: [10.1103/PhysRev.150.30](https://doi.org/10.1103/PhysRev.150.30) (cit. on pp. 31, 32, 115, 116, 129).
- [74] O. A. Fojon, J. Fernandez, A. Palacios, R. D. Rivarola, and F. Martin. "Interference effects in H₂ photoionization at high energies." In: *J. Phys. B* 37 (2004), p. 3035. DOI: [10.1088/0953-4075/37/15/003](https://doi.org/10.1088/0953-4075/37/15/003) (cit. on p. 31).
- [75] X. J. Liu et al. "Young's double-slit experiment using core-level photoemission from N₂: Revisiting Cohen-Fano's two-centre interference phenomenon." In: *J. Phys. B* 39 (2006), p. 4801. DOI: [10.1088/0953-4075/39/23/001](https://doi.org/10.1088/0953-4075/39/23/001) (cit. on p. 31).
- [76] J. Fernandez, O. Fojon, and F. Martin. "Double-slit, confinement, and non-Franck-Condon effects in photoionization of H₂ at high photon energy." In: *Phys. Rev. A* 79 (2009), p. 023420. DOI: [10.1103/PhysRevA.79.023420](https://doi.org/10.1103/PhysRevA.79.023420) (cit. on p. 31).
- [77] S. E. Canton, E. Plésiat, J. D. Bozek, B. S. Rude, P. Declava, and F. Martín. "Direct observation of Young's double-slit interferences in vibrationally resolved photoionization of diatomic molecules." In: *Proc. Natl. Acad. Sci.* 108 (2011), pp. 7302–7306. DOI: [10.1073/pnas.1018534108](https://doi.org/10.1073/pnas.1018534108) (cit. on p. 31).

- [78] G. Hartmann. *Coherence effects of diatomic homonuclear molecules and sequential two-photon processes of noble gases in the photoionization*. PhD thesis, 2014 (cit. on p. 31).
- [79] A. Pier et al. "Chiral photoelectron angular distributions from ionization of achiral atomic and molecular species." In: *Phys. Rev. Res.* 2 (2020), p. 033209. DOI: [10.1103/PhysRevResearch.2.033209](https://doi.org/10.1103/PhysRevResearch.2.033209) (cit. on pp. 33, 145, 153).
- [80] J. E. Lennard-Jones. "The electronic structure of some diatomic molecules." In: *Trans. Farad. Soc.* 25 (1929), p. 668 (cit. on p. 35).
- [81] T. E. Sharp. "Potential-energy curves for molecular hydrogen and its ions." In: *Atomic Data* 2 (1970), p. 119. DOI: [10.1016/S0092-640X\(70\)80007-9](https://doi.org/10.1016/S0092-640X(70)80007-9) (cit. on pp. 36–38).
- [82] M. Born and J. R. Oppenheimer. "Zur Quantentheorie der Molekeln." In: *Ann. Phys.* 84 (1927), p. 457. DOI: [10.1002/andp.19273892002](https://doi.org/10.1002/andp.19273892002) (cit. on p. 37).
- [83] M. Lundqvist, D. Edvardsson, P. Baltzer, and B. Wannberg. "Doppler-free kinetic energy release spectrum of N_2^+2+ ." In: *J. Phys. B* 29 (1996), p. 1489. DOI: [10.1088/0953-4075/29/8/013](https://doi.org/10.1088/0953-4075/29/8/013) (cit. on p. 37).
- [84] M. S. Schöffler et al. "Ultrafast Probing of Core Hole Localization in N_2 ." In: *Science* 320 (2008), p. 920. DOI: [10.1126/science.1154989](https://doi.org/10.1126/science.1154989) (cit. on pp. 37, 39, 130, 131, 141).
- [85] N. A. Cherepkov et al. "Separation of Auger transitions into different repulsive states after K-shell photoionization of N_2 molecules." In: *Phys. Rev. A* 80 (2009), 051404(R). DOI: [10.1103/physreva.80.051404](https://doi.org/10.1103/physreva.80.051404) (cit. on pp. 37, 130, 131, 141).
- [86] S. K. Semenov et al. "Auger decay of gerade and ungerade hole states of the N_2 molecule: Disentangling decay routes from coincidence measurements." In: *Phys. Rev. A* 81 (2010), p. 043426. DOI: [10.1103/PhysRevA.81.043426](https://doi.org/10.1103/PhysRevA.81.043426) (cit. on pp. 37, 130, 131, 141).
- [87] D. Metz. *Symmetriebrechung und Elektronenkorrelationen*. PhD thesis, 2016 (cit. on pp. 37, 53, 83).
- [88] I. Kaplan and A. Markin. "Interference phenomena in the photoionization of molecules." In: *Dokl. Akad. Nauk SSSR* 184 (1969), p. 66 (cit. on p. 39).
- [89] D. Akoury et al. "The Simplest Double Slit: Interference and Entanglement in Double Photoionization of H_2 ." In: *Science* 318 (2007), p. 949. DOI: [10.1126/science.1144959](https://doi.org/10.1126/science.1144959) (cit. on pp. 39, 115–117).
- [90] T. Weber et al. "Complete photo-fragmentation of the deuterium molecule." In: *Nature* 431.7007 (2004), pp. 437–440 (cit. on pp. 39, 71, 102).
- [91] D. A. Horner, S. Miyabe, T. N. Rescigno, C. W. McCurdy, F. Morales, and F. Martín. "Classical two-slit interference effects in double photoionization of molecular hydrogen at high energies." In: *Phys. Rev. Lett.* 101 (2008), p. 183002. DOI: [10.1103/PhysRevLett.101.183002](https://doi.org/10.1103/PhysRevLett.101.183002) (cit. on pp. 39, 116).
- [92] J. Fernández, O. Fojón, A. Palacios, and F. Martín. "Interferences from fast electron emission in molecular photoionization." In: *Phys. Rev. Lett.* 98 (2007), p. 043005. DOI: [10.1103/PhysRevLett.98.043005](https://doi.org/10.1103/PhysRevLett.98.043005) (cit. on p. 39).
- [93] K. Kreidi et al. "Interference in the collective electron momentum in double photoionization of H_2 ." In: *Phys. Rev. Lett.* 100 (2008), p. 133005. DOI: [10.1103/PhysRevLett.100.133005](https://doi.org/10.1103/PhysRevLett.100.133005) (cit. on pp. 39, 115, 125).

- [94] L. Ph. H. Schmidt et al. "Momentum transfer to a free floating double slit: Realization of a thought experiment from the Einstein-bohr debates." In: *Phys. Rev. Lett.* 111 (2013), p. 103201. DOI: [10.1103/PhysRevLett.111.103201](https://doi.org/10.1103/PhysRevLett.111.103201) (cit. on p. 39).
- [95] M. Waitz et al. "Two-Particle Interference of Electron Pairs on a Molecular Level." In: *Phys. Rev. Lett.* 117 (2016), p. 083002. DOI: [10.1103/PhysRevLett.117.083002](https://doi.org/10.1103/PhysRevLett.117.083002) (cit. on pp. 39, 115, 117, 120, 125).
- [96] B. Zimmermann et al. "Localization and loss of coherence in molecular double-slit experiments." In: *Nat. Phys.* 4 (2008), p. 649. DOI: [10.1038/nphys993](https://doi.org/10.1038/nphys993) (cit. on pp. 39, 40).
- [97] J. Fernandez, F. L. Yip, T. N. Rescigno, C. W. McCurdy, and F. Martin. "Two-center effects in one-photon single ionization of H_2^+ , H_2 , and Li_2^+ with circularly polarized light." In: *Phys. Rev. A* 79 (2009), p. 043409. DOI: [10.1103/PhysRevA.79.043409](https://doi.org/10.1103/PhysRevA.79.043409) (cit. on p. 39).
- [98] M. S. Schöffler et al. "Photo-double-ionization of H_2 : Two-center interference and its dependence on the internuclear distance." In: *Phys. Rev. A* 78 (2008), p. 013414. DOI: [10.1103/PhysRevA.78.013414](https://doi.org/10.1103/PhysRevA.78.013414) (cit. on pp. 39, 71, 74, 115, 116).
- [99] N. A. Cherepkov et al. "Auger decay of $1\sigma_g$ and $1\sigma_u$ hole states of the N_2 molecule. II. Young-type interference of Auger electrons and its dependence on internuclear distance." In: *Phys. Rev. A* 82 (2010), p. 023420. DOI: [10.1103/PhysRevA.82.023420](https://doi.org/10.1103/PhysRevA.82.023420) (cit. on pp. 39, 130).
- [100] T. Jahnke et al. "Circular Dichroism in K-Shell Ionization from Fixed-in-Space CO and N_2 Molecules." In: *Phys. Rev. Lett.* 88 (2002), p. 073002. DOI: [10.1103/PhysRevLett.88.073002](https://doi.org/10.1103/PhysRevLett.88.073002) (cit. on p. 40).
- [101] D. Rolles et al. "Isotope-induced partial localization of core electrons in the homonuclear molecule N_2 ." In: *Nature* 437 (2005), p. 711. DOI: [10.1038/nature04040](https://doi.org/10.1038/nature04040) (cit. on p. 40).
- [102] K. Ueda. "To Be or Not to Be Localized." In: *Science* 320 (2008), p. 884. DOI: [10.1126/science.1157968](https://doi.org/10.1126/science.1157968) (cit. on p. 40).
- [103] H. Sann et al. "Delocalization of a Vacancy across Two Neon Atoms Bound by the van der Waals Force." In: *Phys. Rev. Lett.* 117 (2016), p. 263001. DOI: [10.1103/PhysRevLett.117.263001](https://doi.org/10.1103/PhysRevLett.117.263001) (cit. on p. 40).
- [104] M. Kunitski et al. "Double-slit photoelectron interference in strong-field ionization of the neon dimer." In: *Nat. Comm.* 10 (2019). DOI: [10.1038/s41467-018-07882-8](https://doi.org/10.1038/s41467-018-07882-8) (cit. on p. 40).
- [105] J. Itatani, J. Lavesque, D. Zeidler, H. Niikura, H. Pepin, J. C. Kieffer, P. B. Corkum, and D. M. Villeneuve. "Tomographic imaging of molecular orbitals." In: *Nature* 432 (2004), p. 867. DOI: [10.1038/nature03183](https://doi.org/10.1038/nature03183) (cit. on p. 40).
- [106] R. Santra. "Imaging molecular orbitals using photoionization." In: *Chem. Phys.* 329 (2006), p. 357. DOI: [10.1016/j.chemphys.2006.07.008](https://doi.org/10.1016/j.chemphys.2006.07.008) (cit. on p. 40).
- [107] N. Stolterfoht et al. "Evidence for Interference Effects in Electron Emission from H_2 Colliding with 60 MeV/u Kr_{34}^+ Ions." In: *Phys. Rev. Lett.* 87 (2001), p. 023201. DOI: [10.1103/PhysRevLett.87.023201](https://doi.org/10.1103/PhysRevLett.87.023201) (cit. on p. 40).

- [108] D. Misra, U. Kadhane, Y. P. Singh, L. C. Tribedi, P. D. Fainstein, and P. Richard. "Interference effect in electron emission in heavy ion collisions with H₂ detected by comparison with the measured electron spectrum from atomic hydrogen." In: *Phys. Rev. Lett.* 92 (2004), p. 153201. DOI: [10.1103/PhysRevLett.92.153201](https://doi.org/10.1103/PhysRevLett.92.153201) (cit. on p. 40).
- [109] N. Dhankhar and R. Choubisa. "Electron impact single ionization of hydrogen molecule by twisted electron beam." In: *J. Phys. B* 54 (2020), p. 015203. DOI: [10.1088/1361-6455/abcb52](https://doi.org/10.1088/1361-6455/abcb52) (cit. on p. 40).
- [110] G. L. Yudin, S. Chelkowski, and A. D. Bandrauk. "Coulomb continuum effects in molecular interference." In: *J. Phys. B* 39 (2006), p. L17. DOI: [10.1088/0953-4075/39/2/L01](https://doi.org/10.1088/0953-4075/39/2/L01) (cit. on p. 42).
- [111] A. H. Zewail. "Laser Femtochemistry." In: *Science* 242 (1998), p. 1645. DOI: [10.1038/7275824a](https://doi.org/10.1038/7275824a) (cit. on p. 44).
- [112] G. Sansone, E. Benedetti, F. Calegari, and C. Vozzi. "Isolated Single-Cycle Attosecond Pulses." In: *Science* 314 (2006), p. 443. DOI: [DOI: 10.1126/science.1132838](https://doi.org/10.1126/science.1132838) (cit. on p. 44).
- [113] H. Kossmann, O. Schwarzkopf, B. Kämmerling, and V. Schmidt. "Unexpected behaviour of double photoionization in H₂." In: *Phys. Rev. Lett.* 63 (1989), p. 2040. DOI: [10.1103/PhysRevLett.63.2040](https://doi.org/10.1103/PhysRevLett.63.2040) (cit. on p. 48).
- [114] B. Zimmermann, V. McKoy, S. H. Southworth, E. P. Kanter, B. Krässig, and R. Wehlitz. "Dipole and nondipole photoionization of molecular hydrogen." In: *Phys. Rev. A* 91 (2015), p. 053410. DOI: [10.1103/PhysRevA.91.053410](https://doi.org/10.1103/PhysRevA.91.053410) (cit. on p. 48).
- [115] P. W. Langhoff, J. C. Arce, J. A. Sheehy, O. Hemmers, H. Wang, P. Focke, I. A. Sellin, and D. W. Lindle. "On the angular distributions of electrons photoejected from fixed-in-space and randomly oriented molecules." In: *J. Electron Spectrosc. Relat. Phenom.* 114-116 (2001), p. 23. DOI: [10.1016/S0368-2048\(00\)00418-7](https://doi.org/10.1016/S0368-2048(00)00418-7) (cit. on p. 48).
- [116] O. Hemmers, H. Wang, P. Focke, I. A. Sellin, D. W. Lindle, J. C. Arce, J. A. Sheehy, and P. W. Langhoff. "Large Nondipole Effects in the Angular Distributions of K-Shell Photoelectrons from Molecular Nitrogen." In: *Phys. Rev. Lett* 87 (2001), p. 273003. DOI: [10.1103/PhysRevLett.87.273003](https://doi.org/10.1103/PhysRevLett.87.273003) (cit. on p. 48).
- [117] K. Hosaka, J. Adachi, A. V. Golovin, M. Takahashi, T. Teramoto, N. Watanabe, A. Yagishita, S. K. Semenov, and N. A. Cherepkov. "Nondipole effects in the angular distribution of photoelectrons from the K-shell of the N₂ molecule." In: *J. Phys. B* 39 (2006), p. L25. DOI: [10.1088/0953-4075/39/2/L02](https://doi.org/10.1088/0953-4075/39/2/L02) (cit. on p. 48).
- [118] O. Hemmers et al. "Low-energy nondipole effects in molecular nitrogen valence-shell photoionization." In: *Phys. Rev. Lett.* 97 (2006), p. 103006. DOI: [10.1103/PhysRevLett.97.103006](https://doi.org/10.1103/PhysRevLett.97.103006) (cit. on p. 48).
- [119] K. Hosaka et al. "Nondipole effects in the angular distribution of photoelectrons from the C K shell of the CO molecule." In: *Phys. Rev A* 73 (2006), p. 022716. DOI: [10.1103/PhysRevA.73.022716](https://doi.org/10.1103/PhysRevA.73.022716) (cit. on p. 48).
- [120] A. N. Grum-Grzhimailo. "On the angular distributions in molecular photoionization beyond the dipole approximation." In: *J. Phys. B* 36 (2003), p. 2385. DOI: [10.1088/0953-4075/36/12/301](https://doi.org/10.1088/0953-4075/36/12/301) (cit. on p. 48).

- [121] G. M. Seabra, I. G. Kaplan, and J. V. Ortiz. "Molecular photoionization cross sections in electron propagator theory: Angular distributions beyond the dipole approximation." In: *J. Chem. Phys.* 123 (2005), p. 114105. DOI: [10.1063/1.2043087](https://doi.org/10.1063/1.2043087) (cit. on p. 48).
- [122] H. Liang, M.-X. Wang, X.-R. Xiao, Q. Gong, and L.-Y. Peng. "Photon-momentum transfer in diatomic molecules: An ab initio study." In: *Phys. Rev. A* 98 (2018), p. 063413. DOI: [10.1103/PhysRevA.98.063413](https://doi.org/10.1103/PhysRevA.98.063413) (cit. on p. 48).
- [123] M. Kircher et al. "Photon-Momentum-Induced Molecular Dynamics in Photoionization of N₂ at $h\nu = 40$ keV." In: *Phys. Rev. Lett.* 123 (2019), p. 193001. DOI: [10.1103/PhysRevLett.123.193001](https://doi.org/10.1103/PhysRevLett.123.193001) (cit. on p. 48).
- [124] R. Guillemin et al. "Nondipolar electron angular distributions from fixed-in-space molecules." In: *Phys. Rev. Lett.* 89 (2002), p. 033002. DOI: [10.1103/PhysRevLett.89.033002](https://doi.org/10.1103/PhysRevLett.89.033002) (cit. on p. 48).
- [125] M. Kircher et al. "Recoil-Induced Asymmetry of Nondipole Molecular Frame Photoelectron Angular Distributions in the Hard X-ray Regime." In: *Phys. Rev. Lett.* 123 (2019), p. 243201. DOI: [10.1103/PhysRevLett.123.243201](https://doi.org/10.1103/PhysRevLett.123.243201) (cit. on p. 48).
- [126] D. Toffoli and P. Decleva. "Photoelectron angular distributions beyond the dipole approximation : a computational study on the N₂ molecule." In: *J. Phys. B* 39 (2006), pp. 2681–2691. DOI: [10.1088/0953-4075/39/12/005](https://doi.org/10.1088/0953-4075/39/12/005) (cit. on pp. 49, 50, 129, 137, 138, 140, 141).
- [127] G. Kastirke. *Angeregt und Abgefragt: Moleküle im Reaktionsmikroskop*. PhD thesis, 2020 (cit. on p. 53).
- [128] J. Viefhaus, F. Scholz, S. Deinert, L. Glaser, M. Ilchen, J. Seltmann, P. Walter, and F. Siewert. "The Variable Polarization XUV Beamline Po₄ at PETRA III : Optics, mechanics and their performance." In: *Nucl. Instrum. Methods Phys. Res. A* 710 (2013), p. 151. DOI: [10.1016/j.nima.2012.10.110](https://doi.org/10.1016/j.nima.2012.10.110) (cit. on p. 53).
- [129] A. Hofmann. *The Physics of Synchrotron Radiation*. Cambridge University Press, 2004. DOI: [10.1017/CB09780511534973](https://doi.org/10.1017/CB09780511534973) (cit. on pp. 53, 54).
- [130] S. Lidia and R. Carr. "An Elliptically-Polarizing Undulator with Phase Adjustable Energy and Polarization." In: *Nucl. Instrum. Methods Phys. Res. A* 347 (1994), pp. 77–82. DOI: [10.1016/0168-9002\(94\)91858-9](https://doi.org/10.1016/0168-9002(94)91858-9) (cit. on p. 53).
- [131] K. Wille. "Introduction to Insertion Devices." URL: <http://www.isa.au.dk/accfys/E08/Download/Wille.pdf> (cit. on p. 54).
- [132] T. Jahnke. *Interatomic Coulombic Decay*. PhD thesis, 2005 (cit. on p. 54).
- [133] S. Grundmann. *Observation of the quadrupole contribution to photo-double-ionization of helium*. Master thesis, 2018 (cit. on pp. 54, 70).
- [134] M. S. Schöffler. *Entwicklung und Aufbau eines Abbildungssystems zur Messung von Elektronen jenseits niedriger Energien*. Diploma thesis, 2002 (cit. on pp. 54, 70).
- [135] W. C. Wiley and I. H. McLaren. "Time-of-Flight Mass Spectrometer with Improved Resolution." In: *Rev. Sci. Instrum.* 26 (1955), pp. 1150–1157. DOI: [10.1063/1.1715212](https://doi.org/10.1063/1.1715212) (cit. on p. 55).
- [136] J. L. Wiza. "Microchannel plate detectors." In: *Nucl. Instrum. Meth.* 162 (1979), pp. 587–601. DOI: [10.1016/0029-554X\(79\)90734-1](https://doi.org/10.1016/0029-554X(79)90734-1) (cit. on p. 56).

- [137] O. Jagutzki, J. S. Lapington, L. B. C. Worth, U. Spillman, V. Mergel, and H. Schmidt-Böcking. “Position sensitive anodes for MCP read-out using induced charge measurement.” In: *Nucl. Instrum. Methods Phys. Res. A* 477 (2002), p. 256. DOI: [10.1016/S0168-9002\(01\)01843-5](https://doi.org/10.1016/S0168-9002(01)01843-5) (cit. on p. 56).
- [138] O. Jagutzki et al. “Multiple hit readout of a microchannel plate detector with a three-layer delay-line anode.” In: *IEEE Transactions on Nuclear Science* 49 (2002), pp. 2477–2483. DOI: [10.1109/TNS.2002.803889](https://doi.org/10.1109/TNS.2002.803889) (cit. on pp. 56, 63).
- [139] K. Fehre et al. “Absolute ion detection efficiencies of microchannel plates and funnel microchannel plates for multi-coincidence detection.” In: *Review of Scientific Instruments* 89 (2018), p. 045112. DOI: [10.1063/1.5022564](https://doi.org/10.1063/1.5022564) (cit. on p. 56).
- [140] S. Grundmann et al. “Revealing the two-electron cusp in the ground states of He and H₂ via quasifree double photoionization.” In: *Phys. Rev. Res.* 2 (2020), p. 033080. DOI: [10.1103/PhysRevResearch.2.033080](https://doi.org/10.1103/PhysRevResearch.2.033080) (cit. on pp. 59, 61, 88, 101, 102, 106, 110–113, 186).
- [141] S. Grundmann et al. “Separating Dipole and Quadrupole Contributions to Single-Photon Double Ionization.” In: *Phys. Rev. Lett.* 121 (2018), p. 173003. DOI: [10.1103/PhysRevLett.121.173003](https://doi.org/10.1103/PhysRevLett.121.173003) (cit. on pp. 59, 88, 108, 109, 186).
- [142] J. Rist. *Nachweis und Zerfallsraten von ICD in Argon-Dimeren*. Master thesis, 2015 (cit. on pp. 63, 72).
- [143] M. Hattass, T. Jalowy, A. Czasch, T. Weber, T. Jahnke, S. Schössler, L. P. Schmidt, O. Jagutzki, R. Dörner, and H. Schmidt-Böcking. “A 2pi spectrometer for electron-electron coincidence studies on surfaces.” In: *Rev. Sci. Instrum.* 75 (2004), p. 2373. DOI: [10.1063/1.1765764](https://doi.org/10.1063/1.1765764) (cit. on p. 67).
- [144] R. N. Zare. “Photoejection Dynamics.” In: *Mol. Photochem.* 4 (1972), pp. 1–37 (cit. on p. 71).
- [145] L. Ph. H. Schmidt, T. Jahnke, A. Czasch, M. Schöffler, H. Schmidt-Böcking, and R. Dörner. “Spatial imaging of the H₂⁺ vibrational wave function at the quantum limit.” In: *Phys. Rev. Lett.* 108 (2012), p. 073202. DOI: [10.1103/PhysRevLett.108.073202](https://doi.org/10.1103/PhysRevLett.108.073202) (cit. on p. 71).
- [146] S. Grundmann et al. “Observation of Photoion Backward Emission in Photoionization of He and N₂.” In: *Phys. Rev. Lett.* 124 (2020), p. 233201. DOI: [10.1103/PhysRevLett.124.233201](https://doi.org/10.1103/PhysRevLett.124.233201) (cit. on pp. 88, 90, 93, 95, 96, 186, 199).
- [147] Si-Ge Chen et al. “Photon Momentum Transfer in Single-Photon Double Ionization of Helium.” In: *Phys. Rev. Lett.* 124 (2020), p. 043201. DOI: [10.1103/physrevlett.124.043201](https://doi.org/10.1103/physrevlett.124.043201) (cit. on pp. 88–90, 94, 98, 99, 102, 105, 186).
- [148] S. Grundmann et al. “Zeptosecond birth time delay in molecular photoionization.” In: *Science* 370 (2020), p. 339. DOI: [10.1126/science.abb9318](https://doi.org/10.1126/science.abb9318) (cit. on pp. 88, 118, 122–124, 156, 186, 200).
- [149] H. Liang, S. Grundmann, Y. Fang, L. Geng, Q. Gong, and L. Peng. “Nondipole effects in interference patterns of a two-electron wave.” In: *Phys. Rev. A* 104 (2021), p. L021101. DOI: [10.1103/PhysRevA.104.L021101](https://doi.org/10.1103/PhysRevA.104.L021101) (cit. on pp. 88, 115, 117, 122–125, 127, 186).
- [150] P. Auger. “Direction of emission of photoelectrons.” In: *J. Phys. Radium* 8 (1927), pp. 85–92. DOI: [10.1051/jphysrad:019270080208500](https://doi.org/10.1051/jphysrad:019270080208500) (cit. on p. 89).
- [151] A. Sommerfeld and G. Schur. “Über den Photoeffekt in der K-Schale der Atome.” In: *Ann. Phys.* 4 (1930), p. 409. DOI: [10.1002/andp.19303960402](https://doi.org/10.1002/andp.19303960402) (cit. on pp. 89, 143).

- [152] G. Michaud. "Diffusion Processes in Peculiar A Stars." In: *Astrophys. J.* 160 (1970), p. 641. DOI: [10.1086/150459](https://doi.org/10.1086/150459) (cit. on p. 89).
- [153] S. Vauclair and G. Vauclair. "Element Segregation in Stellar Outer Layers." In: *Ann. Rev. Astron. Astrophys.* 20 (1982), pp. 37–60. DOI: [10.1146/annurev.aa.20.090182.000345](https://doi.org/10.1146/annurev.aa.20.090182.000345) (cit. on p. 89).
- [154] M. J. Seaton. "Momentum transfer in photo-ionization processes." In: *J. Phys. B: At. Mol. Opt. Phys.* 28 (1995), p. 3185. DOI: [10.1088/0953-4075/28/15/011](https://doi.org/10.1088/0953-4075/28/15/011) (cit. on p. 89).
- [155] M. J. Seaton. "Levitation." In: *Astrophys. Space Sci.* 237 (1996), pp. 107–123. DOI: doi.org/10.1007/BF02424428 (cit. on p. 89).
- [156] G. Massacrier. "Momentum transfer in photoionization of one-electron ions." In: *Astron. Astrophys.* 309 (1996), pp. 979–990 (cit. on p. 89).
- [157] G. Michaud, G. Alecian, and J. Richer. *Atomic Diffusion in Stars*. Cham: Springer, 2015. DOI: [10.1007/978-3-319-19854-5](https://doi.org/10.1007/978-3-319-19854-5) (cit. on p. 89).
- [158] V. Schmidt. "The power and beauty of ($\gamma,2e$) experiments." In: *Pramana - J. Phys.* 50 (1998), pp. 501–514. DOI: [10.1007/BF02846041](https://doi.org/10.1007/BF02846041) (cit. on pp. 101, 110).
- [159] J. H. McGuire. *Electron Correlation Dynamics in Atomic Collisions*. Cambridge: Cambridge University Press, 1997 (cit. on p. 101).
- [160] J. A. R. Samson. "Proportionality of electron-impact ionization to double photoionization." In: *Phys. Rev. Lett.* 65 (1990), pp. 2861–2864. DOI: [10.1103/PhysRevLett.65.2861](https://doi.org/10.1103/PhysRevLett.65.2861) (cit. on p. 101).
- [161] R. Dörner et al. "Fully differential cross sections for double photoionization of He measured by recoil ion momentum spectroscopy." In: *Phys. Rev. Lett.* 77.6 (1996), pp. 1024–1027. DOI: [10.1103/PhysRevLett.77.1024](https://doi.org/10.1103/PhysRevLett.77.1024) (cit. on p. 101).
- [162] V. V. Serov and B. B. Joulakian. "Implementation of the external complex scaling method in spheroidal coordinates: Impact ionization of molecular hydrogen." In: *Phys. Rev. A* 80 (2009), p. 062713. DOI: [10.1103/PhysRevA.80.062713](https://doi.org/10.1103/PhysRevA.80.062713) (cit. on p. 102).
- [163] A. G. Galstyan, O. Chuluunbaatar, Yu. V. Popov, and B. Piraux. "Effects of photon momentum in nonrelativistic ($\gamma,2e$) processes." In: *Phys. Rev. A* 85 (2012), p. 023418. DOI: [10.1103/PhysRevA.85.023418](https://doi.org/10.1103/PhysRevA.85.023418) (cit. on p. 108).
- [164] D. R. Yarkony. *Modern Electronic Structure Theory*. Singapore: World Scientific Publishing, 1995, pp. 459–500 (cit. on p. 110).
- [165] A. S. Eddington. *Fundamental Theory*. Cambridge: Cambridge University Press, 1946 (cit. on p. 110).
- [166] A. J. Thakkar and V. H. Smith Jr. "Accurate charge densities and two-electron intracule functions for the heliumlike ions." In: *J. Chem. Phys.* 67.3 (1977), pp. 1191–1196. DOI: [10.1063/1.434974](https://doi.org/10.1063/1.434974) (cit. on p. 111).
- [167] T. Koga and K. Matsui. "Optimal Hylleraas wave functions." In: *Z. Phys. D Atom. Mol. Cl.* 27.2 (1993), pp. 97–102. DOI: [10.1007/BF01426755](https://doi.org/10.1007/BF01426755) (cit. on p. 111).
- [168] R. P. Feynman. *The Feynman Lectures on Physics, Volume III: Quantum Mechanics*. New York: Basic Books, 1965 (cit. on p. 115).
- [169] W. Zurek. "Decoherence and the Transition from Quantum to Classical." In: *Physics Today* 44 (1991), p. 36. DOI: [10.1063/1.881293](https://doi.org/10.1063/1.881293) (cit. on p. 116).

- [170] K. Hornberger, S. Uttenthaler, B. Brezger, L. Hackermüller, M. Arndt, and A. Zeilinger. “Collisional Decoherence Observed in Matter Wave Interferometry.” In: *Phys. Rev. Lett.* 90 (2003), p. 160401. DOI: [10.1103/PhysRevLett.90.160401](https://doi.org/10.1103/PhysRevLett.90.160401) (cit. on p. 116).
- [171] L. Hackermüller, K. Hornberger, B. Brezger, A. Zeilinger, and M. Arndt. “Decoherence of matter waves by thermal emission of radiation.” In: *Nature* 427 (2004), p. 711. DOI: [10.1038/nature02276](https://doi.org/10.1038/nature02276) (cit. on p. 116).
- [172] I. A. Ivanov, Anatoli S. Kheifets, and K. T. Kim. “Effect of the finite speed of light in ionization of extended systems.” In: *Sci. Rep.* 11 (2021), p. 21457. DOI: [10.1038/s41598-021-00818-1](https://doi.org/10.1038/s41598-021-00818-1) (cit. on p. 125).
- [173] M. S. Schöffler et al. “Matter wave optics perspective at molecular photoionization: K-shell photoionization and Auger decay of N₂.” In: *New J. Phys.* 13 (2011), p. 095013. DOI: [10.1088/1367-2630/13/9/095013](https://doi.org/10.1088/1367-2630/13/9/095013) (cit. on p. 130).
- [174] R. W. Wetmore and R. K. Boyd. “Theoretical investigation of the dication of molecular nitrogen.” In: *J. Phys. Chem.* 90 (1986), p. 5540. DOI: [10.1021/j100280a013](https://doi.org/10.1021/j100280a013) (cit. on p. 130).
- [175] J. P. Cryan et al. “Molecular frame Auger electron energy spectrum from N₂.” In: *J. Phys. B* 45 (2012), p. 055601. DOI: [10.1088/0953-4075/45/5/055601](https://doi.org/10.1088/0953-4075/45/5/055601) (cit. on p. 130).
- [176] A. Mhamdi. *Molecular-Frame Angular Distributions of Electrons Emitted by Photoionization and Interatomic Coulombic Decay*. PhD Thesis, 2020 (cit. on p. 136).
- [177] A. Landers et al. “Photoelectron Diffraction Mapping: Molecules Illuminated from Within.” In: *Phys. Rev. Lett.* 87 (2001), p. 013002. DOI: [10.1103/PhysRevLett.87.013002](https://doi.org/10.1103/PhysRevLett.87.013002) (cit. on p. 145).
- [178] O. D. McGinnis. *Photoelectron Diffraction Imaging of SF₆*. Bachelor Thesis, 2021 (cit. on p. 145).
- [179] A. Pier. *Konstruktion und Aufbau eines stationären COLTRIMS-Reaktionsmikroskops am PETRA III Synchrotron*. Master Thesis, 2021 (cit. on p. 145).
- [180] K. Fehre. *Multikoinzidenzstudien Zur Ionisation Chiraler Moleküle in Kurzen Laserpulsen*. PhD Thesis, 2020 (cit. on p. 145).
- [181] T. Jahnke et al. “Circular Dichroism in K-Shell Ionization from Fixed-in-Space CO and N₂ Molecules.” In: *Phys. Rev. Lett.* 88 (2002), p. 073002. DOI: [10.1103/PhysRevLett.88.073002](https://doi.org/10.1103/PhysRevLett.88.073002) (cit. on p. 155).
- [182] S. Grundmann, T. Jahnke, and R. Dörner. “Wie ein Photon ein Wasserstoffmolekül durchquert.” In: *Phys. Unserer Zeit* 52 (2021), pp. 9–10. DOI: [10.1002/piuz.202170106](https://doi.org/10.1002/piuz.202170106) (cit. on p. 187).

Die vorliegende Arbeit basiert auf sechs Publikationen, zu denen der Autor dieser Arbeit einen wesentlichen Beitrag geleistet hat [140, 141, 146–149]. Die behandelten Themen werden in der vorliegenden Arbeit ausführlicher und zusammenhängend dargestellt. Darüber hinaus werden aber auch einige bislang unveröffentlichte Ergebnisse präsentiert.

Die Arbeit befasst sich mit Experimenten zur Photoionisation von einzelnen Atomen und Molekülen bei Photonenenergien zwischen 385 eV und 2160 eV. Photoionisation bezeichnet hier die Emission von einem oder mehreren Elektronen aus einem Atom oder einem Molekül ausgelöst durch die Absorption eines einzelnen Photons. Der untersuchte Energiebereich lässt sich in der theoretischen Beschreibung der Photoionisation nicht mehr im Rahmen der elektrischen Dipolnäherung beschreiben und wir sprechen hier deshalb von *nicht-dipol-Photoionisation*. Die elektrische Dipolnäherung vernachlässigt sowohl die Ortsabhängigkeit des elektromagnetischen Feldes als auch den Photonenimpuls. Die vorliegende Arbeit fokussiert sich auf die Untersuchung des Einflusses dieser beiden Eigenschaften auf den Photoionisationsprozess.

Teil I liefert die physikalischen und mathematischen Grundlagen, die notwendig sind, um die experimentellen Ergebnisse zu verstehen und einzuordnen. Teil I umfasst die Kapitel 2 bis 7.

Kapitel 2 beschreibt, wo der Gültigkeitsbereich der elektrischen Dipolnäherung endet. Das ist der Fall, wenn der Photonenimpuls vergleichbar groß ist wie die Impulse der Reaktionsfragmente oder wenn die Wellenlänge des Lichts von vergleichbarer Größe ist wie die räumliche Ausdehnung des Systems, das ionisiert wird. Letzterer Zusammenhang wird in Abbildung 2.1 illustriert.

Kapitel 3 behandelt den Wirkungsquerschnitt der Photoionisation. Der Wirkungsquerschnitt liefert ein Maß für die Wahrscheinlichkeit, mit der ein bestimmter Ausgang einer Reaktion zu erwarten ist. Der Wirkungsquerschnitt lässt sich aus theoretischen Modellen berechnen und in Experimenten messen. Er eignet sich daher gut für Vergleiche zwischen Experiment und Theorie. Anhand eines Minimalbeispiels wird im Kapitel 3 der Wirkungsquerschnitt für die Photoionisation eines Elektrons aus einem *s*-Orbital hergeleitet. Gleichung 3.27 entspricht dem Ergebnis dieser Herleitung. In Abbildung 3.1 und in Tabelle 3.1 werden einige Ergebnisse, die sich aus Gleichung 3.27 ergeben, mit ausgefeilteren Berechnungen des Wirkungsquerschnitts verglichen. Gemessen an der Einfachheit der Herleitung liefert Gleichung 3.27 erstaunlich gute Ergebnisse.

Kapitel 4 befasst sich mit der Winkelverteilung von Photoelektronen im Laborsystem. Zunächst wird die Winkelverteilung eines Photoelektrons aus einem *s*-Orbital diskutiert. Der verwendete nicht-dipol-Wechselwirkungsoperator (Gleichung 4.3) führt hierbei zu einem reinen Dipolübergang, einem Mischterm und einem reinen Quadrupolübergang. Der Mischterm beschreibt die Interferenz zwischen dem Dipol- und dem Quadrupolbeitrag. Wie Abbildung 4.2 veranschaulicht, haben alle drei Beiträge unterschiedliche Auswirkungen auf die Winkelverteilung der Photoelektronen. Den stärksten Beitrag zur Photoionisation liefert in der Regel der Dipolbeitrag. Der Mischterm ist für die vorwärts-rückwärts-Asymmetrie in Lichtausbreitungsrichtung verantwortlich. Der Quadrupolbeitrag ist schwach gegenüber dem Dipolbeitrag und kommt nur selten direkt zum Vorschein. Ein Beispiel für das Produkt des reinen Quadrupolbeitrags zur Photoionisation ist der *quasifree mechanism*, der in Kapitel 5 eingeführt wird.

Schließlich wird im Kapitel 4 noch eine Formel zur Beschreibung von Winkelverteilungen anhand verschiedener Parameter hergeleitet. Gleichung 4.25 entspricht dieser Formel für zirkular polarisiertes Licht. Die Abhängigkeit der Form der Photoelektronenwinkelverteilung von den verschiedenen Parametern ist in den Abbildungen 4.3 & 4.4 illustriert.

Für die Beschreibung der Photoionisation wird in den ersten Kapiteln vereinfachend angenommen, dass ein Photon auch nur ein einzelnes Elektron aus dem System ionisieren kann. Es wird dabei von Einfachionisation gesprochen. In Kapitel 5 werden nun die physikalischen Prozesse beschrieben, die dafür sorgen, dass mehrere Elektronen als Folge auf die Absorption eines einzelnen Photons emittiert werden können.

Aufgrund ihrer sehr ähnlichen elektronischen Struktur gelten für He und H₂ hierbei die gleichen Zusammenhänge. Die Doppelionisation dieser beiden Systeme geschieht über einen von drei Prozessen: (1) Der *Two-step-one* (TS₁) ist ein zweistufiger Prozess. Zunächst wird ein vergleichsweise niederenergetisches Elektron durch Einfachionisation erzeugt. Dieses erste Elektron kann nun das zweite durch einen Stoß aus dem System herausschlagen. (2) Beim *shake-off* (SO) verlässt zunächst ein vergleichsweise hochenergetisches Elektron das System. Aufgrund der Verschränkung der elektronischen Anfangszustände kann daraufhin ein weiteres Elektron aus dem System entkommen. (3) Der letzte der Doppelionisationsprozesse ist der *quasifree mechanism* (QFM). Der QFM ist ein reiner quadrupol-Effekt, denn die Dipolauswahlregeln verbieten das kinematische Profil des QFM im Endzustand: Zwei Elektronen mit nahezu gleicher Energie, deren Impulsvektoren einen Winkel von 180° einschließen, und damit einen verschwindenden Rückstoßimpuls. Die Benennung des QFM leitet sich aus der Anschauung ab, dass die Doppelionisation hier frei von der Beteiligung der Atomkerne geschieht. Abbildung 5.1 zeigt die Feynman-Diagramme der drei Prozesse.

Abschließend wird in Kapitel 5 kurz die K-Schalen-Ionisation von N₂ und der darauf folgende Zerfall unter Emission eines Auger-Elektrons beschrieben.

Kapitel 6 befasst sich ausführlich mit dem *Doppelspaltexperiment an zweiatomigen Molekülen*.¹ Wenn kohärente Wellen aus zwei nahe beieinanderliegenden Spalten emittiert werden, erzeugen sie auf einem Nachweisschirm ein Interferenzmuster (siehe Abbildung 6.2). Wird ein Elektron aus einem homonuklearen zweiatomigen Molekül wie H₂ oder N₂ durch Photoionisation emittiert, passiert etwas ganz Ähnliches. Entsprechend dem Welle-Teilchen-Dualismus verhält sich das Elektron wie eine Kugelwelle, welche an beiden Atomen des Moleküls gleichzeitig startet. Beide Teilwellen interferieren und die Auftreffwahrscheinlichkeit auf einem Detektor hängt vom Winkel ab, unter dem das Elektron in Bezug auf die Molekülachse emittiert wurde: Es entsteht ebenfalls das charakteristische Interferenzmuster (siehe Abbildung 6.3).

In Unterkapitel 6.1 werden einige wichtige Einschränkungen der Doppelspaltanalogie zu den durchgeführten Experimenten diskutiert. So treten bei der Doppelionisation von H₂ durch ein Photon die Interferenzeffekte nur auf, wenn das betrachtete Elektron fast die gesamte verfügbare kinetische Energie trägt und das zweite Elektron damit sehr langsam ist. Um hingegen das Interferenzmuster in der Winkelverteilung der Photoelektronen aus der K-Schale des N₂ zu sehen, muss die Parität des Photoelektrons bekannt sein.

Die Auswirkungen von nicht-dipol-Effekten auf das Doppelspaltexperiment an zweiatomigen Molekülen werden in Unterkapitel 6.2 besprochen und man kann sich ihnen aus drei verschiedenen Erklärungsperspektiven nähern. Einerseits kann man sich vorstellen, dass das Molekül zum Zeitpunkt der Photoionisation das ortsabhängige elektrische Feld des Lichts spürt. Die interferierenden

¹Siehe Ref. [182] für eine Publikation des Autors zum Thema in deutscher Sprache.

Elektronen-Teilwellen starten daher je nach Orientierung des Moleküls relativ zum Licht mit unterschiedlichen Phasen. Eine weitere Vorstellung ist die einer Wellenfront mit konstanter Phase, die zu unterschiedlichen Zeitpunkten an den Atomkernen auftritt und die Teilwellen zeitverzögert starten lässt. Diese Modellvorstellung beschreibt das in dieser Arbeit geprägte Konzept des *birth time delays*. Die beiden Perspektiven werden in Abbildung 6.7 grafisch dargestellt. Die dritte Erklärungsperspektive betrachtet den Übertrag des Photonenimpulses auf den Grundzustand der Elektronen und sie ist in Abbildung 6.10 illustriert. Alle drei Perspektiven erklären nahezu gleichermaßen den beobachtbaren nicht-dipol-Effekt beim Doppelspaltexperiment an zweiatomigen Molekülen: Eine Asymmetrie des Interferenzmusters, welches in der Elektronenwinkelverteilung im molekülfesten Koordinatensystem erscheint (siehe Abbildungen 6.6 & 6.8).

In den Kapiteln 5 & 7 wurden die nicht-dipol-Effekte isoliert im labor- bzw. molekülfesten Koordinatensystem beschrieben. Kapitel 7 bringt diese beiden Perspektiven nun zusammen und behandelt wie die Effekte sich gegenseitig beeinflussen. Die Zusammenhänge sind grafisch in den Abbildungen 7.1 & 7.2 dargestellt.

Teil II behandelt die in dieser Arbeit verwendeten Methoden zur Durchführung und Auswertung der Experimente. Teil II umfasst die Kapitel 8 und 9.

Kapitel 8 beschreibt den Aufbau und die Durchführung der Experimente. Für alle Experimente dieser Arbeit wurde ein COLTRIMS-Reaktionsmikroskop verwendet. COLTRIMS steht für *Cold Target Recoil Ion Momentum Spectroscopy* und bezeichnet eine Methode der Impulsspektroskopie. In einem COLTRIMS-Experiment wird ein Projektilstrahl (Photonen, Elektronen oder Ionen) mit einem Strahl des gasförmigen Targets gekreuzt. Die im Überlappungsbereich der beiden Strahlen entstehenden Elektronen und Ionen werden mit elektrischen und magnetischen Feldern auf orts- und zeitauflösende Detektoren geleitet. Das elektrische Feld wird dabei von einem Spektrometer erzeugt und das magnetische Feld von einem Helmholtz-Spulenpaar. Das Spektrometer und die Detektoren befinden sich während des Experiments in einer Vakuumkammer. Das Helmholtz-Spulenpaar befindet sich außerhalb des Vakuums. Die Funktionsweise eines COLTRIMS-Reaktionsmikroskops ist in Abbildung 8.1 dargestellt. Abbildung 8.2 zeigt beispielhaft ein Spektrometer und die Trajektorien von Elektronen und Ionen. Aus den gemessenen Flugzeiten und Auftrefforten lassen sich schließlich die Impulse berechnen, welche die Elektronen und Ionen direkt nach der Reaktion getragen haben. Die Stärke der COLTRIMS-Methode liegt in der Möglichkeit, ein vollständiges Bild des Impulsraums aller in einer Reaktion entstandenen Teilchen gleichzeitig aufzunehmen.

Für diese Arbeit wurden ausschließlich Photonen als Projektile verwendet. Als Photonenquelle diente für alle Experimente die *Variable Polarization XUV Beamline Po4* des Elektronenspeicherrings PETRA III am DESY in Hamburg.

Als Targets wurden He, H₂ und N₂ eingesetzt. Die Daten für diese Arbeit wurden im Rahmen von drei Messzeiten aufgenommen. Während der ersten Messzeit wurde He bei 800 eV und 1100 eV Photonenenergie gemessen. Während der zweiten Messzeit wurde H₂ einer Photonenenergie von 800 eV ausgesetzt. Im Rahmen der letzten Messzeit wurde zunächst N₂ mit Photonenenergien zwischen 880 eV und 2160 eV und später He mit Energien zwischen 300 eV und 1775 eV ionisiert. Weitere Details zu den Messzeiten sind im Unterkapitel 8.2 aufgeführt.

Kapitel 9 behandelt die Auswertung der aufgenommenen Rohdaten. Zunächst wird dargestellt, wie aus den Detektorsignalen die Auftrefforte (Gleichung 9.1) und die Flugzeiten (Gleichungen 9.2 & 9.3) der Teilchen ermittelt werden. Durch die Auswahl von physikalisch sinnvollen Flugzeiten und Auftrefforten der Teilchen können die Rohdaten vorsortiert werden, um den Rechenaufwand der anschließenden Impulsberechnung möglichst gering zu halten. Unterkapitel 9.2 stellt dar,

wie die Elektronenimpulse aus den Flugzeiten und Auftrefforten, unter Berücksichtigung der Spektrometergeometrie und den Stärken des elektrischen und des magnetischen Feldes, berechnet werden (Gleichungen 9.5–9.7). Gleichmaßen zeigt Unterkapitel 9.3 diesen Prozess für Ionen (Gleichungen 9.11 & 9.12). Bei der Impulsberechnung der Ionen mussten einige Besonderheiten des experimentellen Aufbaus und der Ionisation bei hohen Photonenenergien berücksichtigt werden. Einerseits beeinflussten die starken Photonenimpulse die gemessenen Ionenimpulse (siehe Unterkapitel 9.3.1). Andererseits machte auch der Einsatz einer elektrostatischen Linse in der Ionenseite des Spektrometers (siehe Abbildung 8.2) aufwendige Korrekturen erforderlich (siehe Unterkapitel 9.3.2 & 9.3.3).

Teil III stellt die experimentellen Ergebnisse dieser Arbeit dar und vergleicht sie an vielen Stellen mit den Ergebnissen theoretischer Vorhersagen, welche im Rahmen unserer Kollaborationen entstanden sind. Teil III umfasst die Kapitel 10 bis 13.

Kapitel 10 behandelt die vorwärts-rückwärts-Asymmetrien in den Impulsverteilungen der Reaktionsfragmente nach der Photoionisation bei hohen Energien.

In Unterkapitel 10.1 wird gezeigt, wie sich der Photonenimpuls auf die beiden Reaktionsfragmente der Einfachionisation überträgt. Die experimentellen Ergebnisse zur Einfachionisation von He zwischen 300 eV und 1775 eV Photonenenergie werden mit theoretischen Vorhersagen (Gleichungen 10.1 & 10.2) verglichen und stimmen sehr gut mit diesen überein (siehe Abbildung 10.1). Das Überraschende an den Ergebnissen ist, dass die Impulsverteilung der Elektronen im Mittel um $8/5$ des Photonenimpulses in Lichtausbreitungsrichtung nach vorne verschoben ist. Entsprechend der Impulserhaltung ist der Mittelwert der Ionenverteilung um $-3/5$ des Photonenimpulses in die Richtung der Lichtquelle verschoben (siehe Abbildung 10.2). Der Photonenimpuls muss jedoch auf den Massenschwerpunkt übertragen werden und das ist hier näherungsweise das He^+ -Ion. Erwartungsgemäß müsste sich das Ion also von der Lichtquelle wegbewegen. Dieser Widerspruch wird im weiteren Verlauf des Kapitels untersucht. Es zeigt sich, dass der Photonenimpuls in der Tat auf das Ion übertragen wird (siehe Abbildung 10.3). Das Photoelektron erfährt durch die Interferenz zwischen Dipol- und Quadrupolanteilen der möglichen Endzustände einen starken mittleren Impuls in Vorwärtsrichtung (siehe Abbildung 10.4). Der Rückstoßimpuls auf das Ion ist danach so stark, dass er den vorwärts gerichteten Photonenimpulsübertrag überkompensiert.

Schließlich wird in Unterkapitel 10.2 die vorwärts-rückwärts-Asymmetrie der beiden Elektronen bei der Doppelionisation von He untersucht. Wie in Abbildung 10.1 zu sehen ist, verhalten sich die He^{++} -Ionen wie die einfach geladenen Ionen und sie haben im Mittel einen Impuls von $-3/5$ des Photonenimpulses in Richtung der Lichtquelle. In Abbildung 10.5 ist der mittlere Impuls der beiden Elektronen in Lichtausbreitungsrichtung aufgetragen. Es zeigt sich, dass der übertragene Anteil der $8/5$ des Photonenimpulses proportional zum Anteil der Energie eines Elektrons an der Gesamtenergie der beiden Elektronen ist.

In Kapitel 11 werden die Ergebnisse zum QFM (*quasifree mechanism*) der Doppelionisation von He und H_2 untersucht. In der Einleitung des Kapitels wird besprochen, wie der QFM dem Teil des Wechselwirkungsoperators zwischen Licht und zwei Elektronen außerhalb der Dipolnäherung entstammt, der direkt auf die Relativkoordinaten der Elektronen wirkt (siehe Gleichung 11.3). Das unterstreicht, dass der QFM keinen Einfluss auf den Massenschwerpunkt ausübt.

In Unterkapitel 11.1 wird das kinematische Profil des QFM im Endzustand der Doppelionisation gesucht. Der QFM zeichnet sich durch zwei Elektronen mit nahezu gleicher kinetischer Energie aus, deren Impulsvektoren einen Winkel von etwa 180° einschließen. Der Rückstoßimpuls auf das He^{++} -Ion oder den H_2^{++} -Zwischenzustand verschwindet daher. Abbildung 11.1 zeigt die Messung

dieser Rückstoßimpulse für verschiedene Photonenenergien und vergleicht sie mit theoretischen Vorhersagen innerhalb und außerhalb der Dipolnäherung. Nur die nicht-dipol-Berechnungen zeigen einen Beitrag bei niedrigen Rückstoßimpulsen und können damit den QFM richtig vorhersagen. Abbildung 11.2 trägt für die Doppelionisation von He und H₂ bei 800 eV Photonenenergie den Winkel zwischen den beiden Elektronenimpulsvektoren als Funktion der Elektronenenergie auf. Auch in dieser Darstellung erscheint der QFM deutlich. Während die Existenz des QFM für die Doppelionisation von He schon bekannt war, wurde sie für die Doppelionisation von H₂ durch diese Beobachtungen erst bestätigt. Schließlich wird in Abbildung 11.3 gezeigt, dass der Photonenimpuls beim QFM nicht auf das He⁺⁺-Ion übertragen wird.

Unterkapitel 11.2 geht darauf ein, dass der QFM ein reiner Quadrupoleffekt ist. In den Elektronenwinkelverteilungen, die in Abbildung 11.4 gezeigt sind, wird das durch die Vierfachsymmetrie verdeutlicht.

In Unterkapitel 11.3 wird abschließend zum QFM noch gezeigt, wie dessen Wirkungsquerschnitt benutzt werden kann, um Aussagen über den relativen Abstand der Elektronen in einem Zwei-Elektronensystem zu machen.

Kapitel 12 stellt die experimentellen Ergebnisse zum Doppelspaltexperiment am H₂ bei 800 eV Photonenenergie dar und vergleicht diese an einigen Stellen mit theoretischen Vorhersagen.

In Unterkapitel 12.1 werden zunächst Ergebnisse präsentiert, die auch in der Vergangenheit schon aus Experimenten bekannt waren. Jedoch wurden diese Experimente bei niedrigeren Photonenenergien durchgeführt und zeigten daher etwas andere Strukturen in den beobachteten Interferenzmustern. Abbildungen 12.1 & 12.2 unterstreichen die Analogie zwischen dem klassischen Doppelspaltexperiment und der Emission eines schnellen Elektrons während der Doppelionisation von H₂. Die Anzahl und der Abstand der Interferenzmaxima verhalten sich als Funktion des internuklearen Abstands der beiden Protonen ebenso wie die Interferenzstrukturen des klassischen Doppelspalts als Funktion des Spaltabstandes. Die Energieaufteilung zwischen den Elektronen kann als Maß für die Stärke der Dekohärenz herangezogen werden, welche die Interferenzmuster verschwinden lassen kann. Während Abbildung 12.1 C zeigt, wie das Interferenzmuster eines Elektrons graduell als Funktion der Energieaufteilung verschwindet, offenbart Abbildung 12.3, dass die Interferenz unabhängig von der Energieaufteilung für das verschränkte Elektronenpaar erhalten bleibt.

In Unterkapitel 12.2 werden die Auswirkungen der nicht-dipol-Effekte auf das Doppelspaltexperiment am H₂ gezeigt und anhand des *birth time delay*-Konzepts interpretiert. Das betrachtete Elektron trägt hier mindestens 96% der verfügbaren kinetischen Energie.

Die stärkste Verzögerung zwischen der ersten und zweiten Teilwelle ist zu erwarten, wenn das Molekül parallel oder antiparallel zum Licht ausgerichtet ist. Die Strecke, die das Licht vom einen Atom des Moleküls zum anderen zurücklegen muss, ist dann nämlich am längsten. Trifft das Licht hingegen senkrecht zur Molekülachse ein, sollte es keine Verzögerung geben.

Abbildung 12.4 B zeigt das gemessene Interferenzmuster für die parallele Ausrichtung zwischen Licht und Molekül. Hier ist das zentrale Interferenzmaximum etwas nach rechts verschoben. Abbildung 12.4 A stellt das Interferenzmuster umfassend als Funktion des Winkels zwischen Molekülachse und Lichtausbreitungsrichtung dar. Für jede Spalte dieses Histogramms wurde die Position des zentralen Maximums ermittelt, in eine Zeitverzögerung umgerechnet (Gleichung 6.18) und schließlich in Abbildung 12.4 C aufgetragen. Zum Vergleich stellt die blaue Linie in Abbildung 12.4 C dar, wie lange ein Photon braucht, um die Projektion des

mittleren Bindungsabstands auf die Lichtachse zu überwinden. Unsere Messung deutet auf etwas längere Verzögerungen hin, als es das einfache Modell vorhersagt. Vermutlich kommt diese Abweichung durch einen zusätzlichen Phasenversatz zwischen den beiden Ein-Elektronen-Teilwellen zustande, der durch die Verbindung zum zweiten Elektron entsteht. Belege für diese Vermutung liefern die Ergebnisse in Unterkapitel 12.3, in welchem das Interferenzmuster des verschränkten Elektronenpaares der gleichen Analyse unterzogen wird, wie das des einzelnen schnellen Elektrons im vorigen Unterkapitel. Abbildung 12.5 zeigt das Resultat dieser Analyse. Hier stimmen die experimentellen Ergebnisse innerhalb des systematischen Fehlerbereichs mit den Vorhersagen des *birth time delay*-Modells überein.

Kapitel 13 dokumentiert schließlich den Versuch, die Auswirkungen der nicht-dipol-Effekte am molekularen Doppelspalt auf die vorwärts-rückwärts-Asymmetrie im Laborsystem von Photoelektronen aus der *K*-Schale des N_2 zu beobachten. Voraussetzung hierfür ist ein Verfahren (siehe Unterkapitel 13.1), bei dem durch die Auswahl bestimmter Emissionswinkel des Auger-Elektrons im Molekül und bestimmter kinetischer Energien der Ionen eine Teilmenge der experimentellen Daten isoliert wird, in der eine Parität des Photoelektrons deutlich überwiegt. Erstaunlicherweise konnten solche Verfahren, die in der Vergangenheit bereits erfolgreich eingesetzt wurden, um Photoelektronen von gerader und ungerader Parität zu isolieren, hier nicht verwendet werden (siehe Abbildungen 13.1 & 13.2). Schließlich wurde jedoch festgestellt, dass die Auswahl von Auger-Elektronen, die parallel zur Molekülachse emittiert wurden, überwiegend Photoelektronen gerader Parität isoliert (siehe Abbildungen 13.3, 13.4 & 13.5).

In Unterkapitel 13.2 wird die vorwärts-rückwärts-Asymmetrie dieser geraden Photoelektronen mit der Asymmetrie aller Photoelektronen verglichen. Abbildung 13.6 zeigt diesen Vergleich für alle gemessenen Photonenenergien zwischen 880 eV und 2160 eV. Zusätzlich werden hier die experimentellen Ergebnisse den theoretischen Vorhersagen (siehe Abbildung 7.1) gegenübergestellt. Die experimentellen Ergebnisse erfüllten nicht die Erwartungen und die Abweichungen konnten bislang nicht erklärt werden. Möglicherweise funktionierte hier das Verfahren zum Isolieren von Photoelektronen gerader Parität nicht oder der Unterschied in der vorwärts-rückwärts-Asymmetrie ist schlicht zu klein, um in diesem Experiment entdeckt zu werden. Die Lösung dieser Ungereimtheiten könnte den Gegenstand nachfolgender Forschungsarbeiten darstellen.

DANKSAGUNG

Die experimentelle Forschung der Frankfurter Atomphysik erfordert enormes Teamwork, welches ich in den letzten Jahren sehr genossen habe und ohne das diese Arbeit wohl ziemlich dünn geworden wäre. Hiermit möchte ich mich bei allen Personen bedanken, die mich während meiner Zeit in der Arbeitsgruppe unterstützt und begleitet haben. Einige von euch verdienen besonderen Dank oder einfach ein paar persönliche Worte:

- **Reinhard.*** In den letzten Jahren durfte ich unbeschreiblich viele Erfahrungen auf Konferenzen, Auslandsaufenthalten, Strahlzeiten und natürlich auch an jedem *gewöhnlichen* Tag in der Gruppe sammeln. Das hast du mir alles ermöglicht und dafür bin ich dir ungeheuer dankbar.
- **Till.*** Gefühlst hältst du mit deinem ruhigen Auftreten und deiner Erfahrung die ganze Community zusammen und am Laufen. Auch ich habe davon oft profitiert und mir dein Credo *Alles wird Gut!* oder die ColAHell Sprüche zu Herzen genommen.
- **Markus S.*** Am Anfang meiner Zeit in der Gruppe hast du dir extrem viel Mühe gegeben, um mir alles zum Experiment und zur Auswertung ganz genau zu erklären. Von dieser Grundlage profitiere ich immer noch und du hast mit deiner sympathischen Art entscheidend dazu beigetragen, dass ich nach meinem Bachelorabschluss in der Gruppe geblieben bin.
- **Flo.*** Mit deinem unermüdlichen Einsatz und deiner positiven Laune hast du vielen unserer Experimente zum Erfolg verholfen und immer wieder bewiesen, dass man auf dich einfach immer zählen kann!
- **Daniel.** Während und außerhalb der Arbeit haben wir uns immer grandios verstanden. Du warst häufig mein erster Ansprechpartner bei allen möglichen Angelegenheiten und ich bin sehr froh, dass wir den Weg der Promotion weitestgehend parallel zurücklegen durften.
- **Andi & Nico.** Unser gemeinsamer Einsatz in Hamburg im Februar 2021 war eines meiner Highlights der letzten Jahre. Auch sonst hatten wir immer eine sehr gute Zeit zusammen und waren praktisch immer auf einer Wellenlänge.
- **Gregor & Miriam.** Von euch beiden habe ich echt viel gelernt, insbesondere wie das auf Strahlzeiten *so läuft*. Besonders gerne erinnere ich mich an unsere gemeinsame Zeit bei Klaus-Martin zurück. Trotz der stressigen Lage in der Hamburger Unterwelt konnten wir die Zeit an der Elbe doch insgesamt genießen und das Beste aus der Situation machen.
- **Max K., Isabel & Giammarco.** Insbesondere am Anfang meiner Promotion haben wir viele Strahlzeiten zusammen geschmissen und auch privat viel unternommen. Unser Ausflug nach Bordeaux war phänomenal. Hoffentlich kommen wir alle noch mal zusammen! Max, vielen Dank für deine Hilfe mit den Grafiken und LaTeX. Ohne deinen guten Geschmack wäre diese Arbeit viel weniger hübsch!

*These persons have contributed equally to this work :-)

- **Yannick, Brandon & Josh.** Wir haben uns alle immer super verstanden und eine spektakuläre Zeit in Reno gehabt. An das Novi, McMaster, SixFlags, BurgerMe, den Jeep und viele andere Eindrücke denke ich immer sehr gerne zurück.
- **Nils.** Leider habe ich es nicht geschafft, dich für das Synchrotron-Team anzuwerben, aber für Daniel habe ich mich natürlich gefreut, dass es nicht geklappt hat. Trotzdem hast du bei einigen Strahlzeiten ordentlich mit angepackt, dich hatte ich immer gerne dabei. Die Zeit in Japan zusammen mit Leon, aber auch die Vergiftung am Soleil 2018, die wir gemeinsam durchgemacht haben, werde ich nie vergessen.
- **Kilian.** Wir haben in etwa zur selben Zeit in der Gruppe angefangen, du als Doktorand und ich als Bachelorstudent. Ich war immer sehr beeindruckt von deiner Auffassungsgabe und noch viel mehr von deinem Pragmatismus. Von Letzterem habe ich versucht zu lernen. Ohne dein Vorbild hätte ich sicher etwas länger für die Promotion gebraucht.
- **Sebastian.** Wir haben uns beim Schwimmen, beim Radfahren aber auch im Büro immer sehr gut verstanden. Ich war froh, dich als Diskussionspartner einbeziehen zu können, und habe deine Meinung sehr geschätzt. Ich wünsche dir ganz viel Erfolg für deine Karriere in der Forschung (oder ggf. auch außerhalb).
- **Markus W.** Als ich in die Gruppe kam, hast du mich gleich nett empfangen, mir Arbeitshandschuhe gegeben und mich um 11:37 Uhr mit zum Mittagessen genommen. Ich denke gerne an die Zeit zurück, als du noch unsere LKWs zu den Strahlzeiten gefahren hast. Auch unsere Motorradtouren sind mir in schöner Erinnerung geblieben. Ich hoffe, wir wiederholen das irgendwann mal, gerne auch mit dem Zweirad ohne Motor.
- **Jonas.** Du hast mir am Anfang meiner Zeit in der Gruppe sehr viel beigebracht. Insbesondere auf den gemeinsamen Strahlzeiten und beim Einsatz von SIMION. Deine Methode die Potentiale zu setzen ist wirklich viel praktischer als die von Flo!
- **Max H.** Ich durfte dir unser Labor zeigen, bevor du dich für die Promotion in unserer Gruppe entschieden hast. Danach habe ich mich sehr gefreut, dass du (trotzdem?) zu uns gekommen bist :)
- **Alex H. & Klaus.** Nicht selten waren wir drei am Morgen die ersten auf dem Gang. Ich mochte immer, dass wir so früh am Tag auch mal über Themen außerhalb der Physik reden konnten. Alex, wenn ich mal Nachwuchs haben sollte, hoffe ich dass du einer ihrer Schullehrer sein wirst.
- **Dimi.** Unsere gemeinsamen Ausflüge nach Hamburg habe ich sehr genossen. Ich helfe dir auch gerne in Zukunft noch bei Problemen mit der deutschen Bürokratie!
- **Maksim.** Wir haben zwar nie ein gemeinsames Projekt gehabt, ich habe mich aber immer sehr gerne mit dir in der Kaffeeküche über Investments unterhalten.
- **Kim.** Unser Ausflug zum Reiterhof mit einem Anhänger voller Sand, der dann mit einem Anhänger voller Mist zu Lothars Garten weiterging, war wohl der skurrilste Tag meiner Zeit in der Gruppe. Immerhin konnte ich an dem Tag Sandy kennenlernen und die Zeit mit dir hat generell immer viel Spaß gemacht!

- **Nils, Niklas, Andi, Leon, Jan & Angi.** Ihr habt alle einige Zeit nach mir mit eurer Promotion angefangen und ich habe mich bei jedem (jeder) von euch sehr gefreut, dass er (sie) in der Gruppe bleibt. Schön zu sehen, dass in Zukunft alles in guten Händen ist.
- **Laura & Dennis.** Die Messungen am DESY für eure Abschlussarbeiten und die anschließenden gemeinsamen Auswertungen waren eine tolle Ablenkung vom Schreiben meiner eigenen Arbeit. Ich wünsche euch alles Gute und viel Erfolg für eure kommende Zeit in der Gruppe!
- **Sven S.** Unsere Projekte waren immer eine willkommene Abwechslung, die ich in Zukunft echt vermissen werde. Handwerklich konnte ich viel von dir lernen und auch persönlich habe ich die Zusammenarbeit immer genossen.
- **Lothar.** Du konntest mir in den letzten Jahren wirklich alles beantworten, sogar manchmal Fragen, die ich nicht gestellt habe. Vielen Dank für deine Unterstützung und dafür, dass du immer hilfsbereit bist, wenn es wirklich drauf ankommt.
- **Marianne.** Danke dass du dich immer mit vollem Einsatz um uns Studenten und Doktoranden kümmerst und auf unserer Seite stehst!
- **Anatoli.** Als Student habe ich mir die Zusammenarbeit zwischen Experiment und Theorie immer genau so vorgestellt, wie wir es dann umgesetzt haben. Das war eine tolle Erfahrung. Die Zeit bei dir in Australien war ein Highlight meiner Promotion.
- **Alle Mitinsassen des Büros 01.313.** Mit Hendrik, Kevin, Christoph, Arnab, Derya, Pia, Leonie, Huipeng, Safak, Jonathan, Dennis, Raghu und natürlich Niklas durfte ich mir unser Büro in den letzten Jahren teilen. Ich bin immer sehr gerne ins Büro gekommen, das hat sich nie wirklich angefühlt wie Arbeit. Vielen Dank für die gemeinsame Zeit und die gute Atmosphäre.
- **Heiner, Max & Tim.** Ohne euch hätte das Physikstudium viel weniger Spaß gemacht. Wer weiß, ob ich ohne euch überhaupt bis hierhin gekommen wäre. Vielen Dank für die tolle Freundschaft!

Phys. Rev. X 11 (2021), 041044

Inner-Shell-Ionization-Induced Femtosecond Structural Dynamics of Water Molecules Imaged at an X-Ray Free-Electron Laser

T. Jahnke, R. Guillemin, L. Inhester, S.-K. Son, G. Kastirke, M. Ilchen, J. Rist, D. Trabert, N. Melzer, N. Anders, T. Mazza, R. Boll, A. De Fanis, V. Music, Th. Weber, M. Weller, S. Eckart, K. Fehre, S. Grundmann, A. Hartung, M. Hofmann, C. Janke, M. Kircher, G. Nalin, A. Pier, J. Siebert, N. Strenger, I. Vela-Perez, T. M. Baumann, P. Grychtol, J. Montano, Y. Ovcharenko, N. Rennhack, D. E. Rivas, R. Wagner, P. Ziolkowski, P. Schmidt, T. Marchenko, O. Travnikova, L. Journal, I. Ismail, E. Kukk, J. Niskanen, F. Trinter, C. Vozzi, M. Devetta, S. Stagira, M. Gisselbrecht, A. L. Jäger, X. Li, Y. Malakar, M. Martins, R. Feifel, L. Ph. H. Schmidt, A. Czasch, G. Sansone, D. Rolles, A. Rudenko, R. Moshhammer, R. Dörner, M. Meyer, T. Pfeifer, M. S. Schöffler, R. Santra, M. Simon, and M. N. Piancastelli.

Nat. Commun. 12 (2021), 6657

Measuring the photoelectron emission delay in the molecular frame

J. Rist, K. Klysssek, N. M. Novikovskiy, M. Kircher, I. Vela-Perez, D. Trabert, S. Grundmann, D. Tsitsonis, J. Siebert, A. Geyer, N. Melzer, Ch. Schwarz, N. Anders, L. Kaiser, K. Fehre, A. Hartung, S. Eckart, L. Ph. H. Schmidt, M. S. Schöffler, V. T. Davis, J. B. Williams, F. Trinter, R. Dörner, Ph. V. Demekhin, and T. Jahnke.

Phys. Chem. Chem. Phys. 23 (2021), 17248

Photoelectron circular dichroism of O 1s-photoelectrons of uniaxially oriented trifluoromethyloxirane: energy dependence and sensitivity to molecular configuration

G. Nalin, K. Fehre, F. Trinter, N. M. Novikovskiy, N. Anders, S. Grundmann, D. Trabert, M. Kircher, A. Khan, R. Tomar, M. Hofmann, M. Waitz, I. Vela-Perez, G. Kastirke, J. Siebert, D. Tsitsonis, H. Fukuzawa, K. Ueda, J. B. Williams, D. Kargin, M. Maurer, C. Küstner-Wetekam, L. Marder, J. Viehmann, A. Knie, T. Jahnke, M. Ilchen, R. Dörner, R. Pietschnig, P. V. Demekhin, and M. S. Schöffler.

Phys. Rev. Lett. 127 (2021), 103201

Fourfold Differential Photoelectron Circular Dichroism

K. Fehre, N. M. Novikovskiy, S. Grundmann, G. Kastirke, S. Eckart, F. Trinter, J. Rist, A. Hartung, D. Trabert, C. Janke, G. Nalin, M. Pitzer, S. Zeller, F. Wiegandt, M. Weller, M. Kircher, M. Hofmann, L. Ph. H. Schmidt, A. Knie, A. Hans, L. Ben Ltaief, A. Ehresmann, R. Berger, H. Fukuzawa, K. Ueda, H. Schmidt-Böcking, J. B. Williams, T. Jahnke, R. Dörner, M. S. Schöffler, and Ph. V. Demekhin.

Phys. Rev. A 104 (2021), L021101

Nondipole effects in interference patterns of a two-electron wave

H. Liang, S. Grundmann, Y.-K. Fang, L. Geng, Q. Gong, and L.-Y. Peng.

Nat. Commun. 12 (2021), 1697

Angular dependence of the Wigner time delay upon tunnel ionization of H₂
D. Trabert, S. Brennecke, K. Fehre, N. Anders, A. Geyer, S. Grundmann, M. S. Schöffler, L. Ph. H. Schmidt, T. Jahnke, R. Dörner, M. Kunitski, and S. Eckart.

Faraday Discuss. 228 (2021), 571–596

Multi-channel photodissociation and XUV-induced charge transfer dynamics in strong-field-ionized methyl iodide studied with time-resolved recoil-frame covariance imaging

F. Allum, N. Anders, M. Brouard, P. Bucksbaum, M. Burt, B. Downes-Ward, S. Grundmann, J. Harries, Y. Ishimura, H. Iwayama, L. Kaiser, E. Kukk, J. Lee, X. Liu, R. S. Minns, K. Nagaya, A. Niozu, J. Niskanen, J. Oneal, S. Owada, J. Pickering, D. Rolles, A. Rudenko, S. Saito, K. Ueda, C. Vallance, N. Werby, J. Woodhouse, D. You, F. Ziaee, T. Driver, and R. Forbes.

Science 370 (2020), 339–341

Zeptosecond birth time delay in molecular photoionization

S. Grundmann, D. Trabert, K. Fehre, N. Strenger, A. Pier, L. Kaiser, M. Kircher, M. Weller, S. Eckart, L. Ph. H. Schmidt, F. Trinter, T. Jahnke, M. S. Schöffler, and R. Dörner.

Phys. Rev. Lett. 125 (2020), 163201

Double Core-Hole Generation in O₂ Molecules Using an X-Ray Free-Electron Laser: Molecular-Frame Photoelectron Angular Distributions

G. Kastirke, M. S. Schöffler, M. Weller, J. Rist, R. Boll, N. Anders, T. M. Baumann, S. Eckart, B. Erk, A. De Fanis, K. Fehre, A. Gattori, S. Grundmann, P. Grychtol, A. Hartung, M. Hofmann, M. Ilchen, C. Janke, M. Kircher, M. Kunitski, X. Li, T. Mazza, N. Melzer, J. Montano, V. Music, G. Nalin, Y. Ovcharenko, A. Pier, N. Rennhack, D. E. Rivas, R. Dörner, D. Rolles, A. Rudenko, P. Schmidt, J. Siebert, N. Strenger, D. Trabert, I. Vela Perez, R. Wagner, T. Weber, J. B. Williams, P. Ziolkowski, L. Ph. H. Schmidt, A. Czasch, F. Trinter, M. Meyer, K. Ueda, P. V. Demekhin, and T. Jahnke.

Phys. Rev. Res. 2 (2020), 033209

Chiral photoelectron angular distributions from ionization of achiral atomic and molecular species

A. Pier, K. Fehre, S. Grundmann, I. Vela Perez, N. Strenger, M. Kircher, D. Tsitsonis, J. B. Williams, A. Senftleben, T. Baumert, M. S. Schöffler, P. V. Demekhin, F. Trinter, T. Jahnke, and R. Dörner.

Phys. Rev. Res. 2 (2020), 033080

Revealing the two-electron cusp in the ground states of He and H₂ via quasifree double photoionization

S. Grundmann, V. V. Serov, F. Trinter, K. Fehre, N. Strenger, A. Pier, M. Kircher, D. Trabert, M. Weller, J. Rist, L. Kaiser, A. W. Bray, L. Ph. H. Schmidt, J. B. Williams, T. Jahnke, R. Dörner, M. S. Schöffler, and A. S. Kheifets.

In: *Phys. Rev. Lett.* 124 (2020), 233201

Observation of Photoion Backward Emission in Photoionization of He and N₂

S. Grundmann, M. Kircher, I. Vela Perez, G. Nalin, D. Trabert, N. Anders, N. Melzer, J. Rist, A. Pier, N. Strenger, J. Siebert, P. V. Demekhin, L. Ph. H. Schmidt, F. Trinter, M. S. Schöffler, T. Jahnke, and R. Dörner.

Phys. Rev. X 10 (2020), 021052

Photoelectron Diffraction Imaging of a Molecular Breakup Using an X-Ray Free-Electron Laser

G. Kastirke, M. S. Schöffler, M. Weller, J. Rist, R. Boll, N. Anders, T. M. Baumann, S. Eckart, B. Erk, A. De Fanis, K. Fehre, A. Gatton, S. Grundmann, P. Grychtol, A. Hartung, M. Hofmann, M. Ilchen, C. Janke, M. Kircher, M. Kunitski, X. Li, T. Mazza, N. Melzer, J. Montano, V. Music, G. Nalin, Y. Ovcharenko, A. Pier, N. Rennhack, D. E. Rivas, R. Dörner, D. Rolles, A. Rudenko, P. Schmidt, J. Siebert, N. Strenger, D. Trabert, I. Vela Perez, R. Wagner, T. Weber, J. B. Williams, P. Ziolkowski, L. Ph. H. Schmidt, A. Czasch, F. Trinter, M. Meyer, K. Ueda, P. V. Demekhin, and T. Jahnke.

Nat. Phys. 16 (2020), 756–760

Kinematically complete experimental study of Compton scattering at helium atoms near the threshold

M. Kircher, F. Trinter, S. Grundmann, I. Vela Perez, S. Brennecke, N. Eicke, J. Rist, S. Eckart, S. Houamer, O. Chuluunbaatar, Y. V. Popov, I. P. Volobuev, K. Bagschik, M. N. Piancastelli, M. Lein, T. Jahnke, M. S. Schöffler, and R. Dörner.

Phys. Rev. Lett. 124 (2020), 043201

Photon Momentum Transfer in Single-Photon Double Ionization of Helium

S.-G. Chen, W.-C. Jiang, S. Grundmann, F. Trinter, M. S. Schöffler, T. Jahnke, R. Dörner, H. Liang, M.-X. Wang, L.-Y. Peng, and Q. Gong.

Phys. Rev. Lett. 123 (2019), 243201

Recoil-Induced Asymmetry of Nondipole Molecular Frame Photoelectron Angular Distributions in the Hard X-ray Regime

M. Kircher, J. Rist, F. Trinter, S. Grundmann, M. Waitz, N. Melzer, I. Vela Perez, T. Mletzko, A. Pier, N. Strenger, J. Siebert, R. Janssen, L. Ph. H. Schmidt, A. N. Artemyev, M. S. Schöffler, T. Jahnke, R. Dörner, and Ph. V. Demekhin.

J. Chem. Phys. 151 (2019), 184305

Electron spectroscopic study of nanoplasma formation triggered by intense soft x-ray pulses

A. Niozu, N. Yokono, T. Nishiyama, H. Fukuzawa, T. Sakurazawa, K. Matsuda, T. Takanashi, D. You, Y. Li, T. Ono, T. Gaumnitz, M. Schöffler, S. Grundmann, S. Wada, P. Carpeggiani, W. Q. Xu, X. J. Liu, S. Owada, K. Tono, T. Togashi, M. Yabashi, N. V. Kryzhevoi, K. Gokhberg, A. I. Kuleff, L. S. Cederbaum, K. Ueda, and K. Nagaya.

Phys. Rev. Lett. 123 (2019), 193001

Photon-Momentum-Induced Molecular Dynamics in Photoionization of N₂ at $h\nu = 40$ keV

M. Kircher, J. Rist, F. Trinter, S. Grundmann, M. Waitz, N. Melzer, I. Vela Perez, T. Mletzko, A. Pier, N. Strenger, J. Siebert, R. Janssen, V. Honkimäki, J. Drnec, Ph. V. Demekhin, L. Ph. H. Schmidt, M. S. Schöffler, T. Jahnke, and R. Dörner.

Phys. Rev. Lett. 121 (2018), 243002

Breakdown of the Spectator Concept in Low-Electron-Energy Resonant Decay Processes

A. Mhamdi, J. Rist, D. Aslitürk, M. Weller, N. Melzer, D. Trabert, M. Kircher, I. Vela Perez, J. Siebert, S. Eckart, S. Grundmann, G. Kastirke, M. Waitz, A. Khan, M. S. Schöffler, F. Trinter, R. Dörner, T. Jahnke, and Ph. V. Demekhin.

Phys. Rev. A 98 (2018), 050701(R)

Frustrated Coulomb explosion of small helium clusters

S. Kazandjian, J. Rist, M. Weller, F. Wiegandt, S. Grundmann, D. Aslitürk, G. Nalin, M. Kircher, D. Pitters, I. Vela Perez, M. Waitz, G. Schiwietz, B. Griffin, J. B. Williams, R. Dörner, M. Schöffler, T. Miteva, F. Trinter, T. Jahnke, and N. Sisourat.

Phys. Rev. Lett. 121 (2018), 173003

Separating Dipole and Quadrupole Contributions to Single-Photon Double Ionization

S. Grundmann, F. Trinter, A. W. Bray, S. Eckart, J. Rist, G. Kastirke, D. Metz, S. Klumpp, J. Viefhaus, L. Ph. H. Schmidt, J. B. Williams, R. Dörner, T. Jahnke, M. S. Schöffler, and A. S. Kheifets.

PRESS REVIEW

In response to *Observation of Photoion Backward Emission in Photoionization of He and N₂* [146]:

- "Light can attract atoms and molecules by photoionisation"
DESY Photon Science 2020 Annual Report.
- "C'EST PROUVÉ, LA LUMIÈRE PEUT ATTIRER DE LA MATIÈRE"
(It's proven, light may attract matter)
Science & Vie – August 1, 2020.
- "Fyysikot mittasivat ensi kertaa 1930 ennustetun paradoksin: Kun valo-
hiukkanen iskee atomiin, atomi kimpoaa takaisin eikä eteenpäin"
(Physicists first measured the paradox predicted in 1930: When a particle of
light strikes an atom, the atom bounces back and not forward)
Tekniikka & Talous – June 21, 2020.
- "Fotoeffekt podaril ionam obratnyy impul's"
(Photoelectric effect gave ions a reverse pulse)
nplus1.ru – June 19, 2020.
- "Atomphysik: Strahlungsdruck mit Rückstoß"
(Atomic physics: Radiation pressure with recoil)
Goethe University press release – June 15, 2020.
- "Ion Recoil from Photon Beam Observed"
Physics Magazine – June 9, 2020.

In response to *Zeptosecond Birth Time Delay in Molecular Photoionization* [148]:

- "A photon's journey through a hydrogen molecule is the shortest event ever timed"
ScienceNews – October 27, 2020.
- "Zeptoseconds: new world record in short time measurement"
europhysicsnews 51/5.
- "Scientists Clocked the Shortest Time Period Ever"
VICE – October 20, 2020.
- "Die kürzeste Zeitspanne, die je gemessen wurde"
Spektrum.de – October 19, 2020.
- "Physicists Reach New Record With Shortest Time Measurement Yet"
IFLSCIENCE – October 19, 2020.
- "Deutsche Forscher messen kürzeste je erfasste Zeitspanne"
SPIEGEL ONLINE – October 16, 2020.
- "Physiker messen kürzeste Zeitspanne der Welt"
FAZ.NET – October 16, 2020.
- "Zeptoseconds: New world record in short time measurement"
Goethe University press release – October 16, 2020.

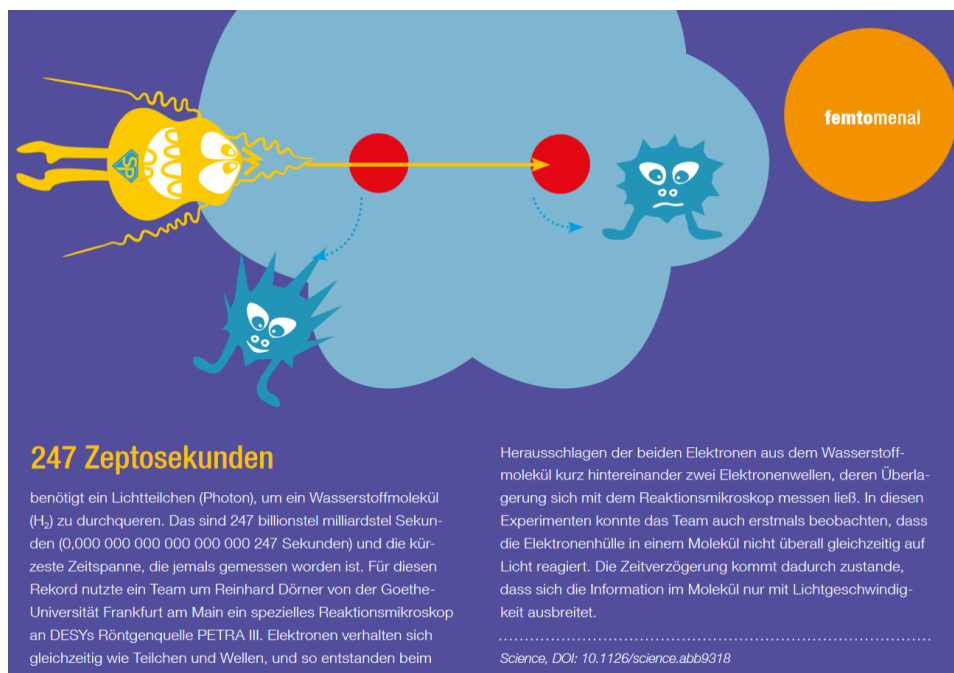


Figure C.18: Comic from **femto**, The DESY research magazine – Issue 01/21.

Inspired by our findings, The Sun investigated the following significant questions in an online article published on October 25, 2020.

”ZEPTOMANIA How many zeptoseconds did Usain Bolt’s 100m World Record & Boris Becker’s quickie take? BOFFINS have measured the smallest period of time ever recorded. To do it researchers at the Goethe University, in Germany, used the zeptosecond, a trillionth of billionth of a second. They found that it takes 247 zeptoseconds for a photon — a type of particle — to cross a hydrogen molecule. Talk about the blink of an eye. The physicists measured the time interval using a technique involving X-rays and a super-powerful microscope. (...) Sarah Arnold reveals how many zeptoseconds it took Usain Bolt to set the 100m World Record, how long Boris Becker’s infamous restaurant “quickie” was (...)

- *Boris Becker’s five-minute Nobu quickie sex:
300,000,000,000 000,000,000,001 zeptoseconds.*
- *Usain Bolt’s 100m World Record:
19,190,000,000,000,000, 000,001 zeptoseconds.*

(...)”

CONTRIBUTIONS TO CONFERENCES AND SEMINARS

07/2021: Talk. The travel time of light across a molecule. 32nd International Conference on Photonic, Electronic and Atomic Collisions (ICPEAC, Virtual).

07/2021: Poster. Observation of photoion backward emission. 32nd International Conference on Photonic, Electronic and Atomic Collisions (ICPEAC, Virtual).

06/2021: Talk. Nondipolar photoionization under the reaction microscope. Seminar Atomphysik GSI.

06/2021: Talk. The travel time of light across a molecule. 52nd Annual Meeting of the APS Division of Atomic, Molecular and Optical Physics (DAMOP, Virtual).

08/2019: Talk. Separating Dipole and Quadrupole Contributions to Single-Photon Double Ionization. 20th International Symposium on Correlation, Polarization and Ionization in Atomic and Molecular Collisions (COPIAMC).

07/2019: Poster. Non-dipole and Quadrupole Photoionization of H₂. 31st International Conference on Photonic, Electronic and Atomic Collisions (ICPEAC).

08/2018: Talk. Separating the Quadrupole Contribution to Photo-Double-Ionization. Tohoku University's Chemistry Summer School.

PRACTICAL EXPERIENCE RELATED TO RESEARCH

- 11/2021:** Electron Storage Ring BESSY II, Berlin, Germany. Beamtime, 2 weeks.
- 09/2021:** PETRA III, DESY, Hamburg, Germany. Beamtime, 1 week.
- 05–06/2021:** PETRA III, DESY, Hamburg, Germany. Beamtime, 2 weeks.
- 05/2021:** PETRA III, DESY, Hamburg, Germany. Assembly of a new target preparation system, 1 week.
- 03/2021:** PETRA III, DESY, Hamburg, Germany. Commissioning beamtime, 1 week.
- 02/2021:** PETRA III, DESY, Hamburg, Germany. Assembly of a new reaction microscope, 2 weeks.
- 08/2020:** PETRA III, DESY, Hamburg, Germany. Beamtime, 1 week.
- 02/2020:** SPring-8 synchrotron radiation facility, Japan. Beamtime, 3 weeks.
- 10–11/2019:** PETRA III, DESY, Hamburg, Germany. Beamtime, 2 weeks.
- 10/2019:** MID, European XFEL, Hamburg, Germany. Beamtime, 1 week.
- 06/2019:** Electron Storage Ring BESSY II, Berlin, Germany. Beamtime, 1 week.
- 04–06/2019:** Australian National University, Canberra, Australia. Research stay, 10 weeks.
- 03–04/2019:** PETRA III, DESY, Hamburg, Germany. Beamtime, 1 week.
- 02–03/2019:** SQS, European XFEL, Hamburg, Germany. Beamtime, 1 week.
- 01/2019:** SQS, European XFEL, Hamburg, Germany. Commissioning of a new reaction microscope and beamtime, 2 weeks.
- 09/2018:** PETRA III, DESY, Hamburg, Germany. Beamtime, 1 week.
- 08–09/2018:** Synchrotron SOLEIL, Saint-Aubin, France. Beamtime, 3 weeks.
- 05–06/2018:** Electron Storage Ring BESSY II, Berlin, Germany. Beamtime, 1 week.
- 04–05/2018:** European Synchrotron Radiation Facility, Grenoble, France. Beamtime, 2 weeks.
- 01–04/2018:** University of Nevada, Reno, Department of Physics, USA. Construction and assembly of a new reaction microscope, 12 weeks.

06–08/2017: Tohoku University Sendai and SPring-8 synchrotron radiation facility, Japan. Research stay and beamtimes, 12 weeks.

04/2017: Synchrotron SOLEIL, Saint-Aubin, France. Beamtime, 1 week.

01–02/2017: Electron Storage Ring BESSY II, Berlin, Germany. Beamtime, 1 week.

10/2016: Synchrotron SOLEIL, Saint-Aubin, France. Beamtime, 1 week.

06/2016: PETRA III, DESY, Hamburg, Germany. Beamtime, 1 week.

05–06/2016: Electron Storage Ring BESSY II, Berlin, Germany. Beamtime, 1 week.

AKADEMISCHER LEBENSLAUF

Sven Eric Grundmann

Geboren am 01.07.1990
in Bad Homburg v. d. Höhe

sven-grundmann@gmx.de



Ausbildung

2018 Goethe Universität, Frankfurt am Main. Master of Science, Physik.

2017 Goethe Universität, Frankfurt am Main. Bachelor of Science, Physik.

2013 Duale Hochschule Baden-Württemberg, Villingen-Schwenningen.
Bachelor of Arts, Betriebswirtschaftslehre.

2010 Augustinerschule, Friedberg. Abitur.

2008 Maple Valley High School, Nashville, Michigan/USA. High School Diploma.

Hochschullehrer

Reinhard Dörner, Till Jahnke, Markus Schöffler, Carsten Greiner, Henner Büsching, Klaus Peters, Benjamin Dönigus, Hartmut Roskos, Michael Lang, Peter Kopietz, Christian Böinghoff, Sven Jarohs, Eberhard Engel, Giuliano Franchetti, Andreas Roth, Robert Grisenti, Marcus Iberler, Ulrich Ratzinger, Claudius Gros, Ulrich Bantleon, Gerhard Hellstern, Eduard Hilger, Andre Kuck, Thomas Häring, Alexander Götz, Michael Bungert, Peter Stebel, Jens Siebert, Marcus Vögtle, Wolfgang Disch.